UNIVERSITY OF OKLAHOMA

GRADUATE COLLEGE

DESIGN AND ASSESSMENT OF INNOVATIVE DUAL-MODE ROLLING ISOLATION SYSTEMS

A DISSERTATION

SUBMITTED TO THE GRADUATE FACULTY

in partial fulfillment of the requirements for the

Degree of

DOCTOR OF PHILOSOPHY

By

MOHAMMAD HADIKHAN TEHRANI
Norman, Oklahoma
2019

DESIGN AND ASSESSMENT OF INNOVATIVE DUAL-MODE
ROLLING ISOLATION SYSTEMS

A DISSERTATION APPROVED FOR THE
SCHOOL OF CIVIL ENGINEERING AND ENVIRONMENTAL SCIENCE

BY

Dr. Philip Scott Harvey Jr., Chair

Dr. Royce W. Floyd

Dr. Kanthasamy K. Muraleetharan

Dr. Yingtao Liu

To my beloved family

Acknowledgements

I would like to express my special appreciation to my advisor Dr. Philip Scott Harvey Jr. for his guidance, advice, mentoring, and support throughout my Ph.D. program. This piece of work would not be possible without his invaluable advisement. I am blessed to have the chance of working with a smart, knowledgeable, kind, and professional advisor like him. He brought the lost confidence back to me by his patience and made the research fun and enjoyable.

Correspondingly, I would like to acknowledge the interest, encouragement, and support of the rest of my committee members: Dr. Kanthasamy K. Muraleetharan, Dr. Royce W. Floyd, and Dr. Yingtao Liu. Their feedback and comments have elevated the quality of this piece of work.

I also would like to extend my gratitude to Dr. Rouzbeh Ghabchi for being the support that I needed in the most challenging times in my Ph.D. program. He always has been there with his endless support.

I would like to span this acknowledgment to my beloved parents and siblings. They have been believing in my abilities and aspirations and providing me with all the possible support, encouragement, and endless love at its best. It would not be possible to be where I am without their enduring support.

Last but not least, I want to thank all my friends, Keyvan Mohammadi, Dr. Shadi Salahshoor, Dr. Hessam Yazdani, Elahe Khosravi, Dr. Hadi Saeidi Manesh, and Elaheh Jafarigol, to name a few, for all their sincere help and support on hard days and making the life fun.

This material is based upon work supported by the National Science Foundation under Grant No. NSF-CMMI-1663376. This support is greatly appreciated.

Contents

List of Figures

List of Tables

Abstract

Loss of operation or devastating damage to buildings and industrial structures, as well as equipment housed in them, has been observed due to earthquake-induced vibrations. A common source of operational downtime is due to the performance reduction of vital equipment, which are sensitive to the total transmitted acceleration. A well-known method of protecting such equipment is seismic isolation of the equipment itself (or a group of equipment), as opposed to the entire structure due to the lower cost of implementation. The first objective of this dissertation is assessing a rolling isolation system (RIS) based on existing design guidelines for telecommunications equipment. A discrepancy is observed between the required response spectrum (RRS) and the one and only accelerogram recommended in the guideline. Several filters are developed to generate synthetic accelerograms that are compatible with the RRS. The generated accelerograms are used for probabilistic assessment of a RIS that is acceptable per the guideline. This assessment reveals large failure probability due to displacement demands in excess of the displacement capacity of the RIS. When the displacement demands on an isolation system are in excess of its capacity, impacts result in spikes in transmitted acceleration. Therefore, the second objective of this dissertation is to design impact prevention/mitigation mechanisms. A dual-mode system is proposed where the behavior changes when the displacement exceeds a predefined threshold. A new piecewise optimal control approach is developed and applied to find the best possible mechanism for the region beyond the threshold. By utilizing the designed curves obtained from the proposed optimal control procedure, a Kelvin-Voigt device is tuned for

illustrative purposes.

On the other hand, the preference for protecting equipment decreases as the earthquake intensity increases. In extreme seismic loading, the response mitigation of the primary structure (i.e., life safety and collapse prevention) is of greater concern than protecting isolated equipment. Therefore, the third objective of this dissertation is to develop an innovative dual-mode system that can behave as equipment isolation under low to moderate seismic loading and passively transition to behave as a vibration absorber for the primary structure under extreme seismic loading. To reduce the computational cost of simulating a large linear elastic structure with nonlinear attachments (i.e., equipment isolation with cubic hardening nonlinearity), a reduced order modeling method is introduced that can capture the behavior of such nonlinear coupled systems. The method is applied to study the feasibility of dual-mode vibration isolation/absorber. To this end, nonlinear transmissibility curves for the roof displacement and isolated mass total acceleration are developed from the steady-state responses of dual-mode systems using the harmonic balanced method. The final objective of this dissertation is to extend the reduced order modeling method developed for linear elastic structure with nonlinear attachment to inelastic structures (without attachments). The new inelastic model condensation (IMC) method uses the modal properties of the full structural model (in the elastic range) to construct a linear reduced order model in conjunction with a hysteresis model to capture the hysteretic inter-story restoring forces. The parameters of these hysteretic forces are easily tuned, in order to fit the inelastic behavior of the condensed structure to that of the full model under a variety of simple loading scenarios. The fidelity of structural models condensed in this way is demonstrated via simulation for different ground motion intensities on three different building structures with various heights. The simplicity, accuracy, and efficiency of this approach could significantly alleviate the computational burden of performance-based earthquake engineering.

Chapter 1
Introduction and Background

Earthquake-induced vibrations can cause loss of operation or harmful damage to buildings and industrial structures (Astroza et al., 2012; Eberhard et al., 2010; Olsen et al., 2012; Stone, 2008), as well as equipment housed in them (Chapin et al., 2009; Dueñas-Osorio and Kwasinski, 2012; Miranda et al., 2012; Parajuli and Haynes, 2016). This loss of operation or damage is due to the reduction in the performance of vital equipment, such as computer servers, backup emergency generators, electric transformers (Zhang and Makris, 2001), telecommunications equipment, air conditioning equipment, medical equipment (Konstantinidis and Makris, 2009; Sato et al., 2011), etc., which have secondary consequences on providing services, emergency responses, and recovery of a community after a seismic event (Alhan and Şahin, 2011; Petrone et al., 2016). Such equipment usually suffers from inertial loads excited by the total acceleration applied to them. Reduction of accelerations usually happens by shifting the natural frequency of the system from the acceleration-sensitive region to the displacement-sensitive region in the response spectrum (Calhoun and Harvey, 2018; Tehrani and Harvey, 2019a), which is the fundamental concept behind *seismic isolation* (Kelly, 1990; Warn and Ryan, 2012).

The behavior of isolation systems is well studied in the literature under Service Level Earthquake (SLE*) and Design Basis Earthquake (DBE†) shaking (see Section

*SLE has 50% probability of exceedance in 30 years.
†DBE has 10% probability of exceedance in 50 years.

1.1). Past studies showed that isolation systems perform well for low-intensity events, while under high-intensity extreme events, an impact may occur producing spikes in accelerations. Researchers have proposed several approaches including passive, semi-active, and active control of isolation systems to enhance these systems' performance (Housner et al., 1997; Spencer and Sain, 1997). In passive systems, the input energy is dissipated by some mechanical devices (Soong and Dargush, 1997). Structures equipped with such devices can dissipate a huge amount of input energy by converting that energy to heat or sound. Semi-active systems use sensors to collect the structures' responses and send them to a computer (Ramallo et al., 2002; Symans and Kelly, 1999; Yoshioka et al., 2002). Then, based on a predefined algorithm, the computer sends a command to the actuator to adjust the behavior of a passive device (Harvey et al., 2014a; Yang and Agrawal, 2002). Active control systems, compared to passive and semi-active systems, use external power to drive actuators to generate required forces (potentially non-passive) to suppress vibration while getting feedback from the structure responses (Housner et al., 1996). However, requiring large external power in active systems to generate large forces and computer processing in both semi-active or active systems make passive systems more practical and of interest.

The focus of this dissertation is on developing innovative passive isolation systems for equipment to protect the isolated equipment, to mitigate the impacts caused by exceeding the displacement capacity, and to reduce the response of the primary structure supporting the isolated equipment. To this end, the introduction of this dissertation can be outlined as follows. First, in Section 1.1, a short review on isolation systems with an emphasis on equipment and floor isolation using rolling isolation systems is presented, followed by an assessment of the existing guidelines and criteria for designing telecommunications equipment (Section 1.2). Following this assessment on the safety of such systems against impact, in Section 1.3 an optimal mechanism to mitigate im-

pacts while not affecting the normal operation is discussed. A short review on dynamic vibration absorbers with an emphasis on tuned mass dampers is discussed in Section 1.4, followed by an introduction to a dual-mode vibration isolator/absorber by engineering nonlinearity to protect isolated objects under low to moderate seismic events and mitigate seismic responses of the primary structure under extreme seismic events is introduced in Section 1.5. Then, in Section 1.6, an introduction to the reduced order modeling technique is introduced, which can reduce the computational cost of large nonlinear elastic/inelastic structures and make their assessment practical. The reduced order modeling technique can be employed to study the feasibility of utilizing a dual-mode vibration isolator/absorber.

1.1 Equipment and Floor Isolation

Isolation systems have shown promise by suppressing and controlling the total transferred acceleration to buildings and their contents (Baggio et al., 2015; Chadwell et al., 2009; Fenz and Constantinou, 2008a,b,c; Harvey and Gavin, 2013, 2015; Jeon et al., 2015; Khechfe et al., 2002; Notohardjono et al., 2004; Tsai et al., 2010; Vargas and Bruneau, 2009; Yaghoubian, 1991; Zargar et al., 2013). This reduction of acceleration results in the reduction of downtime and uninterrupted operation of mission-critical facilities, which indirectly improve the resilience of the serving community. To date in general, several approaches to protecting equipment housed in buildings are sought (see Figure 1.1):

1. Isolating an entire building to elongate the natural period of building (Naeim and Kelly, 1999; Ryan and Dao, 2016; Warn and Ryan, 2012);

2. Isolating an object or equipment housed inside a building or industrial facility (Harvey and Gavin, 2013; Tsai et al., 2010); and

3. Isolating a group of objects or a floor inside a building (Hamidi and El Naggar,

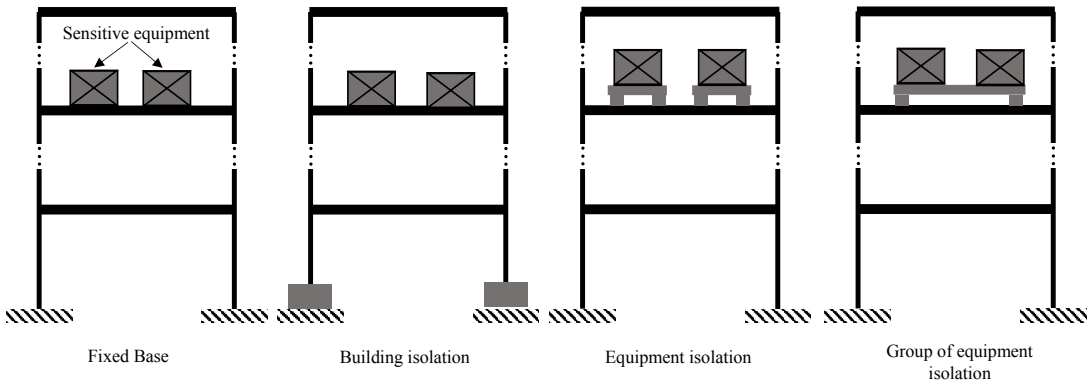

Figure 1.1: Different types of protecting equipment housed in buildings.

2007; Ismail et al., 2009; Lambrou and Constantinou, 1994).

The cost of implementing base isolation systems for an entire building is larger than the isolation of individual equipment or a group of equipment. So, due to the relatively lower cost and easier installation of the equipment or a group of equipment comparing to the isolation of the entire building, there is a growing interest in the second two approaches (Ismail et al., 2009). The mechanisms of these isolation systems for equipment and floor isolation can be grouped into several categories, such as

(a) isolation bearings, e.g., roll-in-cage isolation system (Ismail et al., 2009) and lead-rubber bearing (Naeim and Kelly, 1999);

(b) sliding isolators, e.g., multiple friction pendulum system isolator (Tsai et al., 2005) and double friction-pendulum bearing (Fenz and Constantinou, 2008c); and

(c) rolling isolation systems, e.g., static dynamics interchangeable-ball pendulum system (Tsai et al., 2010) and ball-in-cone rolling isolation system (Kemeny, 1997).

Examples of these types of bearings are shown in Figure 1.2.

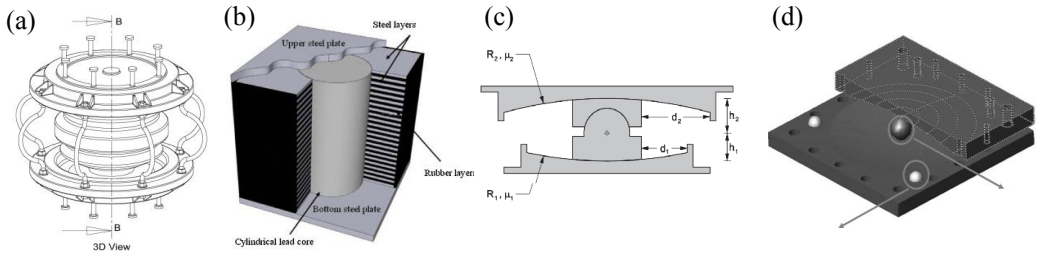

Figure 1.2: Example equipment isolation bearings: (a) roll-in-cage bearing (Ismail et al., 2009); (b) lead-rubber bearing (Zeynali et al., 2018); (c) friction-pendulum bearing (Fenz and Constantinou, 2008c); and (d) rolling isolation bearing (Tsai et al., 2010).

The focus of this dissertation is on rolling isolation systems (RISs), which are one of the isolation systems that are used for isolating telecommunications equipment inside buildings or industrial structures (Harvey and Kelly, 2016). Due to the high degree of adaptability, low installation cost, and low finished height, RISs are of interest and are well suited for isolating single equipment or a group of equipment (Cui, 2012; Jeon et al., 2015; Tsai et al., 2010). As shown in Figure 1.3, these isolation systems consist of two surfaces sliding through a rolling ball or a rod. If the profile of these surfaces is flat, the RIS has no capability to re-center, and they need supplemental devices to provide the system with re-centering forces (Guerreiro et al., 2007; Jangid, 2000). The required re-centering forces can alternatively be obtained through non-flat surfaces such as parabolic or spherical (Tsai et al., 2010; Zhou et al., 1998). These re-centering forces are produced by changes in the potential energy of the system through the increased in the height of the mass of the system with lateral displacement across the isolator. These systems are inherently lightly damped, and supplemental damping can be easily introduced by adhering visco-elastic sheets to the bowl surfaces (Harvey et al., 2014b; Muhr and Bergamo, 2010).

The performance of equipment isolation systems is extremely good for small displacement demands associated with low-intensity excitations (Alhan and Gavin, 2005; Gavin and Zaicenco, 2007). However, their performance for higher intensities depends

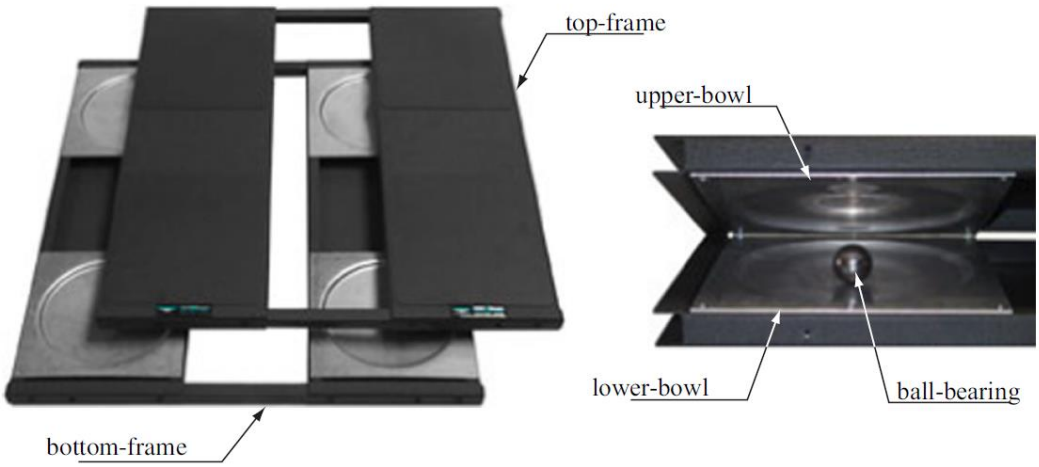

Figure 1.3: Configuration of a rolling isolation system (RIS) (Harvey and Gavin, 2013).

on the displacement demands of the floor motion. Isolation systems are shown to perform well in SLE and DBE events (Nagarajaiah and Sun, 2001; Sato et al., 2011). However, in practice, the isolation systems have limited displacement capacity due to the isolation device limitation and/or the environment that they are housed in. So, isolation systems may reach their displacement capacities under extreme loadings such as Maximum Considered Earthquake (MCE[‡]) events and impact may occur.

There are two possible solutions to reduce the likelihood of impact. The first solution is to increase the displacement capacity, which is not always feasible since the seismic gap is usually limited and the cost of components increases exponentially by the size of them (Jia et al., 2014), or by stacking two isolation systems on top of each other (Calhoun et al., 2019; Harvey and Gavin, 2014a). The next solution is to reduce the displacement demands by adhering visco-elastic sheets to the bowl surfaces (Harvey et al., 2014b; Muhr and Bergamo, 2010).

[‡]MCE has 2% probability of exceedance in 50 years.

1.2 On the Safety of RISs

Earthquake-induced vibrations can cause loss of operations or harmful damage to buildings, industrial structures, and the equipment housed therein (Astroza et al., 2012; Eberhard et al., 2010; Iwatsubo, 1998; Konstantinidis and Makris, 2010; Olsen et al., 2012; Stone, 2008). The loss of operations or reduction in the performance of vital equipment such as computer servers, backup emergency generators, electric transformers, air conditioning equipment, telecommunications equipment, etc., has secondary consequences on continued services, emergency response, and the overall recovery of a community after a seismic event (Alhan and Şahin, 2011; Petrone et al., 2016). Such equipment usually suffers from the total transmitted accelerations (Lopez Garcia and Soong, 2003a,b). The sustained accelerations may be mitigated by shifting the natural frequency of the system from the acceleration-sensitive region (high frequency) to the displacement-sensitive region (low frequency) in the response spectrum. The reduction of accelerations, therefore, happens at the expense of increasing displacements (Chopra, 2012; Kelly, 1986). Usually the longer the natural period, the larger the displacement and the smaller the acceleration (Chopra, 2012; Masaeli et al., 2014; Tehrani and Khoshnoudian, 2014). This is the basic premise behind seismic isolation.

Isolation systems have shown promise as an effective seismic hazard mitigation strategy for suppressing and controlling the transmitted total acceleration to buildings and other structures (Alhan and Şahin, 2011; Dolce et al., 2007; Lee and Constantinou, 2018; Saha et al., 2016; Zargar et al., 2013), as well as mounted equipment inside buildings (Baggio et al., 2015; Chadwell et al., 2009; Harvey and Gavin, 2013, 2015; Iemura et al., 2007; Jeon et al., 2015; Marin-Artieda and Han, 2015; Tsai et al., 2010; Vargas and Bruneau, 2009). Methods have been developed and used to limit and control displacement demands (Tehrani and Harvey, 2019b; Zargar et al., 2013, 2017). However, in practice, isolation systems have limited displacement capacity due to the isolation

device geometry or the environment in which they are housed. When the displacement capacity is limited, for instance, by the existence of moat walls or retainer rims the isolation system may experience harsh impacts when the displacement demand is too large. Extremely large accelerations, caused by an impact, degrade the isolation performance and make the system unsafe.

RISs are a viable and popular form of equipment isolation used for protecting telecommunications equipment inside buildings or industrial structures, by decoupling the equipment motion from the floor motion. These isolation systems utilize rolling pendulum bearings (RPBs), which are comprised of two concave surfaces enclosing a ball or a cylindrical rod. Horizontal displacements across the bearing result in vertical displacements, generating a gravitational recentering force. Different surface profiles provide different response behavior. For example, spherical rolling surfaces produce approximately linear recentering forces (like in the friction pendulum bearing (Zayas et al., 1990)). The most common profile for RPBs is conical with a rounded (circular) portion at the center, commonly referred to as the "ball-in-cone" (Kemeny, 1997). This surface profile ensures a constant peak acceleration, dictated by the slope and friction. Moreover, the low profile of RISs makes them a practical and attractive device for protecting telecommunications equipment. However, these systems suffer from limited displacement capacity dictated by the rolling surface's in-plan diameter.

Regarding the design criteria for isolated structures, ASCE/SEI 7-16 (2017, §17) discusses the design of isolated structures with permission to use response history procedure for any isolated structures. ASCE/SEI 7-16 (2017) focuses on ground motions rather than building floor motions, whereas Network Equipment-Building System (NEBS) GR-63-CORE (Telcoridia, 2012) provides environmental design guidelines for telecommunications equipment located inside structures. In this guideline, four different zones are defined based on the different seismic risk categories. For each zone,

a required response spectrum (RRS) at the base of equipment is specified, and a single synthetic accelerogram (e.g., the VERTEQII waveform for zone 4 (highest risk)) is used for design and testing purposes. Several earthquake records for various building and soil types were used for synthesizing the VERTEQII accelerogram (Telcoridia, 2012). Shaking is applied to the telecommunications equipment to "simulate conditions that would be encountered in service when building floors apply earthquake motions to the equipment" (Telcoridia, 2012). Therefore, the prescribed VERTEQII accelerogram can be used for design, analysis, and assessment of RISs used for protecting telecommunications equipment and the safety of such systems against impact. In the following section, the methods for impact mitigating is discussed.

1.3 Dual-Mode Impact Mitigation

Devastating economic losses can arise from damage to mission-critical facilities, structures, and systems supporting vital equipment (systems in general). One of the sources of damage to such systems is displacements in excess of the displacement capacity. The increase in displacement demand is more pronounced in systems located on soft soils (Khoshnoudian et al., 2015a; Masaeli et al., 2014; Tehrani and Khoshnoudian, 2014) or when they are exposed to long period seismic loadings or near-fault excitations with large pulse duration (Jangid and Kelly, 2001; Khoshnoudian et al., 2015b). Exceeding the displacement capacity results in the pounding between adjacent structures or the impact in system's components (Cole et al., 2012; Pratesi et al., 2014; Takabatake et al., 2014). Pounding/impact produces harmful undesired transmitted acceleration to the system (Harvey and Gavin, 2013, 2014a; Polycarpou and Komodromos, 2010; Raheem, 2014), which is detrimental for acceleration sensitive components.

The most straightforward solution to mitigate impact is to increase the displacement capacity. However, it is not always possible to increase the displacement capacity because of environmental limitations or cost prohibitions, in both new construction and

retrofit of an existing structure (Polycarpou and Komodromos, 2010; Takabatake et al., 2014). In the literature, different solutions for pounding mitigation have been proposed and assessed. One method is to connect adjacent structures at some specific locations. These connections enforce the adjacent structures to have in-phase motions with one another (Abdullah et al., 2001; Jankowski and Mahmoud, 2016; Jankowski et al., 2000). For instance, the use of hard rubber bumpers or stiff linking between the segments of a bridge can improve the bridge behavior during severe earthquakes (Jankowski et al., 2000) or inserting a shock-absorbing material such as rubber for pounding mitigation in buildings (Takabatake et al., 2014). Alternatively, a pair of pressurized fluid-viscous dissipaters was used for pounding mitigation between a church structure and its bell tower (Pratesi et al., 2014). Applying a similar concept, a share tuned mass damper between two adjacent tall buildings can reduce both structural responses and the probability of pounding (Abdullah et al., 2001). Others have shown that using links such as springs, dashpots, or viscoelastic elements between two adjacent 3-story buildings can significantly reduce the gap size and prevent pounding (Jankowski and Mahmoud, 2016).

Another solution to this problem is to reduce the displacement demand via some energy dissipative mechanisms, which has been studied extensively. For instance, increasing the damping in an isolation system reduces the isolator displacement and base shear (Harvey et al., 2014b; Kelly, 1999; Makris and Chang, 2000). Approaches based on semi-active control have also been developed to decrease structural displacement (Azimi et al., 2017).

Although the above-mentioned solutions have been shown to be effective, there are some drawbacks with these approaches, and several studies showed that devastating damage to systems had been observed under high-amplitude seismic loadings, even with the presence of some energy dissipative mechanisms (Jangid and Kelly, 2001;

Makris and Chang, 2000; Pratesi et al., 2014). One of the disadvantages of connecting adjacent structures is the impairing of the dynamics of each individual structure. In addition, reducing the displacement demand comes at the expense of increasing the total transferred accelerations (Harvey et al., 2014b; Jangid and Kelly, 2001; Zargar et al., 2013). Moreover, energy dissipative devices also alter the normal operations of the systems or the responses under low-amplitude seismic loadings, where they have shown acceptable performance (Nagarajaiah and Sun, 2001; Sato et al., 2011).

Recently, in order to not affect the performance of systems under low-amplitude seismic loadings and at the same time improve their performance under high-amplitude seismic loadings, researchers developed devices with mechanisms that work at only some regions, and let the system respond freely at other regions. These devices rely on nonlinear force-displacement relationships that have been engineered to exhibit multi-phased responses. For instance, Panchal and Jangid (2008) used a variable friction pendulum system, in which the friction coefficient varies with displacement. The friction coefficient increases with increasing displacement, and after a certain displacement this trend reverses; the variable friction helps to decrease structural responses such as isolator displacement and base shear under near-fault ground motions (Panchal and Jangid, 2008).

Lu et al. (2011) experimentally studied sliding isolators with variable curvature, where instead of having spherical surfaces, the sliding surfaces have variable curvatures. Variation in sliding surfaces provides variable stiffness as a function of displacement. In that study, they used sliding surfaces with a sixth-order polynomial function to reduce the isolator drift under long-period near-fault earthquakes (Lu et al., 2011).

The roll-in-cage isolation bearing decouples vertical and lateral load bearing and is equipped with a buffer mechanism, which activates only under earthquakes larger than the design earthquake (Ismail, 2015b,c,a). This buffer produces a hardening stiff-

ness only when the displacement is greater than the chosen design displacement. This isolation bearing was shown to be effective at mitigating pounding and reducing large displacements when the gap size is limited (Ismail, 2015c,a).

By taking advantage of both a rubber damper (for the first phase) and buckling-restrained brace (for the second phase), a hybrid passive device has also been proposed that can produce large dissipation at all levels and large stiffness at large seismic events to protect frame structures (Marshall and Charney, 2010).

To mitigate the pounding between the isolated structure and the perimeter moat wall, Zargar et al. (2013, 2017) proposed an isolation system with a "phased gap damper." This phased gap damper is composed of a gap element and an energy dissipation device, where the gap element allows the system to have additional damping only at large intensity shaking and no effect at low to medium intensity shaking. They assessed several candidates for the energy dissipation device such as hysteretic, viscous, Kelvin, two-phase viscoelastic, and two-phase viscoplastic gap dampers (Zargar et al., 2013, 2017). Using numerical assessment and optimization, they showed that viscous, two-phase viscoelastic, and two-phase viscoplastic gap dampers are more effective for reducing the base displacements, but they introduce larger acceleration spikes into the system (Zargar et al., 2013, 2017).

It is important to note that all of the examples mentioned above assume some prescribed form of the device and an associate force-displacement or force-velocity relationship. The methods mentioned above can be utilized to develop an innovative RIS for impact mitigation. Another innovative RIS of interest is to engineer a nonlinear RIS as a tuned mass damper to protect the isolated equipment and at the same time reduce the responses of the primary structure. In the following section, tuned mass dampers are briefly described, and their application in seismic mitigation of structures as vibration absorbers are discussed in the section after that.

1.4 Dynamic Vibration Absorbers

Tuned mass dampers (TMDs) are a kind of vibration absorber consisting of a mass that is connected to the primary structure through a spring and/or a dashpot. They have been implemented to reduce wind induced vibrations (Demetriou et al., 2016; Elias et al., 2017; Liu et al., 2008; Ramezani et al., 2018; Wang et al., 2015a) and to mitigate seismic responses of high-rise buildings (De Angelis et al., 2012; De Domenico and Ricciardi, 2018a,b; Lazar et al., 2014; Lu et al., 2017; Matta, 2018; Pietrosanti et al., 2017; Shi et al., 2018; Simoneschi et al., 2017). Passive TMDs have several advantages such as (a) they do not require external power to operate; (b) they are easy to be tuned for different types of dynamic loading; and (c) they are relatively cost-effective in terms of production and maintenance. Despite all the advantages, in order to be effective, they require a relatively large mass, and consequently, they require a large space for housing and installation. The required space may be large since they tend to experience large deformations due to tuning to the resonance of the structure. All in all, these systems have shown to be effective in seismic mitigation of structures (De Angelis et al., 2012; De Domenico and Ricciardi, 2018a,b; Demetriou et al., 2016; Elias et al., 2017; Lazar et al., 2014; Liu et al., 2008; Lu et al., 2017; Matta, 2018; Pietrosanti et al., 2017; Ramezani et al., 2018; Shi et al., 2018; Simoneschi et al., 2017; Wang et al., 2015a). The application of a linear TMD is usually limited by its constant natural frequency. That is, only one targeted mode can be considered for suppression. The vibration of the primary structure dissipates due to the resonance of the TMD at the tuned frequency. On the other hand, nonlinear TMDs with softening behavior are able to be tuned for a broader frequency range in the vicinity of the targeted frequency (Hunt and Niessen, 1982; Rice and McCraith, 1987; Soom and Lee, 1983). Later, nonlinear TMDs with hardening gained attention as energy pumping devices (i.e., nonlinear energy sink) (Gendelman, 2011; Gendelman et al., 2001; Gendelman, 2001; Gourdon et al., 2007; Gourdon and

Lamarque, 2005; Vakakis, 2001; Vakakis and Gendelman, 2001).

This brief introduction on TMDs serves as a background for Section 1.5 on innovative isolation where RISs are engineered for dual-purpose of protecting equipment isolation and primary structures' response reduction. On the other hand, assessing large nonlinear structures is computationally prohibiting. So, Section 1.6 discusses the reduced order modeling technique that can be employed to reduce the computational cost of assessing large nonlinear structures.

1.5 Dual-Mode Vibration Isolator/Absorber

Isolation systems, by elongating the natural period, have shown promise by suppressing and controlling the total transferred acceleration to buildings and their content (Baggio et al., 2015; Chadwell et al., 2009; Harvey and Gavin, 2013, 2015; Jeon et al., 2015; Tsai et al., 2010; Vargas and Bruneau, 2009; Zargar et al., 2013). This reduction of acceleration results in the reduction of downtime and uninterrupted operation of mission-critical facilities. Moreover, these systems push the behavior of the supported structure into its linear elastic range. Consequently, structural responses such as story drifts are considerably reduced, which improves the safety and normal operation of the supporting structures. To date in general, the use of equipment isolation (Harvey and Gavin, 2013; Tsai et al., 2010) and a group of isolated objects or a floor inside a building (Hamidi and El Naggar, 2007; Ismail et al., 2009; Lambrou and Constantinou, 1994) have gained more attention compared to base isolation of the entire buildings (Naeim and Kelly, 1999; Warn and Ryan, 2012). This is due to the relatively lower cost of implementation for equipment or a group of equipment (Ismail et al., 2009). In addition, requirements for large seismic gap, the heavy loads, and the large flexibility of the superstructure, especially in high-rise buildings, limit the application of base isolations.

An alternative solution for vibration mitigation is tuned mass damper (TMD), which has been shown effective to mitigate seismic responses of buildings (Gendelman, 2011;

Gendelman et al., 2001; Gendelman, 2001; Gourdon et al., 2007; Gourdon and Lamarque, 2005; Luo et al., 2014a,b; Vakakis, 2001; Vakakis and Gendelman, 2001; Wang et al., 2015b, 2016; Wierschem et al., 2017). In order to address some of the challenges with TMDs (see Section 1.4), Villaverde (1998) proposed the use of floor isolation as a vibration absorber. He isolated the roof of a building, which relatively has a large mass, with elastomeric bearings. At the same time, Ziyaeifar and Noguchi (1998) used a 10-story shear type building to study the changes in the dynamic characteristics when floor isolation is introduced to that building. They performed several time-history analyses to show the effectiveness of the proposed method. Since then, the concept of using floor isolation as vibration absorber has gained popularity (Anajafi and Medina, 2018a,b; Reggio and Angelis, 2015; Wang et al., 2018) and researchers have been working on various aspects of floor isolation such as finding the optimal placements (Charmpis et al., 2015), applying this concept to other structures (Dai et al., 2018; Hoang et al., 2008), experimentally evaluating the effectiveness of this method (Gallanti and Forcellini, 2016; Schellenberg et al., 2017), and extending this idea by utilizing other dissipative devices (Liu et al., 2018) or considering nonlinearity in the system (Ding et al., 2015; Ryan and Earl, 2010).

Charmpis et al. (2015) studied the selection and placement of floor isolation systems through the elevation of a multi-story building to retrofit. They concluded that their procedure outperforms the case of base isolation only. Anajafi and Medina (2018a) studied 6, 12, and 20 story linear building structures equipped with linear partial mass isolation at each floor considering them as inherent vibration suppressions. They considered input motions with different frequency content by applying a Kanai-Tajimi filter to Gaussian white noise excitations. That study was limited to the mass ratios of 5% and 90%. Then, in a similar study by Anajafi and Medina (2018b), they considered different structural frequency and mass ratios. They concluded that the mass ratio of

25% to 50% is more efficient in mitigating the seismic responses of the main structure and controlling the responses of the isolated system.

Hoang et al. (2008) used a floor deck isolation system to reduce the seismic forces applied to a truss bridge. They considered the optimal design of such a system through a single-degree-of-freedom system with a TMD. They conclude that a large TMD is more effective in reducing the seismic responses and more robust in handling the uncertainties in system parameters. Dai et al. (2018) proposed a probabilistic framework for the optimal design of buildings with partial mass isolation systems. They applied their framework to design a thermal power plant building in which the coal scuttle serves as a partial mass isolation system coupled to a linear SDOF model of the building. Liu et al. (2018) investigated the effectiveness of utilizing a fluid-viscous damper in conjunction with floor isolations in buildings. They placed an isolation system between the second and third floors of a 7-story building and tuned the parameters of dampers placed inside the isolation system. The considered objective was to minimize both the displacement of the isolator and the total drift of the main structure.

Gallanti and Forcellini (2016) tested a 3D-printed structure with floor isolation on a shake table to verify the effectiveness of utilizing floor isolation in comparison with base isolation. Through experimental tests, they showed that floor isolation is beneficial in reducing the top floor accelerations. In another study, the effectiveness of floor isolation is experimentally tested on a shake table using a hybrid simulation where the part below the isolation layer was modeled numerically, and the part above the isolation layer was tested physically on the shake table (Schellenberg et al., 2017). The results concluded the beneficial effect of utilizing floor isolation for mitigation of seismic responses.

Despite this benefit, considering nonlinearity in the floor isolation has gained little attention. For instance, Ryan and Earl (2010) considered several configurations of non-linear inter-story isolation systems in a multi-story building frame and concluded that

as the isolation level increases its effectiveness decreases. Despite the least effectiveness of roof isolation, considerable response reductions have been obtained. In another study, Ding et al. (2015) assessed unconstrained floor slabs as non-conventional TMDs. They studied the tuning of the TMD parameters considering the nonlinear structure and nonlinear response history analyses. They also concluded that considering the dynamic interaction may lead to a reduction in the acceleration responses compared to the uncoupled approach and increasing in mass ratio results in a reduction in response spectrum.

Neglecting the dynamic coupling between the primary structure and secondary systems (i.e., equipment isolation systems) is a common assumption in the design and assessment of such systems. This coupling is negligible if the secondary system's mass to the primary structure's mass is relatively small and their frequencies are detuned (Chen and Soong, 1988; Igusa and Der Kiureghian, 1985). Moreover, these criteria are based on the linear behavior of structures. The errors in the estimation of the frequency are shown in Figure 1.4 for different mass and frequency ratios. Introducing nonlinearity brings new challenges to the problem by impairing the common assumptions used for linear systems. Therefore, the existing criteria for considering or ignoring the dynamic coupling may no longer be valid for nonlinear systems. Furthermore, building on the concept of using floor isolation systems as TMDs, these interactions may be engineered to serve an alternative purpose, which is the focus of this work.

1.6 Reduced Order Modeling

While nonlinear response history analysis (NLRHA) is the most rigorous procedure to estimate seismic demand parameters (ASCE/SEI 7-16, 2017, §16.2), it is computationally expensive. This is true, especially, when there is a need to perform that analysis for a large quantity of scenarios such as required for surrogate modeling, optimization, or the reliability analysis and design of structures (Gholizadeh and Samavati, 2011; Gidaris and Taflanidis, 2013; Gidaris et al., 2015; Harvey and Gavin, 2015; Herrada

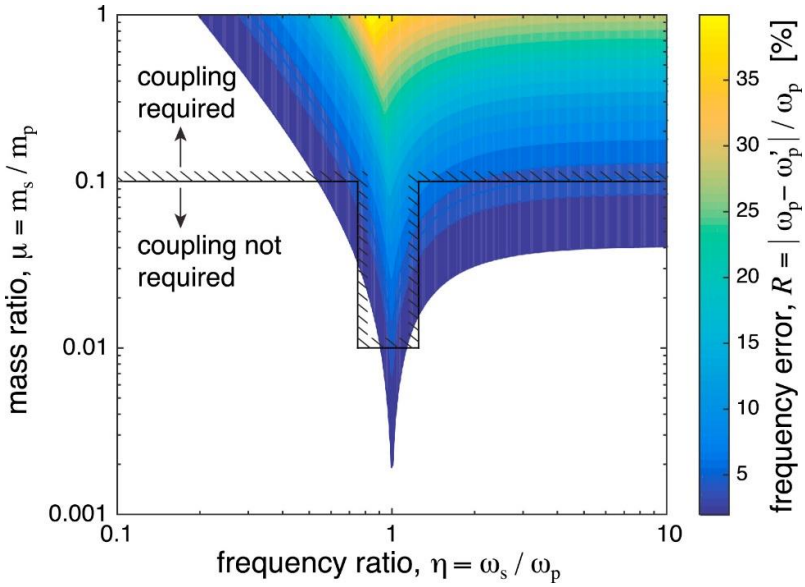

Figure 1.4: Errors in the estimation of the frequency for different mass and frequency ratios (Harvey et al., 2018).

et al., 2017; Tesfamariam and Goda, 2017; Tesfamariam et al., 2015). Considering the time-consuming nature of detailed time-history analyses of high-dimensional nonlinear elastic/inelastic models, an accurate and computationally efficient method of predicting responses of nonlinear structures, e.g., displacements, accelerations, and inter-story drift ratios, would be of significant value in performance-based earthquake engineering (PBEE) (Bozorgnia and Bertero, 2004).

As alternatives to NLRHA, methods involving pushover analyses alone or in combination with inelastic response spectra are well developed (ASCE/SEI 41-13, 2014; Manoukas et al., 2011; Reyes and Chopra, 2011; Sahraei and Behnamfar, 2014). The dynamics of the problem are captured only by the response spectrum, which reflects the dynamics of inelastic single degree of freedom (SDOF) systems. The mechanics of the detailed structural model is reflected only by the pushover analysis, which does not involve dynamics and does require the specification of distribution of lateral static loads. Several studies have focused on the specification of lateral load distributions for pushover analyses, such as (Goel and Chopra, 2004; Lagaros and Fragiadakis, 2011;

Sucuoğlu and Gïnay, 2011; Tehrani et al., 2013b,a), among others. Unfortunately, simple pushover analyses neglect the effect of higher modes on the response. To tackle this, a few notable studies incorporate the higher modes' dynamics in pushover analyses (Alıcı and Sucuoğlu, 2015; Chopra and Goel, 2002; Tehrani and Khoshnoudian, 2014). Nevertheless, the errors in the predictions of displacements and drift ratios are in the order of 30% (Chopra and Goel, 2002).

Other researchers have approached this problem using reduced (condensed) structural models (Gidaris and Taflanidis, 2013; Harvey and Gavin, 2015; Weng et al., 2017). This trend started when the static and dynamic condensations were introduced (Guyan, 1965; Paz, 1985), and it continues to be refined (Boo and Lee, 2017; Soheilifard, 2015). Previous methods of model reduction for hysteretic structures have either been limited to reducing only the linear aspects of the system (Mousavi and Gandomi, 2016), retaining all the nonlinear elements present in the system at some computational expense (Bamer and Bucher, 2012; Kappagantu and Feeny, 1999), or to approximating the nonlinear system using modal superposition with time-varying modes (Geschwindner, 1981; Villaverde and Hanna, 1992). Recently, researchers are developing and evaluating model reductions for modeling the hysteretic behavior of structures (Gidaris and Taflanidis, 2013), identifying damage detection (Mousavi and Gandomi, 2016; Yin et al., 2017), modeling elastomers (Flodén et al., 2018), and glass structures (Fröling et al., 2014).

For instance, in a study on the nonlinear tuned mass damper by Alexander and Schilder (2009), the responses of the primary structure was considered to be the product of temporal and spatial functions (i.e., reducing to the first natural mode) while the nonlinear attachment was kept in the retained equations of motion. This imposes a linear behavior for the primary structure. Although the first normalized natural mode shape is used for reducing the primary structure's model, no attempt is taken to estimate the

responses of the primary structure using the solution obtained from the reduced model. Similarly, a shape vector is used to reduce the response of a multiple degree of freedom structure with an attachment to a single degree of freedom with an attachment. However, the formulation is limited to employing only one shape vector and one attachment (Reggio and De Angelis, 2013, 2014).

In another study, Kuether et al. (2015) used mode shapes to reduce geometrically nonlinear structures. In their method, the model is transformed into modal coordinate and the response of the modal displacement is fitted to the response of the full finite element model. The full finite element model is excited by static loads or deformed based on a combination of mode shapes. To consider hysteretic behavior, Gidaris and Taflanidis (2013) developed a reduced order model for hysteretic nonlinear structures considering the inter-story restoring forces. They assessed three candidate solutions for the hysteretic restoring forces, namely piece-wise linear models with ideal elasto-plastic or peak-oriented hysteresis, and generalized Masing model. They concluded that the peak-oriented model provides better estimates among the assessed models.

1.7 Dissertation Outline

The organization of this dissertation can be outlined as follows:

First, Chapter 2 focuses on a probabilistic assessment of rolling isolation systems (RISs) designed for equipment protection, using the GR-63-CORE guideline (Telcoridia, 2012). The safety assessment of the RISs reveals the discrepancy between the prescribed accelerogram and the recommended criteria in the GR-63-CORE guideline. It is shown that a RIS designed using the accelerogram prescribed in the GR-63-CORE guideline can fail dramatically (i.e., displacements exceeding the RIS's capacity) under a suite of generated synthetic accelerograms conforming to the required response spectrum according to the same guidelines. Following this conclusion, in Chapter 3, a method to reduce the displacement demand under extreme seismic loading while not

affecting the normal operation under low to moderate seismic loading is proposed. In this method, the system is allowed to respond freely when the displacement demand remains under some threshold and an impact mitigation mechanism is applied for displacements beyond that threshold. Optimal control is applied to find the best control action trajectory for the active control region. In the active control region the objective of the optimal control problem is to mitigate impact and to control the total acceleration.

Under low to moderate seismic loading the objective is usually to protect equipment (i.e., serviceability limit states); however, under extreme seismic loading, the main focus shifts from the protection of the isolated equipment toward the protection of the primary structure (i.e., collapse prevention and life safety limit states). Therefore, the focus of Chapter 4 is to study the feasibility of a dual-mode vibration isolation/absorber. This dual-mode system is aimed to protect isolated equipment or a group of equipment under low to moderate seismic loading, while it reduces the response of the primary structure under extreme seismic loading. To study the feasibility of a dual-mode vibration isolation/absorber, a cubic nonlinearity with hardening behavior is considered for the isolation system where its stiffness increases as the excitation increases. This provides a changing frequency from isolation behavior toward vibration absorber behavior. In order to reduce the computation cost of studying a large (high degree of freedom) system with nonlinear attachments, a reduced order modeling technique is introduced in Chapter 4, and the accuracy of the approach is evaluated. Then, the resulting nonlinear reduced order models (ROMs) are used in a feasibility study assessment. The reduced order modeling technique introduced in Chapter 4 is limited to linear elastic structures with nonlinear attachments. Therefore, in Chapter 5, an approach for inelastic condensed dynamic modeling is proposed for the condensation of inelastic building structures. This inelastic model condensation approach is validated and compared to

the modal pushover analysis (MPA) approach popularized by Chopra and Goel (2002). Finally, Chapter 6 summarizes the findings of this dissertation, and future research directions motivated by this work are discussed.

Chapter 2
On the Safety of Rolling Isolation Systems

2.1 Overview

In this chapter, probabilistic analyses are performed to assess the safety of a rolling isolation system (RIS). To supplement the singular accelerogram prescribed by GR-63-CORE in order to investigate building floor motion variability (D'Amico et al., 2017), several suites of synthetic accelerograms are developed with different characteristics based on the GR-63-CORE guideline. These filters are developed by fitting both parametric filters and piecewise filters to the VERTEQII accelerogram and to the required response spectrum (RRS). Then, the equation of motion for a RIS with double, conical rolling surfaces is developed using Lagrange's equation, and it is shown that the RIS performs satisfactorily under the zone-4 VERTEQII accelerogram. After that, probabilistic analyses are performed to assess the floor motion characteristics on the RIS's performance, and the results are discussed. It is shown that one accelerogram is not enough to adequately judge the safety of the RIS and more importantly, the singular accelerogram (VERTEQII) in GR-63-CORE may not be representative of the RRS recommended for testing telecommunications equipment. At the end, the results of probabilistic analyses are used to generate empirical fragility curves, which show the probability of exceeding a given displacement versus floor-motion intensity (RRS multiplier).

2.2 Synthetic Accelerograms

As discussed before, there is only one accelerogram for testing the performance and safety of telecommunications equipment in GR-63-CORE (Telcordia, 2012), which is unable to incorporate the variability that exists in seismic motions. Thus, there is a need to employ a suite of consistent accelerograms to consider the seismic variability into the design and testing procedure. However, such a suite of accelerograms is not available. One common way to overcome this is to generate synthetic accelerograms (Batou and Soize, 2014; Boore and Goulet, 2014).

The GR-63-CORE guideline (Telcordia, 2012) prescribes accelerograms for testing telecommunications equipment for various zones with different risk categories. These accelerograms have some characteristics that satisfy the requirements for testing telecommunications equipment. For instance, Figure 2.1 shows the VERTEQII accelerogram developed for zone 4, the zone with the highest risk. The 2% damped response spectrum of this accelerogram is shown in Figure 2.2 with the RRS for zone 4, which has 10% probability of exceeding this intensity over a 50-year return period (Telcordia, 2012). These response spectra are evaluated at 6th octave frequencies ranging from 0.5 to 50 Hz. As stated in GR-63-CORE (Telcordia, 2012), a consistent accelerogram should exceed the RRS between 1 and 50 Hz, while it should not exceed by more than 30% between 1 and 7 Hz. These impermissible regions (A and B, respectively) are shaded in Figure 2.2. Note that no requirement is enforced at frequencies less than 1 Hz and greater than 50 Hz.

Keeping these requirements in mind, the general procedure to produce synthetic accelerograms can be summarized as the following four steps (Clough and Penzien, 2003):

i. Generate a series, $x(t)$, of random standard Gaussian numbers, $\mathcal{N}(0, 1)$, which can be considered as a stochastic stationary Gaussian process (i.e., unit root-mean-

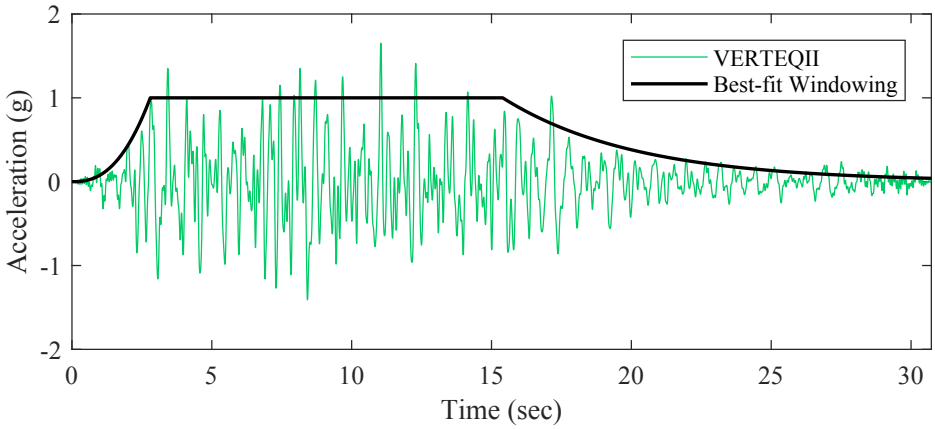

Figure 2.1: VERTEQII accelerogram and the fitted windowing function, $w(t)$.

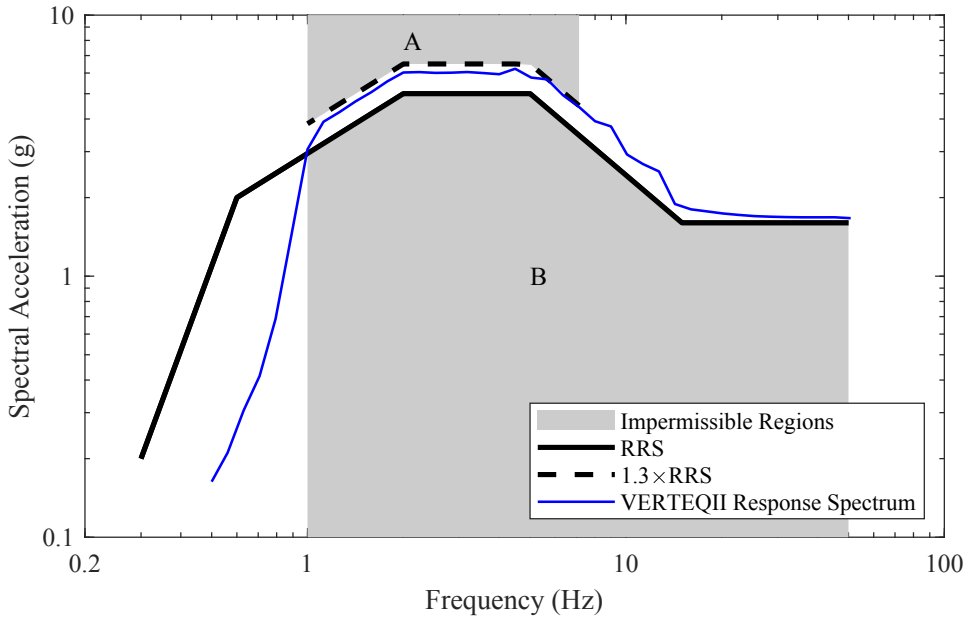

Figure 2.2: Zone 4 required response spectrum (RRS) and VERTEQII response spectrum (2% damping).

square white noise).

ii. Window the stochastic stationary Gaussian process to a nonstationary process, $y(t) = w(t) \circ x(t)$, where $w(t)$ is a windowing function and "$\circ$" indicates element-wise product. See the details in Section 2.2.1.

iii. Apply a filter — a transfer function in the frequency domain — to modify the fre-

quency content of the nonstationary process, $y(t)$, to give a filtered nonstationary process, $z(t)$. See the details in Section 2.2.2.

iv. Scale the filtered nonstationary process, $z(t)$, by an appropriate scaling factor to match the target response spectrum. See the details in Section 2.2.3.

In the following, first, a parametric windowing function is described, and the best-fit parameters are estimated. Then, several approaches for developing a transfer function are described. Finally, the best scaling factor for each transfer function is tabulated. The results of the following section should be used in the previous three steps to generate synthetic accelerograms.

2.2.1 Windowing Function

In order to generate synthetic accelerograms that mimic the characteristics of VERTE-QII, similar time step (0.005 sec), duration (30 sec), and windowing are used. While varying the duration may have an effect on the response (increase (Khoshnoudian et al., 2015b,a; Raghunandan and Liel, 2013) or decrease (Pan et al., 2018)), this effect is not considered here. These synthetic accelerograms should satisfy the response spectrum requirements mentioned before (i.e., exceed the RRS between 1 and 50 Hz, but by no more than 30% between 1 and 7 Hz), while retaining the desired seismic variability required for probabilistic analysis.

A windowing function $w(t)$ is required to convert a stochastic stationary Gaussian process (i.e., white noise) to a nonstationary process. In this study, a piecewise windowing function (Jennings et al., 1968) is used, which has four parameters (t_1, t_2, p, and c) to control the shape of the window, and a dummy parameter ($\overline{w}$) that scales the window to the desired amplitude. The equation of this windowing function is

$$w(t) = \overline{w} \times \begin{cases} (t/t_1)^p, & 0 \le t < t_1 \\ 1, & t_1 \le t < t_2 \\ e^{-c(t-t_2)}, & t_2 \le t \end{cases} \tag{2.1}$$

To obtain the best windowing parameters, the windowing function is fitted to the absolute value of the VERTEQII accelerogram by solving the following nonlinear least squares problem:

$$\min_{t_1,t_2,p,c,\overline{w}} \int \left(w(t) - |a(t)|\right)^2 \mathrm{d}t \tag{2.2}$$

where $a(t)$ is the VERTEQII accelerogram. This optimization problem is solved using the Levenberg–Marquardt algorithm (Levenberg, 1944; Marquardt, 1963), which is briefly described in Tehrani et al. (2018); the implementable MATLAB code can be found in Gavin (2017). The best-fit parameters are found to be $\hat{t}_1 = 2.8$ sec, $\hat{t}_2 = 15.4$ sec, $\hat{p} = 2.48$ and $\hat{c} = 0.21$. Note that the dummy parameter $\overline{w}$ is only used for the fitting purpose and has no influence on the shape of the function; $\overline{w}$ is taken to be unity hereinafter. Figure 2.1 shows the VERTEQII accelerogram and the fitted windowing function.

2.2.2 Developing Transfer Functions

In this section, the frequency content of a nonstationary windowed process, generated in step ii, should be modified to provide the desired response spectrum. Four different approaches are considered in this study, which can be categorized generally into two classes: (1) VERTEQII-based parametric filters and (2) response spectral-based filters. These approaches are described in Sections 2.2.2(a) and 2.2.2(b), respectively.

2.2.2(a) VERTEQII-based Parametric Filters

The following VERTEQII-based filters are considered in this study: (a) Kanai-Tajimi filter; (b) Modified Kanai-Tajimi filter; and (c) Piecewise filter. The VERTEQII accelerogram is used for developing these filters, which are described here.

Kanai-Tajimi (KT) filter. Kanai (1957) and Tajimi (1960) used a single oscillator as a transfer function, which relates the ground motion at the surface over the motion at

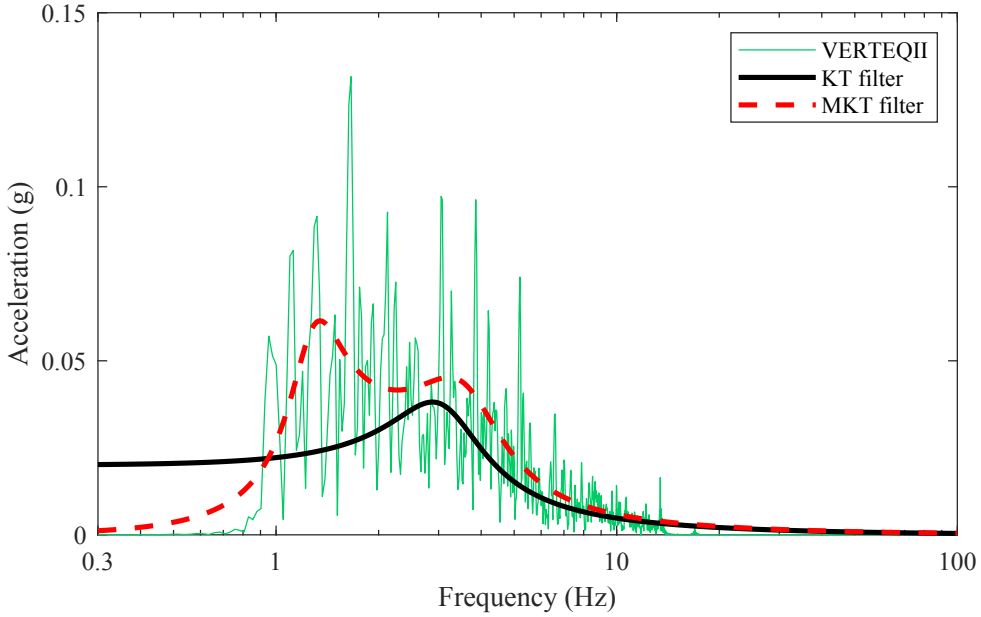

Figure 2.3: Fourier transform of the VERTEQII accelerogram, the fitted Kanai-Tajimi (KT) filter, and the fitted modified Kanai-Tajimi (MKT) filter.

the bedrock as the following function:

$$S_{\mathrm{KT}}(\omega) = \overline{S}_{\mathrm{KT}} \frac{1 + 2\xi_{\mathrm{KT}}(\omega/\omega_{\mathrm{KT}})i}{[1 - (\omega/\omega_{\mathrm{KT}})^2] + 2\xi_{\mathrm{KT}}(\omega/\omega_{\mathrm{KT}})i} \tag{2.3}$$

where $\overline{S}_{\mathrm{KT}}$ is a constant scale factor; ω_{KT} and ξ_{KT} are ground (here floor) motion frequency and damping ratio, respectively; and $i = \sqrt{-1}$. These parameters are usually estimated by the observation of the characteristics (zero crossings and other statistics) of historical earthquakes (Alotta et al., 2014). However, in this study, the best value of these parameters are obtained by fitting Eq. (2.3) to the single-sided Fourier transform amplitude of the VERTEQII accelerogram, which is shown in Figure 2.3, using the Levenberg–Marquardt optimization algorithm. The best-fit values of the parameters are $\hat{\omega}_{\mathrm{KT}} = 19.59$ rad/s and $\hat{\xi}_{\mathrm{KT}} = 0.32$, with standard errors of 0.213 and 0.009, respectively. Note that the constant $\overline{S}_{\mathrm{KT}}$ has no influence on the shape of the filter and only affects the amplitude; therefore, $\overline{S}_{\mathrm{KT}}$ is (arbitrarily) taken to be 1 g in the filtering step (Step iii). The appropriate scale factor is obtained in Section 2.2.3.

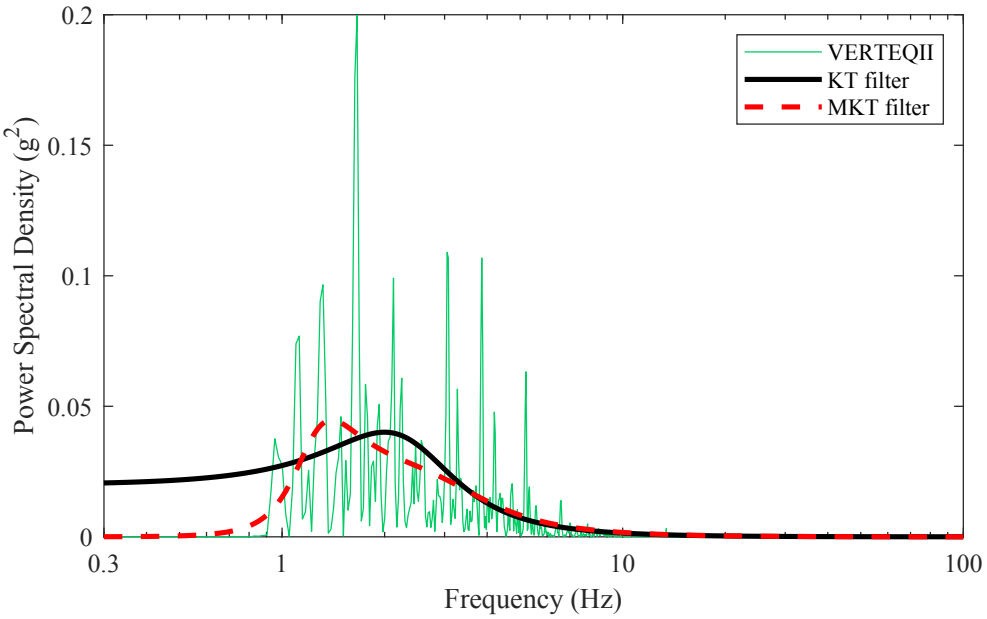

Figure 2.4: Power spectral density (PSD) of the VERTEQII accelerogram, the fitted Kanai-Tajimi (KT) filter, and the fitted modified Kanai-Tajimi (MKT) filter.

Another way to obtain the KT filter parameters, as used in the literature such as by Hoang et al. (2008), is to fit to the power spectral density (PSD) of the VERTEQII accelerogram. The PSD of the KT filter is

$$P_{\mathrm{KT}}(\omega) = \left|S_{\mathrm{KT}}\right|^2 \equiv \overline{S}^2_{\mathrm{KT}} \frac{1 + 4\xi^2_{\mathrm{KT}}(\omega/\omega_{\mathrm{KT}})^2}{[1 - (\omega/\omega_{\mathrm{KT}})^2]^2 + 4\xi^2_{\mathrm{KT}}(\omega/\omega_{\mathrm{KT}})^2} \tag{2.4}$$

The best-fit to the PSD is shown in Figure 2.4, and the best-fit values of the parameters are $\hat{\omega}_{\mathrm{KT}} = 14.93$ rad/s and $\hat{\xi}_{\mathrm{KT}} = 0.54$, with standard errors of 0.290 and 0.023, respectively. While $\overline{S}_{\mathrm{KT}}$ was determined in the fitting process, it is taken to be 1 g in the filtering step (Step iii). The appropriate scale factor is obtained in Section 2.2.3.

Modified Kanai-Tajimi (MKT) filter. The modified Kanai-Tajimi (MKT) filter is proposed to remove the effect of residual velocities and displacements by greatly attenuating the low frequency accelerations (Clough and Penzien, 2003). The function of this filter is

$$S_{\mathrm{MKT}}(\omega) = \overline{S}_{\mathrm{MKT}} \frac{1 + 2\xi_1(\omega/\omega_1)i}{[1 - (\omega/\omega_1)^2] + 2\xi_1(\omega/\omega_1)i} \frac{(\omega/\omega_2)^2}{[1 - (\omega/\omega_2)^2] + 2\xi_2(\omega/\omega_2)i} \tag{2.5}$$

where $\overline{S}_{\mathrm{MKT}}$ is a constant scale factor, ω_1 and ω_2 are the ground (here floor) motion frequencies, and ξ_1 and ξ_2 are the damping ratios. The best-fit MKT parameters are obtained by fitting Eq. (2.5) to the single-sided Fourier transform amplitude of the VERTEQII accelerogram, which is shown in Figure 2.3. The best-fit values of parameters are $\hat{\omega}_1 = 22.80$ rad/s, $\hat{\omega}_2 = 8.05$ rad/s, $\hat{\xi}_1 = 0.31$, and $\hat{\xi}_2 = 0.19$, with standard errors of 0.222, 0.074, 0.009, and 0.007, respectively.

Similar to the KT filter, the MKT parameters are also obtained by fitting to the PSD of the VERTEQII accelerogram. The PSD of the MKT filter is

$$P_{\mathrm{MKT}}(\omega) = \left|S_{\mathrm{MKT}}\right|^2 \equiv \overline{S}^2_{\mathrm{MKT}} \frac{1 + 4\xi_1^2(\omega/\omega_1)^2}{[1 - (\omega/\omega_1)^2]^2 + 4\xi_1^2(\omega/\omega_1)^2} \frac{(\omega/\omega_2)^4}{[1 - (\omega/\omega_2)]^2 + 4\xi_2^2(\omega/\omega_2)^2} \tag{2.6}$$

The best-fit MKT to the PSD is shown in Figure 2.4. The best-fit values of the parameters are $\hat{\omega}_1 = 19.29$ rad/s, $\hat{\omega}_2 = 7.77$ rad/s, $\hat{\xi}_1 = 0.63$, and $\hat{\xi}_2 = 0.29$, with standard errors of 0.820, 0.124, 0.042, and 0.016, respectively.

Note that, while $\overline{S}_{\mathrm{MKT}}$ was determined when fitting to the Fourier transform and to the PSD, it is taken to be 1 g in the filtering step (Step iii). The appropriate scale factor is obtained in Section 2.2.3.

Piecewise (PW) filter. The third approach of fitting a filter is to develop a piecewise filter by averaging the Fourier transform of the VERTEQII accelerogram around each octave point frequency. The value at each octave frequency should be obtained by averaging over a frequency band, which contains the information around that frequency. To do so, a band can be defined between the middle points of octave frequencies. That is, the frequency band for octave point j, can be obtained as:

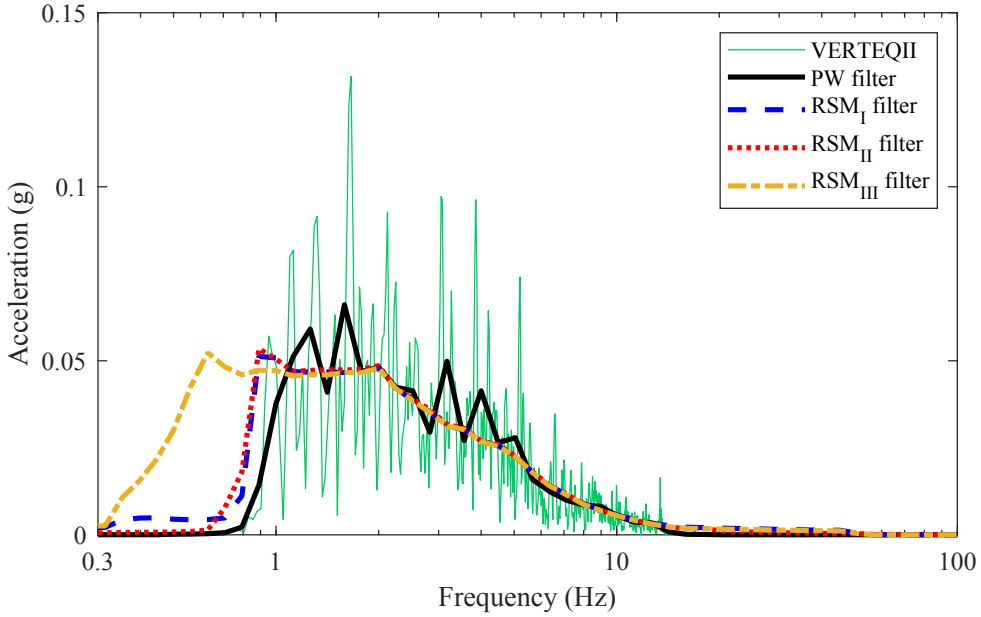

Figure 2.5: Frequency spectrum of the VERTEQII accelerogram and the fitted filters at the octave points.

$$f \in \left[e^{\frac{1}{2}\ln(f_{j-1}f_j)}, e^{\frac{1}{2}\ln(f_j f_{j+1})} \right] \tag{2.7}$$

where, f_k is the frequency at octave point k.

To be able to apply the above band for all the octave frequencies, two dummy octave frequencies are added: one lower than the 0.5 Hz (i.e., 0.4454 Hz) and one higher than 50.7968 Hz (i.e., 57.0175 Hz). The value of 0 is assigned to the 0 Hz frequency, and the band $[0, 0.4719]$ Hz is assigned to the first added octave frequency and the band $[75.5099, 100]$ Hz is assigned to the 100 Hz frequency. By doing so, the resulted filter is plotted in Figure 2.5 and tabulated in Table 2.1. For the frequencies other than the octave frequencies, linear interpolation should be used. The appropriate scale factor is obtained in Section 2.2.3.

Table 2.1: Filters at the octave frequencies for a target response spectrum of 1.15×RRS. PW: piecewise filter; RSM_I: RSM with bandpass of 0.2 to 50 Hz and matched between 1 and 50 Hz; RSM_{II}: RSM with bandpass of 0.7 to 20 Hz and matched between 1 and 50 Hz; RSM_{III}: RSM with bandpass of 0.2 to 50 Hz and matched between 0.3 and 50 Hz.

Freq.	Acceleration (10^{-3} g)				Freq.	Acceleration (10^{-3} g)			
(Hz)	PW	RSM_I	RSM_{II}	RSM_{III}	(Hz)	PW	RSM_I	RSM_{II}	RSM_{III}
0	0	0	0	0	5.6569	15.92	17.98	18.19	17.90
0.445	0.02	4.91	0.78	21.67	6.350	12.48	14.17	14.14	14.08
0.500	0.17	4.48	0.82	30.01	7.127	9.90	11.57	11.71	11.48
0.561	0.21	4.32	0.96	42.52	8.000	8.59	8.93	8.83	8.70
0.630	0.33	4.38	1.35	52.33	8.980	8.17	7.12	7.02	6.97
0.707	0.60	4.84	7.75	48.24	10.079	5.35	5.62	5.49	5.41
0.794	2.21	11.21	18.08	45.99	11.314	3.66	4.37	4.15	4.12
0.891	14.33	51.26	53.46	47.29	12.699	3.38	3.36	3.08	3.07
1.000	37.80	50.84	50.47	47.18	14.254	0.81	2.59	2.17	2.28
1.414	40.96	46.78	47.48	45.93	20.159	0.01	1.91	1.13	1.63
1.587	66.10	46.61	47.37	46.63	22.627	0.01	1.84	0.92	1.59
1.782	46.86	46.98	47.52	46.57	25.398	0.01	1.75	0.80	1.52
2.000	48.14	47.81	48.62	47.91	28.509	0.01	1.60	0.67	1.39
2.245	42.42	42.12	42.22	42.06	32.000	0.01	1.53	0.58	1.33
2.520	41.38	38.64	38.99	38.51	35.919	0.01	1.42	0.49	1.22
2.824	29.46	35.27	35.96	35.16	40.318	0.02	1.35	0.42	1.19
3.175	49.87	31.38	31.73	31.31	45.255	0.03	1.32	0.35	1.13
3.564	27.06	30.10	30.57	30.23	50.797	0.02	0.45	0.34	0.40
4.000	41.38	26.79	26.96	26.81	57.018	0.02	0.01	0.12	0.01
4.490	26.48	25.61	25.92	25.40	100	0.01	0.01	0.04	0.01
5.040	27.92	22.36	22.59	22.45					

2.2.2(b) Response Spectral-based Filters

In this class, the RRS in GR-63-CORE (Telcordia, 2012) (see Figure 2.2) is used directly for developing filters. This method is called response spectral matching (RSM), which is an iterative procedure that is described here.

Response Spectral Matching (RSM). In this approach, the Fourier transform of a nonstationary Gaussian process is modified, iteratively, in a way that its response spectrum satisfies the desired requirements. To do so, at each iteration, the Fourier transform of a nonstationary Gaussian process is scaled up or down based on the ratio of the target response spectrum (TRS) to the response spectrum of the signal at a given frequency. In this section and Section 2.2.3, the TRS is taken to be the RRS for zone 4 (Telcordia, 2012) increased by 15% (i.e., 1.15×RRS) to be halfway between the two impermissible regions; see Figure 2.2.

The RSM-based filter is developed by averaging the spectrally matched Fourier transforms of N accelerograms. The step by step procedure is summarized as follow:

1. Generate N series of nonstationary Gaussian processes, $y_n(t)$, $n = 1, \ldots, N$, as described in Steps i and ii.

2. Apply a bandpass filter between 0.2 and 50 Hz (Telcordia, 2012) to each $y_n(t)$.

3. Perform the following iterative RSM steps for each bandpass-filtered signal, $\tilde{y}_n(t)$:

   (a) Calculate the Fourier transform and the response spectrum of $\tilde{y}_n(t)$.

   (b) If the response spectrum satisfies the necessary conditions (i.e., exceeds the RRS between 1 and 50 Hz, but by no more than 30% between 1 and 7 Hz) at all the octave frequencies, go to step 4; otherwise, continue to step 3c.

   (c) Scale the response spectrum by a scaling factor determined by fitting (via least squares regression) the response spectrum to the TRS at the octave

frequencies (between 1 and 50 Hz).

(d) Calculate a modification factor for each octave frequency (between 1 and 50 Hz) as the ratio of the TRS to the scaled response spectrum.

(e) Design a piecewise filter using these modification factors, interpolating at frequencies between the octave frequencies, and apply this filter to the Fourier transform of $\tilde{y}_n(t)$.

(f) Using the inverse Fourier transform, recover the updated (filtered) $\tilde{y}_n(t)$, and return to step 3a.

4. For each spectrally-matched signal, $\tilde{y}_n^*(t)$, assign to each octave frequency the average of the Fourier transform of $\tilde{y}_n^*(t)$ in the corresponding frequency band (Eq. (2.7)), giving the nth spectrally-matched piecewise filter.

5. Average the N spectrally-matched piecewise filters to give the RSM filter.

Following this procedure, the filter (denoted RSM_I) is found by averaging $N = 100$ spectrally-matched piecewise filters, which is shown in Figure 2.5 and tabulated in Table 2.1.

Although the recommended frequency band in GR-63-CORE (Telcordia, 2012) is 0.2 to 50 Hz, having a closer look at the Fourier transform of VERTEQII (see Figure 2.3), it can be observed that the VERTEQII accelerogram has negligible acceleration content lower than 0.7 Hz and higher than 20 Hz. So, another filter is developed by applying the RSM procedure (Steps 1 to 5), but replacing the bandpass filter range in Step 2 by 0.7 to 20 Hz. The developed filter (denoted RSM_II) is shown in Figure 2.5 and is tabulated in Table 2.1.

In the RSM procedure described above, the focus is on the frequency band between 1 and 50 Hz, while frequencies shorter than 1 Hz are allowed to be greatly attenuated. A reason for this is the performance limitations of most shake tables to generate such

strong motions.* Near-field excitations may have large pulses, resulting in higher accelerations at long periods (low frequencies) (Khoshnoudian et al., 2015b). Here, to include the low frequency content in the filter, the above procedure is repeated by replacing the frequency band (1 to 50 Hz) in Steps 3b, 3c, and 3d by the frequency band between 0.3 and 50 Hz. The resulting filter (denoted RSM_{III}) is shown in Figure 2.5 and tabulated in Table 2.1.

Note that the RSM filter values reported in Table 2.1, which are applied to the windowed nonstationary process (Step ii), require an additional scaling factor to match the target response spectrum. This is because the scaling factor determined in Step 3c is not retained in the resulting filters. The appropriate scale factors for all three RSM filters are determined in the following section.

2.2.3 Scale Factors

In this section a constant scale factor is obtained for each of the filters developed above. To do so, the following steps, for each filter, are followed:

1. Generate 1000 series of nonstationary Gaussian processes as described in Steps i and ii.

2. Obtain the Fourier transforms of the nonstationary processes.

3. Apply the developed filter (Step iii).

4. Transform the filtered signals back to the time domain using the inverse Fourier transform.

5. Find the response spectrum of each record.

*For example, the mean peak displacement and velocity of 1000 accelerograms generated with RSM_{III} are 73.8 cm and 156.6 cm/s, respectively, which are near the performance capabilities (i.e., 75 cm and 180 cm/s) of the largest shake table in the United States (LHPOST at the University of California, San Diego).

6. Find the scale factor for each filtered signal, separately, to fit to the 15% increased RRS at the evaluated octave frequencies using least squares regression.

Applying the above steps for each filter, the mean and standard deviation of the scale factors are tabulated in Table 2.2.

Now, several suites of synthetic accelerograms are generated using Steps i to iv (Section 2.2) by applying each filter separately. The response spectra of these accelerograms are shown in Figure 2.6. Included in these figures are their mean and their dispersion (i.e., ± one standard deviation). These suites will be used in Section 2.4 for the probabilistic analysis of a rolling isolation system.

2.3 Dynamics of a Rolling Isolation System

The RIS considered in this study uses a double rolling pendulum bearing (Figure 2.7) consisting of a concave up surface attached to the floor, a concave down surface attached to the bottom of the isolated equipment, and a ball that rolls between these surfaces. The profile of these surfaces contain two regions: a central circular region with radius R (located at the apex) and a constant slope region with angle θ. This constant slope causes the system to have a constant maximum acceleration over this region.

In the following section, the equation of motion governing the RIS are developed. Then, this equation is used for designing the profile of the RIS and also controlling the

Table 2.2: Scale factors for a target response spectrum of 1.15×RRS.

Filter	Mean ($\times 10^3$)	Standard Deviation ($\times 10^3$)
KT (fit to the Fourier Transform)	8.59	0.606
KT (fit to the PSD)	10.5	0.569
MKT (fit to the Fourier Transform)	6.19	0.430
MKT (fit to the PSD)	7.53	0.388
PW	325	22.7
RSM_I	345	22.3
RSM_{II}	345	22.9
RSM_{III}	343	21.9

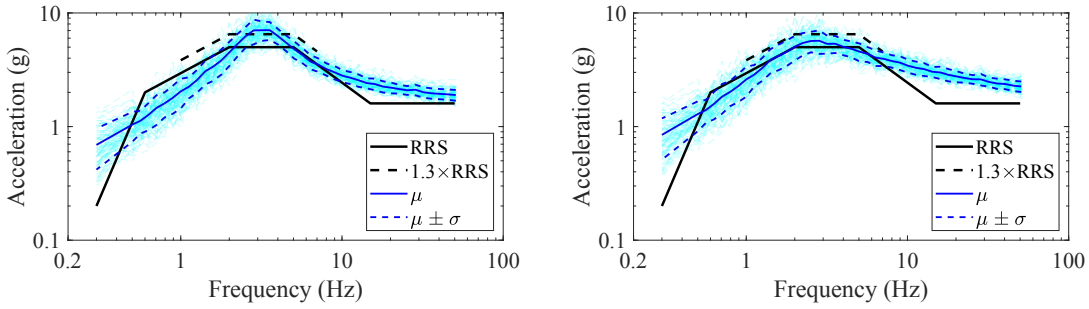

(a) KT (fit to the Fourier Transform)

(b) KT (fit to the PSD)

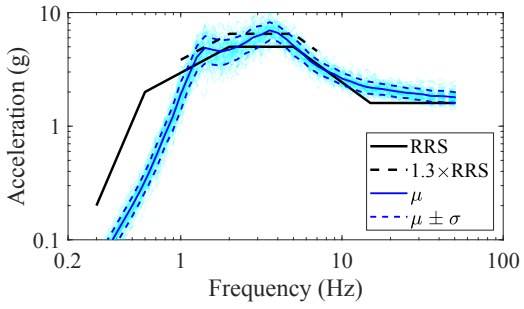

(c) MKT (fit to the Fourier Transform)

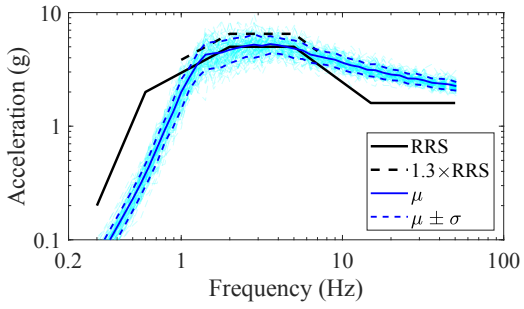

(d) MKT (fit to the PSD)

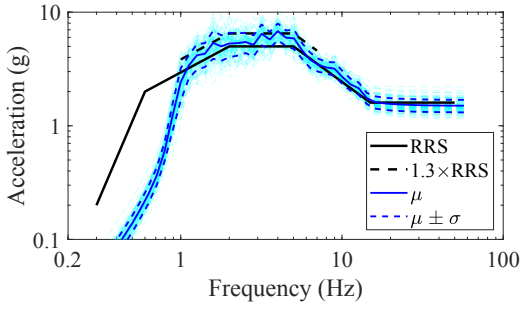

(e) PW

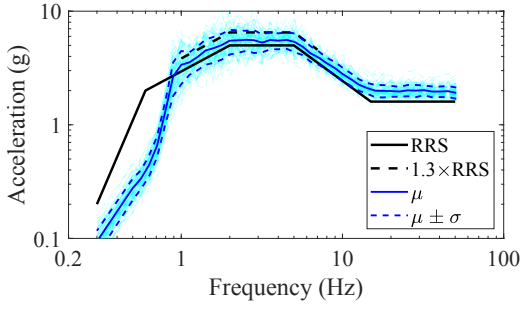

(f) RSM_{I}

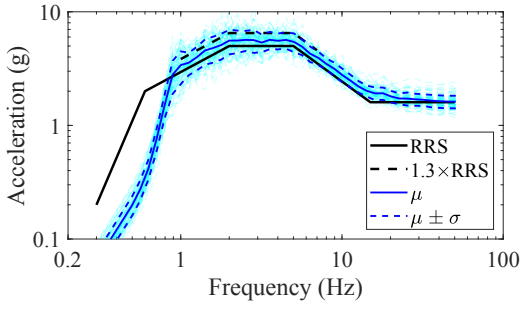

(g) RSM_{II}

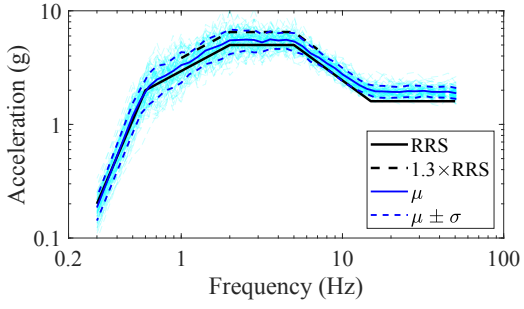

(h) RSM_{III}

Figure 2.6: Response spectra of 100 accelerograms with their means (μ) and standard deviations (σ), scaled to 1.15×RRS (i.e., scale factors reported in Table 2.2).

performance of the designed RIS under the VERTEQII accelerogram described earlier.

2.3.1 Equation of Motion

In this study, the equation of motion governing the RIS is developed through Lagrange's equation. The potential energy of the system due to displacement $u(t)$ is

$$V = mgh(u) \tag{2.8}$$

where m is the isolated mass (including the upper isolation layer and the isolated equipment), g is the gravitational acceleration, and $h(u)$ is the increase in the height of the system as a function of the ball location $(u/2)$. For the considered rolling pendulum bearing (Figure 2.7),

$$h(u) = 2 \times \begin{cases} R - \sqrt{R^2 - (u/2)^2}, & |u| \le u_o \\ R - \sqrt{R^2 - (u_o/2)^2} + (u/2 - u_o/2)\tan(\theta), & |u| > u_o \end{cases} \tag{2.9}$$

where $u_o = 2R\sin(\theta)$ is the displacement at which the ball moves from the central spherical region to the constant slope region. Accordingly, the slope function and its derivative are

$$h'(u) = \begin{cases} \dfrac{u}{2\sqrt{R^2 - (u/2)^2}}, & |u| \le u_o \\ \operatorname{sgn}(u)\tan(\theta), & |u| > u_o \end{cases}, \tag{2.10a}$$

$$h''(u) = \begin{cases} \dfrac{R^2}{8\sqrt{(R^2 - (u/2)^2)^3}}, & |u| \le u_o \\ 0, & |u| > u_o \end{cases}. \tag{2.10b}$$

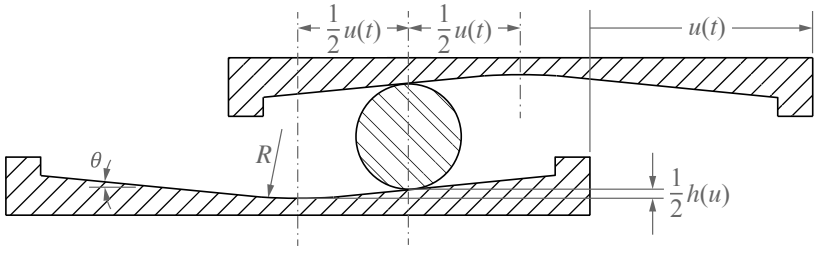

Figure 2.7: Configuration of a double conical rolling pendulum bearing.

The kinetic energy of the system is

$$T = \frac{1}{2}m[(\dot{u}_\mathrm{f} + \dot{u})^2 + \dot{h}^2] \equiv \frac{1}{2}m[(\dot{u}_\mathrm{f} + \dot{u})^2 + (h'(u)\,\dot{u})^2] \tag{2.11}$$

where $\dot{u}_\mathrm{f}(t)$ is the (horizontal) building floor motion.

The equation of motion can be found from Lagrange's equation:

$$\frac{\mathrm{d}}{\mathrm{d}t}\frac{\partial}{\partial \dot{u}}(T - V) - \frac{\partial}{\partial u}(T - V) = Q \tag{2.12}$$

where Q is the generalized force. Taking Q to be the dissipative forces, the resulting equation of motion is given by:

$$m[1 + h'^2(u)]\ddot{u} + mh''(u)h'(u)\,\dot{u}^2 + c\dot{u} + \mu mg\tanh(\dot{u}/V_s) + mgh'(u) = -m\ddot{u}_\mathrm{f} \tag{2.13}$$

where c is the viscous damping coefficient, μ is the friction coefficient, and V_s is the velocity scaling constant (Harvey et al., 2014b), which controls the transition from static friction to kinetic friction. The smaller the V_s, the sharper the transition. In this study, V_s is taken to be 0.5 cm/s. Eq. (2.13) can be approximated to

$$m\ddot{u} + c\dot{u} + \mu mg\tanh(\dot{u}/V_s) + mgh'(u) = -m\ddot{u}_\mathrm{f} \tag{2.14}$$

assuming shallow rolling surfaces (i.e., small $h'(u)$ and large R).

2.3.2 Design of the RIS

In this study, the term related to viscous damping is ignored, due to the minuscule effect of this dissipative force compared to friction (or rolling resistance) (Harvey et al., 2014b). The effect of all dissipative forces are modeled using the friction term in the equation of motion. This can help to simplify Eq. (2.14) as follows, which is independent of mass,

$$\ddot{u} + \mu g\tanh(\dot{u}/V_s) + gh'(u) = -\ddot{u}_\mathrm{f} \tag{2.15}$$

This simplification helps when performing a parametric study without considering the mass of the isolated object.

In this study, the same RIS configuration as described in Vargas and Bruneau (2009) is taken as the reference design. In this configuration, the radius R at the apex is 127 mm, the constant slope region has the slope of 1:10 ($\theta = 6^\circ$). The axisymmetric rolling surfaces have diameters of 213 mm. Based on the configuration of the RIS, the maximum allowable displacement is 17.8 cm, and it is assumed that the maximum tolerable acceleration by equipment is 0.3 g (Gidaris et al., 2016; IBM, 2010). To be in the acceptable region, a friction coefficient μ of 0.0175 seems satisfactory by the analyses. In general, increasing friction decreases the displacement demand at the expense of increasing acceleration demand.

Using Eq. (2.15), the time history of the displacements and accelerations are plotted in Figure 2.8 for the two cases, without and with friction. The corresponding force-displacement hysteresis are plotted in Figure 2.9. In these figures, the unacceptable regions are shaded in grey. As can be seen, this friction coefficient is satisfactory. Note that this amount of friction coefficient is achievable by adhering thin rubber sheets (Harvey et al., 2014b) or by encasing the rolling ball with damping material (Tsai et al., 2006).

2.4 Probabilistic Assessment of the RIS

In this section, a probabilistic analysis is performed on the safety of a RIS. The RIS designed in Section 2.3.2 is assessed with several suites of accelerograms generated in Section 2.2.3 using the different filters (Section 2.2.2). These suites possess different frequency characteristics (Figure 2.6). Each suite of accelerograms consists of 100 independently generated accelerograms.

The suites of accelerograms generated in Section 2.2.3 were for a TRS of 1.15×RRS. In this section, different *RRS multipliers* (other than 1.15) are considered

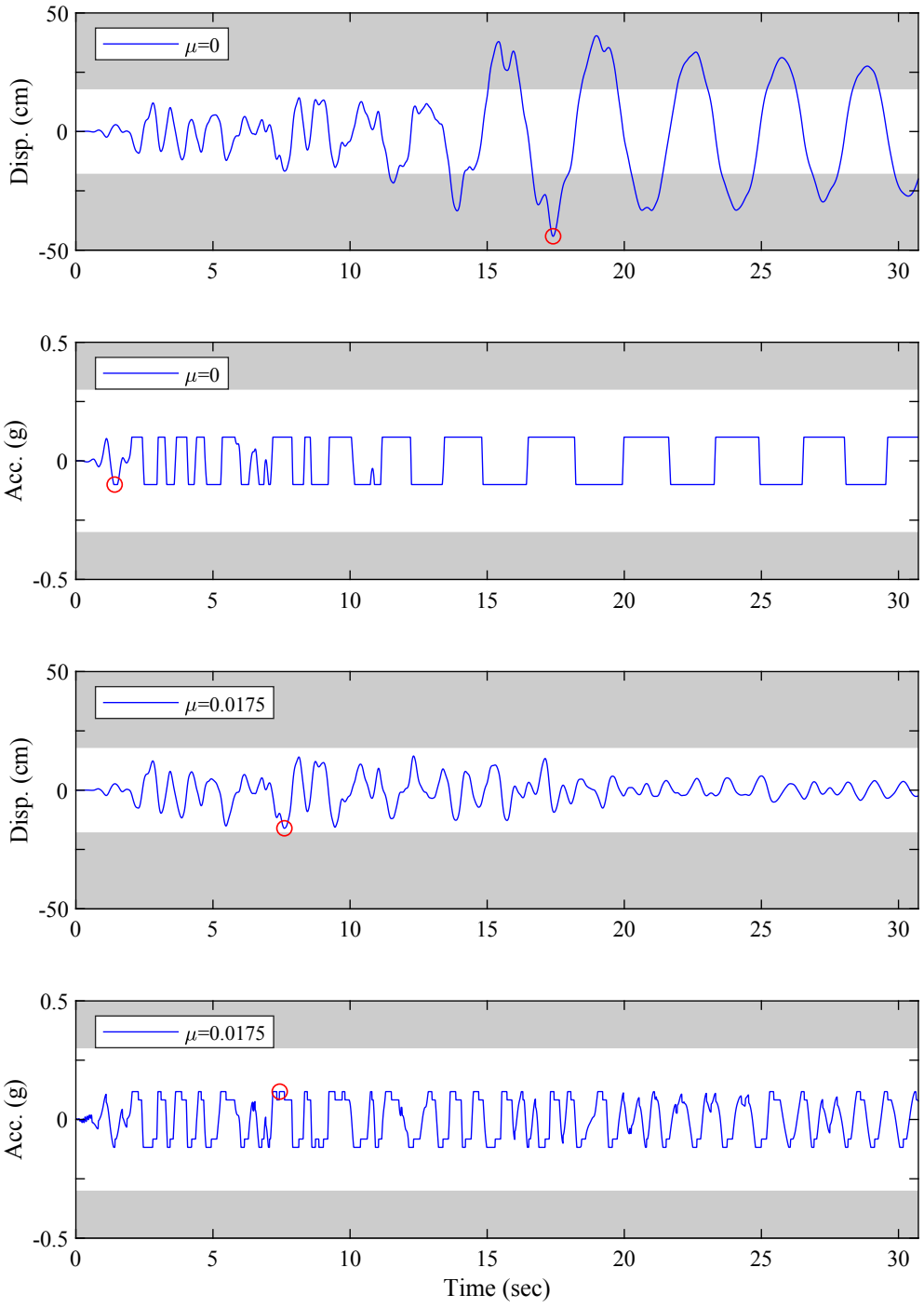

Figure 2.8: The relative displacement and total acceleration time-histories of the RIS, without and with friction under the VERTEQII accelerogram.

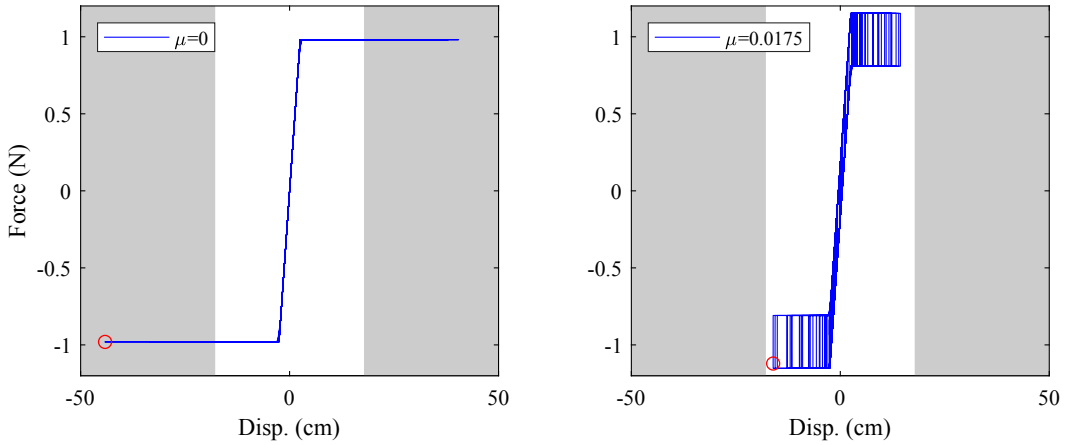

Figure 2.9: The force-displacement hysteresis of the RIS (unit mass, $m = 1$ kg), without and with friction, under the VERTEQII accelerogram.

by scaling the previously generated suites. A range of intensities is assessed by varying RRS multipliers between 0.05 and 1.3, with increment step of 0.05, providing insights on the nonlinear (amplitude-dependent) behavior of the RIS.

Due to the constant slope of the RIS (i.e., 1:10) and the constant friction coefficient (i.e., $\mu = 0.0175$), the maximum acceleration that occurs in each case is a constant fixed value (i.e., 0.12 g) and is not presented and discussed further in this study. Instead, the focus is on displacement demands, which are used as a proxy for isolation performance. That is, if the displacement response exceeds the bearing's capacity, then an impact is assumed to have occured (though not explicitly modeled), constituting a failure.

The results corresponding to the KT filters are not shown from this point forward because the KT filter does not capture well the shape of the RRS and produces high accelerations (significantly above the RRS) for low frequencies (< 0.5 Hz), causing excessively large displacements in the system. This is illustrated in Figures 2.6a and 2.6b. The mean spectral accelerations at 0.3 Hz are 0.690 and 0.845 g for KT filters fit to the Fourier transform and PSD, respectively. These accelerations correspond to pseudo-displacements of 190.3 and 233.3 cm, which are unrealistically large.

The results of the probabilistic analyses are presented in Figure 2.10, which shows

the distributions of displacements for different RRS multipliers. In these scatter plots, the blue circles represent the displacements associated with the accelerograms that remain below the 1.3×RRS (between 1 and 7 Hz), and the red crosses representing the displacements associated with accelerograms that exceed the 1.3×RRS (between 1 and 7 Hz). These blue circles in comparison with the black horizontal dashed line (i.e., displacement capacity of the considered RIS) for different intensities help to distinguish the cases when the accelerograms do not exceed the 1.3×RRS yet the displacement demands are larger than the displacement capacity.

The results of the probabilistic analyses are presented in Figure 2.11 using the fragility concept. The fragility curves, which are obtained empirically without any prior assumption of distributions, illustrate the probability of exceeding a given displacement versus the intensity measure (RRS multiplier). In this study, the considered displacements are 5, 10, 15, 20, 25, 30, 35, 40, 45, and 50 cm, as well as 17.80 cm, which is related to the displacement capacity of the considered RIS. Figures 2.10 and 2.11 collectively reveal the following observations.

For a RRS multiplier of 1.15, the failure rates (i.e., probability of exceeding 17.8 cm) are 92, 95, 67, 99, 96, and 100% for MKT fit to the Fourier transform, MKT fit to the PSD, PW, RSM_I, RSM_{II}, and RSM_{III}, respectively. For a RRS multiplier of 1, these failure rates decrease to 77, 84, 50, 97, 90 and 100%, respectively. These failure rates for a RRS multiplier of 0.85 further decrease to 49, 59, 22, 83, 71, and 100%, respectively. These failure rates are remarkably high, which question the currently used criteria for RISs designed for protecting telecommunications equipment.

The MKT filter and PW filter greatly attenuate the low frequency content of the accelerograms and, as a result, produce smaller displacements compared to other cases. The mean accelerations at 0.3 Hz for MKT (fit to the Fourier transform), MKT fit to the PSD, and PW are respectively 0.057, 0.062, and 0.045 g, which correspond to pseudo-

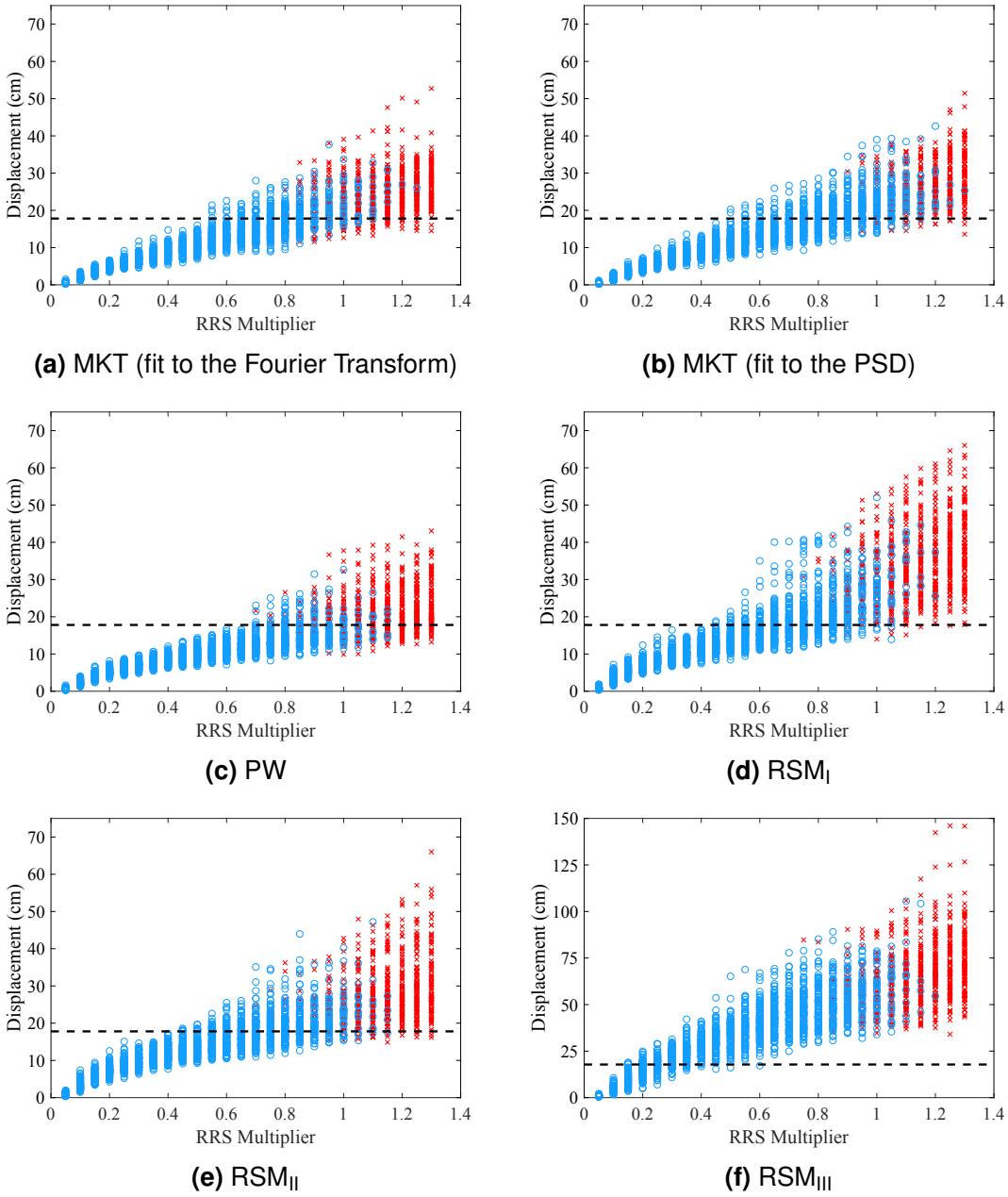

(a) MKT (fit to the Fourier Transform)

(b) MKT (fit to the PSD)

(c) PW

(d) RSM_{I}

(e) RSM_{II}

(f) RSM_{III}

Figure 2.10: Distribution of peak displacements for varying required response spectrum (RRS) multipliers. The red crosses are the responses associated with the records that exceed the RRS by more than 30% (i.e., impermissible region A in Figure 2.2), and the blue circles are those that do not. The dashed line is the displacement capacity of the considered RIS. Note the scale difference in the subplot (f).

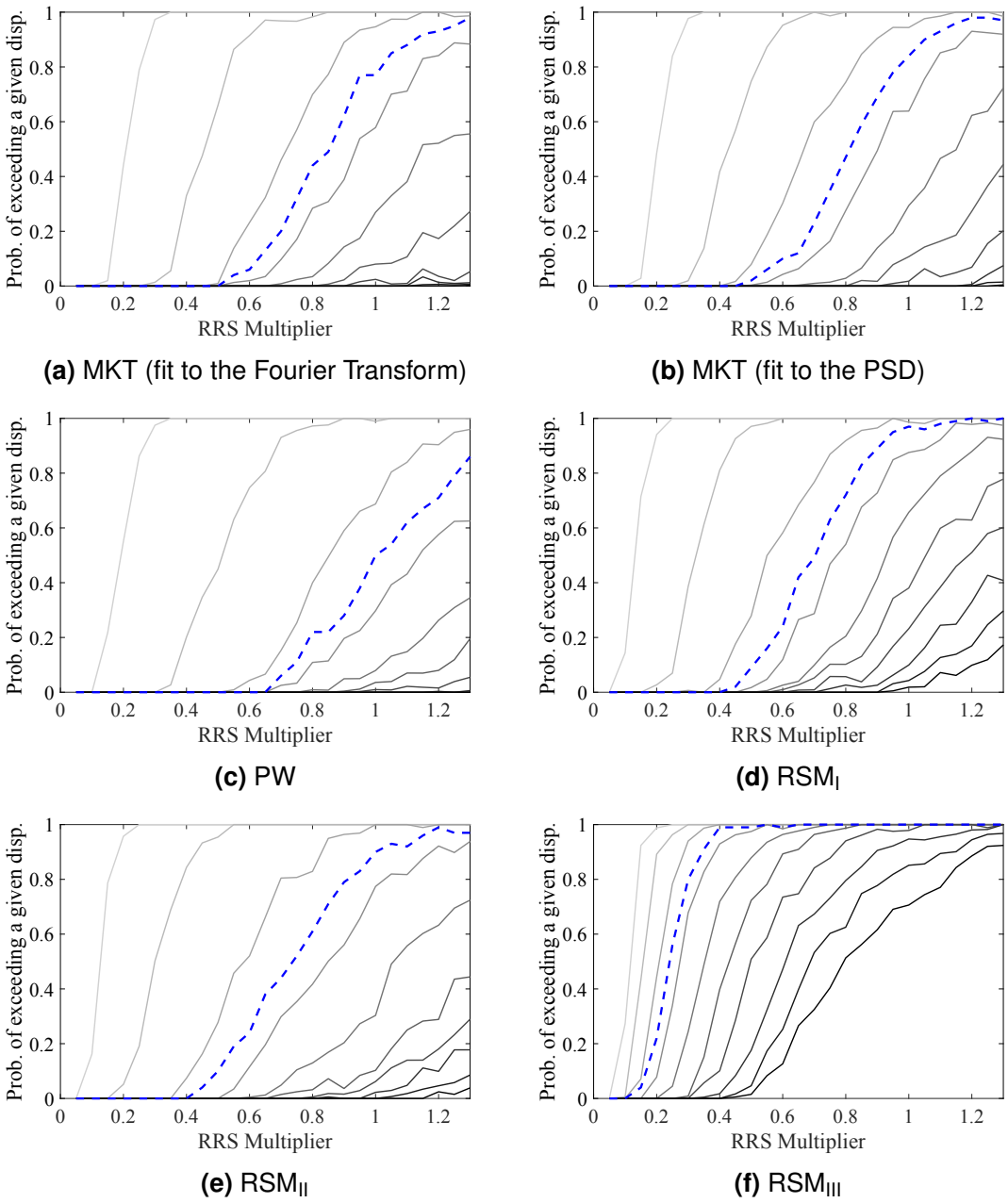

(a) MKT (fit to the Fourier Transform)

(b) MKT (fit to the PSD)

(c) PW

(d) RSM_{I}

(e) RSM_{II}

(f) RSM_{III}

Figure 2.11: Fragility curves — probability of exceeding a given displacement versus floor-motion intensity (required response spectrum (RRS) multiplier) — for accelerograms generated with different methods. The curves from light grey to dark grey correspond to displacement levels of 5 to 50 cm, respectively, in increments of 5 cm. The blue dashed line fragility curves are associated with a displacement of 17.8 cm (capacity of the considered RIS).

displacements of 15.6, 17.2, and 12.4 cm.

The RSM_I filter incorporates the criteria that are recommended in GR-63-CORE (Telcordia, 2012). As shown in Figure 2.6f, the mean of the generated accelerograms satisfies the recommended criteria (i.e., the bandpass frequency between 0.2 and 50 Hz, and exceeding the RRS between 1 and 50 Hz, but not by more than 30% between 1 and 7 Hz). However, the failure rates are extremely high — 99, 97, and 83% for RRS multipliers of 1.15, 1, and 0.85, respectively. This is due to the relatively high accelerations in low frequencies — the mean acceleration at 0.3 Hz is 0.094 g, which corresponds to pseudo-displacements of 25.9 cm.

The main difference between the prescribed accelerogram in GR-63-CORE (i.e., VERTEQII) and the generated accelerograms with RSM_I is in their frequency contents. As can be seen in Figure 2.3, the Fourier transform of VERTEQII has negligible acceleration content lower than 0.7 Hz and higher than 20 Hz. This contradicts the recommendations for testing telecommunications equipment in GR-63-CORE. In this study, the low frequency content is important since isolation systems shift the system's frequency toward the low frequency region and usually high frequency motions do not contribute significantly to the displacement responses. This is the main reason why the RSM_I has high failure rates. In comparison, RSM_I case RSM_{II} is also assessed. In this case, the nonstationary signals are passed through a bandpass filter between 0.7 and 20 Hz (similar to what can be seen in VERTEQII). This case has lower failure rates compared to the RSM_I — 96, 90, and 71% compared to 99, 97, and 83% for RRS multipliers of 1.15, 1, and 0.85, respectively; however, the failure rates remain quite large.

GR-63-CORE recommends that the accelerograms should exceed the RRS (Figure 2.2) between 1 and 50 Hz and it has no criteria for frequencies lower than 1 Hz. However, the RRS has 0.2-g spectral acceleration at 0.3 Hz, which corresponds to a pseudo-displacement of 55.2 cm. Buildings or structures that house telecommunica-

tions equipment usually transfer (or even amplify) the low frequency vibrations and filter (attenuate) the high frequency content. That means the low frequency vibrations appears more than the high frequency vibrations at the location of telecommunications equipment. Thus, these low frequency vibrations need more attention. The RRS includes the expected acceleration content at low frequencies, whereas the prescribed accelerogram fails to capture it. These limitations are applied mostly due to the performance limits of shaker tables (Biondi et al., 2015), as previously discussed. For this reason, the case RSM_{III} is assessed for representing a more realistic scenario that happens at the location of equipment. Doing so, this filter produce low frequency accelerations (i.e., 0.186 *g* at 0.3 Hz) close to the RRS (i.e., 0.2 *g* at 0.3 Hz). A 0.186-*g* acceleration at 0.3 Hz has a pseudo-displacement of 51.2 cm. As stated before, this case produces shocking failure rates of 100% for all three intensity levels (RRS multipliers of 1.15, 1, and 0.85).

Another observation that can be made from Figure 2.10 is that there are many accelerograms, for each case, that are below the 1.3×RRS (blue circles) yet demand large displacements. These observations support the insufficiency of using only one accelerogram for testing and designing telecommunications equipment. Consequently, a suite of accelerograms should be introduced that can be a good representation of the variability that exists in seismic excitations. Moreover, it can be concluded that VERTEQII is not representative of the RRS in GR-63-CORE (Telcordia, 2012) at low frequencies and, hence, is not conservative. Furthermore, these observations raise the question about whether ignoring the low frequency accelerations is reasonable and realistic for isolated telecommunications equipment and whether RISs designed using this guideline are safe.

2.5 Conclusions

This chapter aimed to answer questions regarding the safety of rolling isolation systems (RISs) used for protecting telecommunications equipment through the GR-63-CORE guideline (Telcordia, 2012). This was motivated by observing the discrepancy between the prescribed accelerogram for testing (VERTEQII), the recommended criteria, and the required response spectrum (RRS). The RRS is specified between 0.3 and 50 Hz, yet the testing protocol requires that the RRS be met or exceeded only between 1 and 50 Hz. The prescribed accelerogram, therefore, has little to no acceleration content below 1 Hz. It is at these low frequencies that long displacements are likely to occur, which can lead to impacts in the isolator. On top of that, there is only one record for testing, which is unable to represent the variability that exists in earthquakes.

To assess the safety of a RIS, the first step was to produce several suites of accelerograms; each suite represents different assumptions and approaches. Several filters were developed, including Kanai-Tajimi (KT), modified Kanai-Tajimi (MKT), piecewise (PW), and response spectral matching (RSM). The procedure for generating building floor motions (accelerograms) was outlined in detail in Section 2.2. Then, it was shown that a RIS with friction coefficient 0.0175 can pass the GR-63-CORE requirements. This RIS design was further used for the probabilistic analyses under different suites of accelerograms and intensities. The accelerograms produced by the KT filter have large acceleration in low frequencies and produced huge displacements. The results of the probabilistic analyses for the other filters (i.e., KT, MKT, PW, and RSM) were presented as the distribution of displacements for each intensity level, as well as through fragility curves, which show the probability of exceeding a given displacement. In these fragility curves, the RRS multiplier is used as an intensity measure. These fragility curves can guide the design of a RIS to achieve the required displacement capacity; however, additional analyses are required to extend these fragility curves to

other RIS configurations.

The MKT, PW and RSM_{II} filters produce accelerograms that are most similar to VERTEQII. However, large displacement demands were observed for these cases. RSM_I is the case where the recommendations in GR-63-CORE are implemented, which produces larger displacement demands compared to MKT, PW, and RSM_{II}. The RRS shows the expected acceleration content at each frequency; however, MKT, PW, RSM_I, and RSM_{II} fail to produce such expected acceleration contents, more specifically at low frequencies. These low frequency accelerations are associated with large displacement demands. This shortcoming (absence of low frequency content) led to the generation of RSM_{III}, which has the best agreement with the RRS. The resulting probabilities of exceeding the displacement capacity are large enough to question the prescribed accelerogram for testing (i.e., VERTEQII) and the recommendations in GR-63-CORE (Telcordia, 2012). These recommendations are not consistent with the RRS, especially at low frequencies where RISs are designed to operate.

While the filters and methodology were developed in the context of assessing the fragility of a RIS for telecommunications equipment, it is worth noting that the filters and methods may find broader application. For example, accelerograms generated with the proposed methods can readily be used to evaluate the safety of non-isolated telecommunications equipment, incorporating low frequency content (e.g., RSM_{III}) and accelerogram variability in a probabilistic analysis. Also, the parametric filters (KT and MKT) and piecewise filters (PW and RSM) could be used to design vibration absorbers (i.e., tuned mass dampers) for telecommunications equipment under random excitations (Hoang et al., 2008).

Even though the produced accelerograms are similar to VERTEQII, large displacements were observed. These large displacement demands are in excess of displacement capacity. One way to address this issue is to increase displacement capacity. The other

way is to reduce displacement demand via some mechanism to avoid harmful impacts. Accordingly, in the following chapter, a dual-mode system for impact mitigation is introduced.

Chapter 3
Dual-Mode Impact Mitigation

3.1 Overview

Following the observed displacement demands in excess of displacement capacity in Chapter 2, in this chapter a method to reduce the displacement demand for mitigation of the harmful effect of impact is proposed. As discussed in Section 1.3, other researchers have proposed impact mitigation mechanisms that work only when a triggered displacement threshold is reached. However, the mechanisms considered in previous studies to reduce displacements and mitigate impacts had some predefined force-displacement or force-velocity relationship. Unlike previous studies that limited their solutions to some prescribed relationships, in this chapter, this limitation is relaxed to improve the performance of these systems. A dual-mode system is considered for the suppression of responses (i.e., displacements) under extreme seismic loading by allowing the system to respond without any control action at small to moderate displacements as would be experienced under design level seismic loading while controlling the system at large displacements under extreme seismic loading. To do so, an innovative solution is sought that can more effectively utilize the available displacement capacity while simultaneously seeking to reduce sustained total accelerations. To determine the best possible control action trajectory, optimal control is used to achieve both performance objectives (i.e., mitigating pounding/impact and controlling total acceleration).

Open-loop solutions are found by solving the Euler-Lagrange equations with the

control action trajectories unconstrained only in the large displacement region. Finding the optimal solution to this problem is not trivial, and the solution requires the knowledge of the external loading in the future, so it is not immediately implementable. To overcome these challenges, the optimal control problem is redefined to be solved in a piecewise fashion only in the regions that the control action is active. The duration of each excursion into an active control region is not known, constituting an unknown final time. To solve this optimal control problem with unknown fixed final time, an iterative procedure is proposed. This procedure is then used to find the best control action mechanism that can be used for dual-mode systems. After that, using the linear quadratic regulator (LQR), a non-iterative suboptimal procedure (i.e., clipped-LQR) is used to solve the optimal control problem with unknown fixed final time. Following that, an extensive numerical assessment is performed to understand the piecewise optimal control behaviors, to assess the effect of various initial conditions, and to evaluate the clipped-LQR procedure. Using this numerical assessment, several design curves are developed that can guide the design of passive control devices for linear time-invariant dual-mode systems. Finally, using the developed design curves, a dual-mode system equipped with a Kelvin-Voigt device is designed for the purpose of illustration, and is evaluated under an accelerogram scaled to the maximum considered earthquake.

3.2 Bench-marking Framework

Consider a linear time-invariant (LTI) system with a displacement capacity of $d_{\max}$. When the system undergoes large-amplitude events, displacement demand may exceed $d_{\max}$, which causes impact and spikes in the transmitted acceleration. Incorporating energy dissipative mechanisms affects the system's performance at low-amplitude events if the damping is applied everywhere. So, in order to improve the performance of systems under large-amplitude events such as maximum considered earthquake (MCE) while not affecting the system's performance at low-amplitude seismic events such as

design basis earthquake (DBE), a dual-mode system is utilized, which applies some dissipative mechanism in the region beyond the DBE demand. In the region that the control action is active, the performance is defined as to control the maximum displacements to be within the allowable limits while at the same time not producing large accelerations.

Following this general idea, the system should be designed in such a way that the system should be allowed to respond with its own dynamics under a DBE-level event (i.e., when the absolute value of the displacement is smaller than or equal to a predefined threshold), and when the system undergoes events larger than the DBE level event such as MCE level event (i.e., when the absolute value of the displacement is larger than the predefined threshold), the system should be equipped with some energy dissipative devices in the regions beyond the predefined threshold. The threshold can be chosen to be a fraction (or factor) ϕ of the displacement capacity $d_{\max}$ (Zargar et al., 2017).

As described in the introduction, researchers studied different passive devices to mitigate the pounding of structures and experimentally evaluated some of those devices. However, those studies are based on some predefined passive devices, which can possibly be improved. In order to identify the best possible mechanism and consequently the most appropriate dissipative devices, an optimal control approach is sought in this chapter. The optimal control results in the best possible impact avoidance mechanism, which then can be used as a benchmark to identify the most appropriate devices.

3.3 Optimal Control Formulation

3.3.1 System's Dynamics

The governing dynamic equation of motion for a LTI single-degree-of-freedom system is given by

$$\ddot{x}(t) + \frac{c}{m}\dot{x}(t) + \frac{k}{m}x(t) + u(t) = -\ddot{x}_g(t) \tag{3.1}$$

where k, c, and m are the stiffness, damping and mass of the system, respectively;

$x(t)$, $u(t)$, and $\ddot{x}_g(t)$ are the displacement relative to the ground, the control action, and the external ground acceleration, respectively; and overdot denotes the derivative with respect to time t. The state space representation of the equation of motion (Eq. (3.1)) is given by

$$\dot{\boldsymbol{x}}(t) = \boldsymbol{f}(\boldsymbol{x}(t), u(t), t) \equiv \boldsymbol{A}\boldsymbol{x}(t) + \boldsymbol{B}u(t) + \boldsymbol{W}\ddot{x}_g(t) \tag{3.2}$$

where $\boldsymbol{x}(t) = [x(t), \dot{x}(t)]^T$; the state matrix $\boldsymbol{A}$, the input matrix $\boldsymbol{B}$, and the exogenous input matrix $\boldsymbol{W}$ are

$$\boldsymbol{A} = \begin{bmatrix} 0 & 1 \\ -\omega^2 & -2\xi\omega \end{bmatrix} \quad \text{and} \quad \boldsymbol{B} = \boldsymbol{W} = \begin{bmatrix} 0 \\ -1 \end{bmatrix} \tag{3.3}$$

where $\omega = \sqrt{k/m}$ and $\xi = c/\sqrt{4km}$. The optimal control problem is formulated in the following section.

3.3.2 Optimal Control – Known Fixed Final Time

The objective of this optimal control problem is to control displacements while keeping accelerations within the allowable limits. So, the cost functional is defined as the minimization over a finite-horizon ($t \in [0, t_\mathrm{f}]$) in a quadratic form as follows:

$$J = \int_0^{t_\mathrm{f}} L(\boldsymbol{x}(t), u(t), t)\,\mathrm{d}t \equiv \int_0^{t_\mathrm{f}} \left(q_d x^2(t) + q_a(\ddot{x}(t) + \ddot{x}_g(t))^2 + q_u u^2(t)\right)\mathrm{d}t \tag{3.4}$$

where q_d, q_a, and q_u are the weighting factors for displacement, total acceleration, and control action, respectively. The cost functional can be written in the standard quadratic form as follows:

$$J = \frac{1}{2}\int_0^{t_\mathrm{f}} \left(\boldsymbol{x}^T(t)\boldsymbol{Q}\boldsymbol{x}(t) + 2\boldsymbol{x}^T(t)\boldsymbol{N}u(t) + u(t)^T R u(t)\right)\mathrm{d}t \tag{3.5}$$

where the weighting matrices are:

$$\boldsymbol{Q} = \begin{bmatrix} 2q_d + 2\omega^4 q_a & 4\xi\omega^3 q_a \\ 4\xi\omega^3 q_a & 8\xi^2\omega^2 q_a \end{bmatrix}, \quad \boldsymbol{N} = \begin{bmatrix} 2\omega^2 q_a \\ 4\xi\omega q_a \end{bmatrix}, \quad \text{and} \quad R = 2q_a + 2q_u. \tag{3.6}$$

This optimization problem is subjected to the dynamic constraint (Eq. (3.2)). Lagrange multipliers $\boldsymbol{p}(t)$ (or co-states) are used to augment the dynamic constraint to the cost functional where the Hamiltonian is defined as

$$H = L + \boldsymbol{p}^T \boldsymbol{f}. \tag{3.7}$$

Pontryagin's minimization principle yields the following necessary conditions for optimality (Euler-Lagrange equations):

$$0 = \frac{\partial H}{\partial u} = \frac{\partial L}{\partial u} + \frac{\partial \boldsymbol{f}^T}{\partial u}\boldsymbol{p} \equiv Ru(t) + \boldsymbol{N}^T\boldsymbol{x}(t) + \boldsymbol{B}^T\boldsymbol{p}(t), \tag{3.8a}$$

$$-\dot{\boldsymbol{p}}(t) = \frac{\partial H}{\partial \boldsymbol{x}} = \frac{\partial L}{\partial \boldsymbol{x}} + \frac{\partial \boldsymbol{f}^T}{\partial \boldsymbol{x}}\boldsymbol{p} \equiv \boldsymbol{Q}^T\boldsymbol{x}(t) + \boldsymbol{N}u(t) + \boldsymbol{A}^T\boldsymbol{p}(t), \tag{3.8b}$$

$$\dot{\boldsymbol{x}}(t) = \frac{\partial H}{\partial \boldsymbol{p}} = \boldsymbol{f} \equiv \boldsymbol{A}\boldsymbol{x}(t) + \boldsymbol{B}u(t) + \boldsymbol{W}\ddot{x}_g(t). \tag{3.8c}$$

The solution to this system of equations leads to the optimal states, co-states, and control action. The control action is obtained from the first Euler-Lagrange equation as follows:

$$u(t) = -R^{-1}\left(\boldsymbol{N}^T\boldsymbol{x}(t) + \boldsymbol{B}^T\boldsymbol{p}(t)\right). \tag{3.9}$$

The second and third Euler-Lagrange equations represent the co-state and state dynamics, respectively, which must be solve simultaneously. This two-point boundary value problem (TPBVP) has the initial boundary condition on the states $\boldsymbol{x}(0) = [x_0, \dot{x}_0]^T$, and the terminal boundary condition on the co-states $\boldsymbol{p}(t_f) = [0, 0]^T$.

3.3.2(a) Nondimensional Formulation

It will be convenient to recast the optimal control problem in nondimensional form. The following nondimensional scheme is introduced:

$$\begin{gathered} x(t) = \phi d_{\max} X(\tau), \quad \dot{x}(t) = \omega\phi d_{\max}\dot{X}(\tau), \quad \ddot{x}(t) = \omega^2\phi d_{\max}\ddot{X}(\tau), \\ t = \tau/\omega, \quad u(t) = \omega^2\phi d_{\max}U(\tau), \quad \ddot{x}_g(t) = \omega^2\phi d_{\max}\ddot{X}_g(\tau) \end{gathered} \tag{3.10}$$

where X, τ, U, and $\ddot{X}_g$ are the nondimensional displacement, time, control action, and ground acceleration, respectively. It is understood that an overdot on the nondimen-

sional variables denotes differentiation with respect to the scaled time τ. Inserting these transformations into Eq. (3.2), the dynamics of the LTI system can be written in the nondimensionalized form as follows:

$$\dot{\boldsymbol{X}}(\tau) = \mathcal{A}\boldsymbol{X}(\tau) + \mathcal{B}U(\tau) + \mathcal{W}\ddot{X}_g(\tau) \tag{3.11}$$

where $\boldsymbol{X}(\tau) = [X(\tau), \dot{X}(\tau)]^T$; the input matrix $\mathcal{B} \equiv \boldsymbol{B}$, the exogenous input matrix $\mathcal{W} \equiv \boldsymbol{W}$, and the state matrix $\mathcal{A}$ is given by

$$\mathcal{A} = \begin{bmatrix} 0 & 1 \\ -1 & -2\xi \end{bmatrix}. \tag{3.12}$$

Likewise, the cost functional (Eq. (3.4)) can be re-expressed as follows:

$$J = \int_0^{\tau_f} \mathcal{L}(\boldsymbol{X}(\tau), U(\tau), \tau)\, \mathrm{d}\tau \equiv \int_0^{\tau_f} \left(Q_d X^2(\tau) + Q_a(\ddot{X}(\tau) + \ddot{X}_g(\tau))^2 + Q_u U^2(\tau) \right) \mathrm{d}\tau \tag{3.13}$$

where $Q_d = d_{\max}^2 q_d/\omega$, $Q_a = d_{\max}^2 \omega^3 q_a$, and $Q_u = d_{\max}^2 \omega^3 q_u$. Alternatively, the cost functional can be written in the standard quadratic form:

$$J = \frac{1}{2} \int_0^{\tau_f} \left(\boldsymbol{X}^T(\tau)\boldsymbol{Q}\boldsymbol{X}(\tau) + 2\boldsymbol{X}^T(\tau)\boldsymbol{\mathcal{N}}U(\tau) + U^T(\tau)\mathcal{R}U(\tau) \right) \mathrm{d}\tau \tag{3.14}$$

where the nondimensional weighting matrices are

$$\boldsymbol{Q} = \begin{bmatrix} 2Q_d + 2Q_a & 4\xi Q_a \\ 4\xi Q_a & 8\xi^2 Q_a \end{bmatrix}, \quad \boldsymbol{\mathcal{N}} = \begin{bmatrix} 2Q_a \\ 4\xi Q_a \end{bmatrix}, \quad \text{and} \quad \mathcal{R} = 2Q_a + 2Q_u. \tag{3.15}$$

The first Euler-Lagrange equation in the nondimensionalized form gives the nondimensional control action

$$U(\tau) = -\mathcal{R}^{-1}(\boldsymbol{\mathcal{N}}^T\boldsymbol{X}(\tau) + \mathcal{B}^T\boldsymbol{P}(\tau)), \tag{3.16}$$

and the second Euler-Lagrange equation gives the nondimensional co-state dynamics:

$$-\dot{\boldsymbol{P}}(\tau) = \boldsymbol{Q}^T\boldsymbol{X}(\tau) + \boldsymbol{\mathcal{N}}U(\tau) + \mathcal{A}^T\boldsymbol{P}(\tau). \tag{3.17}$$

This equation along with the nondimensionalized dynamic constraint (Eq. (3.11)) have the initial boundary condition on the states $\boldsymbol{X}(0) = [X_0, \dot{X}_0]^T$, and the terminal boundary condition on the co-states $\boldsymbol{P}(\tau_\mathrm{f}) = [0, 0]^T$. In this TPBVP, the co-states should be solved backward in time and the states should be solved forward in time. For a linear system with quadratic Lagrangian, this TPBVP is straightforward to solve. However, in the presence of constraints on the control action, additional consideration is required. Of interest to this study is a problem in which the control action is active in only some regions (denoted $\boldsymbol{\mathcal{X}}$) of the state space and is inactive in other regions (denoted $\boldsymbol{\mathcal{X}}'$), where $\boldsymbol{\mathcal{X}}$ and $\boldsymbol{\mathcal{X}}'$ are complemented subspaces of $\mathbb{R}^2$. In the active region $\boldsymbol{X}(\tau) \in \boldsymbol{\mathcal{X}}$, the variation of the control action, $\delta U(\tau)$, is arbitrary, so the derivative $\partial \mathcal{H}/\partial U$ is necessarily zero and $U(\tau)$ is given by Eq. (3.16). In the inactive region $\boldsymbol{X}(\tau) \in \boldsymbol{\mathcal{X}}'$, $U(\tau) = 0$, so the permissible variation $\delta U(\tau)$ is necessarily equal to zero. This means that in the inactive region the values of the co-states are not used for identifying the control action; however, the co-states are still required to be determined in the TPBVP since the determination of states depend on the co-states.

As a check to ensure that no external energy is added to the system, the following condition should be satisfied:

$$\int_0^\tau U(s)\dot{X}(s)\,\mathrm{d}s \geqslant 0, \forall \tau \in [0, \tau_\mathrm{f}]. \tag{3.18}$$

This inequality constitutes a passivity condition on the control action. A passive device is able to absorb and release energy, but it cannot generate energy. Otherwise, it would be an active device, whereas the focus here is on passive control measures. However, as will be discussed later, the optimal control formulation by itself does not ensure a passive device and a negative stiffness device is suggested.

3.3.3 Piecewise Optimal Control – Unknown Fixed Final Time

As previously discussed, due to the presence of additional constraint on the control action, finding the optimal solution on the full time horizon ($0 \leqslant \tau \leqslant \tau_f$) is not trivial. In this study, a *piecewise* open-loop optimal control approach is proposed. The full time horizon is broken up into multiple shorter segments based on when the system is in the inactive and active regions, and unconstrained TPBVPs are solved independently over each active interval. Starting at $\tau = 0$, the state dynamics are initialized to $\boldsymbol{X}(0) = [X_0, \dot{X}_0]^T$, and the following steps are followed:

I. While the system is in the inactive region ($\boldsymbol{X}(\tau) \in \boldsymbol{\mathcal{X}}'$), the uncontrolled state dynamics (Eq. (3.11) with $U(\tau) = 0$) are solved forward in time, until either the final time τ_f is reached or the system transitions to the active region ($\boldsymbol{X}(\tau) \in \boldsymbol{\mathcal{X}}$). If the former, break; if the latter, take τ_1 to be the time at which the system enters the active region, and proceed to Step II.

II. The unconstrained TPBVP (Eqs. (3.11), (3.16), and (3.17)) is solved on the active interval $\tau \in [\tau_1, \tau_2]$, where τ_2 is the time at which the system first transitions from the active region ($\boldsymbol{X}(\tau) \in \boldsymbol{\mathcal{X}}$) to the inactive region ($\boldsymbol{X}(\tau) \in \boldsymbol{\mathcal{X}}'$). The states are initialized to $\boldsymbol{X}(\tau_1)$ found in step I, and terminal co-states $\boldsymbol{P}(\tau_2) = [0, 0]^T$. Return to Step I.

In Step II, the control action $U(\tau)$ is unconstrained and optimal on $\tau \in [\tau_1, \tau_2]$. However, τ_2 is unknown *a priori*. To determine τ_2, the following procedure is proposed that iteratively converges to the true final time τ_2:

1. Assume a lower bound τ_{low} and an upper bound τ_{upp} for the final time, and provide an initial guess for the final time, $\tau_2^{(1)}$.

2. Solve the unconstrained TPBVP (Eqs. (3.11), (3.16), and (3.17)) with initial conditions on the states $\boldsymbol{X}(\tau_1)$ and terminal conditions on the co-states $\boldsymbol{P}(\tau_2^{(i)}) =$

$[0, 0]^T$.

3. If the state of the system at $\tau_2^{(i)}$ is in the active control region (i.e., $\boldsymbol{X}(\tau_2^{(i)}) \in \boldsymbol{\mathcal{X}}'$), update the lower bound: $\tau_{\text{low}} \leftarrow \tau_2^{(i)}$. Otherwise, update the upper bound: $\tau_{\text{upp}} \leftarrow \tau_2^{(i)}$.

4. Update the final time using, for example, a simple bisection: $\tau_2^{(i+1)} \leftarrow (\tau_{\text{low}} + \tau_{\text{upp}})/2$.

5. Increment the iteration index ($i \leftarrow i+1$), and repeat Steps 2 to 4 until the stopping criterion (e.g., $\tau_{\text{upp}} - \tau_{\text{low}} < \varepsilon$) is met.

In Step 1, reasonable initial values for τ_{low}, τ_{upp}, and $\tau_2^{(1)}$ would be the initial time (τ_1), one period of the uncontrolled system later ($\tau_1 + 2\pi$), and the time the uncontrolled system would first transition from the active region to the inactive region, respectively.

In the above procedures, each TPBVP (Steps II and 3) is easier to solve since the constraint on the control action does not need to be imposed. This is because the constraint is handled outside of the TPBVP by breaking up the full time horizon into inactive and active intervals. Note that the resulting (piecewise) control action is not necessarily optimal on the full time horizon, but it is optimal on each sub-interval $[\tau_1, \tau_2]$.

At the exiting point, the values of the co-states are necessarily zero (i.e., $\boldsymbol{P}(\tau_2) = \boldsymbol{0}$). Substituting the terminal co-states condition into Eq. (3.16) gives the following control action:

$$U(\tau_2) = -\frac{1}{2Q_a + Q_u}(2Q_a X(\tau_2) + 4\xi Q_a \dot{X}(\tau_2)). \tag{3.19}$$

Plugging this control action into the system's dynamics (Eq. (3.11)) results in the following acceleration:

$$\ddot{X}(\tau_2) = -\frac{Q_u}{Q_a + Q_u} X(\tau_2) - \frac{2\xi Q_u}{Q_a + Q_u} \dot{X}(\tau_2) - \ddot{X}_g(\tau_2). \tag{3.20}$$

These expressions for the conditions at exit of the active region will be discussed further in the following section.

It is worth noting that the optimal control formulation developed in this section for an LTI system can easily be extended to linear time-varying systems by substituting the LTI state matrix $\mathcal{A}$ by $\mathcal{A}(t)$.

3.4 Numerical Exploration of Free Responses

To assess the performance of the proposed piecewise optimal control approach, a nondimensionalized LTI system under free response is considered here. This system has a nondimensional displacement capacity of $1/\phi$. The active control region is given by $\mathcal{X} = \{X(\tau) : |X| \geqslant 1\}$. The damping coefficient ξ is taken to be 0.5% (i.e., lightly damped) (Calhoun and Harvey, 2018). In the following, the optimal response of the nondimensional system is evaluated for only one excursion into the active control region, which results in an optimal solution for the considered excursion (i.e., $\tau \in [\tau_1\ \tau_2]$, given $\tau_1 = 0$, and τ_2 is unknown *a priori*). The effect of various initial conditions are assessed, and a comparison to clipped-LQR is made.

3.4.1 Piecewise Optimal Solution

The system is given an initial velocity of $\dot{X}(0) = 1$ at the boundary of the active region. So, the initial nondimensional condition is $\boldsymbol{X}(0) = [1, 1]^T$. Considering unit nondimensional acceleration and zero control action weights (i.e., $Q_a = 1$, and $Q_u = 0$), displacement-to-acceleration weight ratios of $Q_d/Q_a = 0.01$, 0.02, 0.05, 0.1, 0.2, 0.5, 1, 2, 5, 10, 20, 50, 100, 200, 500, 1000, 2000, and 5000 are considered. The optimal displacement trajectories for several weight ratios are depicted in Figure 3.1(a) along with the displacement time history of the uncontrolled (UC) system, and the corresponding accelerations versus displacements are depicted in Figure 3.1(b). As expected, by applying relatively more weight to the displacements, the peak displacements decrease

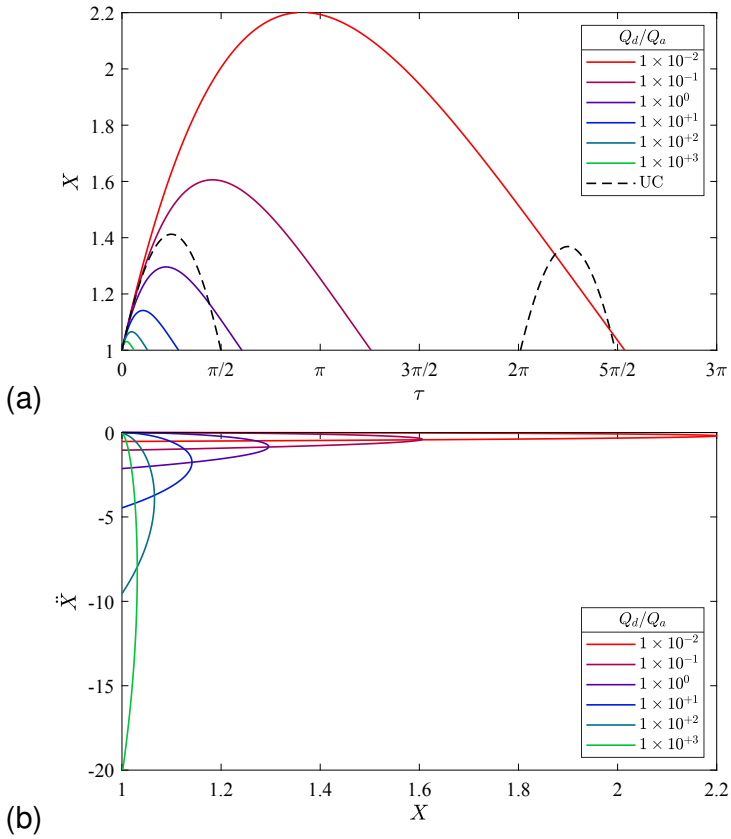

Figure 3.1: Piecewise optimal trajectories—(a) displacement time histories and (b) accelerations versus displacements—for varying displacement-to-acceleration weight ratios Q_a/Q_d; $\boldsymbol{X}(0) = [1, 1]^T$.

and consequently the peak accelerations increase. An interesting observation is that the peak displacements for the cases with relatively small weight ratios ($Q_d/Q_a < 1$) are larger than the peak displacement of the uncontrolled system and consequently their peak accelerations are smaller than the uncontrolled system. For these cases, acceleration reduction is more important than the displacement reduction; in order to reduce acceleration, the control action should inject energy into the system to reduce the accelerations, which causes an increase in displacements. It is also worth noting that all of the control trajectories exit the control region with similar velocity and zero acceleration despite having different displacement-to-acceleration weight ratios. This is apparent from Eq. (3.20): given $Q_u = 0$ and $X(\tau_2) = 1$ results in $\ddot{X}(\tau_2) = -\ddot{X}_g(\tau_2) = 0$.

The requirement for an active device can be deduced from the time histories of

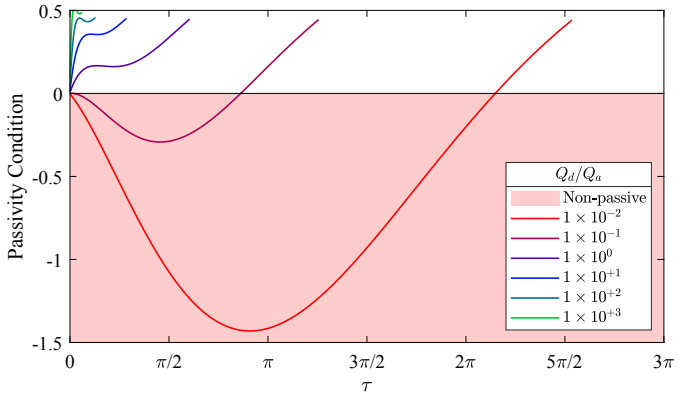

Figure 3.2: The trajectory of the passivity condition for varying displacement-to-acceleration weight ratios; $\boldsymbol{X}(0) = [1, 1]^T$.

the passivity condition in Figure 3.2. As can be observed in this figure, the control actions in the piecewise optimal trajectories associated with smaller displacement-to-acceleration weight ratios ($Q_d/Q_a < 1$) require energy to be injected into the system (i.e., passivity condition less than zero). These cases are not the focus of this study for two reasons: (1) the focus of this study is to develop a benchmark solution for the design of a passive device; (2) these piecewise optimal trajectories require more displacement capacity, which does not align with the scope of this study (i.e., to decrease the required displacement capacity). Nevertheless, these cases will be discussed further in Section 3.4.3.

The optimal control action versus displacement is shown in Figure 3.3(a), and the optimal control action versus velocity is shown in Figure 3.3(b). Figure 3.3 does not include the results associated with the displacement-to-acceleration weight ratios of 0.01 and 0.1, which require an active device to generate such control actions. As can be seen in Figure 3.3, larger control actions are needed for smaller displacement-to-acceleration weight ratios. Moreover, as the system enters into the active control region, a large control action is initially required, and the control action then decreases till it converges to a specific value (i.e., $U(\tau_2) \approx -1$) regardless of having different displacement-to-acceleration weight ratios. Given $Q_u = 0$ and $X(\tau_2) = 1$, Eq. (3.19) re-

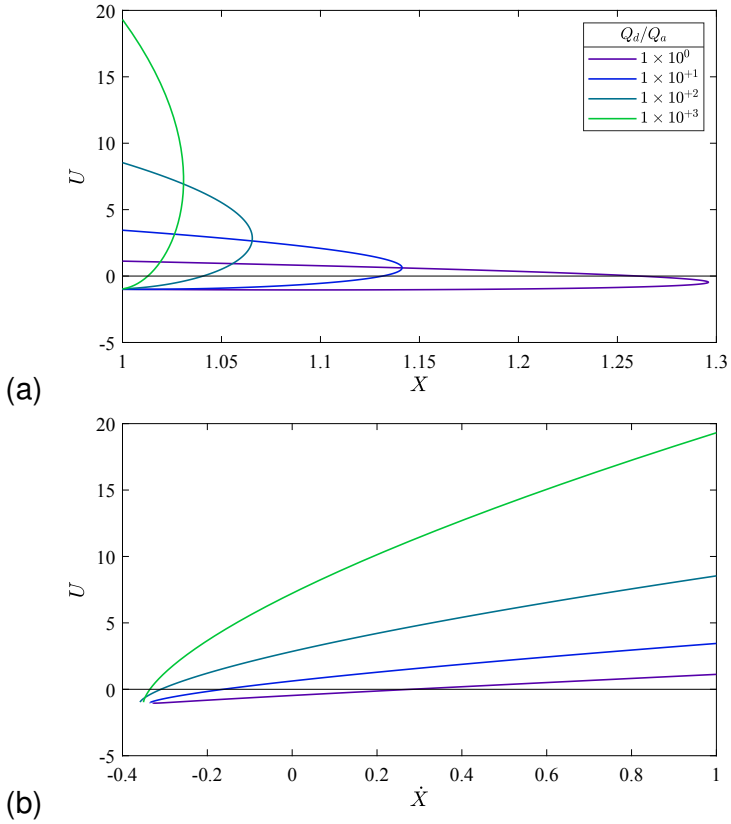

Figure 3.3: Optimal control action U versus (a) displacement X and (b) velocity $\dot{X}$ for varying displacement-to-acceleration weight ratios; $\boldsymbol{X}(0) = [1, 1]^T$.

duces to $U(\tau_2) = -(1 + 2\xi\dot{X}(\tau_2))$. In the case of a lightly damped system with relatively small exiting velocity ($\dot{X}(\tau_2) \approx -0.3$, see Figure 3.3(b)), the second term in parentheses has negligible contribution, and hence $U(t_2) \approx -1$. Moreover, Figure 3.3(b) indicates that as the weight ratio increases, the nonlinearity of the control action increases. These control action behaviors can be used as a benchmark to guide the design of passive control devices to improve the performance of systems in high-intensity motions.

3.4.2 Effect of Initial Condition

In order to have a better understanding of the optimal control action behavior, the same problem is solved for different initial nondimensional velocities of $\dot{X}(0) = 1$ to 10 (with increment step of 1) for the same initial displacement of $X(0) = 1$. The results for only initial velocities of $\dot{X}(0) = 1$, 2, 3, and 4 are presented, and the other cases are discussed

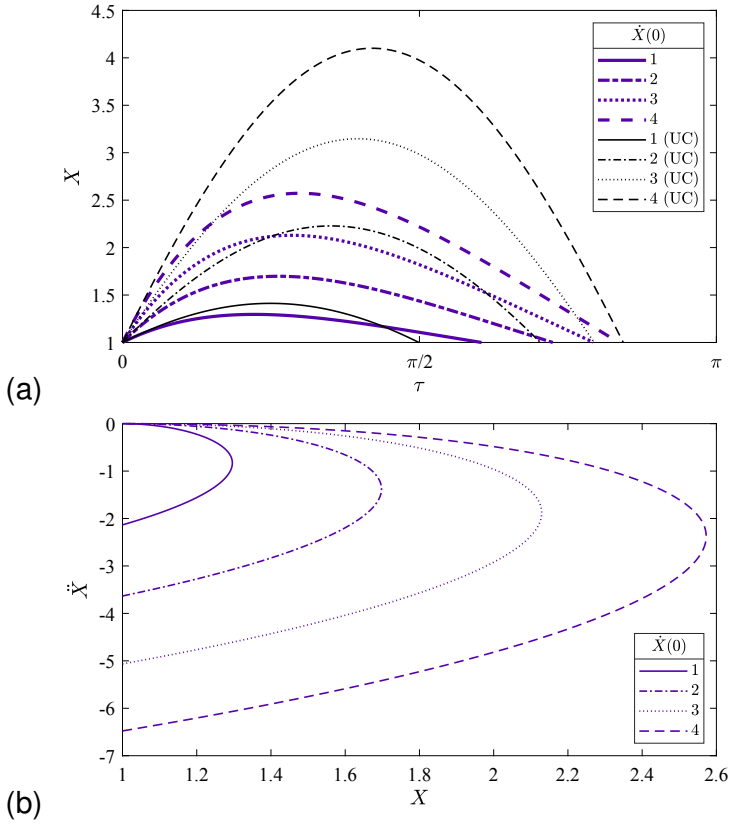

Figure 3.4: Piecewise optimal trajectories—(a) displacement time history and (b) acceleration versus displacement—for displacement-to-acceleration weight ratio $Q_a/Q_d = 1$ and varying initial velocities: $\dot{X}(0) = 1$, 2, 3, and 4.

later.

The optimal displacement trajectories for a unit displacement-to-acceleration weight ratio (i.e., $Q_d/Q_a = 1$), as well as the displacement time history of the uncontrolled systems, are plotted in Figure 3.4(a) and the corresponding accelerations versus displacements are depicted in Figure 3.4(b). As can be seen, an increase in the initial velocity results in an increase in peak displacements, peak accelerations, and active control times. Although similar trends can be observed among various initial conditions (with the same weight ratio), these changes are not linearly dependent to the initial velocity. The effect of initial velocity on peak displacements and peak accelerations are larger than the effect on the active control times.

Figure 3.5 shows the optimal control action versus (a) displacement and (b) velocity

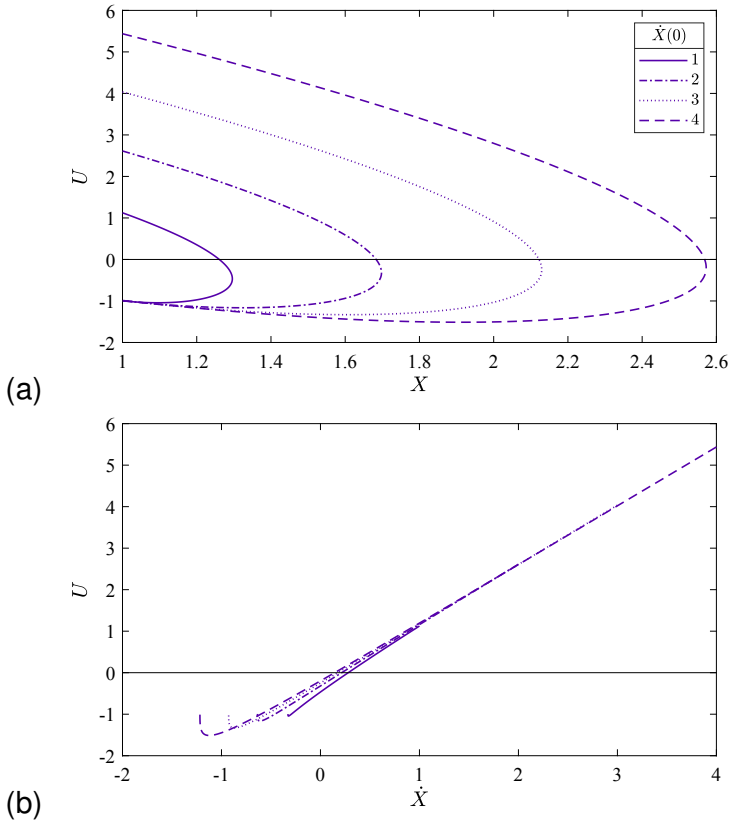

Figure 3.5: Optimal control action U versus (a) displacement X and (b) velocity $\dot{X}$ for displacement-to-acceleration weight ratio $Q_a/Q_d = 1$ and varying initial velocity: $\dot{X}(0) = 1$, 2, 3, and 4.

for the same weight ratio (i.e., $Q_d/Q_a = 1$) with varying initial velocity. As can be observed, the control actions appear to require small stiffness and linear viscous damping for this weight ratio. However, this is not the case for different weight ratios as discussed in the previous section.

The peak displacements, peak accelerations, and active control times for all the weighting ratios are tabulated in Table A.1 through Table A.10 for the initial velocities of 1 to 10 with increment step of 1, respectively. In addition, the root mean square (RMS) values of displacements and accelerations, as well as the values of the cost functional J, are reported in these tables to facilitate the comparison between different scenarios. In these tables, the results associated with scenarios that require an active device are distinguished using (†) next to the weight ratios. Similar trends are observed for

all the considered initial velocities (i.e., $\dot{X}(0) = 1{:}1{:}10$). That is, peak and root mean square (RMS) displacements decrease with increasing weight ratio, whereas the peak and RMS accelerations increase with increasing weight ratio. This means that better performance on controlling displacements and worse performance on controlling accelerations is achieved by increasing the weight ratio. The peak and RMS values of both displacements and accelerations increase by increasing the initial velocity.

3.4.3 Design of Passive Control Devices

The obtained optimal behavior of the control action $U(\tau)$ can now be used to guide the optimal design of a passive control device for dual-mode systems. There is a broad range of passive devices including linear and nonlinear springs and dashpots and their combinations that can be used to achieve the desired piecewise optimal trajectories. One method to come up with a good combination of devices and their properties is to set up an optimization problem by defining a wide range of devices and their combinations and let the optimization select the device. Another method is to compare several devices that can possibly generate such control actions (Zargar et al., 2013, 2017). The present study does not employ such methods, but instead focuses on developing a benchmark to guide the design of passive systems. Note that there are methods that can be used to design a passive device equivalent to an active device, which will be pursued here (Cimellaro et al., 2009; Cimellaro and Lopez-Garcia, 2011).

The obtained piecewise optimal results in the previous sections are now used to develop several figures that can support the design of dual-mode LTI systems. Peak displacements versus weight ratios are shown in Figure 3.6(a) and peak accelerations versus weight ratios are shown in Figure 3.6(b) for various initial velocities. In addition, Figure 3.7 shows the (a) peak displacements and (b) peak accelerations versus initial velocities for different weight ratios. These figures are useful to obtain the required weight ratio and the maximum initial velocity that can satisfy both displacement limit

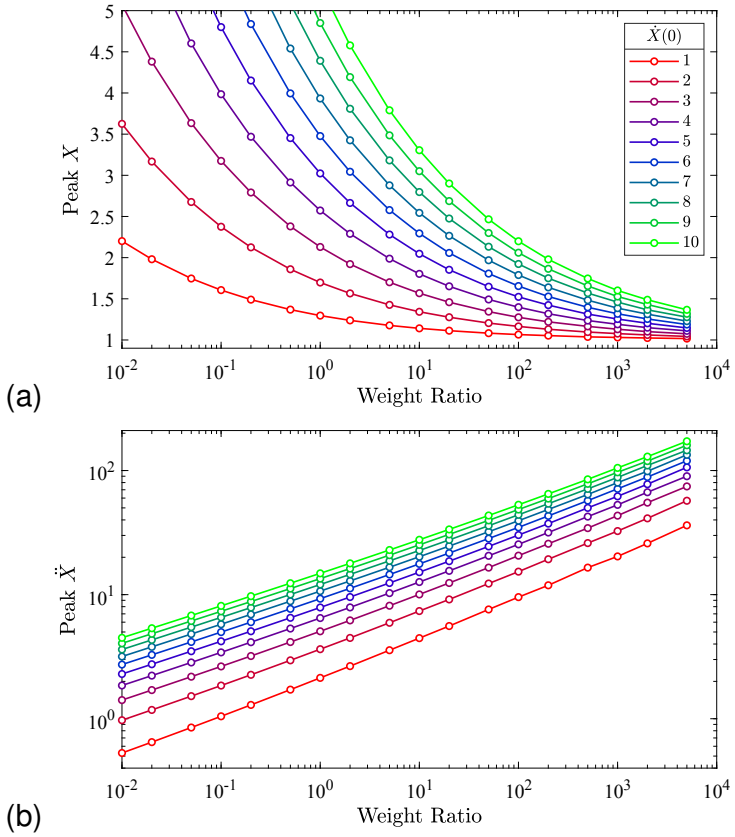

Figure 3.6: (a) Peak displacements and (b) peak accelerations versus displacement-to-acceleration weight ratio Q_a/Q_d for varying initial velocities $\dot{X}(0)$.

$d_{\max}$ and acceleration limit for the desired factor ϕ.

Figures 3.6 and 3.7 can be combined in the compact form of peak accelerations versus peak displacements as shown in Figure 3.8 with contours of initial velocity (solid) and displacement-to-acceleration weight ratio (dashed). By knowing the required factor ϕ, the permissible region on the horizontal access can be obtained as the peak displacements smaller than $1/\phi$. For a given initial velocity $\dot{X}(0)$ (the color coded curves), the satisfaction of the acceleration limit can be assessed. If the acceleration limit cannot be satisfied, a smaller factor ϕ should be considered.

In this study, a nondimensionalized Kelvin-Voigt system (i.e., linear spring-dashpot in parallel) is designed for the purpose of illustration. The form of the model is given by the following:

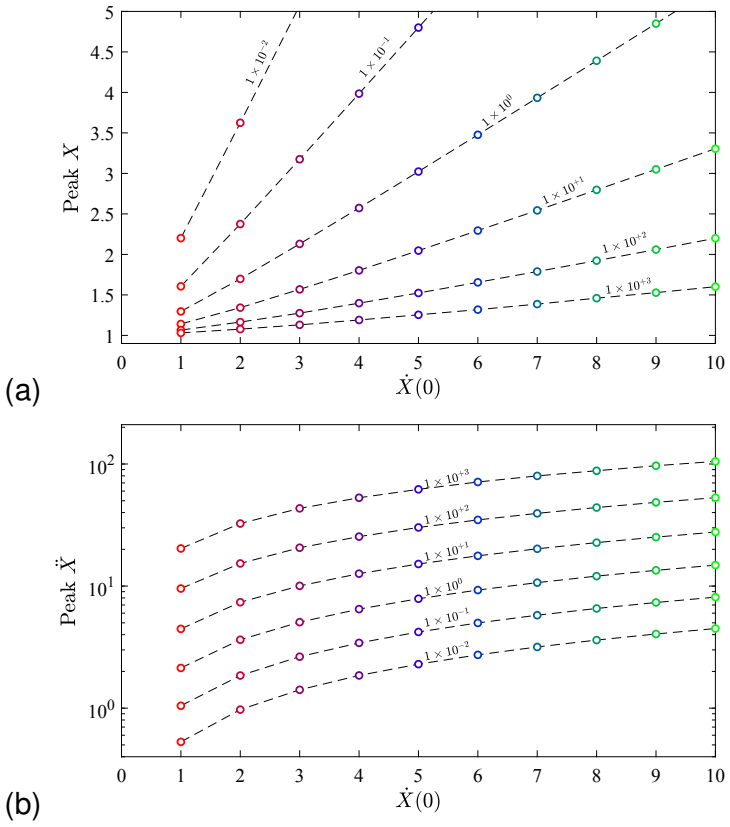

Figure 3.7: (a) Peak displacements and (b) peak accelerations versus initial velocities $\dot{X}(0)$ for varying displacement-to-acceleration weight ratios Q_a/Q_d (- - -).

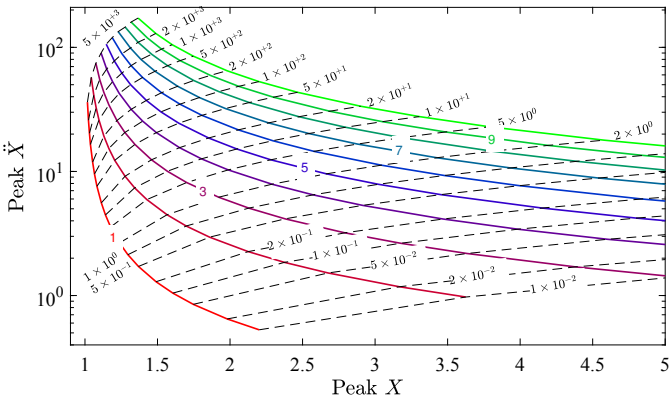

Figure 3.8: Piecewise optimal peak accelerations versus peak displacements for varying initial velocities (——) and varying displacement-to-acceleration weight ratios (- - -).

$$U(\tau) = K^*(|X(\tau)| - 1)\,\mathrm{sgn}(X(\tau)) + C^*\dot{X}(\tau). \tag{3.21}$$

Ordinary least squares method is used to fit the nondimensional stiffness K^* and damping C^* to the control action time histories. The fit of nondimensional stiffness K^* for different initial velocities and displacement-to-acceleration weight ratios are presented in Figure 3.9(a) and the corresponding nondimensional damping values are presented in Figure 3.9(b). After obtaining the required threshold (i.e., $\phi d_{\max}$), initial velocity, and weight ratio from Figure 3.8, the best fit of K^* and C^* can be taken from Figure 3.9. As can be seen in Figure 3.9(a), some cases require negative stiffness; these cases correspond to non-passive devices. This can be achieved by a passive negative stiffness device (Javanbakht et al., 2018; Pasala et al., 2012; Sun et al., 2017), or in case of the rolling isolation system by a variable shape profile (Lu et al., 2013; Shahbazi and Taghikhany, 2017), or stiffness (Lu et al., 2011; Panchal and Jangid, 2008). As the displacement-to-acceleration weight ratio increases, the required stiffness and damping increase. The tuning procedure is demonstrated in Section 3.5.

3.4.4 Comparison to Clipped-LQR

As an alternative to the previous piecewise open-loop optimal control procedure, a similar approach instead with the infinite-horizon continuous-time linear quadratic regulator (LQR) is considered. The feedback control law is $U_{\mathrm{LQR}}(\tau) = -\mathcal{R}^{-1}(\boldsymbol{\mathcal{N}}^T + \boldsymbol{\mathcal{B}}^T\boldsymbol{\mathcal{S}})\boldsymbol{X}(\tau)$, where $\boldsymbol{\mathcal{S}}$ is the solution of the well-known algebraic Riccati equation:

$$\boldsymbol{\mathcal{A}}^T\boldsymbol{\mathcal{S}} + \boldsymbol{\mathcal{S}}\boldsymbol{\mathcal{A}} - \boldsymbol{\mathcal{N}}\mathcal{R}^{-1}\boldsymbol{\mathcal{B}}^T\boldsymbol{\mathcal{S}} - \boldsymbol{\mathcal{S}}\boldsymbol{\mathcal{B}}\mathcal{R}^{-1}\boldsymbol{\mathcal{N}}^T - \boldsymbol{\mathcal{S}}\boldsymbol{\mathcal{B}}\mathcal{R}^{-1}\boldsymbol{\mathcal{B}}^T\boldsymbol{\mathcal{S}} - \boldsymbol{\mathcal{N}}\mathcal{R}^{-1}\boldsymbol{\mathcal{N}}^T + \boldsymbol{\mathcal{Q}} = \mathbf{0}. \tag{3.22}$$

In order to implement $U_{\mathrm{LQR}}(\tau)$ in the state dynamics (Eq. (3.11)), the feedback controls are *clipped* (set to zero) when the system is in the inactive region (i.e., $\boldsymbol{X}(\tau) \in \boldsymbol{\mathcal{X}}'$).

In this part, the clipped-LQR solution of the problem with unknown fix final time is

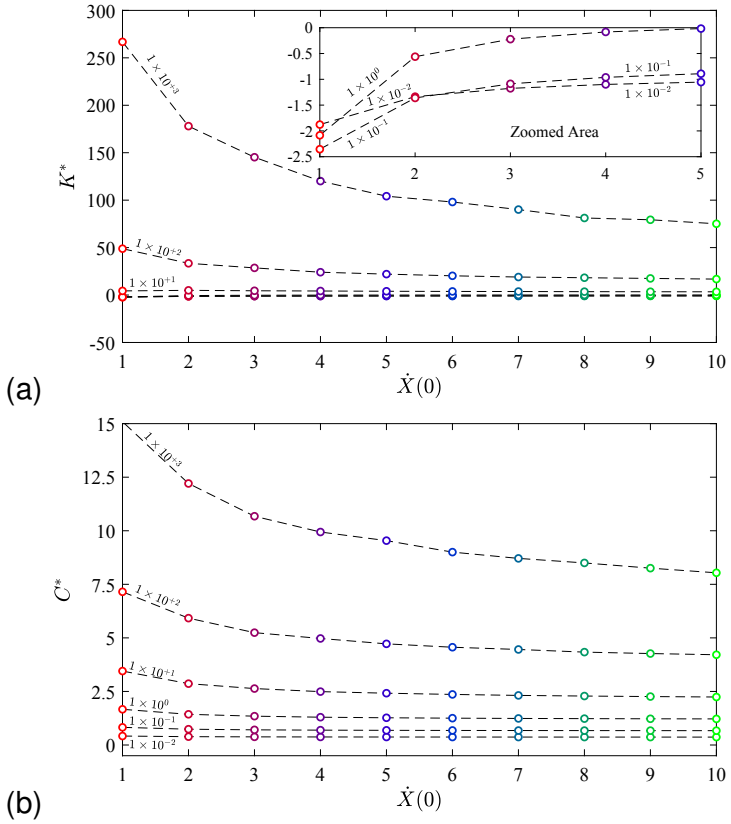

Figure 3.9: Fitted Kelvin-Voigt device parameters—(a) stiffness K^* and (b) damping C^*—versus initial velocities $\dot{X}(0)$ for varying displacement-to-acceleration weight ratios (- - -).

evaluated using the same weightings, weight ratios, and initial velocities. The clipped-LQR displacement trajectories are shown in Figure 3.10(a), and the corresponding accelerations versus displacements are shown in Figure 3.10(b) for the system exposed to an initial velocity of $\dot{X}(0) = 1$. As can be seen, the clipped-LQR solutions for displacements have similar pattern with piecewise optimal solutions. The differences grow as the weight ratio increase; with adjustment in weight ratios, closer solutions to piecewise optimal solutions are expected. The same conclusion can be drawn from the plot of accelerations versus displacements. However, the clipped-LQR solutions exhibit non-zero exiting accelerations. This is due to considering only the steady state response, as opposed to the finite horizon in the optimal trajectory.

Figure 3.11 shows the piecewise optimal and clipped-LQR trajectories of the pas-

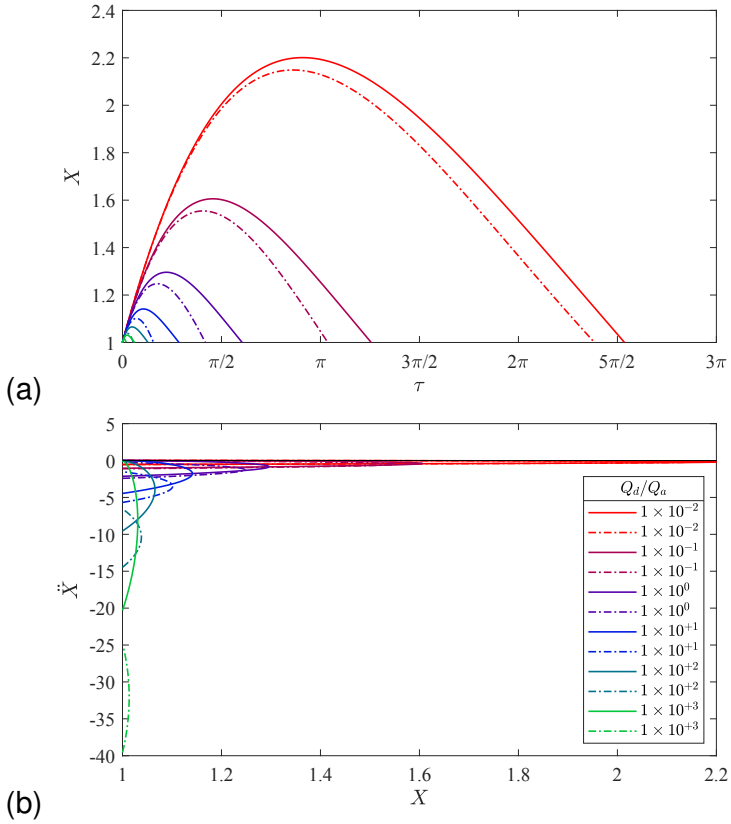

Figure 3.10: Piecewise optimal (——) and clipped-LQR (-·-·) trajectories—(a) displacement time histories and (b) accelerations versus displacements—for varying displacement-to-acceleration weight ratio Q_a/Q_d; $\boldsymbol{X}(0) = [1, 1]^T$; .

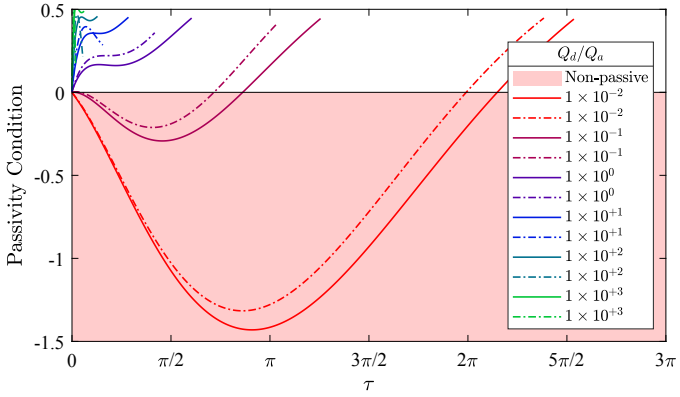

Figure 3.11: Piecewise optimal (——) and clipped-LQR (-·-·) trajectories of the passivity condition for different displacement-to-acceleration weight ratios Q_a/Q_d; $\boldsymbol{X}(0) = [1, 1]^T$.

sivity condition. As can be seen, the two lowest weight ratios (i.e., $Q_d/Q_a = 0.01$ and 0.1) require an active device to generate such control actions.

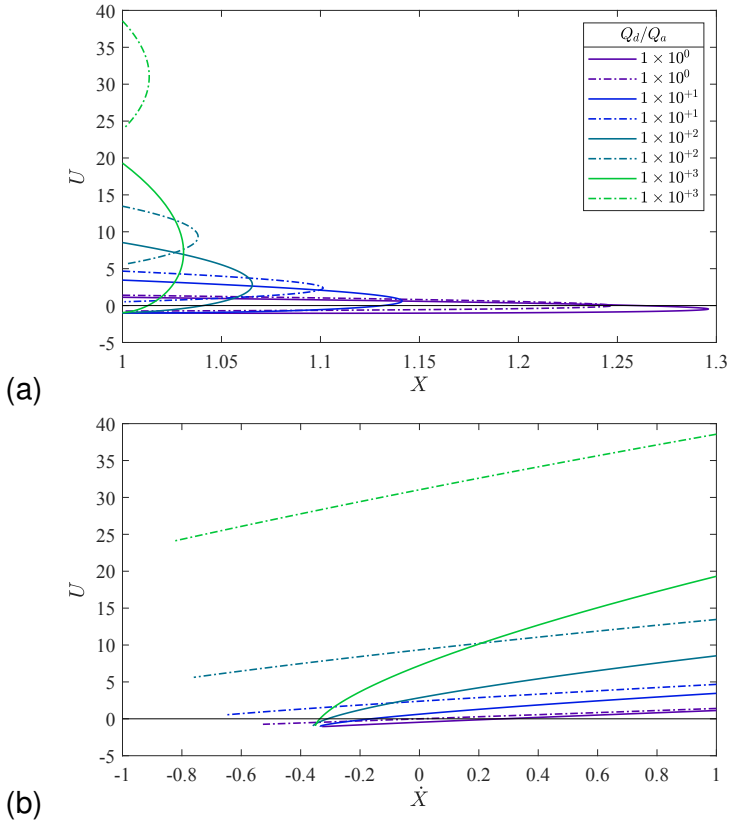

Figure 3.12: Piecewise optimal (——) and clipped-LQR (- · - · -) control actions U versus displacement X (a) and velocity $\dot{X}$ (b) for varying displacement-to-acceleration weight ratio Q_a/Q_d.

Figure 3.12 shows the required piecewise optimal and clipped-LQR control actions versus displacements (a) and velocities (b). Figure 3.12 does not include the results associated with weight ratios of $Q_d/Q_a = 0.01$, and 0.1, which require an active device to generate such control actions. As can be seen, the clipped-LQR procedure requires larger control actions than the optimal procedure (similar to producing larger accelerations). The exiting points in clipped-LQR solutions have larger velocities and accelerations compared to the piecewise optimal solutions; this increased kinetic energy may negatively influence the response of the system on the subsequent inactive control region, resulting in larger displacements. As noted before, by adjusting (increasing) the weight ratios for clipped-LQR procedure, closer responses to piecewise optimal solutions may be realized.

Table 3.1: Comparison summary of piecewise optimal and clipped-LQR results for the system with an initial condition of $\boldsymbol{X}(0) = [1, 1]^T$.

	Piecewise Optimal				**Clipped-LQR**			
Q_d/Q_a	**Peak** X	**Peak** $\ddot{X}$	J	τ_f^*	**Peak** X	**Peak** $\ddot{X}$	J	τ_f^*
1×10^{-2}	2.201	0.529	0.335	7.967	2.149	0.547	0.334	7.489
2×10^{-2}	1.981	0.648	0.429	6.466	1.929	0.673	0.425	5.873
5×10^{-2}	1.747	0.849	0.605	4.887	1.695	0.892	0.595	4.218
1×10^{-1}	1.606	1.046	0.796	3.947	1.554	1.111	0.777	3.258
2×10^{-1}	1.490	1.292	1.063	3.180	1.439	1.393	1.025	2.498
5×10^{-1}	1.369	1.715	1.592	2.381	1.319	1.896	1.505	1.740
1×10^{0}	1.296	2.134	2.195	1.899	1.248	2.414	2.037	1.313
2×10^{0}	1.238	2.654	3.088	1.530	1.191	3.096	2.785	0.983
5×10^{0}	1.177	3.565	4.914	1.126	1.134	4.351	4.268	0.664
1×10^{1}	1.141	4.461	7.115	0.896	1.101	5.677	5.948	0.490
2×10^{1}	1.113	5.583	10.467	0.716	1.076	7.463	8.330	0.359
5×10^{1}	1.083	7.595	17.266	0.512	1.052	10.832	13.088	0.236
1×10^{2}	1.066	9.548	25.871	0.405	1.038	14.472	18.493	0.171
2×10^{2}	1.053	11.892	40.376	0.333	1.028	19.460	26.122	0.123
5×10^{2}	1.038	16.507	65.604	0.224	1.019	29.048	41.628	0.080
1×10^{3}	1.031	20.323	108.151	0.192	1.013	39.575	58.806	0.057
2×10^{3}	1.024	25.885	161.148	0.146	1.010	54.179	82.185	0.040
5×10^{3}	1.017	36.176	264.537	0.097	1.006	82.603	127.847	0.025

Peak displacements, peak accelerations, and total active control action times for the clipped-LQR solutions are tabulated in Tables A.11–A.20 (Appendix A) for the system with initial nondimensional velocities of 1 through 10 with increment of 1. The tables also present RMS values for displacements and accelerations, as well as values of the cost functional J. For all the considered initial velocities (i.e., $\dot{X}(0) = 1{:}1{:}10$), similar patterns to the piecewise optimal results are observed. That is, peak and RMS values for displacements and accelerations, respectively, decrease and increase by increasing the weight ratio. In addition, the peak and RMS values for both displacements and accelerations increase with increasing initial velocity.

Table 3.1 compares the peak displacements, peak accelerations, total active control action times, and the values of cost functional between the piecewise optimal and clipped-LQR procedures where the system is excited with initial velocity of $\dot{X}(0) = 1$. As can be observed, the calculated values of the cost functional for the clipped-LQR procedure are smaller than the piecewise optimal procedure. The reason is the required adjustment in the weight ratios and the differences in the total active control action times. The clipped-LQR procedure requires shorter time compared to piecewise optimal. Nevertheless, the piecewise optimal solution has smaller cost functional normalized by the total active control action time (i.e., J/τ_{f}^{*}).

3.5 Numerical Example

In this section, the design of a dual-mode isolation system is illustrated using the design curves developed in Section 3.4.3. The example isolation system considered in this study utilizes rolling pendulum (RP) bearings, which consists of a rolling ball between a concave-up rolling surface and a concave-down rolling surface. The shape of these surfaces is taken to be circular, which results in a linearized stiffness of $k = mg/2r$, where m is the mass of the system including the isolated object, g is the gravitational acceleration, and r is the radius of the rolling surfaces (Calhoun and Harvey, 2018).

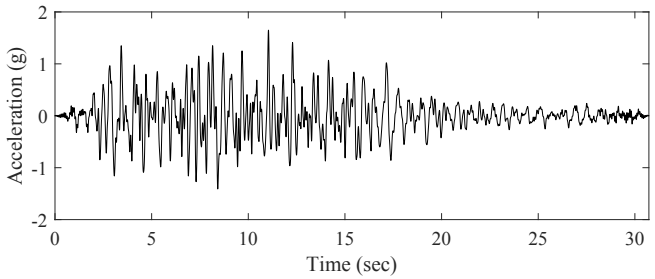

Figure 3.13: VERTEQII accelerogram (adapted from Tehrani and Harvey (2019a)).

This is a pendulum type system with mass-independent natural frequency $\omega = \sqrt{g/2r}$. Taking the radius equal to 50 cm results in a period of around 2 sec. The damping coefficient ξ is taken to be 0.5% (i.e., lightly damped) (Calhoun and Harvey, 2018).

Figure 3.13 shows the VERTEQII accelerogram that is introduced in the Network Equipment-Building System (NEBS) GR-63-CORE for telecommunications equipment (Telcoridia, 2012). This accelerogram was developed for the highest risk category (zone 4), and it corresponds to a 10% probability of exceedance in 50 years. So, it can be used to estimate the displacement of the isolation system under the DBE-level event. In the absence of any control action, the considered isolation system experiences a 16.137-cm peak displacement under the DBE-level event (VERTEQII). Under the MCE-level event (i.e., 1.5×VERTEQII), the peak displacement is 24.205 cm. The DBE- and MCE-level peak displacements, denoted d_{DBE} and d_{MCE}, are used to design the RP bearing's displacement capacity d_{max} and the control boundary ϕd_{max}, as described below.

First, consider an isolation system with a 20.320-cm (8-in.) (Vargas and Bruneau, 2009) displacement capacity d_{max} and a 16.256-cm threshold (i.e., $\phi = 80\%$). The peak displacement of the uncontrolled system under the DBE-level event (i.e., 16.137 cm) is smaller than the threshold ϕd_{max}. However, the peak displacement under the MCE-level event (i.e., 24.205 cm) is larger than the displacement capacity d_{max}. So, impact is highly likely under high-amplitude motions such as MCE-level events. Impacts would result in spikes in the total transmitted accelerations, negatively affecting the isolation

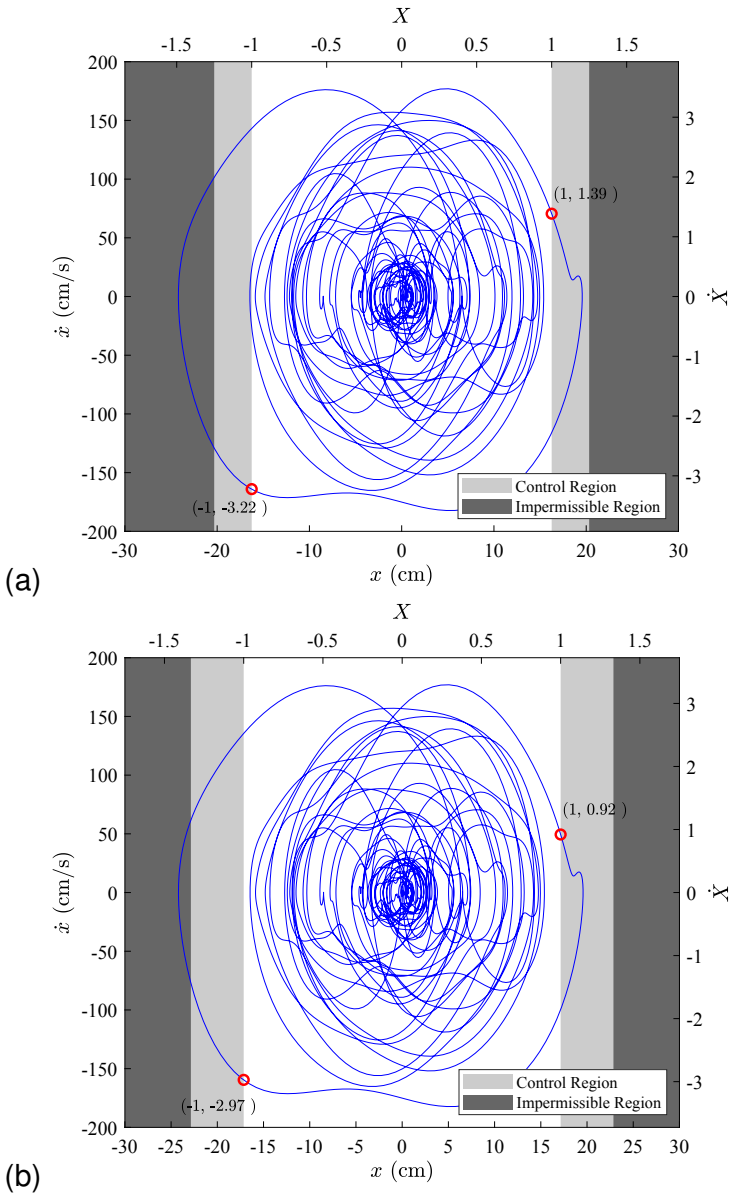

Figure 3.14: Phase space trajectory of the isolation system under the MCE-level event (1.5×VERTEQII): (a) system with a threshold of $\phi d_{\max} = 0.8 \times 20.32 = 16.256$ cm; and (b) system with a threshold of $\phi d_{\max} = 0.75 \times 22.86 = 17.145$ cm.

performance. Figure 3.14(a) shows the phase space trajectory of the system under the MCE-level event (i.e., 1.5×VERTEQII) in dimensional form, as well as nondimensionalized form with $\phi d_{\max} = 0.8 \times 20.32 = 16.256$ cm. The peak nondimensional velocity of entering the control region is 3.22. Considering an 80% factor results in an allowable nondimensional peak displacement of $1/\phi = 1.25$. For these values of initial velocity

(3.22) and peak displacement (1.25), the design curves (Figure 3.8) result in a maximum optimal nondimensional peak acceleration of 26.82 and weight ratio of around 2×10^2. The equivalent peak acceleration is 4275.6 cm/s^2, which is larger than the maximum tolerable acceleration limit for most telecommunications equipment (i.e., 3 g) (IBM, 2010). So, a factor of $\phi = 80\%$ is insufficient to have a safe dual-mode system. Therefore, a different design needs to be considered.

Consider a different RP-bearing configuration with displacement capacity $d_{\max} = 22.860$ cm (9 in.) and a threshold of $\phi d_{\max} = 17.145$ cm (i.e., $\phi = 75\%$). The new initial nondimensional velocity is 2.97 as shown in Figure 3.14(b) and the maximum allowable nondimensional peak displacement is 1.33. For these values, the design curves (Figure 3.8) result in a maximum optimal nondimensional peak acceleration of 16.79 and weight ratio of around 5.5×10^1. The equivalent peak acceleration is 2823.2 cm/s^2, which is smaller than 3 g. So, using Figure 3.9, the best fit K^* and C^* of the nondimensional Kelvin-Voigt element for the weight ratio 5.5×10^1 are 18.00 and 4.39, respectively.

It is worth noting that in the design procedure above, the entering velocity to the active control region is taken as the peak entering velocity of the uncontrolled system when the system crosses the predefined threshold $\phi d_{\max}$; however, there may be other instances such as points (1,1.39) and (1,0.92) in Figures 3.14(a) and 3.14(b), respectively, when the system crosses the predefined threshold that affects the responses of the system and consequently the peak entering vel(a)ocity. This effect has not been taken into account in the current study.

To evaluate the designed dual-mode RP bearing, Eq. (3.11) is solved under the MCE-level event (i.e., 1.5×VERTEQII) by taking the control action in the form of Eq. (3.21) in the control region. The displacements and total accelerations time histories of the uncontrolled and the controlled system with Kelvin-Voigt device are shown in Figure 3.15. As can be seen, excessive displacements (i.e., $X > 1.33$), and accordingly

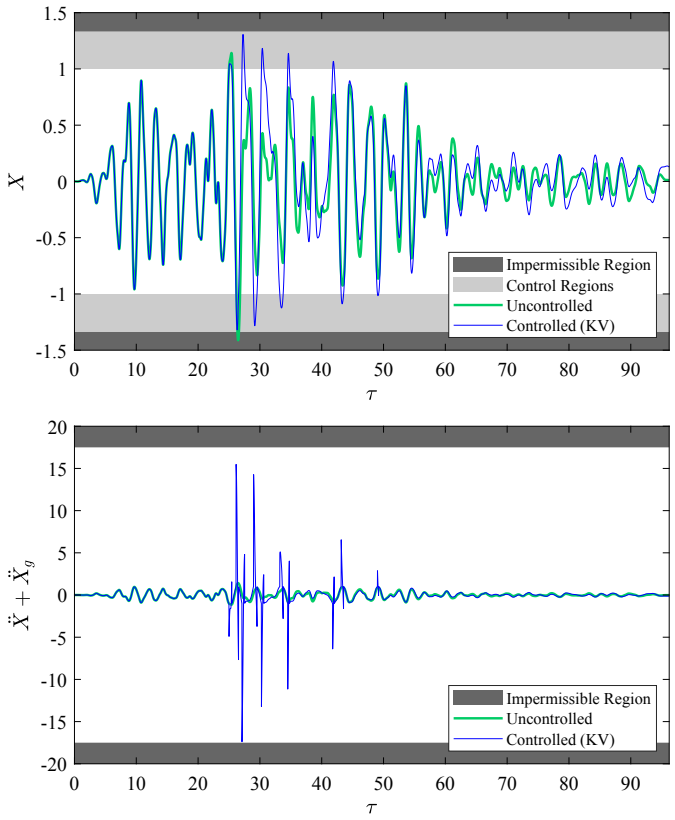

Figure 3.15: Displacement and total acceleration time histories of the uncontrolled and controlled (fitted Kelvin-Voigt (KV) device) systems under the MCE-level event (1.5×VERTEQII).

impacts, are avoided at the expense of increasing accelerations, yet the accelerations are still within the acceptable 3 g limit.

The same system is evaluated under the MCE-level motion via piecewise optimal (Section 3.3.3) and clipped-LQR (Section 3.4.4) with weight ratios of $Q_d/Q_a = 1.5\times10^{1}$ and 9×10^{-1}, respectively. The displacements and total accelerations time histories of the uncontrolled system and the controlled systems with the piecewise optimal solution is shown in Figure 3.16 and with clipped-LQR is shown in Figure 3.17. In both cases, the displacement limit is satisfied, and the peak accelerations are lower than those observed for the fitted KT device (Figure 3.15(b)). It should be noted that the weight ratio obtained from the designed procedure (i.e., $Q_d/Q_a = 5.5 \times 10^{1}$) resulted in high-frequency oscillations between large positive and negative displacements in both the

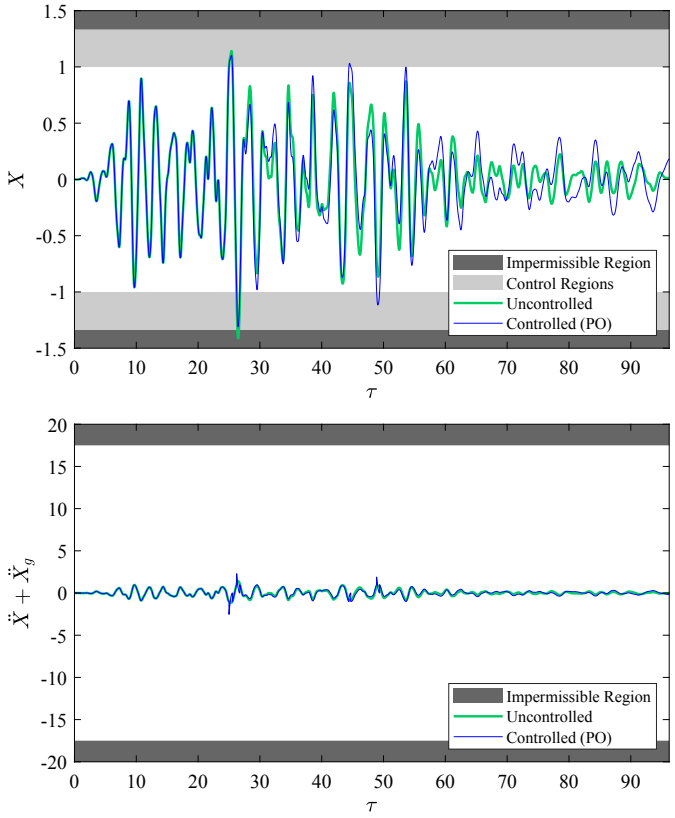

Figure 3.16: Displacement and total acceleration time histories of the uncontrolled and controlled (Piecewise Optimal (PO) solution) systems under the MCE-level event (1.5×VERTEQII).

piecewise optimal and clipped-LQR procedures; such "bouncing" behavior is common in these sorts of impacting systems (Harvey et al., 2018; Komodromos et al., 2007).

The main source of the observed differences in the required weight ratios arise from the fact that the design curves (Figure 3.8) were developed based upon the unforced system excited by only initial conditions. The imposed initial conditions do not equivalently simulate various effects of forced response characteristics such as frequency contents and large amplitude pulses. Moreover, as discussed in Section 3.4.4, an adjustment is needed for the required weight ratio of the clipped-LQR procedure compared to the piecewise optimal procedure. Although, the prospective designed controller with piecewise optimal and clipped-LQR produces can generate smaller peak accelerations, the weight ratio cannot be obtained by the design procedure outlined in this study due to

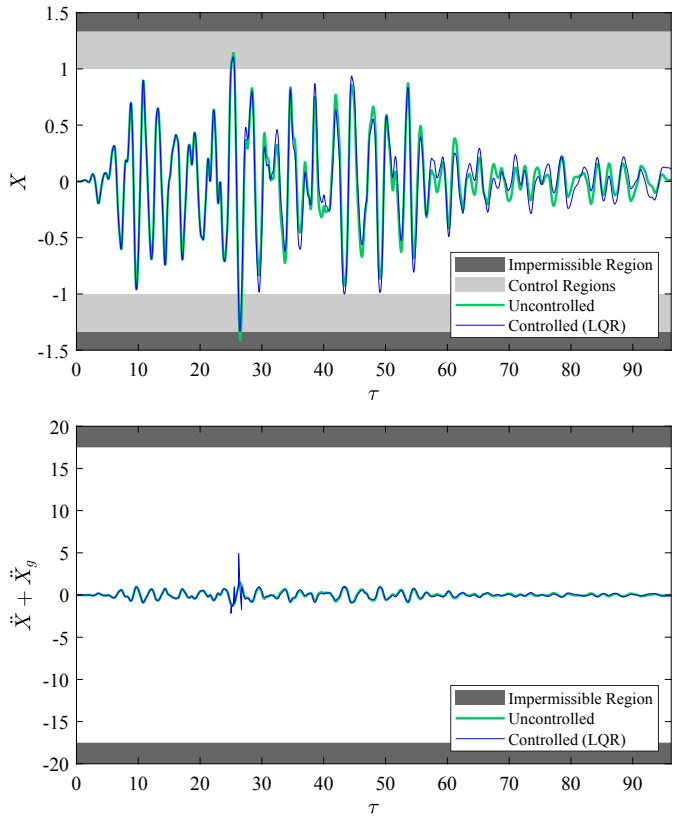

Figure 3.17: Displacements and total accelerations time histories of the uncontrolled and controlled (clipped-LQR (LQR) solution) systems under the MCE-level event (1.5×VERTEQII).

the reasons discussed previously. Consequently, it highlights a need to consider forced systems with various forcing characteristics in order to develop a robust design procedure for dual-mode systems in future studies.

3.6 Conclusions

In this chapter, a dual-mode system is used to improve the performance of systems under extreme events, while not affecting the normal operation. The dual-mode system contains two phases. The first phase is designed to perform well for normal operation under the DBE-level events or lower (when the displacements are below a threshold), and the second phase is designed to avoid impact while controlling the total transmitted acceleration to be within acceptable limits under the MCE-level events (when the displacements are beyond a threshold). In the first phase, the system is allowed to respond

freely, and in the second phase, the system is controlled with a passive mechanism to avoid impact and the resulting large accelerations. So, the performance of the second phase is defined as to effectively utilizing the reserved displacement capacity while not increasing acceleration beyond the tolerable limits.

With the aim of not having a prior assumption of any device (i.e., a predefined force-displacement or force-velocity relationship), an optimal control problem is set up to determine the best possible control force trajectories to achieve both performance objectives. The cost function is defined as the sum of the weighted quadratics of both displacements and total transmitted accelerations. Open-loop solutions are found by solving the Euler-Lagrange equations considering a constraint on control force. Finding the solution to this optimal control problem is nontrivial especially with the constraint on control force, and it requires the knowledge of the future external loading. Therefore, this solution cannot immediately be implemented. To overcome these challenges, the optimal control problem is redefined only for the second phase regions where the control actions are active, giving a piecewise optimal solution. In each excursion into the active control region, the final time is unknown; so, an iterative procedure is proposed to find the solution of this optimal control problem with unknown fixed final time on each excursion. All the formulations are presented in a nondimensionalized form, which makes it easily transformable to any linear time-invariant systems.

This procedure is then used in an extensive numerical assessment to understand the piecewise optimal control behavior under various initial conditions and to develop design curves under the free response condition with different initial velocities. For the purpose of illustration, these solutions are used to develop design curves to obtain the best-fitted stiffness and damping associated with a Kelvin-Voigt device. Then, in a numerical example, a nondimensional dual-mode system is designed based on the criteria outlined in this study. After that, the designed dual-mode system is evaluated under an

MCE-level event, and its performance is compared with the piecewise optimal solution and the suboptimal solution using the linear quadratic regulator (i.e., clipped-LQR). Through the evaluation, it is shown that impact can be avoided and at the same time maintained the total transferred acceleration within the acceptable region. This evaluation also shows that the piecewise optimal and the clipped-LQR procedures can generate smaller peak accelerations; however, the weight ratio obtained from the designed curves cannot be used directly. This study showed the feasibility of applying optimal control for designing dual-mode systems. In the future direction of this study, forced systems with various forcing characteristic need to be considered. Moreover, this study should be extended to inelastic SDOF or MDOF systems, where inelastic reduced order models can be utilized (Tehrani et al., 2018).

The focus of the dual-mode system described in this chapter is on the component level. From a more system-level viewpoint, the design objective would be to protect both the isolated equipment and the primary structure. The protection of the isolated equipment would be of importance under DBE-level event while the protection of the primary structure would be of importance MCE-level event. The next chapter deals with such dual-mode systems while incorporating reduced order modeling to reduce computational cost.

Chapter 4
Dual-Mode Vibration Isolator/Absorber

4.1 Overview

In this chapter, a new reduced order modeling method for elastic structures with nonlinear attachments is proposed where the elastic structure is reduced and analyzed in its modal coordinates and the nonlinear attachments are kept untouched in the formulation. First, the equation of motion for the uncoupled full model is described. Next, the equations of motion for the nonlinear attachments are coupled with the full uncoupled model. The nonlinear attachments considered have a cubic (hardening) term. The hardening nonlinearity helps to reduce the displacement demand (as discussed in Chapter 3) and allows the dual-mode system to smoothly transition from the isolation behavior toward vibration absorber behavior. After that, the linear elastic part of the coupled equation of motion is reduced using the modal properties of the full uncoupled model. This reduced model can be used to estimate the response quantities of interest in the modal coordinates as well as displacements and accelerations of the attachments. Then, the estimated responses are transformed back to the original coordinates using the same modal properties used for model reduction.

After the development of the formulation for the nonlinear reduced order model (NLROM), a 3-story structure is considered and is reduced using the proposed model reduction method in two ways using the modal properties of the full uncoupled model and the modal properties of the full primary structure where the attachment mass is

taken out from the structure. These NLROMs are evaluated under the El Centro ground motion to validate their accuracy. Following that, NLROMs are utilized to assess the feasibility of using partial floor isolation to achieve both objectives of protecting the isolated objects under low amplitude excitation and protecting the primary structure under high amplitude excitation. This assessment is done by developing nonlinear transmissibility curves for roof displacement as the representative of the primary structure and isolated mass total acceleration as the most sensitive response for protecting the isolated objects or equipment.

4.2 Nonlinear Reduced Order Modeling Method

4.2.1 Full Uncoupled Model

Consider a planar frame (structure) with n degrees of freedoms (DOFs), which may include lateral displacements, vertical displacements, and rotations. The set of linear equations that define the n-DOF structural system is given by

$$\mathbf{M}\ddot{\mathbf{q}}(t) + \mathbf{C}\dot{\mathbf{q}}(t) + \mathbf{K}\mathbf{q}(t) = -\mathbf{M}\boldsymbol{\iota}\ddot{u}_{\mathrm{g}}(t) \tag{4.1}$$

where $\mathbf{q}$ is the n-dimensional vector of all DOFs; $\mathbf{M}$, $\mathbf{C}$, and $\mathbf{K}$ are the $n \times n$ mass, damping, and (linear-elastic) stiffness matrices, respectively; and $\boldsymbol{\iota}$ is the n-dimensional influence vector that applies the ground motion acceleration, $\ddot{u}_{\mathrm{g}}$, to the lateral nodal displacements. Eq. (4.1) represents the *full uncoupled model* of the primary system alone.

4.2.2 Full Coupled Model

In general, the dynamics of floor or equipment isolation systems (i.e., secondary systems) are coupled with the primary structure and they interact with each other. This interaction can be neglected when the equipment masses are considerably smaller than the mass of the primary structure and/or if their frequencies are different enough com-

pared to the natural frequency of the primary structure (Reggio and De Angelis, 2014).

Consider partially isolating the mass of ℓ selected floors, as shown in Figure 4.1. The positions are identified by the $n \times \ell$ Boolean position matrix $\mathbf{P}$ where the jth column shows the location of the jth isolation system at the full primary system model (i.e., the value of the corresponding location is one, with zeros everywhere else). The ith partial isolated mass located at the jth floor is given by $m_i = \mu_i M_j$, where μ_i is the proportion of mass M_j that is isolated. The ratio of the isolated masses to the floor masses can be concatenated into a diagonal mass ratio matrix, $\boldsymbol{\mu} = \mathbf{diag}(\mu_1, \ldots, \mu_\ell)$. Defining $\mathbf{M}_p$ to be the modified remaining mass of the primary structure (i.e., excluding all the isolated masses from the mass matrix $\mathbf{M}$), the dynamics of the coupled primary-secondary system is given by the following $n + \ell$ coupled equations:

$$\mathbf{M}_p\ddot{\mathbf{q}}(t) + \mathbf{C}\dot{\mathbf{q}}(t) + \mathbf{K}\mathbf{q}(t) = -\mathbf{M}_p\boldsymbol{\iota}\ddot{u}_g(t) + \mathbf{P}\boldsymbol{\mathcal{F}}(\mathbf{d}(t), \dot{\mathbf{d}}(t)) \tag{4.2a}$$

$$\mathbf{M}_s\ddot{\mathbf{d}}(t) + \boldsymbol{\mathcal{F}}(\mathbf{d}(t), \dot{\mathbf{d}}(t)) = -\mathbf{M}_s\mathbf{P}^{\mathrm{T}}(\ddot{\mathbf{q}}(t) + \boldsymbol{\iota}\ddot{u}_g(t)) \tag{4.2b}$$

where $\boldsymbol{\mathcal{F}} = [f_1, \ldots, f_\ell]^{\mathrm{T}}$ is the ℓ-dimensional vector of restoring forces of the floor isolation systems, $\mathbf{M}_s = \mathbf{diag}(m_1, \ldots, m_\ell)$ is the diagonal matrix of the masses of the isolation systems, and $\mathbf{d}$ is the vector of lateral displacement of isolation systems relative to the floor they are mounted on.

The force f_i, associated with the ith element of the vector $\boldsymbol{\mathcal{F}}$, represents the restoring and damping forces of the isolation system located in the ith floor. Here the restoring forces are taken to be cubic with linear stiffness k_i^L and cubic stiffness* k_i^N, and damping is assumed to be linear viscous with damping coefficient c_i:

$$f_i(d_i, \dot{d}_i; t) = k_i^L d_i(t) + k_i^N [d_i(t)]^3 + c_i\dot{d}_i(t) \; . \tag{4.3}$$

The set of all the restoring forces given by Eq. (4.3) can be written in the matrix form as follows:

*Note that k_i^N has units of force per cubic length, so it is not technically a stiffness.

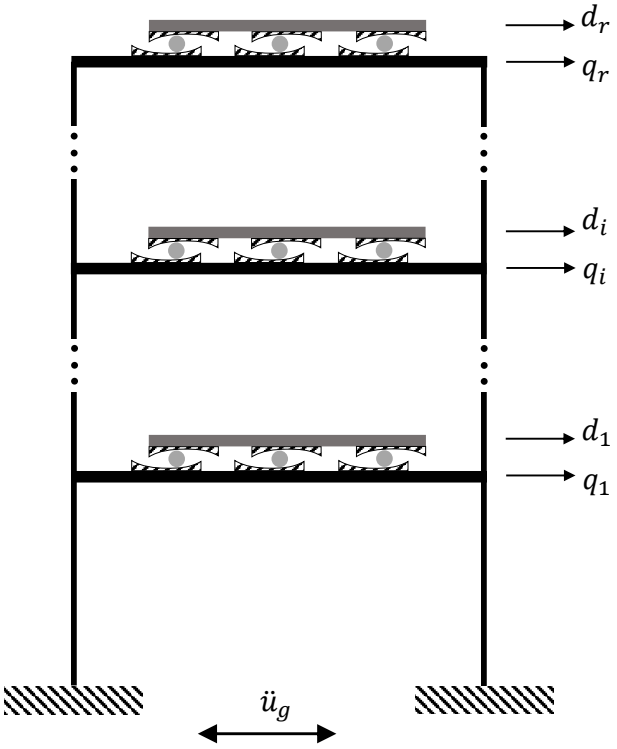

Figure 4.1: Coupled structural model.

$$\mathcal{F}(\mathbf{d}(t), \dot{\mathbf{d}}(t)) = \mathbf{K}_s^L \mathbf{d}(t) + \mathbf{K}_s^N \mathbf{d}(t)^{\circ 3} + \mathbf{C}_s \dot{\mathbf{d}}(t) \tag{4.4}$$

where $\mathbf{K}_s^L = \mathbf{diag}(k_1^L, \ldots, k_\ell^L)$, $\mathbf{K}_s^N = \mathbf{diag}(k_1^N, \ldots, k_\ell^N)$, and $\mathbf{C}_s = \mathbf{diag}(c_1, \ldots, c_\ell)$, and "$(\cdot)^{\circ 3}$" indicates element-wise cube.

Substituting $\mathcal{F}(\cdot)$ from Eq. (4.2b) into Eq. (4.2a) and from Eq. (4.4) into Eq. (4.2b) result in

$$\mathbf{M}_p \ddot{\mathbf{q}}(t) + \mathbf{C}\dot{\mathbf{q}}(t) + \mathbf{K}\mathbf{q}(t) + \mathbf{P}\mathbf{M}_s(\mathbf{P}^{\mathrm{T}}\ddot{\mathbf{q}}(t) + \ddot{\mathbf{d}}(t) + \mathbf{P}^{\mathrm{T}}\boldsymbol{\iota}\ddot{u}_{\mathrm{g}}(t)) = -\mathbf{M}_p\boldsymbol{\iota}\ddot{u}_{\mathrm{g}}(t) \tag{4.5a}$$

$$\mathbf{M}_s(\mathbf{P}^{\mathrm{T}}\ddot{\mathbf{q}}(t) + \ddot{\mathbf{d}}(t)) + \mathbf{K}_s^L \mathbf{d}(t) + \mathbf{K}_s^N \mathbf{d}(t)^{\circ 3} + \mathbf{C}_s \dot{\mathbf{d}}(t) = -\mathbf{M}_s\mathbf{P}^{\mathrm{T}}\boldsymbol{\iota}\ddot{u}_{\mathrm{g}}(t) \tag{4.5b}$$

These equations represent the *full coupled model* of the primary-secondary system, including all nonlinear interactions.

4.2.3 Reduced Coupled Model

To ease the computational burden of analyzing the full coupled model (Eq. (4.5)), the primary structure portion of the coupled model can be transformed into the modal coordinates while keeping the secondary system of equations in the nonlinear reduced order model (NLROM). Transformation to the modal coordinates can be done using r selected frequencies $(\omega_1, \ldots, \omega_r)$ of the full uncoupled model (Eq. (4.1)). The r associated mode shapes $(\boldsymbol{\phi}_1, \ldots, \boldsymbol{\phi}_r)$ with the highest contribution to the lateral responses can be selected based on the modal participation factors $\Gamma_i \equiv \boldsymbol{\phi}_i^{\mathrm{T}}\mathbf{M}\boldsymbol{\iota}$ where $\boldsymbol{\phi}_i$ is the ith mode shape found from the full uncoupled model, i.e., $(\mathbf{K} - \omega_i^2\mathbf{M})\boldsymbol{\phi}_i = \mathbf{0}$. The selected mode shapes are assembled into the $n \times r$ modal matrix $\boldsymbol{\Phi}_r = [\boldsymbol{\phi}_1, \ldots, \boldsymbol{\phi}_r]$.

Considering the selected frequencies, the responses of the primary full model is then approximated by these r modes:

$$\mathbf{q}(t) \approx \boldsymbol{\Phi}_r \boldsymbol{\eta}(t) \tag{4.6}$$

where $\boldsymbol{\eta} = [\eta_1, \ldots, \eta_r]^{\mathrm{T}}$ are the modal coordinates. Alternatively, the model reduction can be achieved by keeping one horizontal degree of freedom at each floor using the modal properties of the full model as described in Tehrani et al. (2018). Using the approximate solution obtained from the modal coordinate (Eq. (4.6)), Eq. (4.5) can be written as follows:

$$\begin{aligned}\boldsymbol{\Phi}_r^{\mathrm{T}}\mathbf{M}_p\boldsymbol{\Phi}_r\ddot{\boldsymbol{\eta}}(t) + \boldsymbol{\Phi}_r^{\mathrm{T}}\mathbf{C}\boldsymbol{\Phi}_r\dot{\boldsymbol{\eta}}(t) + \boldsymbol{\Phi}_r^{\mathrm{T}}\mathbf{K}\boldsymbol{\Phi}_r\boldsymbol{\eta}(t) \\ + \boldsymbol{\Phi}_r^{\mathrm{T}}\mathbf{P}\mathbf{M}_s(\mathbf{P}^{\mathrm{T}}\boldsymbol{\Phi}_r\ddot{\boldsymbol{\eta}}(t) + \ddot{\mathbf{d}}(t) + \mathbf{P}^{\mathrm{T}}\boldsymbol{\iota}\ddot{u}_{\mathrm{g}}(t)) = -\boldsymbol{\Phi}_r^{\mathrm{T}}\mathbf{M}_p\boldsymbol{\iota}\ddot{u}_{\mathrm{g}}(t)\end{aligned} \tag{4.7a}$$

$$\mathbf{M}_s(\mathbf{P}^{\mathrm{T}}\boldsymbol{\Phi}_r\ddot{\boldsymbol{\eta}}(t) + \ddot{\mathbf{d}}(t)) + \mathbf{K}_s^L\mathbf{d}(t) + \mathbf{K}_s^N\mathbf{d}(t)^{\circ 3} + \mathbf{C}_s\dot{\mathbf{d}}(t) = -\mathbf{M}_s\mathbf{P}^{\mathrm{T}}\boldsymbol{\iota}\ddot{u}_{\mathrm{g}}(t) \tag{4.7b}$$

Define the vector of all the coordinates of the reduced system to be $\mathbf{z} = [\boldsymbol{\eta}^{\mathrm{T}}, \mathbf{d}^{\mathrm{T}}]^{\mathrm{T}}$. Doing so, Eq. (4.7) can be reformulated in matrix form as follows:

$$\boldsymbol{\mathcal{M}}\ddot{\mathbf{z}}(t) + \boldsymbol{\mathcal{C}}\dot{\mathbf{z}}(t) + \boldsymbol{\mathcal{K}}_L\mathbf{z}(t) + \boldsymbol{\mathcal{K}}_N\mathbf{z}(t)^{\circ 3} = -\boldsymbol{\mathcal{R}}\ddot{u}_{\mathrm{g}}(t) \tag{4.8}$$

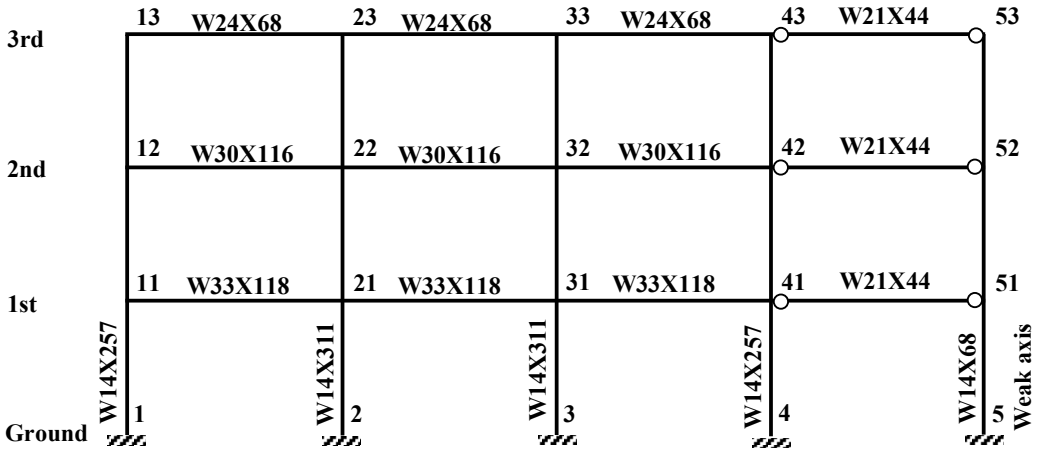

Figure 4.2: The 3-story primary structural model (adopted from Ohtori et al. (2004)).

where $\mathcal{M}$, C, $\mathcal{K}_L$, $\mathcal{K}_N$, and $\mathcal{R}$ are given by

$$\mathcal{M} = \begin{bmatrix} \boldsymbol{\Phi}_r^{\mathrm{T}}\mathbf{M}_p\boldsymbol{\Phi}_r + \boldsymbol{\Phi}_r^{\mathrm{T}}\mathbf{P}\mathbf{M}_s\mathbf{P}^{\mathrm{T}}\boldsymbol{\Phi}_r & \boldsymbol{\Phi}_r^{\mathrm{T}}\mathbf{P}\mathbf{M}_s \\ \mathbf{M}_s\mathbf{P}^{\mathrm{T}}\boldsymbol{\Phi}_r & \mathbf{M}_s \end{bmatrix}, \quad C = \begin{bmatrix} \boldsymbol{\Phi}_r^{\mathrm{T}}\mathbf{C}\boldsymbol{\Phi}_r & \mathbf{0} \\ \mathbf{0} & \mathbf{C}_s \end{bmatrix},$$
$$\mathcal{K}_L = \begin{bmatrix} \boldsymbol{\Phi}_r^{\mathrm{T}}\mathbf{K}\boldsymbol{\Phi}_r & \mathbf{0} \\ \mathbf{0} & \mathbf{K}_s^L \end{bmatrix}, \quad \mathcal{K}_N = \begin{bmatrix} \mathbf{0} & \mathbf{0} \\ \mathbf{0} & \mathbf{K}_s^N \end{bmatrix}, \quad \mathcal{R} = \begin{bmatrix} \boldsymbol{\Phi}_r^{\mathrm{T}}\mathbf{M}_p\boldsymbol{\iota} + \boldsymbol{\Phi}_r^{\mathrm{T}}\mathbf{P}\mathbf{M}_s\mathbf{P}^{\mathrm{T}}\boldsymbol{\iota} \\ \mathbf{M}_s\mathbf{P}^{\mathrm{T}}\boldsymbol{\iota} \end{bmatrix}. \tag{4.9}$$

This equation (or equivalently Eq. (4.7)) represents the *reduced coupled model*, for which the primary structure has been reduced to modal coordinates and the (nonlinear) coupling to the secondary system has been retained.

4.3 Structural Model Considered

The primary structural model considered in this chapter is a 3-story 2D frame structure. This structure is designed as a benchmark control problem for the SAC project located in Los Angeles, California region (Ohtori et al., 2004). The full 3D structure has 3 stories with total elevation of 39 ft, and is 120 ft by 180 ft in plan. The building's lateral load resisting system is steel perimeter moment-resisting frame, and Figure 4.2 shows the N-S frame. The beam and column sections are shown in the same figure. The applied seismic masses to this frame are 2.729 kips sec^2/in. for the first and second floors and 2.958 kips sec^2/in. for the roof. The first three natural frequency of the

primary structure are 0.984, 3.035, and 5.796 Hz. This structure is modeled in OpenSees using elastic Euler-Bernoulli beam elements with lumped masses at the nodes. The mass matrix $\mathbf{M}$ and linear elastic stiffness matrix $\mathbf{K}$ are extracted for further analyses in MATLAB.

A single secondary system (i.e., nonlinear dual-mode vibration isolator/absorber) is placed on the second floor of the primary structure. This system has mass $m_s = \mu \mathbf{P}^{\mathrm{T}} \mathbf{M} \mathbf{P}$ where μ is the the nondimensionalized relative floor *mass ratio*, linear stiffness k_s^L, and cubic nonlinear stiffness $k_s^N = \kappa k_s^L$ where κ is the *nonlinearity parameter* which characterizes the degree of nonlinearity in the secondary system.[†] This results in a (uncoupled) natural frequency of $\omega_s = \sqrt{k_s^L / m_s}$. Therefore, the nondimensionalized *frequency ratio* $\Omega = \omega_1 / \omega_s$ can be defined, where $\omega_1 = 6.18$ rad/sec for the 3-story structure considered here. Note that $\mathbf{M} = \mathbf{M}_p + \mathbf{diag}(\mathbf{P} m_s)$, or for the case of multiple attachments, $\mathbf{M} = \mathbf{M}_p + \mathbf{diag}(\mathbf{P} \boldsymbol{m}_s)$ where $\boldsymbol{m}_s$ is the column vector of all the attachment masses.

Figure 4.3 depicts the normalized force-displacement relationship for different values of κ. Note that $\kappa = 0$ corresponds to the linear case. Also, note that only positive values of κ are considered here, which corresponds to a hardening nonlinearity. The hardening in the secondary system is consistent with the findings in Chapter 3 in which displacements control (limitation) is desired to prevent excessive displacements.

4.4 Effect of Coupling

Of interest to this study is the responses of both the primary structure and the secondary isolation system. The former's response is characterized by the roof displacement, and the latter's by the total acceleration of the isolated mass. So, in this section, the effect of coupling on the responses (i.e., the roof displacement and the isolated mass total accel-

[†]Note that k_s^N has units of force per cubic length, so it is not technically a stiffness. The units of κ are reciprocal of length squared.

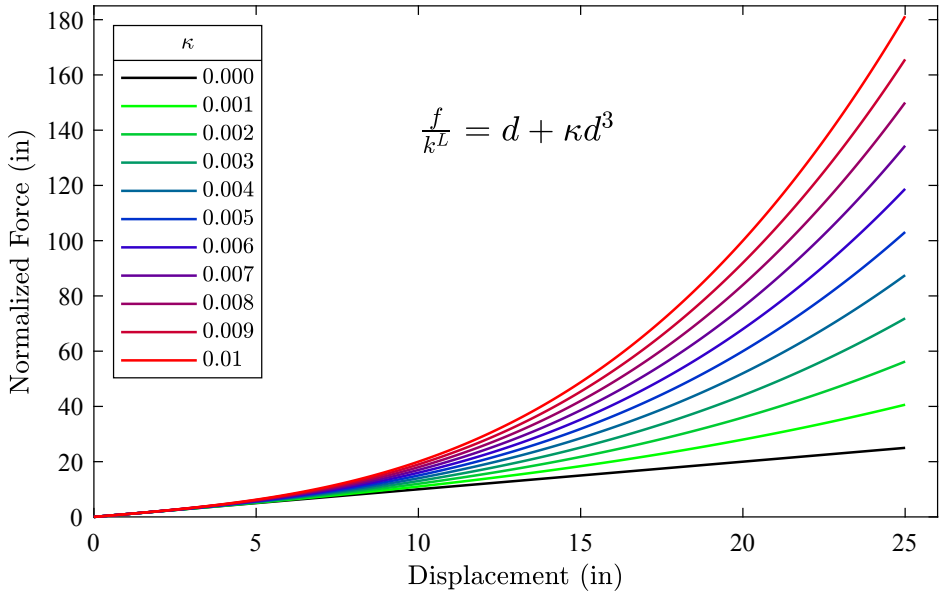

Figure 4.3: Normalized force-displacement relationship of the secondary system for varying nonlinearity parameter κ [in.$^{-2}$].

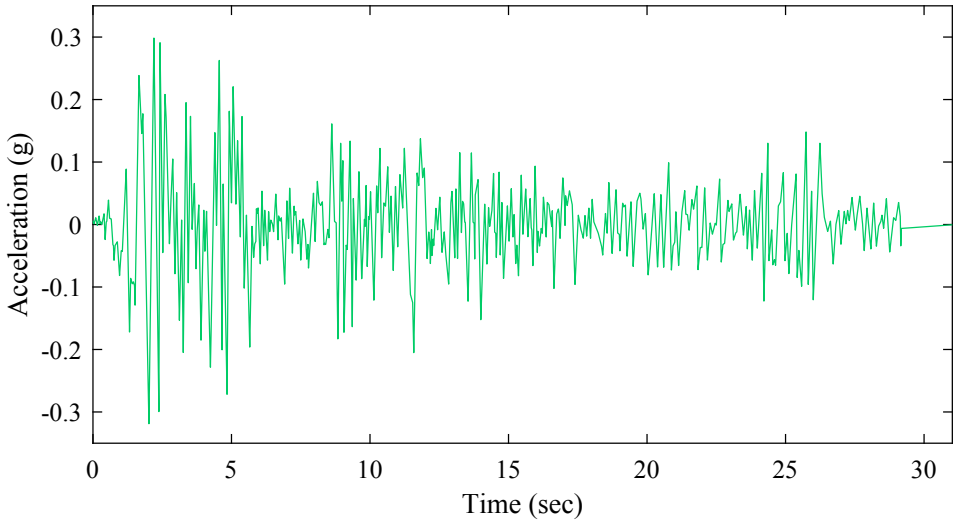

Figure 4.4: El Centro ground motion record.

eration) is assessed by considering the structure described in Section 4.3 excited with El Centro ground motion acceleration, depicted in Figure 4.4, under varying scale factors. Three types of structures are assessed. The first model is the full uncoupled structure (Section 4.2.1). The second model is the full primary structure without the attachment

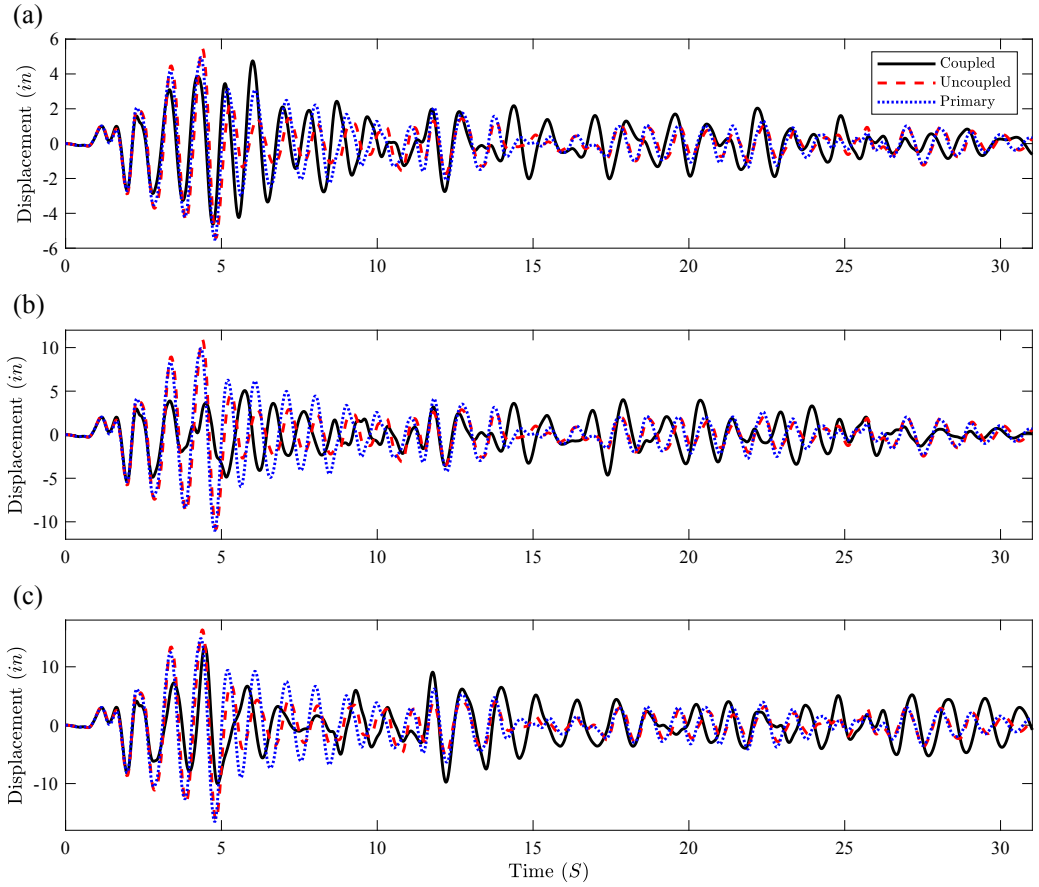

Figure 4.5: Response history of the roof displacement using the full coupled model, full uncoupled model, and full primary model ($\Omega = \sqrt{2}$, $\kappa = 0.010$ in.$^{-2}$, and $\mu = 0.3$) under (a) 1, (b) 2, and (c) 3 $\times$ El Centro.

mass, but excluding the isolated floor mass (i.e., structure with $\mathbf{M}_p$ as described in Section 4.2.2). The last model is the full coupled model where the isolated mass is mounted on the primary structure (Section 4.2.2). The first and second models are the bases of the NLROMs with different mode shapes, called *Method 1* and *Method 2*, respectively, in the following section on the verification of the NLROM.

The estimation of the time history of the roof displacement using the three models under El Centro ground motion acceleration with ground motion (GM) multipliers of 1, 2, and 3 are shown in Figure 4.5. In the coupled model, the secondary system's properties are $\Omega = \sqrt{2}$, $\kappa = 0.010$ in.$^{-2}$, and $\mu = 0.3$ that are expected to produce the

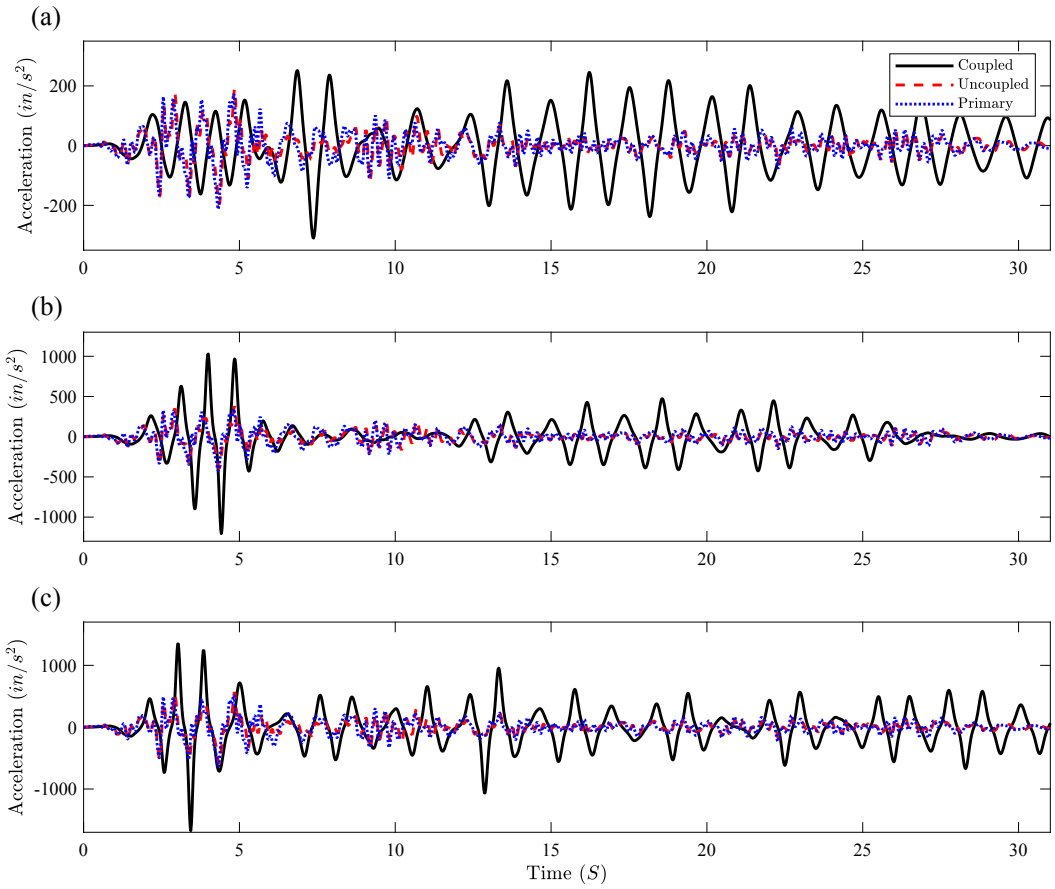

Figure 4.6: Response history of the isolated mass total acceleration using the full coupled model, full uncoupled model, and full primary model ($\Omega = \sqrt{2}$, $\kappa = 0.010$ in.$^{-2}$, and $\mu = 0.3$) under (a) 1, (b) 2, and (c) 3 $\times$ El Centro.

highest level of coupling. As can be seen from this figure, the effect of coupling is clear in the responses even for the GM multiplier of 1. The coupling effect is more pronounced when looking at the isolated mass total acceleration as shown in Figure 4.6. Note that in this figure, the acceleration time history of the isolated mass for the uncoupled and primary models are the responses of the second floor. The changes in the frequency content of the isolated mass total acceleration in the coupled model is the effect of isolation, which filters high frequency content.

Peak roof displacement and peak isolated mass total acceleration versus various GM multipliers using the full uncoupled model, full primary model, and full coupled models

with $\Omega = \sqrt{2}$, 2, and 4 are shown in Figures 4.7, 4.8, and 4.9, respectively. As can be seen from these figures, as expected the uncoupled, primary, and full coupled model with $\kappa = 0$ in.$^{-2}$ behave linearly. As κ increases deviation from the linear response can be observed. As the GM multiplier increases, a marginal increase in the isolated mass total acceleration and reduction in the roof displacement is observed; as desired, this corresponds to a trade-off between isolation performance and primary structure response, representing a *dual-mode* behavior. As the frequency ratio increases, this trend changes and the roof displacement converges to the linear behavior since the interaction between the structure and the secondary system decreases. Moreover, reduction of the roof displacement in the full coupled model usually happens when large peak acceleration is observed in the isolated mass total acceleration. These observations indicate that the coupling effect is not negligible and should be considered on the estimation of the responses, especially when the frequencies of the secondary and primary systems are closer.

4.5 Validation of Reduced Order Modeling Method

In this section, two nonlinear reduced order models (NLROMs) are considered by applying the proposed method to the structure described in Section 4.3, and their accuracy are validated by exciting them with El Centro ground motion acceleration (Figure 4.4). The first model, referred to as *Method 1*, is the one described in Section 4.2.3, in which the mode shapes based on total structure mass ($\mathbf{M}$) is used in the model reduction. The second model, referred to as *Method 2*, is the modification to the method described in Section 4.2.3 by substituting the mode shapes obtained from the full uncoupled model with the mode shapes obtained from the primary uncoupled model ($\mathbf{M}_p$, i.e., the structure without the secondary mass, m_s). The effect of several parameters on the accuracy of the NLROMs is assessed such as GM multipliers of 1, 2, and 3 $\times$ El Centro corresponding to peak ground accelerations of 0.319, 0.638, and 0.956 g, various frequency

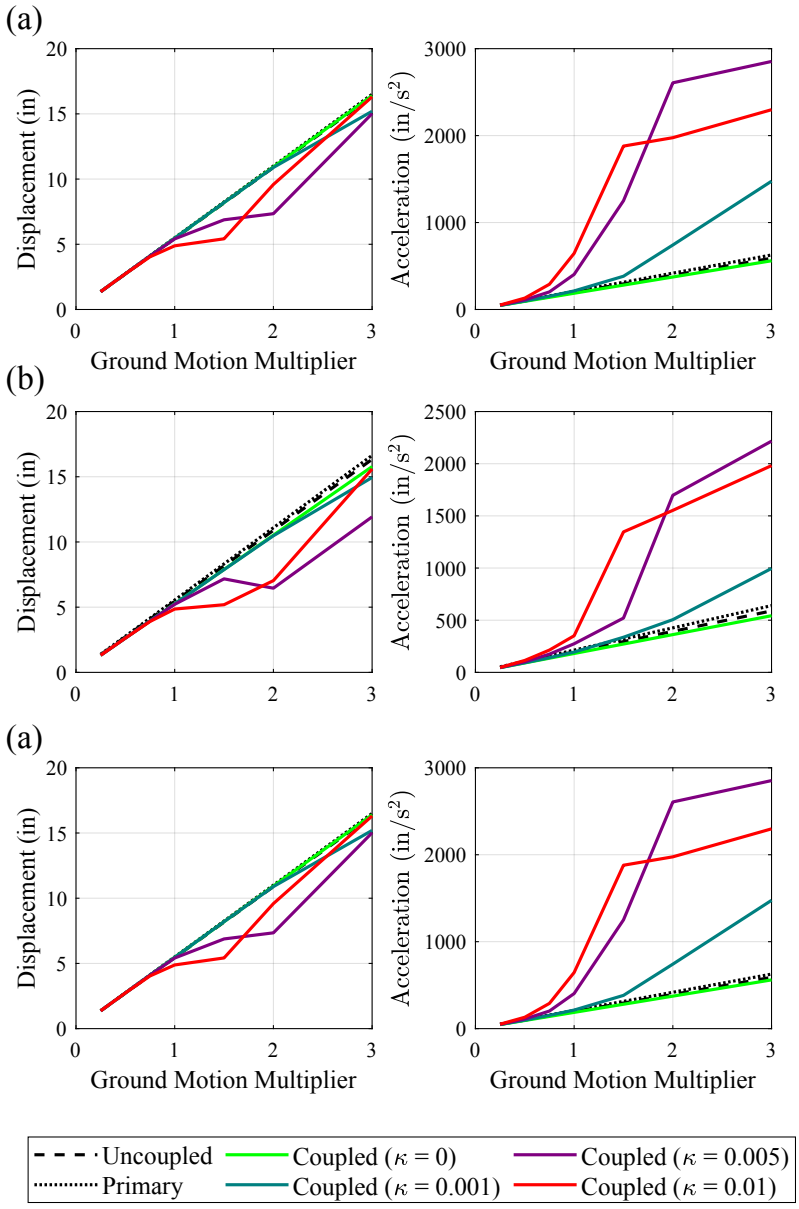

Figure 4.7: Peak roof displacement (left) and peak isolated mass total acceleration (right) versus ground motion multiplier using the full uncoupled model, full primary model, and full coupled model with $\Omega = \sqrt{2}$, varying κ [in.$^{-2}$], and μ = (a) 0.1, (b) 0.2, and (c) 0.3.

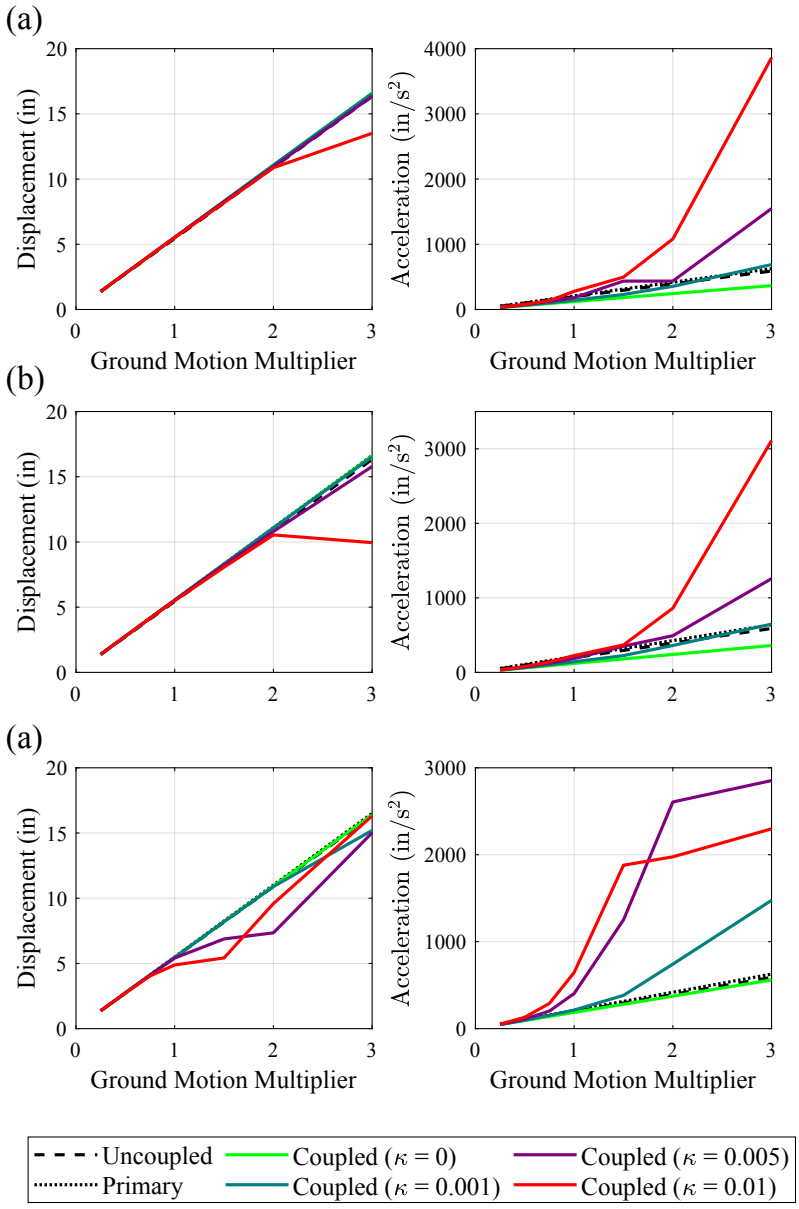

Figure 4.8: Peak roof displacement (left) and peak isolated mass total acceleration (right) versus ground motion multiplier using the full uncoupled model, full primary model, and full coupled model with $\Omega = 2$, varying κ [in.$^{-2}$], and μ = (a) 0.1, (b) 0.2, and (c) 0.3.

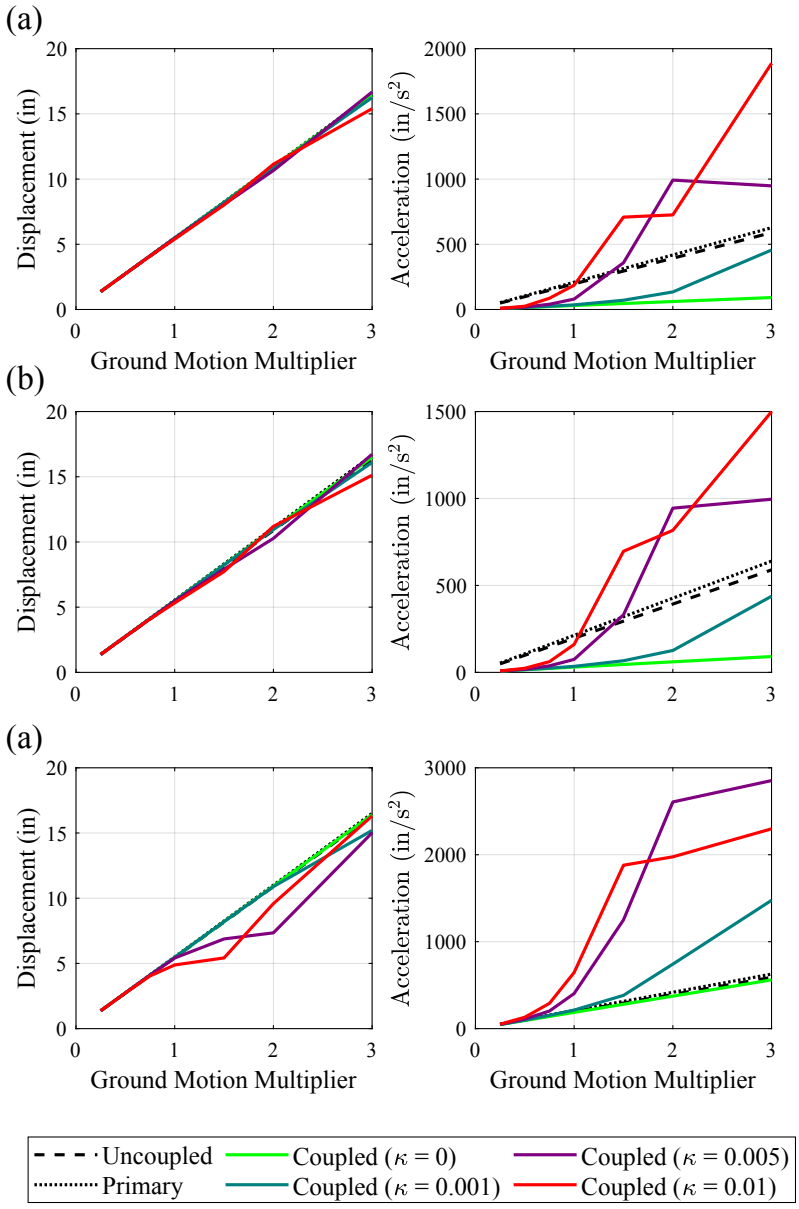

Figure 4.9: Peak roof displacement (left) and peak isolated mass total acceleration (right) versus ground motion multiplier using the full uncoupled model, full primary model, and full coupled model with $\Omega = 4$, varying κ [in.$^{-2}$], and μ = (a) 0.1, (b) 0.2, and (c) 0.3.

ratios (Ω) of $\sqrt{2}$, 2, and 4, and various nonlinearity parameters (κ) of 0, 0.001, 0.005, and 0.010 in.$^{-2}$. Moreover, the effect of including different number of modes in the NL-ROM is assessed by considering 1, 2, and 3 modes in the approximation (Eq. (4.6)). The mass ratio (μ) is kept constant at 0.3 for all the assessed scenarios, which is assumed to produce the highest level of coupling. The numerical integration has been done using the `ode45` solver in MATLAB, which uses the fourth order Runge-Kutta method with variable time steps.

4.5.1 Time History Responses

The simultaneous effects of the GM multiplier and the number of modes used in the NLROMs on the time history of responses using Method 1 are depicted in Figures 4.10–4.12. Similar conclusions as Method 1 can be drawn for Method 2, therefore the results for Method 2 are not presented. A more detailed comparison of Methods 1 and 2 is presented using several accuracy metrics later on.

Figure 4.10 shows the time history of the roof displacement using the full coupled model as well as NLROMs with 1, 2, and 3 modes using Method 1 with GM multipliers of 1, 2, and 3 $\times$ El Centro. As can be seen in this figure, the NLROM shows good agreement with the full coupled model. As the GM multiplier increases, deviations in agreement between the response predictions increase. Response histories are shifted in phase as the GM multiplier increases, which would be a source of large (instantaneous) errors; however, peak responses are of primary interest in this chapter. As expected, increasing the number of modes in the NLROM increases the accuracy of the responses (more pronounced for higher GM multiplier). In addition, relative reduction in the roof displacement can be observed when the GM multiplier increases. Peak roof displacements of 5.4, 9.9, and 10.7 in. are observed for GM multipliers of 1, 2, and 3 $\times$ El Centro.

Figure 4.11 shows similar information as Figure 4.10 for the displacement of the

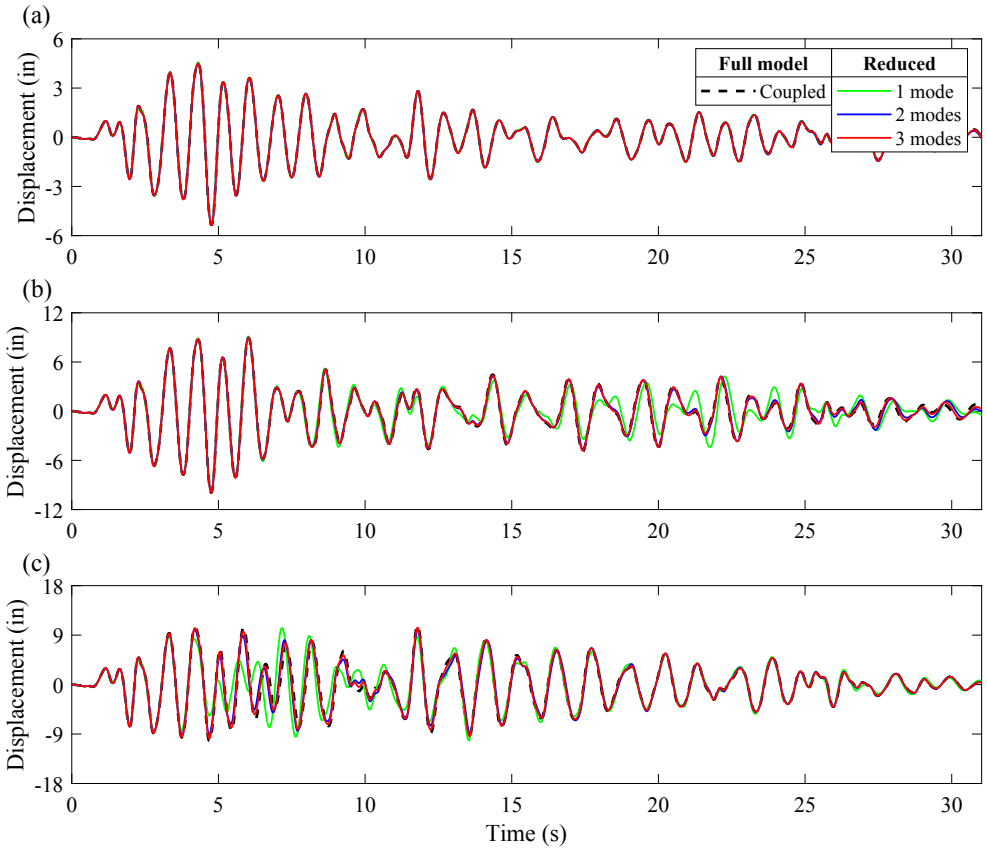

Figure 4.10: Response history of the roof displacement using the full coupled model and reduced coupled model using Method 1 with 1, 2, and 3 modes under (a) 1, (b) 2, and (c) 3 × El Centro: $\Omega = 2$, $\kappa = 0.010$ in.$^{-2}$, and $\mu = 0.3$.

isolated mass. As can be seen in this figure, as the GM multiplier increases, the primary-secondary system's interaction increases, resulted in higher frequency responses; this is especially apparent between 4 and 8 sec, where displacements are stunted at about 26 in. due to the sharply hardening effect. Moreover, phase shifts in the response histories are more pronounced.

The time history of the isolated mass total acceleration using the full coupled model as well as NLROMs with 1, 2, and 3 modes using Method 1 with GM multipliers of 1, 2, and 3 × El Centro is shown in Figure 4.12. As can be seen in this figure, similar but opposite patterns to the estimation of displacements is observed in the estimation of total accelerations. Accelerations grow with GM multiplier, wherein the cubic (hardening)

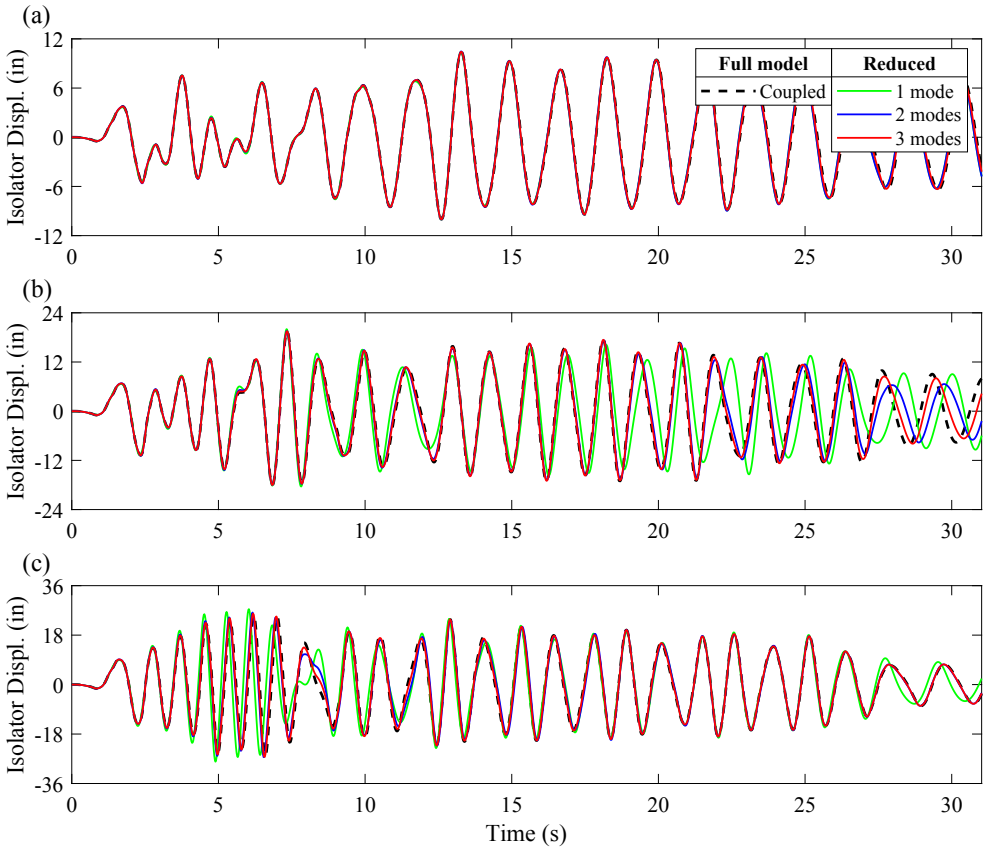

Figure 4.11: Response history of the isolated mass displacement using the full coupled model and reduced coupled model using Method 1 with 1, 2, and 3 modes under (a) 1, (b) 2, and (c) 3 × El Centro: $\Omega = 2$, $\kappa = 0.010$ in.$^{-2}$, and $\mu = 0.3$.

nonlinearity is more influential. This is especially apparent between 4–8 sec where, as previously noted, displacements are stunted and large accelerations result ($\sim 5\ g$).

4.5.2 Accuracy Metrics

In order to quantitatively assess the effects of varying parameters (i.e., GM multipliers, number of modes, frequency ratio Ω, and nonlinearity parameter κ) on the accuracy of the NLROMs, four validation metrics are considered. The engineering demand parameters (EDPs) considered for the validation correspond to roof displacement and isolated mass total acceleration. The first metric is the relative maximum absolute error between the full coupled model and NLROM responses:

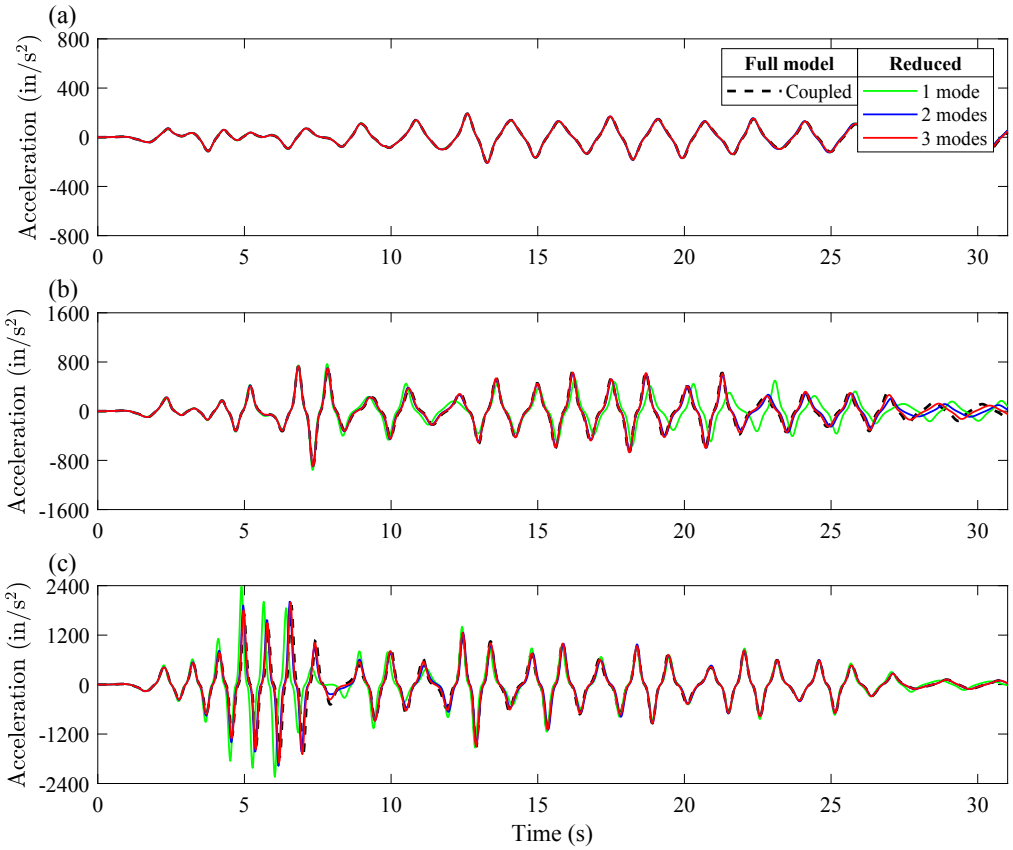

Figure 4.12: Response history of the isolated mass total acceleration using the full coupled model and reduced coupled model using Method 1 with 1, 2, and 3 modes under (a) 1, (b) 2, and (c) 3 × El Centro: $\Omega = 2$, $\kappa = 0.010$ in.$^{-2}$, and $\mu = 0.3$.

$$\text{MAE} = \frac{\max\limits_{i=1,\ldots,N} |\hat{r}_i - r_i|}{\max\limits_{i=1,\ldots,N} |r_i|} \qquad \text{(relative maximum absolute error)} \tag{4.10}$$

where r_i and $\hat{r}_i$ are the responses (roof displacement or isolaor total acceleration) at discrete time i for the full coupled model (i.e., the "true" model) and NLROM, respectively, and N is the total number of observation in the response history. The second metric is the relative root mean squared error (RMSE):

$$\text{RMSE} = \sqrt{\frac{\frac{1}{N}\sum_{i=1}^{N}(\hat{r}_i - r_i)^2}{\frac{1}{N}\sum_{i=1}^{N} r_i^2}} \qquad \text{(relative root mean squared error).} \tag{4.11}$$

The third metric identifies the error between the true and estimated peak responses:

$$\text{PPE} = \frac{\max\limits_{i=1,\ldots,N} |\hat{r}_i| - \max\limits_{i=1,\ldots,N} |r_i|}{\max\limits_{i=1,\ldots,N} |r_i|} \qquad \text{(relative peak prediction error).} \tag{4.12}$$

The fourth metric is the relative difference in the root-mean-squared (RMS) responses:

$$\text{RMSPE} = \frac{\sqrt{\frac{1}{N}\sum_{i=1}^{N} \hat{r}_i^2} - \sqrt{\frac{1}{N}\sum_{i=1}^{N} r_i^2}}{\sqrt{\frac{1}{N}\sum_{i=1}^{N} r_i^2}} \qquad \text{(relative RMS prediction error).} \tag{4.13}$$

The first and second metrics quantify the errors between the full coupled model and the NLROM at each instance in time, whereas the third and fourth metrics quantify the errors between peak and RMS predictions for the two models. The accuracy of the NLROMs is assessed below using the described metrics for both EDPs (roof displacement and isolated mass total acceleration).

4.5.2(a) Roof Displacement

The MAE for the estimation of roof displacement is shown in Figures 4.13, 4.14, and 4.15 for the models with a mass ratio of $\mu = 0.3$ for different GM multipliers, frequency ratio Ω, and nonlinearity parameter κ, using 1, 2, and 3 modes, respectively. As the GM multiplier increases, the MAE increases from around 14% to around 94% for GM multiplier of 1 to 3 when only one mode is considered. Additionally, when the nonlinearity increases, the MAE increases. No general trend can be distinguished for the frequency ratio Ω. Similar conclusions can be drawn for using 2 or 3 modes in the NLROMs. As discussed before, phase shifted responses is the main source of instantaneous errors, resulting in the observed large MAEs. Comparing these figures, it can be understood that increasing the number of modes provide a model with higher accuracy as observed in the time history responses shown in Figures 4.10–4.12. Including more modes in the NLROMs decreases the MAE, from around 94% when using 1 mode to around 40% for Method 1 and 20% for Method 2 when using 3 modes. In general, Method 1

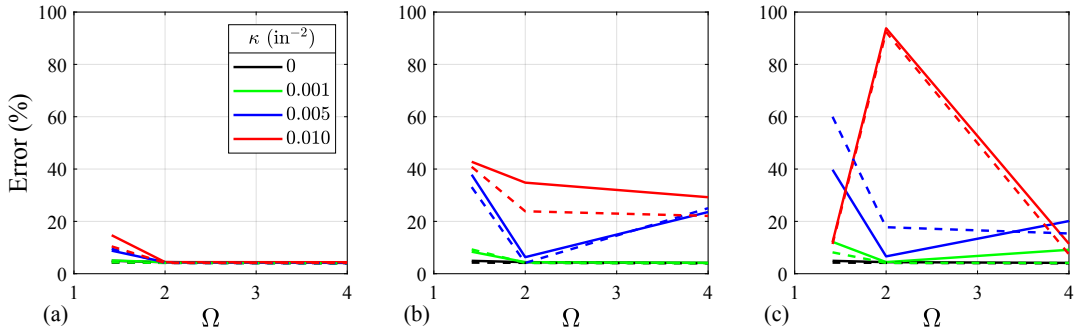

Figure 4.13: Relative maximum absolute error (MAE) of roof displacement for the nonlinear reduced order model using 1 mode and Method 1 (——) or 2 (- - -), with $\mu = 0.3$ under (a) 1, (b) 2, and (c) 3 $\times$ El Centro.

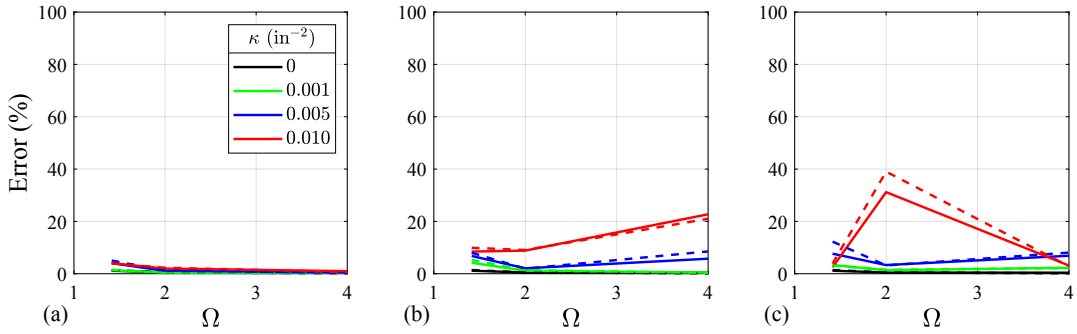

Figure 4.14: Relative maximum absolute error (MAE) of roof displacement for the nonlinear reduced order model using 2 modes and Method 1 (——) or 2 (- - -), with $\mu = 0.3$ under (a) 1, (b) 2, and (c) 3 $\times$ El Centro.

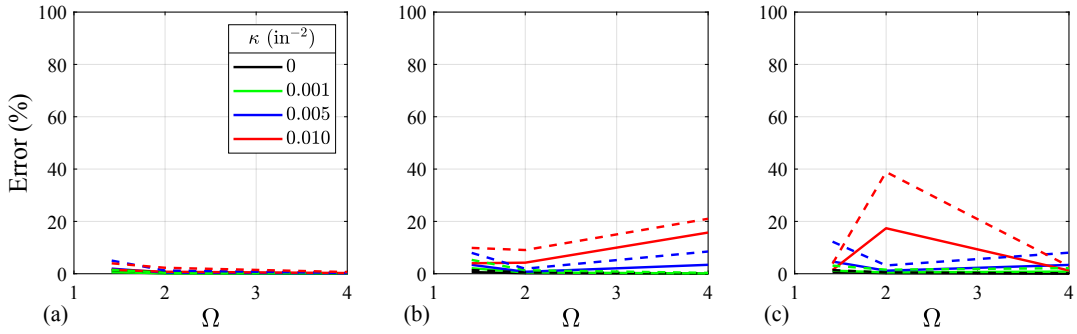

Figure 4.15: Relative maximum absolute error (MAE) of roof displacement for the nonlinear reduced order model using 3 modes and Method 1 (——) or 2 (- - -), with $\mu = 0.3$ under (a) 1, (b) 2, and (c) 3 $\times$ El Centro.

outperforms Method 2 in most cases as the number of modes increases.

The MAE evaluates only the maximum errors, whereas RMSE evaluates the mean (squared) errors over the whole time history. The RMSE for the estimation of roof displacement is shown in Figures 4.16, 4.17, and 4.18 for the NLROMs using 1, 2, and 3 modes, respectively. Similar conclusions to the MAE in general can be observed. As the GM multiplier increases, the RMSE increases. Including more modes reduces the RMSE, and the higher the nonlinearity the larger the RMSE. The RMSE increases from around 17% to around 80% for the model using 1 mode with GM multiplier of 1 to 3, respectively. The RMSE for the highest GM multiplier decreases from around 80% for 1 mode to around 21% for 3 modes.

In addition to MAE and RMSE, PPE and RMSPE are assessed in Figures 4.19, 4.20, and 4.21 and Figures 4.22, 4.23, and 4.24, respectively. Unlike MAE and RMSE, which measure instantaneous errors (i.e., simultaneously in time), PPE and RMSPE measure the error in estimation of absolute peak responses and error in RMS responses, respectively. The PPE, in general, decreases as the number of modes increases and increases as the GM multiplier increases. There is an exception in the general trend described above; namely, for the highest GM multiplier, the PPE increases as the number of mode increases when $\Omega = 2$. Similar conclusion as of PPE can be observed for RMSPE (i.e., increase in RMSPE with increase in GM multiplier and reduction in RMSPE with increasing the number of modes). Overall, PPE and RMSPE show much lower relative errors ($< 10\%$ in all cases), which is because these metrics compare peak responses that may not occur simultaneously in predictions for the full coupled model and NLROMs. PPE is arguably the best metrics for earthquake engineering, where peak responses ultimately control.

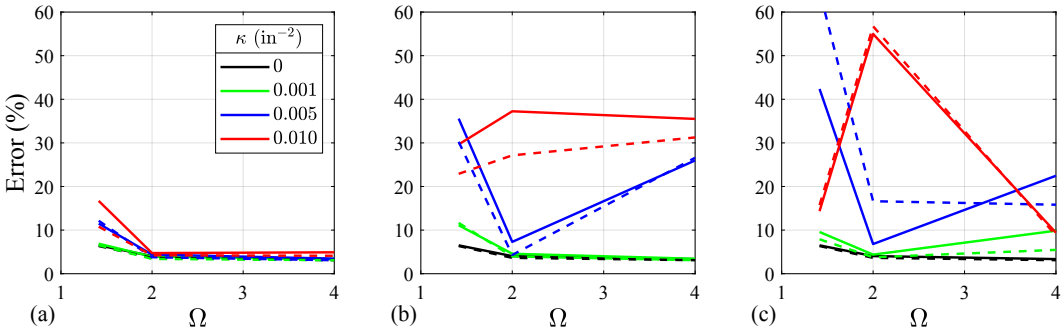

Figure 4.16: Relative root mean squared error (RMSE) of roof displacement for the nonlinear reduced order model using 1 mode and Method 1 (——) or 2 (- - -), with $\mu = 0.3$ under (a) 1, (b) 2, and (c) 3 $\times$ El Centro.

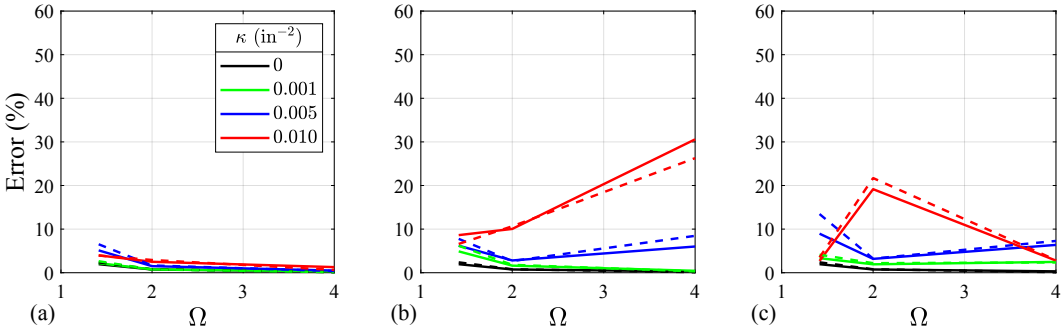

Figure 4.17: Relative root mean squared error (RMSE) of roof displacement for the nonlinear reduced order model using 2 modes and Method 1 (——) or 2 (- - -), with $\mu = 0.3$ under (a) 1, (b) 2, and (c) 3 $\times$ El Centro.

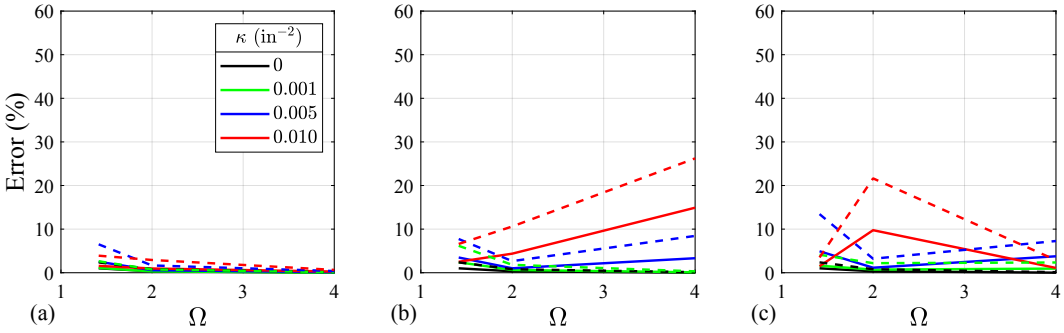

Figure 4.18: Relative root mean squared error (RMSE) of roof displacement for the nonlinear reduced order model using 3 modes and Method 1 (——) or 2 (- - -), with $\mu = 0.3$ under (a) 1, (b) 2, and (c) 3 $\times$ El Centro.

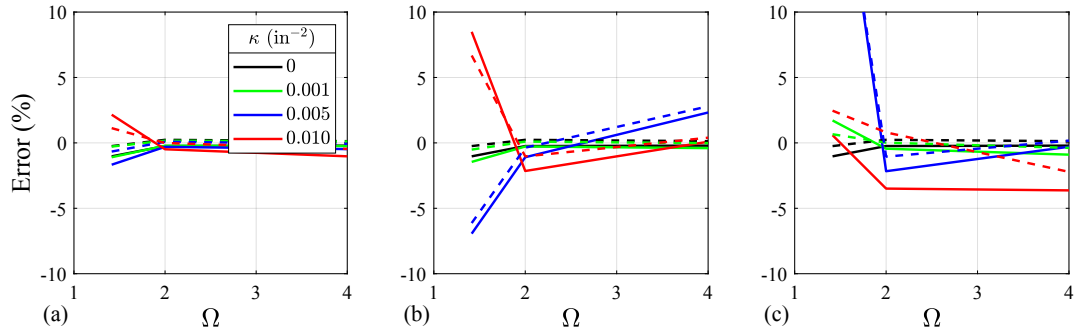

Figure 4.19: Relative peak prediction error (PPE) of roof displacement for the nonlinear reduced order model using 1 mode and Method 1 (——) or 2 (- - -), with $\mu = 0.3$ under (a) 1, (b) 2, and (c) 3 $\times$ El Centro.

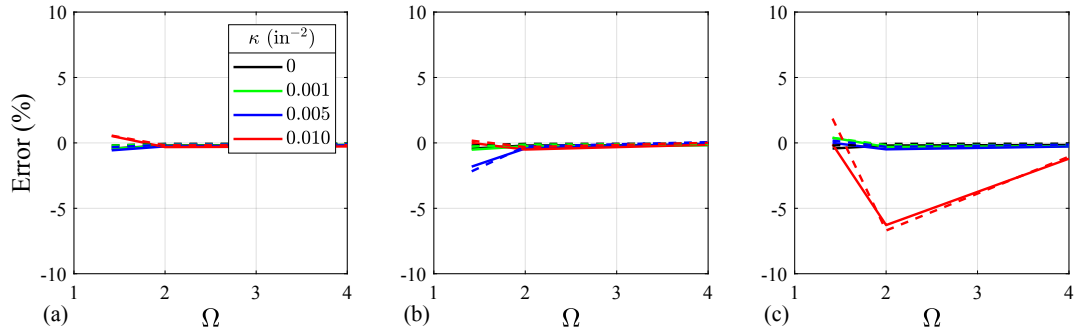

Figure 4.20: Relative peak prediction error (PPE) of roof displacement for the nonlinear reduced order model using 2 modes and Method 1 (——) or 2 (- - -), with $\mu = 0.3$ under (a) 1, (b) 2, and (c) 3 $\times$ El Centro.

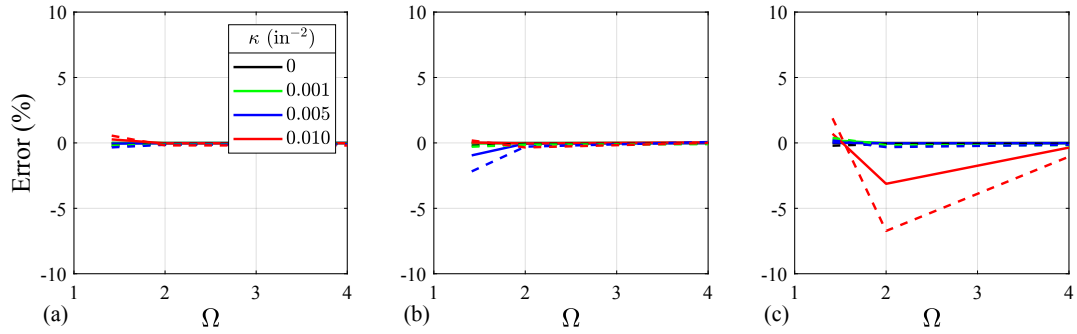

Figure 4.21: Relative peak prediction error (PPE) of roof displacement for the nonlinear reduced order model using 3 modes and Method 1 (——) or 2 (- - -), with $\mu = 0.3$ under (a) 1, (b) 2, and (c) 3 $\times$ El Centro.

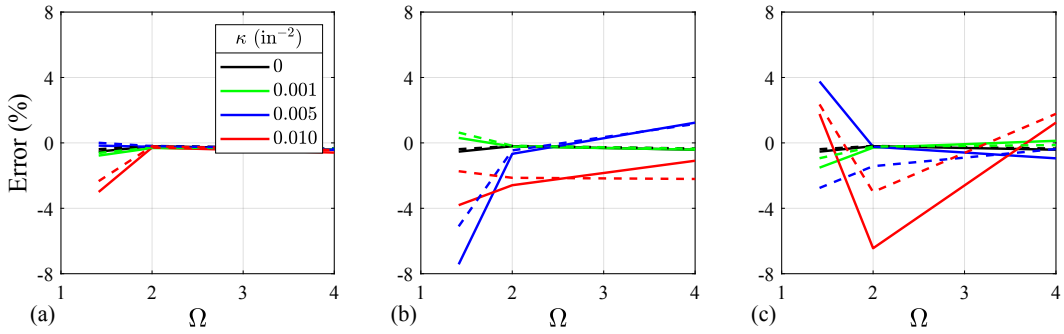

Figure 4.22: Relative RMS prediction error (RMSPE) of roof displacement for the nonlinear reduced order model using 1 mode and Method 1 (——) or 2 (- - -), with $\mu = 0.3$ under (a) 1, (b) 2, and (c) 3 × El Centro.

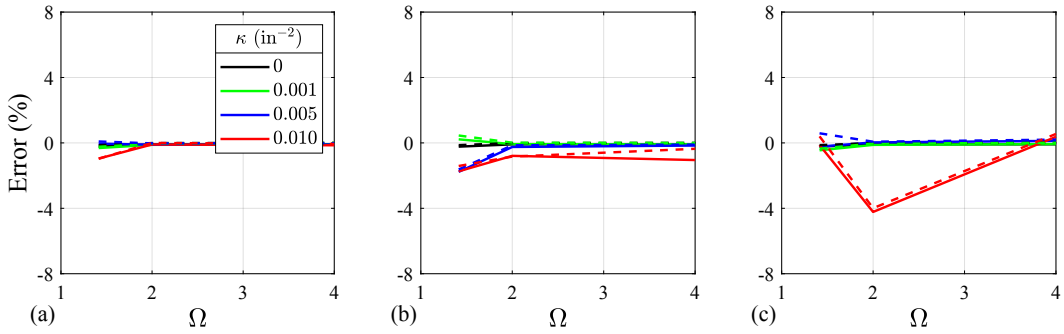

Figure 4.23: Relative RMS prediction error (RMSPE) of roof displacement for the nonlinear reduced order model using 2 modes and Method 1 (——) or 2 (- - -), with $\mu = 0.3$ under (a) 1, (b) 2, and (c) 3 × El Centro.

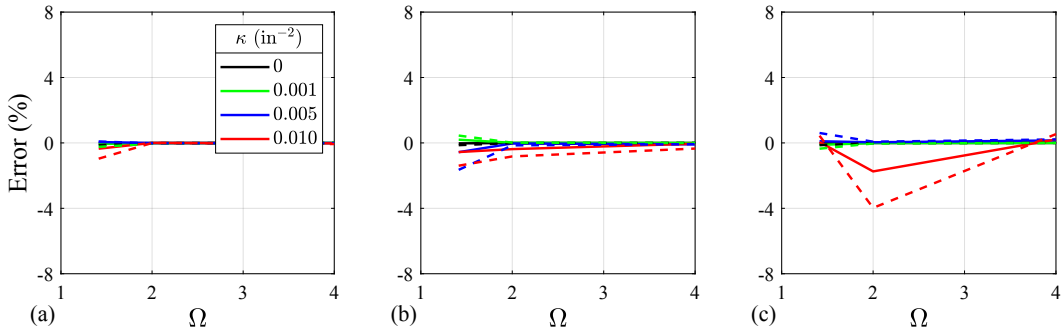

Figure 4.24: Relative RMS prediction error (RMSPE) of roof displacement for the nonlinear reduced order model using 3 modes and Method 1 (——) or 2 (- - -), with $\mu = 0.3$ under (a) 1, (b) 2, and (c) 3 × El Centro.

4.5.2(b) Isolated Mass Total Acceleration

At this point, the described metrics are applied to evaluate the NLROMs for the estimation of the isolated mass total acceleration. Figures 4.25, 4.26, and 4.27 show the MAE of the isolated mass total acceleration versus the frequency ratio Ω for different values of nonlinearity parameter κ, GM multipliers, and the number of modes used in the NLROMs. As the GM multiplier increases, the MAE increases from around 30% to around 120% for the GM multiplier of 1 to 3, respectively. The MAE decreases as more modes are included in the NLROMs, from around 120% to around 60% for the highest GM multiplier with 1 and 3 modes, respectively. As expected, higher nonlinearity corresponds to larger MAE.

The RMSE pattern for the isolated mass total acceleration, shown in Figures 4.28, 4.29, and 4.30, is similar to the MAE. The RMSE fluctuates between about 30%, 110%, and 85% for GM multipliers of 11, and 3, respectively, when only 1 mode is considered (Figure 4.28). The RMSE for the highest intensity decreases from around 85% to less than 40% for the models with 1 and 3 modes, respectively.

PPE and RMSPE for the isolated mass total acceleration is shown in Figures 4.31–4.33 and 4.34–4.36, respectively. Including more modes in the NLROMs decreases the PPE (Figures 4.31–4.33); however, no general trend in the PPE can be observed with respect to GM multiplier. Similar trends are observed for RMSPE (4.34–4.36). With more modes included in the NLROMs, the RMSPE decreases, while no pattern can be understood regarding GM multipliers.

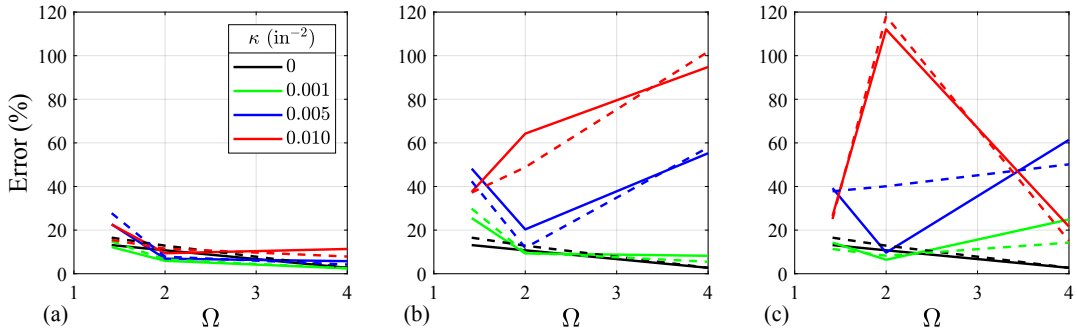

Figure 4.25: Relative maximum absolute error (MAE) of isolated mass total acceleration for the nonlinear reduced order model using 1 mode and Method 1 (——) or 2 (- - -), with $\mu = 0.3$ under (a) 1, (b) 2, and (c) 3 $\times$ El Centro.

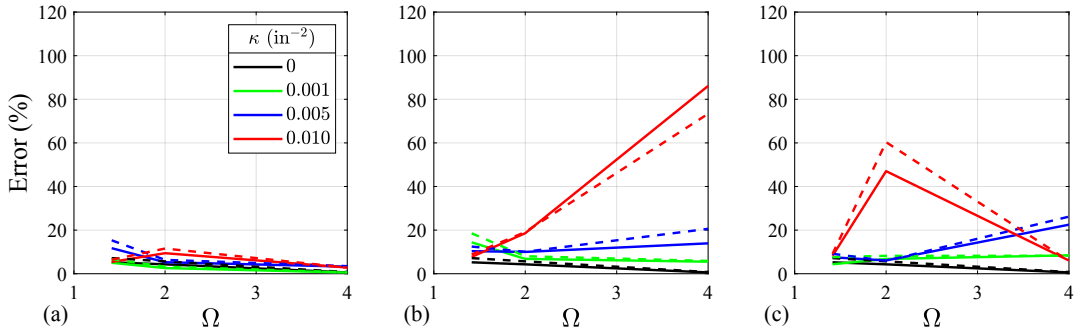

Figure 4.26: Relative maximum absolute error (MAE) of isolated mass total acceleration for the nonlinear reduced order model using 2 modes and Method 1 (——) or 2 (- - -), with $\mu = 0.3$ under (a) 1, (b) 2, and (c) 3 $\times$ El Centro.

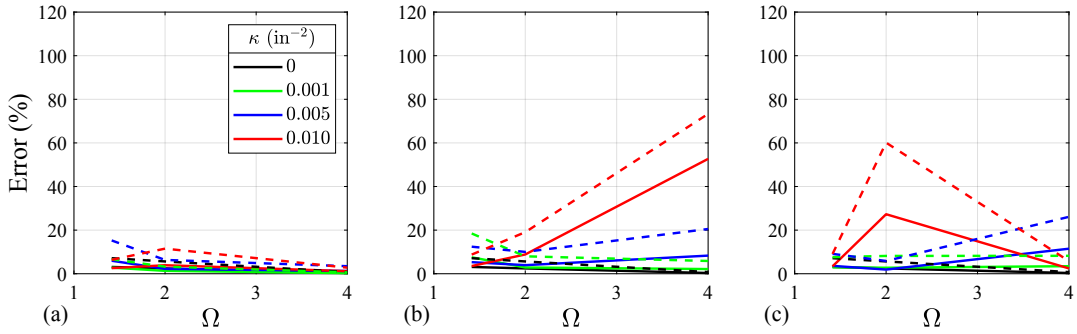

Figure 4.27: Relative maximum absolute error (MAE) of isolated mass total acceleration for the nonlinear reduced order model using 3 modes and Method 1 (——) or 2 (- - -), with $\mu = 0.3$ under (a) 1, (b) 2, and (c) 3 $\times$ El Centro.

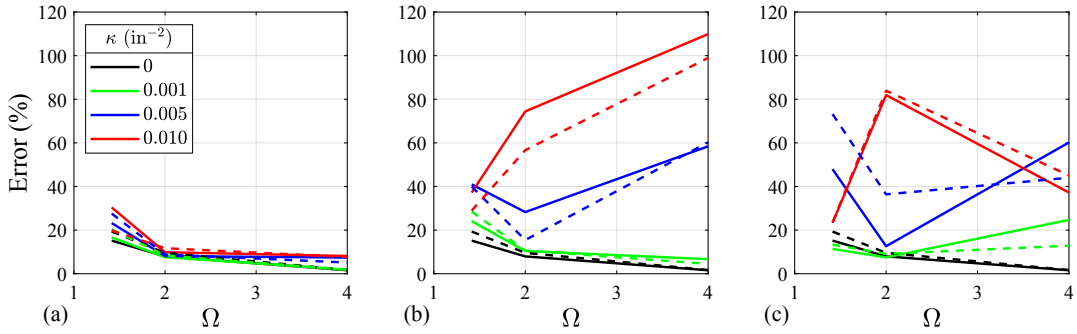

Figure 4.28: Relative root mean squared error (RMSE) of isolated mass total acceleration for the nonlinear reduced order model using 1 mode and Method 1 (——) or 2 (- - -), with $\mu = 0.3$ under (a) 1, (b) 2, and (c) 3 × El Centro.

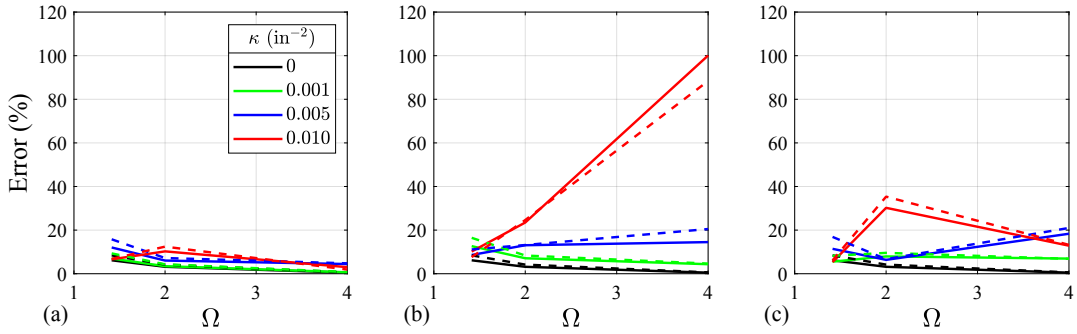

Figure 4.29: Relative root mean squared error (RMSE) of isolated mass total acceleration for the nonlinear reduced order model using 2 modes and Method 1 (——) or 2 (- - -), with $\mu = 0.3$ under (a) 1, (b) 2, and (c) 3 × El Centro.

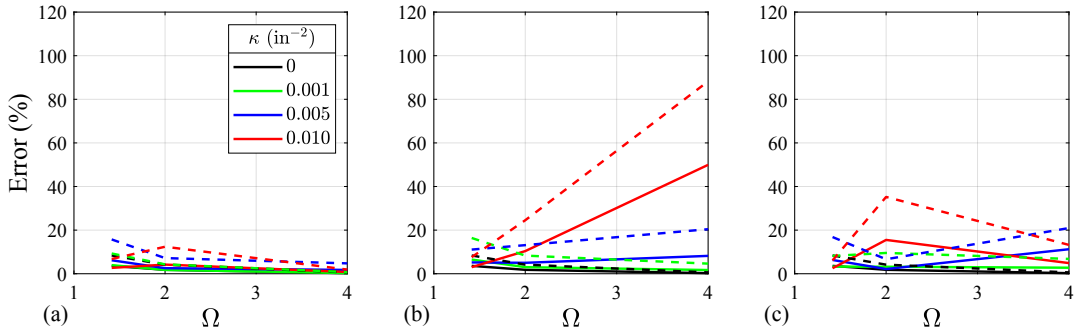

Figure 4.30: Relative root mean squared error (RMSE) of isolated mass total acceleration for the nonlinear reduced order model using 3 modes and Method 1 (——) or 2 (- - -), with $\mu = 0.3$ under (a) 1, (b) 2, and (c) 3 × El Centro.

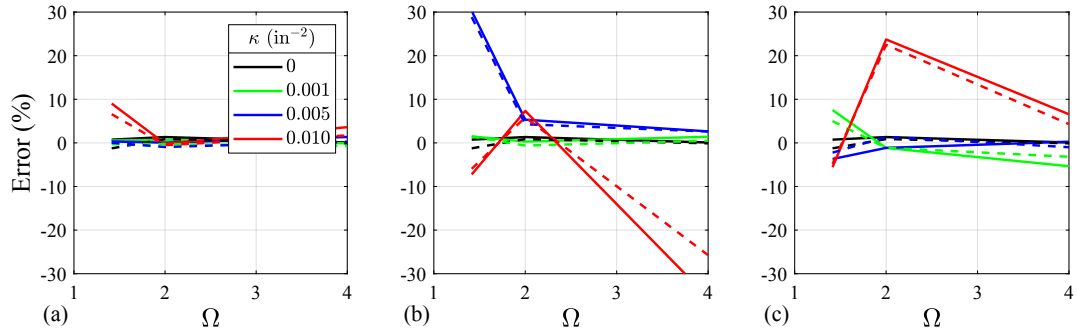

Figure 4.31: Relative peak prediction error (PPE) of isolated mass total acceleration for the nonlinear reduced order model using 1 mode and Method 1 (——) or 2 (- - -), with $\mu = 0.3$ under (a) 1, (b) 2, and (c) 3 $\times$ El Centro.

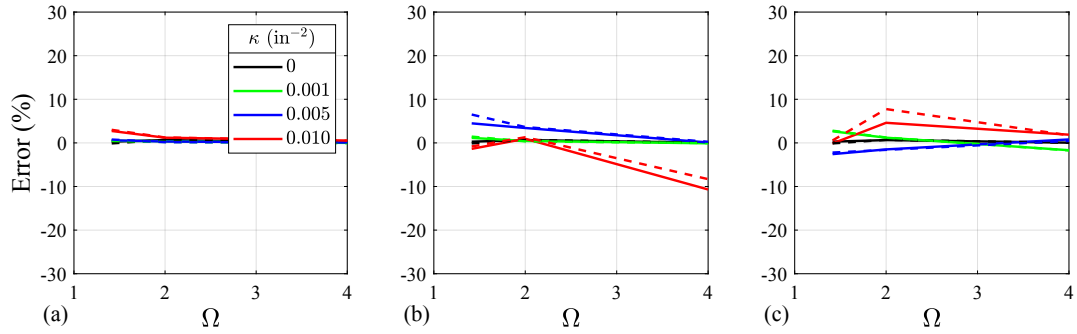

Figure 4.32: Relative peak prediction error (PPE) of isolated mass total acceleration for the nonlinear reduced order model using 2 modes and Method 1 (——) or 2 (- - -), with $\mu = 0.3$ under (a) 1, (b) 2, and (c) 3 $\times$ El Centro.

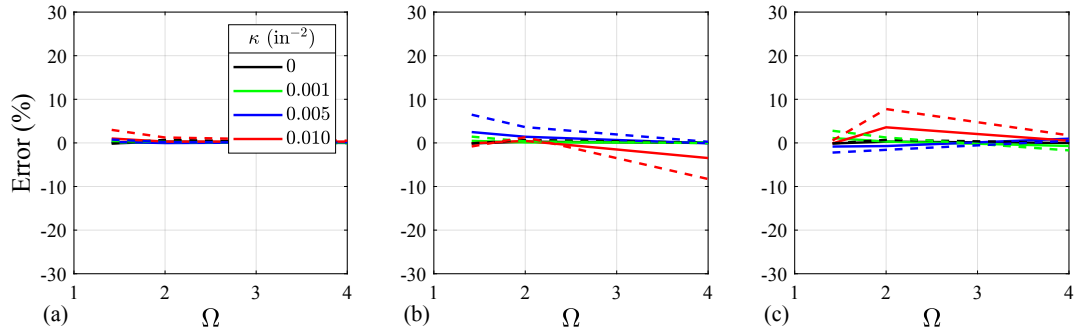

Figure 4.33: Relative peak prediction error (PPE) of isolated mass total acceleration for the nonlinear reduced order model using 3 modes and Method 1 (——) or 2 (- - -), with $\mu = 0.3$ under (a) 1, (b) 2, and (c) 3 $\times$ El Centro.

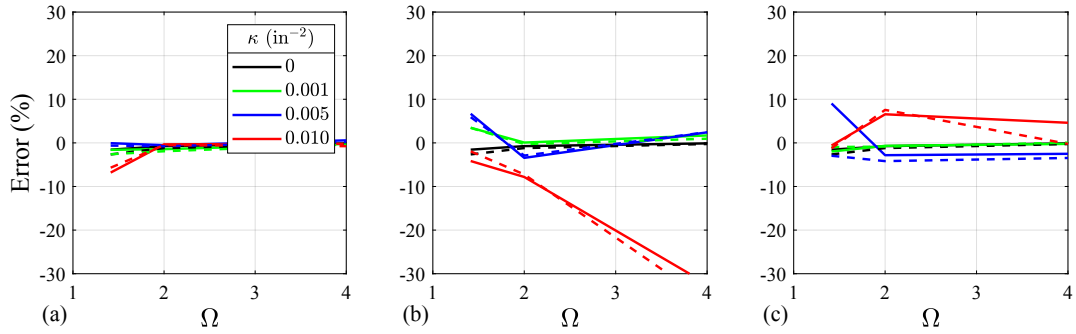

Figure 4.34: Relative RMS prediction error (RMSPE) of isolated mass total acceleration for the nonlinear reduced order model using 1 mode and Method 1 (——) or 2 (- - -), with $\mu = 0.3$ under (a) 1, (b) 2, and (c) 3 $\times$ El Centro.

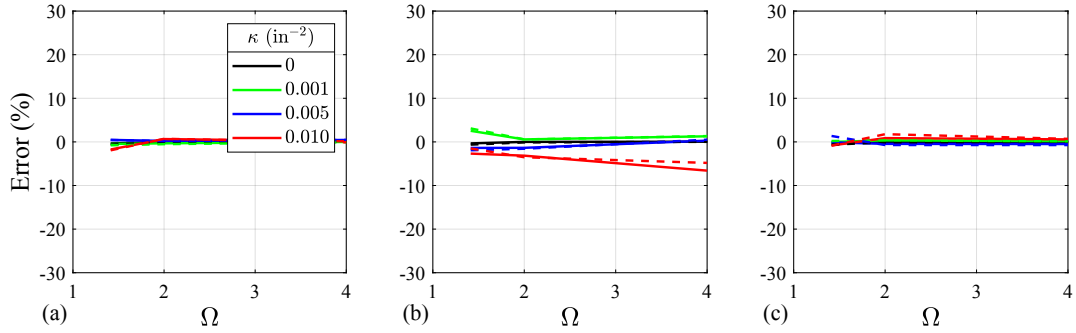

Figure 4.35: Relative RMS prediction error (RMSPE) of isolated mass total acceleration for the nonlinear reduced order model using 2 modes and Method 1 (——) or 2 (- - -), with $\mu = 0.3$ under (a) 1, (b) 2, and (c) 3 $\times$ El Centro.

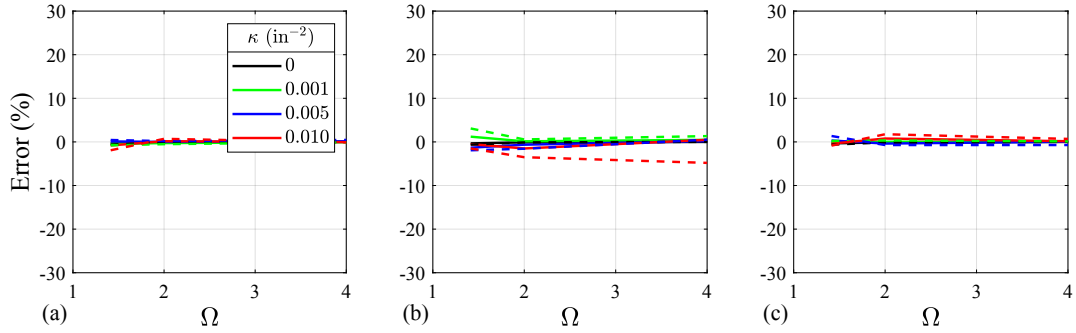

Figure 4.36: Relative RMS prediction error (RMSPE) of isolated mass total acceleration for the nonlinear reduced order model using 3 modes and Method 1 (——) or 2 (- - -), with $\mu = 0.3$ under (a) 1, (b) 2, and (c) 3 $\times$ El Centro.

4.6 Steady-State Response under Frequency-Dependent Harmonic Excitation

In this section, a frequency-dependent harmonic excitation is considered. The harmonic balance method is applied to find the steady-state response of the reduced coupled system.

4.6.1 Harmonic Balance Method

Consider a harmonic base excitation of the form

$$\ddot{u}_{\mathrm{g}}(t) = a_c(\omega)\cos\omega t + a_s(\omega)\sin\omega t \tag{4.14}$$

where ω is the ground-motion frequency, and $a_c(\omega)$ and $a_s(\omega)$ are the frequency-dependent acceleration amplitudes of the cosine and sine components, respectively. Substitution into Eq. (4.8) gives

$$\boldsymbol{\mathcal{M}}\ddot{\mathbf{z}}(t) + \boldsymbol{C}\dot{\mathbf{z}}(t) + \boldsymbol{\mathcal{K}}_L\mathbf{z}(t) + \boldsymbol{\mathcal{K}}_N\mathbf{z}(t)^{\circ 3} = -\boldsymbol{\mathcal{R}}(a_c(\omega)\cos\omega t + a_s(\omega)\sin\omega t). \tag{4.15}$$

Consider the solution of the following form as the basis for the steady-state responses:

$$\mathbf{z}(t) = \mathbf{A}_c\cos\omega t + \mathbf{A}_s\sin\omega t \tag{4.16}$$

where $\mathbf{A}_c$ and $\mathbf{A}_s$ are the vectors of displacement amplitudes. Upon substitution of the assumed solution into the equation of motion (Eq. (4.15)), a system of equations in the unknown coefficients $\mathbf{A}_c$ and $\mathbf{A}_s$ is recovered, abstractly given by

$$\boldsymbol{f}(\mathbf{A}_c, \mathbf{A}_s, a_c, a_s, \omega) = \mathbf{0}. \tag{4.17}$$

The system equation (Eq. (4.17)) is satisfied in a weak sense if

$$\mathbf{0} = \langle\psi, \boldsymbol{f}\rangle \equiv \frac{\omega}{2\pi}\int_0^{2\pi/\omega} \psi(t)\,\boldsymbol{f}\,\mathrm{d}t \tag{4.18}$$

for every real basis function $\psi(t) = \cos\omega t$ and $\sin\omega t$. This is equivalent to applying the

harmonic balance method to Eq. (4.15), assuming the steady-state responses of the form presented in Eq. (4.16) and neglecting the higher order harmonic terms (i.e., $\cos 3\omega t$ and $\sin 3\omega t$). Therefore, applying Eq. (4.18) gives

$$-\boldsymbol{\mathcal{M}}\mathbf{A}_c\omega^2 + \boldsymbol{\mathcal{C}}\mathbf{A}_s\omega + \boldsymbol{\mathcal{K}}_L\mathbf{A}_c + \frac{3}{4}\boldsymbol{\mathcal{K}}_N(\mathbf{A}_c^{\circ 3} + \mathbf{A}_c \circ \mathbf{A}_s^{\circ 2}) = -\boldsymbol{\mathcal{R}}a_c(\omega) \tag{4.19a}$$

$$-\boldsymbol{\mathcal{M}}\mathbf{A}_s\omega^2 - \boldsymbol{\mathcal{C}}\mathbf{A}_c\omega + \boldsymbol{\mathcal{K}}_L\mathbf{A}_s + \frac{3}{4}\boldsymbol{\mathcal{K}}_N(\mathbf{A}_c^{\circ 2} \circ \mathbf{A}_s + \mathbf{A}_s^{\circ 3}) = -\boldsymbol{\mathcal{R}}a_s(\omega). \tag{4.19b}$$

where "$\circ$" indicates the element-wise product and $(\cdot)^{\circ n}$ indicates the element-wise nth power. This nonlinear system of equations should be solved for $\mathbf{A}_c$ and $\mathbf{A}_s$ for a particular ground-motion frequency ω.

Once the coefficients $\mathbf{A}_c$ and $\mathbf{A}_s$ have been solved for, response quantities of interest are found. Of interest here are the lateral displacements (or drifts) in each floor of the primary structure and the total accelerations sustained by the isolated equipment. Substituting the coefficients $\mathbf{A}_c$ and $\mathbf{A}_s$ into Eq. (4.16), the modal coordinates $\boldsymbol{\eta}(t)$ and relative displacements $\mathbf{d}(t)$ of the isolated system are recovered, which must then be transformed to find the response quantities of interest. The responses of all DOFs in the primary structure are recovered using the reduced modal matrix $\boldsymbol{\Phi}_r$ as follows:

$$\mathbf{q}(t) = [\boldsymbol{\Phi}_r \;\; \mathbf{0}]\,(\mathbf{A}_c \cos\omega t + \mathbf{A}_s \sin\omega t). \tag{4.20}$$

The desired drifts are found by selecting the appropriate DOFs from $\mathbf{q}(t)$:

$$\boldsymbol{\Delta}(t) = \mathbf{S}\,[\boldsymbol{\Phi}_r \;\; \mathbf{0}]\,(\mathbf{A}_c \cos\omega t + \mathbf{A}_s \sin\omega t) \tag{4.21}$$

where the matrix $\mathbf{S}$ serves to select the desired DOFs. The total acceleration responses of the isolated masses are given by

$$\boldsymbol{a}_{\text{total}}(t) = -\omega^2[\mathbf{P}^{\mathrm{T}}\boldsymbol{\Phi}_r \;\; \mathbf{I}]\,(\mathbf{A}_c \cos\omega t + \mathbf{A}_s \sin\omega t) + \mathbf{P}^{\mathrm{T}}\boldsymbol{\iota}\,(a_c(\omega)\cos\omega t + a_s(\omega)\sin\omega t). \tag{4.22}$$

Eqs. (4.21) and (4.22) represent the steady-state time-varying responses, but peak

responses are of interest here. Displacement and acceleration *amplitudes* are found by taking the (element-wise) square root of the sum of the squared coefficients of $\cos \omega t$ and $\sin \omega t$ from Eqs. (4.21) and (4.22), respectively.

4.6.2 Specific Forms for $a_c(\omega)$ and $a_s(\omega)$

In the preceding development, no specific form was assumed for the ground motion coefficients $a_c(\omega)$ and $a_s(\omega)$. The most simple form would be *white noise*, which is frequency independent: $a_c(\omega) = a_c$ and $a_s(\omega) = a_s$ for all frequencies ω. The most general form would allow the coefficients to independently vary with ω. Alternatively, the coefficients can vary with ω, but in a consistent fashion:

$$a_c(\omega) = H(\omega)a_c \quad \text{and} \quad a_s(\omega) = H(\omega)a_s$$

where $H(\omega)$ represents the ground motion spectrum. Note that white noise is the degenerate case for which $H(\omega) = 1$. A more informative spectrum commonly used in earthquake engineering is the Kanai-Tajimi (KT) acceleration spectrum (Kanai, 1957; Tajimi, 1960):

$$H_{KT}(\omega) = G_0 \frac{1 + 2\xi_g(\omega/\omega_g)\mathrm{i}}{[1 - (\omega/\omega_g)^2] + 2\xi_g(\omega/\omega_g)\mathrm{i}} \tag{4.23}$$

where ω_g and ξ_g are the natural frequency and the critical damping ratio of the soil layer, G_0 is a scale factor (taken to be unity in this study), and $\mathrm{i} = \sqrt{-1}$.

In the numerical analysis to follow, the KT spectrum will be used. The peak ground acceleration (PGA) and peak ground displacement (PGD) are given by

$$\mathrm{PGA} = H_{KT}(\omega)\sqrt{a_c^2 + a_s^2} \tag{4.24a}$$

$$\mathrm{PGD} = H_{KT}(\omega)\sqrt{a_c^2 + a_s^2}\,/\omega^2 \tag{4.24b}$$

which will be used to normalize responses. Without loss of generality, the cosine and sine coefficients will be taken to be identical (i.e., $a_c = a_s$) in all cases. Therefore, it

will be convenient to define a single variable to represent the excitation amplitude:

$$a \equiv \sqrt{a_c^2 + a_s^2} \qquad \text{(excitation amplitude coefficient).} \tag{4.25}$$

4.6.3 Exploration of Steady-State Responses

In this section, the steady-state responses of the reduced coupled system, presented in Section 4.3, using Method 1 (as described in Section 4.2.3) are assessed. In order to obtain the steady-state responses, the nonlinear system of Eqs. (4.19) should be solved. These responses are path dependent and there may exists several solutions at each excitation frequency ω, for instance when the system is excited by sweeping up or down in frequency. Moreover, the nonlinear system of Eqs. (4.19) may have unstable solutions, which are not physically realizable. These unstable responses are shown with dashed lines in this chapter; stable solutions are shown with solid lines.

To solve those nonlinear system of equations, `fsolve` in MATLAB is employed, which uses the trust-region dogleg algorithm. This algorithm can handle when the Jacobian matrix is singular or the starting solution is far from the true solution. Because `fsolve` uses an iterative procedure to solve the nonlinear system of equations (Eq. (4.19)), an initial guess is needed to start the process. For the first run, the sweep-up case, the system of equations are solved for a low frequency (i.e., 0.01 rad/sec). Then, the obtained solution is used as the initial guess for the next larger frequency. Continuing this process with increasing frequency, up to a highest frequency (i.e., 20 rad/sec), results in the sweep-up branch of the solutions. When there is not a neighboring solution for the next higher frequency, `fsolve` fails to converge, and the frequency sweep is terminated. The same process is performed for the sweep-down case, where a high frequency (i.e., 20 rad/sec) is used as the initial frequency and the process is continued from the obtained solution for the next lower frequency until `fsolve` fails to converge or the lowest frequency is reached, resulted in the sweep-down branch. When the sys-

tem is linear, the sweep-up and sweep-down branches are the same. However, when the system is nonlinear, these two (stable) branches may be different due to the existence of unstable branches (connecting the stable branches). Solving that system of equations for unstable branches is nontrivial, requiring an initial guess that leads the algorithm to a solution on an unstable branch. To do this, a combination (average) of end point solutions, which are obtained from the stable branches, are used as the initial guess for the middle frequency between the two stable branches. Once the first solution on the unstable branch is obtained, a process similar to sweep-up and sweep-down cases can be applied to populate the entire unstable branch.

In this chapter various frequency ratios ($\Omega = \sqrt{2}$, 2, and 4), mass ratios (μ = 0.05, 0.10, 0.15, 0.20, 0.25, and 0.30), and nonlinearity parameter (κ = 0, 0.001, 0.005 and 0.01 in.$^{-2}$) under white noise and Kanai-Tajimi excitations with various excitation amplitude coefficients a are considered. The results are presented in the form of transmissibility curves (input-to-output relationships) for varying excitation frequency ($\omega \in [1, 12]$ rad/s). The peak total acceleration of the isolated mass, denoted $\max|a_{\text{total}}|$, is normalized by the peak ground acceleration:

$$\text{TR}_{a_{\text{total}}} = \frac{\max|a_{\text{total}}|}{H_{KT}(\omega)\, a} \qquad \text{(equipment acceleration transmissibility).} \tag{4.26}$$

The peak roof displacement, denoted $\max|\Delta_{\text{roof}}|$, is normalized by the peak ground displacement:

$$\text{TR}_{\Delta_{\text{roof}}} = \frac{\max|\Delta_{\text{roof}}|}{H_{KT}(\omega)\, a/\omega^2} \qquad \text{(roof displacement transmissibility).} \tag{4.27}$$

The roof displacement transmissibility for the uncoupled case is also presented to emphasize the coupling effect.

In the following subsections, the effect of varying frequency ratio Ω (Section 4.6.3(a)), mass ratio μ (Section 4.6.3(b)), nonlinearity parameter κ (Section 4.6.3(c)),

and excitation amplitude coefficient a (Section 4.6.3(d)) on the two responses of interest (i.e., the displacement of the roof and the total acceleration of the isolated mass) is analyzed. An exhaustive compilation of results, considering all parametric combinations, is presented in Appendix B, and selected representative results are presented in the following subsections for the purpose of demonstrating the key observations and findings. The white noise and Kanai-Tajimi excitations produce similar responses while Kanai-Tajimi excitation produces higher amplitude near the peak of Kanai-Tajimi spectrum. Therefore, in this section, only the steady-state responses under Kanai-Tajimi excitation are presented and similar conclusions can be drawn under white noise excitation.

4.6.3(a) Effect of Varying Frequency Ratio Ω

The effect of varying frequency ratio $\Omega = \sqrt{2}$, 2, and 4, for constant mass ratio μ, nonlinearity parameter κ, and excitation amplitude coeffficient a, is assessed through nonlinear transmissibility curves (presented in full in Appendix B.1). Representative cases ($\kappa = 0$ and 0.005 in.$^{-2}$, $\mu = 0.3$, $a = 1.414\ g$) are presented in Figure 4.37 for the roof displacement and in Figure 4.38 for the isolated mass total acceleration.

Figures 4.37(a) and (b) present the normalized transfer function of the roof displacement for $\kappa = 0$ (i.e., linear) and 0.005 in.$^{-2}$, respectively. As can be seen, considering the coupling effect results in shifting of the primary structure resonant frequency to a slightly larger frequency. The displacement amplitude associated with the resonant frequency decreases as the frequency ratio decreases. As the frequency ratio gets closer to one (i.e., from isolation behavior toward vibration absorber behavior), the shifting of the primary structure resonant frequency toward higher frequencies increases and the amplitude at the secondary system resonant frequency, which happens in different frequencies, increases. As the frequency ratio Ω increases (i.e., more rigid connection of the secondary mass), the transfer function converges to the transfer function of the

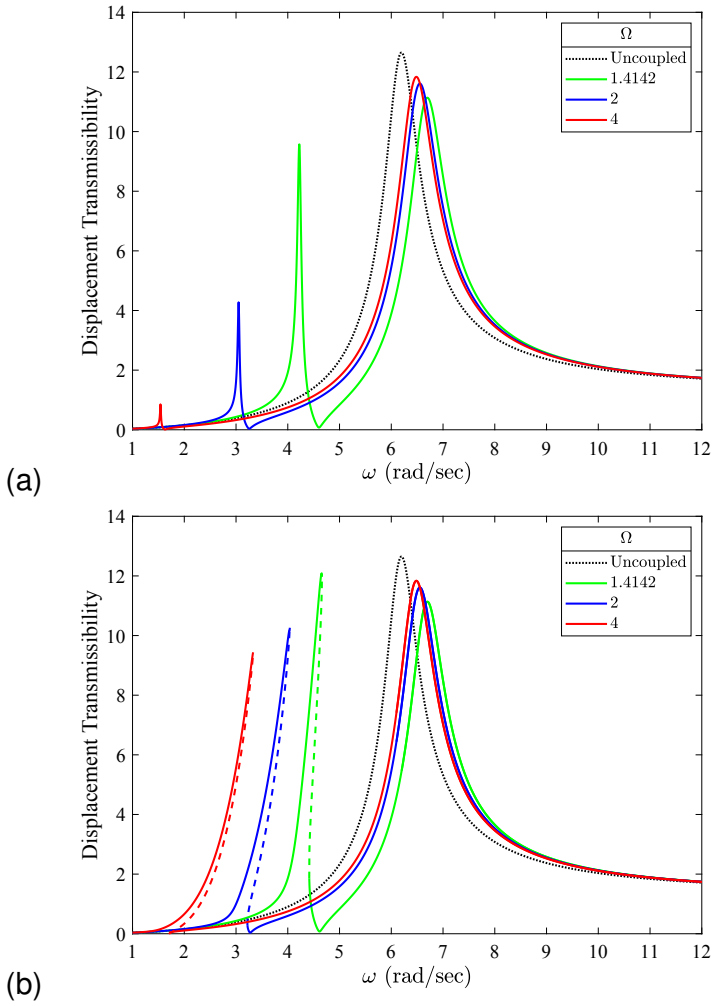

Figure 4.37: Effect of frequency ratio Ω on nonlinear transmissibility $TR_{\Delta_{roof}}$ of the roof displacement, for κ = (a) 0 and (b) 0.005 in.$^{-2}$, $\mu = 0.3$, $a = 1.414\ g$.

uncoupled structure. It is observed that the nonlinearity has almost no effect on the primary structure resonant frequency and the associated amplitude. However, the secondary system resonant frequency skews toward higher frequencies as the nonlinearity increases. In addition, the secondary system resonant amplitude increases with increasing nonlinearity.

The effect of varying frequency ratio Ω on the isolated mass total acceleration is assessed and the case of $\kappa = 0.005$ in.$^{-2}$ is presented in Figure 4.38. As the frequency ratio decreases, the resonant frequency shifts toward higher frequency (i.e., closer to

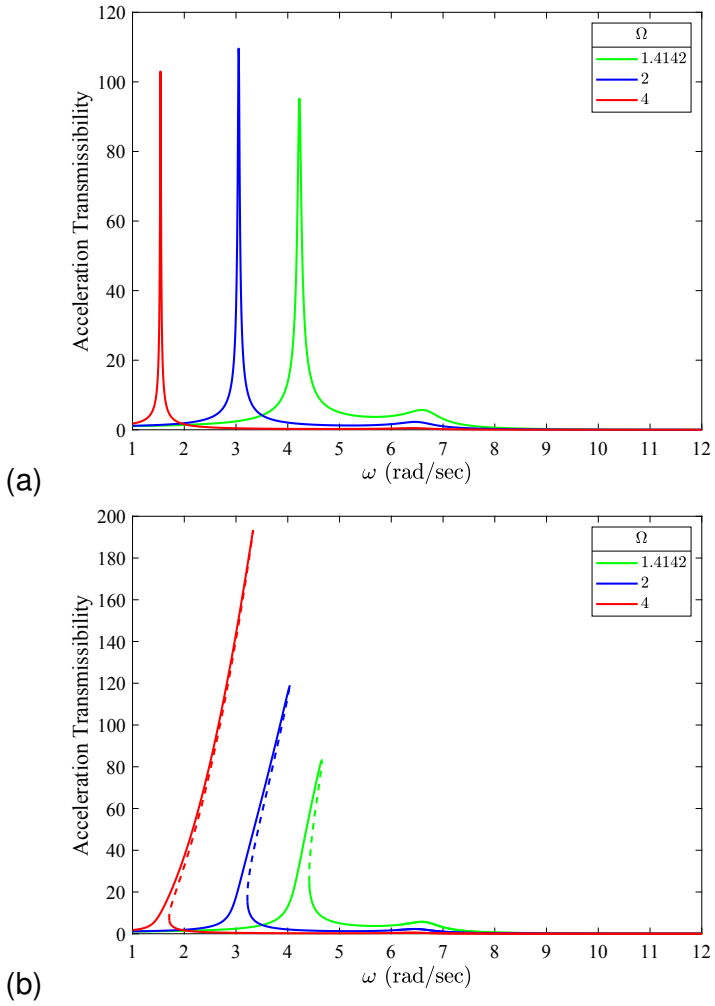

Figure 4.38: Effect of frequency ratio Ω on nonlinear transmissibility $TR_{a_{total}}$ of the isolated mass total acceleration, for κ = (a) 0 and (b) 0.005 $in.^{-2}$, $\mu = 0.3$, $a = 1.414\ g$.

the primary structure's natural frequency). The effect of varying frequency ratio on the resonant frequency amplitude of the isolated mass total acceleration changes for different level of nonlinearity. For the linear case, as the frequency ratio increases, the amplitude at the resonant frequency increases and then decreases. However, when the nonlinearity presents in the model, the amplitude at the resonant frequency increases as the frequency ratio increases.

4.6.3(b) Effect of Varying Mass Ratio μ

The effect of varying mass ratio μ = 0.05, 0.1, 0.15, 0.2, 0.25, and 0.3, for constant frequency ratio Ω, nonlinearity parameter κ, and excitation amplitude coefficient a, is assessed through nonlinear transmissibility curves (presented in full in Appendix B.2). Representative cases (κ = 0 and 0.005 in.$^{-2}$, Ω = 2, a = 1.414 g) are presented in Figure 4.39 for the roof displacement and in Figure 4.40 for the isolated mass total acceleration.

As can be seen from Figure 4.39 for the roof displacement, increasing the mass ratio μ shifts the primary structure resonant frequency to higher frequency (i.e., due to relatively less primary structure mass). Moreover, the amplitude at the primary structure resonant frequency decreases as the mass ratio increases. The amount of shift in the frequency decreases by increasing the frequency ratio (toward more isolation). The secondary system resonant frequency decreases by increasing mass ratio, while the amplitude at the secondary system resonant frequency increases as the mass ratio increases.

The effect of varying mass ratio μ on the transfer function of the isolated mass total acceleration is assessed in Figure 4.40 for the representative cases (κ = 0 and 0.005 in.$^{-2}$, Ω = 2, a = 1.414 g). As can be seen from Figure 4.40, as the mass ratio increases both the resonant frequency and its corresponding amplitude decrease. This effect reduces as the frequency ratio increases. As the nonlinearity increases the peak total acceleration skews toward higher frequencies, as expected with a hardening nonlinearity. The amplitude of the transmissibility at the resonant frequency increases and then decreases as the nonlinearity increases for low mass ratio and high frequency ratio. However, as the mass ratio increases and the frequency ratio decreases, this trend changes. For high mass ratio and low frequency ratio, the amplitude of transmissibility at the resonant frequency decreases as the nonlinearity increases.

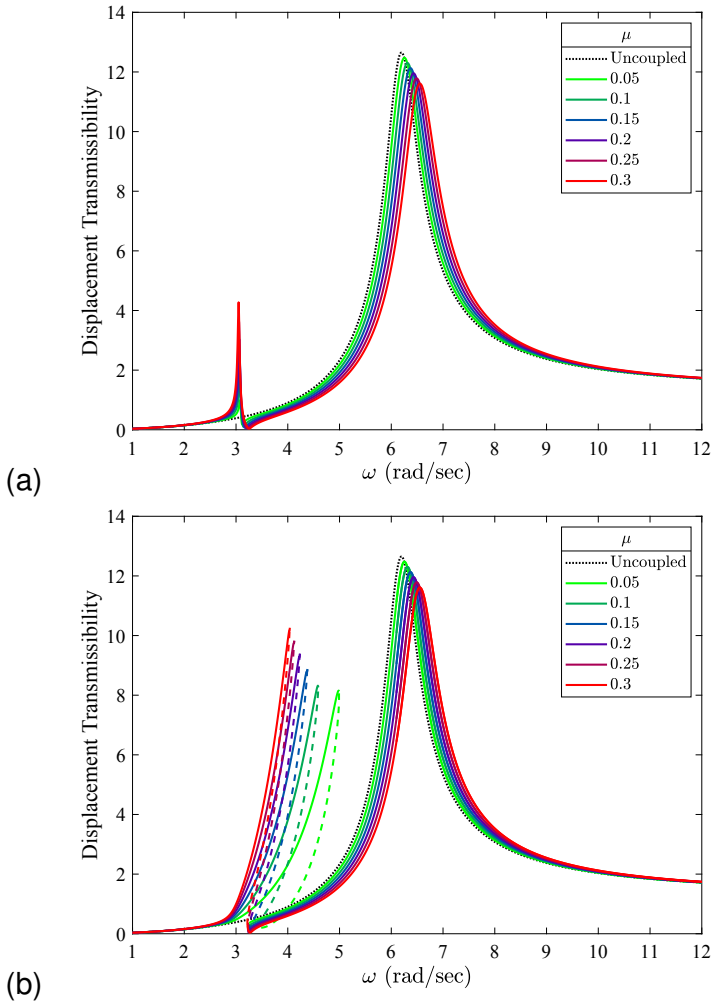

Figure 4.39: Effect of mass ratio μ on nonlinear transmissibility $\mathrm{TR}_{\Delta_{\mathrm{roof}}}$ of the roof displacement, for $\Omega = 2$, κ = (a) 0 and (b) 0.005 in.$^{-2}$, $a = 1.414\ g$.

4.6.3(c) Effect of Varying Nonlinearity Parameter κ

The effect of varying the nonlinearity parameter $\kappa = 0$, 0.001, 0.005, and 0.01 in.$^{-2}$, for constant frequency ratio Ω, mass ratio μ, and excitation amplitude coefficient a, is assessed through nonlinear transmissibility curves (presented in full in Appendix B.3). Representative cases ($\Omega = 2$, $\mu = 0.3$, $a = 1.414\ g$) are presented in Figure 4.41 for the roof displacement and in Figure 4.42 for the isolated mass total acceleration.

As shown in Figure 4.41 and discusses previously, considering the coupling effect shifts the primary structure resonant frequency toward higher frequency and at the same

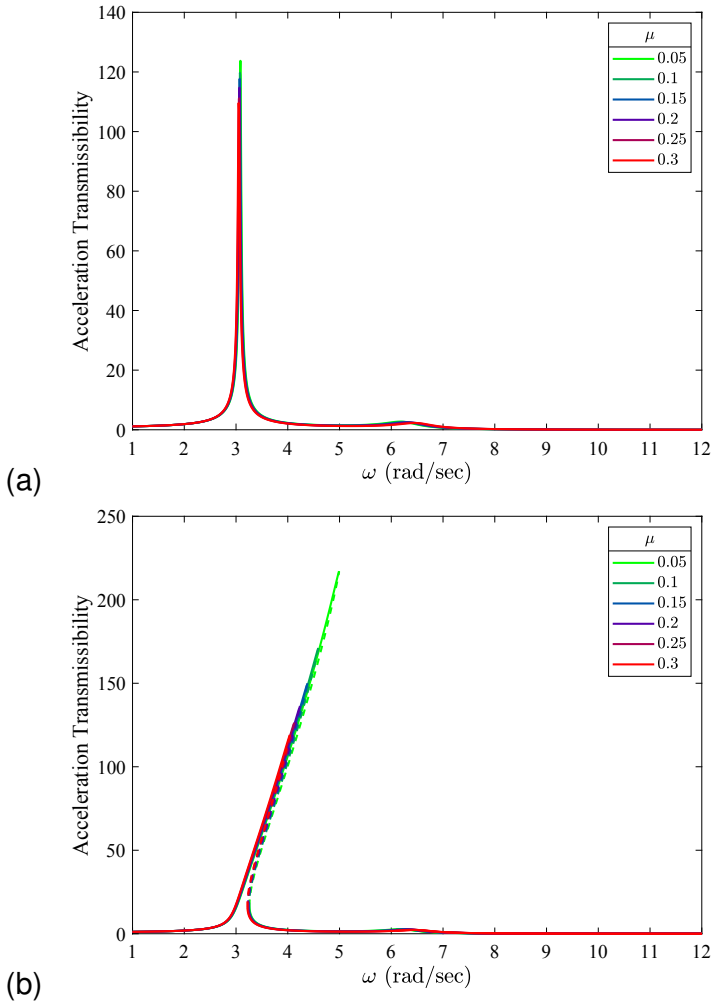

Figure 4.40: Effect of mass ratio μ on nonlinear transmissibility $\mathrm{TR}_{a_{\mathrm{total}}}$ of the isolated mass total acceleration, for $\Omega = 2$, κ = (a) 0 and (b) 0.005 in.$^{-2}$, $a = 1.414\ g$.

time decreases the amplitude at the primary structure resonant frequency. The primary structure resonant frequency and its amplitude do not change with increasing nonlinearity. The secondary system resonant frequency shifts toward higher frequency by increasing nonlinearity and its associated amplitude increases.

The effect of varying κ on the isolated mass total acceleration is demonstrated in Figure 4.42. As can be seen from this figure, as the nonlinearity increases the resonant frequency increases and its corresponding amplitude first increases (for $\kappa = 0 \rightarrow 0.001 \rightarrow 0.005$ in.$^{-2}$) and then decrease (for $\kappa = 0.005 \rightarrow 0.01$ in.$^{-2}$). Similar trend is

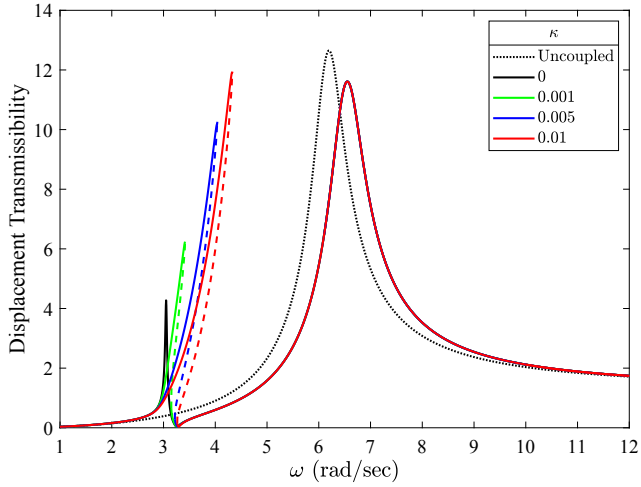

Figure 4.41: Effect of nonlinearity parameter κ [in.$^{-2}$] on nonlinear transmissibility $\mathrm{TR}_{\Delta_{\mathrm{roof}}}$ of the roof displacement, for $\Omega = 2$, $\mu = 0.3$, $a = 1.414\ g$.

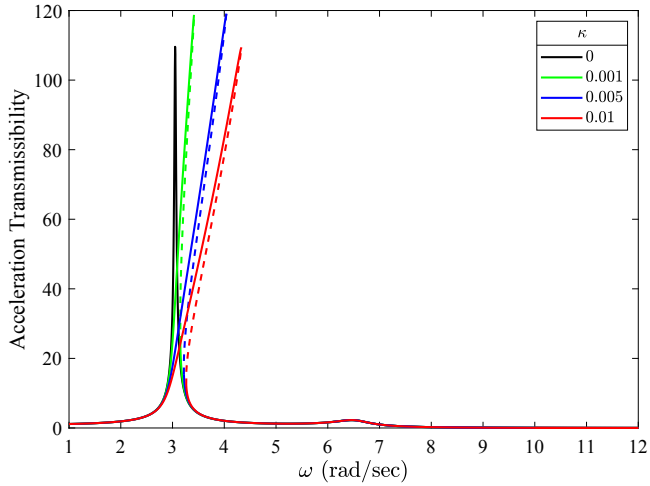

Figure 4.42: Effect of nonlinearity parameter κ [in.$^{-2}$] on nonlinear transmissibility $\mathrm{TR}_{a_{\mathrm{total}}}$ of the isolated mass total acceleration, for $\Omega = 2$, $\mu = 0.3$, $a = 1.414\ g$.

observed for $\Omega = 4$; however, for the case of $\Omega = \sqrt{2}$, as the nonlinearity increases the resonant frequency increases while its corresponding amplitude decreases.

4.6.3(d) Effect of Varying Excitation Amplitude Coefficient a

The effect of varying excitation amplitude coefficient $a = 0.1414,\ 0.2828,\ 0.4243,\ 0.5657,\ 0.7071,\ 0.8485,\ 0.9999,\ 1.1314,\ 1.2728,\ 1.4142,\ 2.8284,\ 5.6569,\ 8.4853,\ 11.3137$, and $14.1421\ g$, for constant frequency ratio Ω, mass ratio μ, and nonlinearity

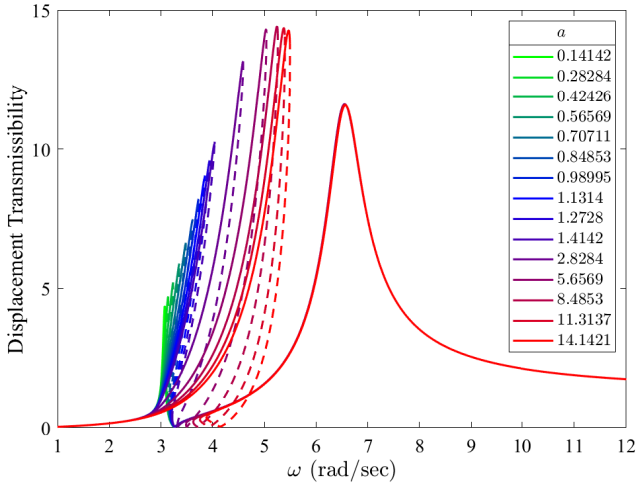

Figure 4.43: Effect of excitation amplitude coefficient a [g] on nonlinear transmissibility $\mathrm{TR}_{\Delta_{\mathrm{roof}}}$ of the roof displacement, for $\Omega = 2$, $\mu = 0.3$, $\kappa = 0.005$ in.$^{-2}$.

parameter κ, is assessed through nonlinear transmissibility curves (presented in full in Appendix B.4). Representative cases ($\Omega = 2$, $\mu = 0.3$, $\kappa = 0.005$ in.$^{-2}$) are presented in Figure 4.43 for the roof displacement and in Figure 4.44 for the isolated mass total acceleration. The linear case ($\kappa = 0$ in.$^{-2}$) is not shown because its normalized response is independent of a.

As shown in Figure 4.43 for the roof displacement, increasing the excitation amplitude a shifts the secondary system resonant frequency toward higher frequency and amplify its associated amplitude. This is due to the cubic hardening nonlinearity in the system, as the amplitude increases the stiffness increases in a cubic order.

The effect of varying excitation amplitude coefficient a on the isolated mass total acceleration is demonstrated in Figure 4.44. As can be seen from this figure, as the excitation amplitude coefficient increases the resonant frequency increases and the corresponding amplitude at the resonant frequency increases and then decreases. This trend changes when the frequency ratio decreases. For the case of low frequency ratio, as the excitation amplitude coefficient increases the resonant frequency increases and its corresponding amplitude decreases.

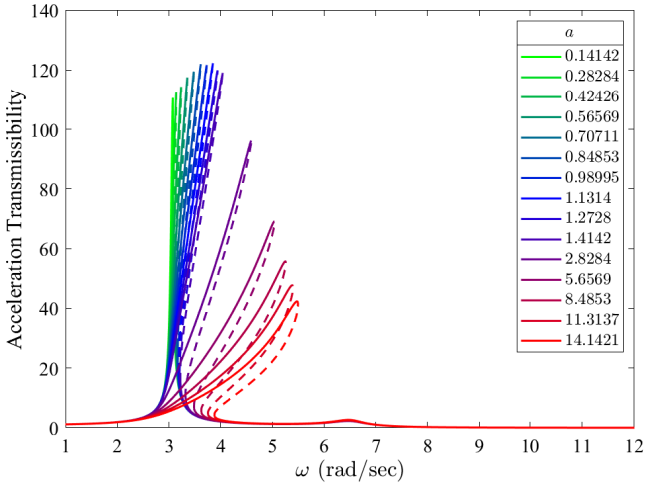

Figure 4.44: Effect of excitation amplitude coefficient a [g] on nonlinear transmissibility $\mathrm{TR}_{a_{\mathrm{total}}}$ of the isolated mass total acceleration, for $\Omega = 2$, $\mu = 0.3$, $\kappa = 0.005$ in.$^{-2}$.

4.7 Conclusions

This chapter presents a new reduced order modeling method and its application on the assessment of the feasibility of a dual-mode vibration isolator/absorber. The methodology is described first by coupling the nonlinear equation of motion for the attachment (i.e., isolated mass), with cubic hardening nonlinearity, with the linear equation of motion of the primary structure. The isolated mass is actually a partial mass of the full model, which is isolated from the main full model by a secondary isolation system with cubic hardening nonlinearity. The part related to the linear primary full coupled model is reduced using the modal properties of either the full uncoupled model for the full primary structure (full uncoupled model minus the isolated mass). These two nonlinear reduced order models (NLROMs) are applied to a 3-story structure from the SAC project and their accuracy are evaluated by imposing the El Centro ground motion with different amplitudes. The NLROM using the modal properties of the full uncoupled model (Method 1) exhibits better robustness and performance according to the assessed metrics.

The NLROM is then used to assess the feasibility of achieving a dual-mode vibra-

tion isolator/absorber. The objective of this dual-mode system is to protect the secondary system (i.e., equipment) under low amplitude seismic motion and protect the primary structure under high amplitude seismic motion. This assessment is performed by developing the steady-state responses for various excitation frequency to obtain the nonlinear transmissibility curves for the roof displacement which represents the primary structure response and the isolated mass total acceleration. These transmissibility curves are obtained by solving the nonlinear projections of the responses to the harmonic bases (i.e., equivalent to the harmonic balanced method). Then, these nonlinear equations are solved in MATLAB to get these transmissibility curves. White noise and Kanai-Tajimi excitations are used as the input motion to excite the system. These two excitations provide similar responses, while Kanai-Tajimi provides higher amplitude responses at the spectrum peak. The effect of varying several parameters are assessed, namely frequency ratio, mass ratio, excitation amplitude coefficient, and nonlinearity parameter.

The assessment reveals that reducing both the primary and secondary structural responses cannot be achieved with the considered parameters and the reduction of one usually comes at the expense of increasing the other one. However, the results obtained from El Centro excitation for frequency ratios closer to unity (i.e., closer design to vibration absorber) indicates the possibility of reducing the primary structural responses by increasing the excitation amplitude compared with the uncoupled case.

The reduced order modeling method introduced in this chapter is limited to a special case of a linear elastic structure with nonlinear elastic attachments. In order to extend the concept to a more general class of nonlinear inelastic structures, the technique needs to be extended for structures with hysteresis behavior. This is the focus of the following chapter on inelastic model condensation.

Chapter 5
Inelastic Model Condensation

5.1 Overview

In this chapter, a new condensation method in conjunction with a framework for application is proposed for condensation of inelastic dynamic structural models, by using the modal properties and replacing the elastic restoring forces with the hysteretic forces. In the following, the inelastic model condensation (IMC) procedure to construct the linear condensed model is first described. Next, the procedure to extend the linear condensed model with hysteretic (Bouc–Wen) elements is presented and the optimal values of the hysteretic parameters are obtained using the Levenberg–Marquardt algorithm for several types of loading regimes. Next, the resulting inelastic condensed models with parameters fit with those different regimes are evaluated by imposing a real earthquake to both the nonlinear finite element model (NFEM) and the condensed model. Finally, the chapter concludes with a discussion of the results and highlights the performance of the proposed IMC approach.

5.2 Inelastic Condensed Dynamic Modeling Procedure

In the reduced-order modeling method presented here, the reduced linear model is derived to match the natural frequencies and mode-shapes of the *full* model at selected modes. The coordinates of the *condensed* model correspond to the selected coordinates of the full model. Then, the elastic restoring forces of the linear condensed model are

simply replaced by hysteretic forces. The hysteretic forces are evolutionary (Park et al., 1986) and are calibrated to match the inelastic behavior of the detailed inelastic frame (*NFEM*) model. Importantly, the number of hysteretic variables need not be larger than the number of condensed coordinates and time-varying (or 'nonlinear') modes are not involved.

5.2.1 Full Model

Consider a planar frame (structure) subject to horizontal ground motion $\ddot{u}_g(t)$. The set of linear equations that define the n-DOF structural system is given by:

$$\mathbf{M}\ddot{\mathbf{q}} + \mathbf{C}\dot{\mathbf{q}} + \mathbf{K}\mathbf{q} = -\mathbf{M}\boldsymbol{\iota}\ddot{u}_g \tag{5.1}$$

where $\mathbf{q}$ is the n-dimensional vector of DOFs, which may include lateral displacements, vertical displacements, and rotations; $\mathbf{M}$, $\mathbf{C}$, and $\mathbf{K}$ are the $n \times n$ mass, damping, and (linear-elastic) stiffness matrices, respectively; and $\boldsymbol{\iota}$ is the n-dimensional influence vector that applies $\ddot{u}_g$ to the lateral nodal displacements.

5.2.2 Condensed Model

First, the full model (Eq. (5.1)) is reduced to a *condensed* model with fewer DOFs, say r DOFs, using the *mass orthonormal* mode shapes found from the full model, $\boldsymbol{\Phi} = [\boldsymbol{\phi}_1, \ldots, \boldsymbol{\phi}_n]$. The mode shapes $\boldsymbol{\phi}_i$ should be sorted by the absolute value of the modal participation factors $\Gamma_i \equiv \boldsymbol{\phi}_i^{\mathrm{T}}\mathbf{M}\boldsymbol{\iota}$ (or equivalently the modal participating mass ratio), as opposed to sorting based on the frequency (lowest to highest), to emphasize the highest contributing modes to the seismic response.

Let $\mathbf{S} \in \mathbb{R}^{r\times n}$ be the *selection matrix* that specifies the DOFs to be retained, denoted $\mathbf{u} \subset \mathbf{q}$; i.e., $\mathbf{u} = \mathbf{S}\mathbf{q}$. Generally, the retained coordinates $\mathbf{u}$ can be taken to be any set of r DOFs. However, in order to introduce the nonlinear behavior in the present application, only horizontal floor displacements should be selected, at most one per floor. In this chapter, all the stories are included, though this need not be the case in general.

The mode shapes in the retained DOFs are defined as $\boldsymbol{\psi}_i = \mathbf{S}\boldsymbol{\phi}_i$ ($i = 1, \ldots, r$). Now, the reduced model is reconstructed directly from the reduced selected mode shapes. That is:

$$\boldsymbol{\Psi}^{\mathrm{T}}\boldsymbol{\mathcal{M}}\boldsymbol{\Psi} = \mathbf{I}_{r\times r}, \quad \boldsymbol{\Psi}^{\mathrm{T}}\boldsymbol{C}\boldsymbol{\Psi} = \mathbf{diag}(2\zeta_1\omega_1, \ldots, 2\zeta_r\omega_r), \quad \boldsymbol{\Psi}^{\mathrm{T}}\boldsymbol{\mathcal{K}}\boldsymbol{\Psi} = \mathbf{diag}(\omega_1^2, \ldots, \omega_r^2) \tag{5.2}$$

where $\boldsymbol{\mathcal{M}}$, $\boldsymbol{C}$, and $\boldsymbol{\mathcal{K}}$ are the reduced mass, damping, and stiffness matrices; the square matrix $\boldsymbol{\Psi} = [\boldsymbol{\psi}_1, \ldots, \boldsymbol{\psi}_r]$; and ω_i and ζ_i are the natural frequency and damping ratio in the ith mode of the full model. Then, the reduced model may be written as:

$$\boldsymbol{\mathcal{M}}\ddot{\mathbf{u}} + \boldsymbol{C}\dot{\mathbf{u}} + \boldsymbol{\mathcal{K}}\mathbf{u} = -\mathbf{R}\ddot{u}_{\mathrm{g}} \tag{5.3}$$

where $\boldsymbol{\Psi}^{\mathrm{T}}\mathbf{R} = [\Gamma_1, \ldots, \Gamma_r]$.

Unlike some reduced models that only match the dominant mode of the full model (Gidaris and Taflanidis, 2013), this condensed model (Eq. (5.3)) exactly matches the modal dynamics of the full model at the selected frequencies ($\omega_1, \ldots, \omega_r$). The condensed model can be thought of as a stick model with communication between all the stories, i.e., $\boldsymbol{\mathcal{M}}$, $\boldsymbol{C}$, and $\boldsymbol{\mathcal{K}}$ are fully populated, in general.

5.2.3 Treatment of Hysteresis

Inelastic restoring forces are then incorporated into the condensed model (Eq. (5.3)) by replacing the inter-story forces with inelastic restoring forces. The lateral deflections $\mathbf{u}$ relative to the ground are related to the inter-story deflections, denoted by $\boldsymbol{\Delta} = [\Delta_1, \ldots, \Delta_r]^{\mathrm{T}}$, through the linear transformation:

$$\mathbf{u} = \mathbf{L}\boldsymbol{\Delta} \;\Rightarrow \boldsymbol{\Delta} = \mathbf{L}^{-1}\mathbf{u} \tag{5.4}$$

where $\mathbf{L}$ is a r-dimensional lower-triangular matrix of unity. The (elastic) inter-story forces are therefore given by $\mathbf{L}^{\mathrm{T}}\boldsymbol{\mathcal{K}}\mathbf{L}\boldsymbol{\Delta}$. Now, instead of elastic restoring forces, the inter-story shear forces are taken to be:

$$\mathbf{L}^{\mathrm{T}}\mathcal{K}\mathbf{L}\boldsymbol{\Delta} \to \boldsymbol{\kappa}\mathbf{L}^{\mathrm{T}}\mathcal{K}\mathbf{L}\boldsymbol{\Delta} + (\mathbf{I} - \boldsymbol{\kappa})\mathbf{L}^{\mathrm{T}}\mathcal{K}\mathbf{L}\mathbf{z} \tag{5.5}$$

in which $\boldsymbol{\kappa}$ is a diagonal matrix where each element κ_i is the ratio of the post-yield stiffness to pre-yield (elastic) stiffness at the ith story. The auxiliary variables $\mathbf{z} = [z_1, \ldots, z_r]^{\mathrm{T}}$ are the hysteretic displacements, which are given by the Bouc–Wen model (Bouc, 1967; Wen, 1976):

$$\dot{z}_i = \dot{\Delta}_i - \beta_i \left|\dot{\Delta}_i\right| |z_i|^{\eta_i - 1} z_i - \gamma_i \dot{\Delta}_i |z_i|^{\eta_i} \,. \tag{5.6}$$

The uniaxial hysteretic behavior at the ith story is governed by the hysteretic parameters η_i, β_i, and γ_i, independent of the other stories. The parameter η_i governs the smoothness of the transition from the linear to the nonlinear range (Wong et al., 1994), effectively adjusting the 'knee' of the hysteretic loop. The parameters β_i and γ_i govern the isotropic yield displacement $z_{i,\mathrm{yield}}$ in the ith story as follows:

$$z_{i,\mathrm{yield}} = (\beta_i + \gamma_i)^{-\frac{1}{\eta_i}} \,. \tag{5.7}$$

Inversely, if the yield displacement $z_{i,\mathrm{yield}}$ is prescribed, then the hysteretic parameters are:

$$\beta_i = \frac{\rho_i}{z_{i,\mathrm{yield}}^{\eta_i}} \quad \text{and} \quad \gamma_i = \frac{1 - \rho_i}{z_{i,\mathrm{yield}}^{\eta_i}} \tag{5.8}$$

where $0 \le \rho_i \le 1$. By varying ρ_i, the hysteretic loop shape changes, as illustrated in Fig. 5.1. (Note that other simplified hysteretic models could alternatively be used, such as discussed by Gidaris and Taflanidis (2013).)

The hysteretic restoring forces (Eq. (5.5)) are incorporated into the condensed model (Eq. (5.3)) through the coordinate transformation (Eq. (5.4)), giving

$$\mathcal{M}\ddot{\mathbf{u}} + \mathcal{C}\dot{\mathbf{u}} + \tilde{\boldsymbol{\kappa}}\mathcal{K}\mathbf{u} + (\mathbf{I} - \tilde{\boldsymbol{\kappa}})\mathcal{K}\mathbf{L}\mathbf{z} = -\mathbf{R}\ddot{u}_{\mathrm{g}} \tag{5.9}$$

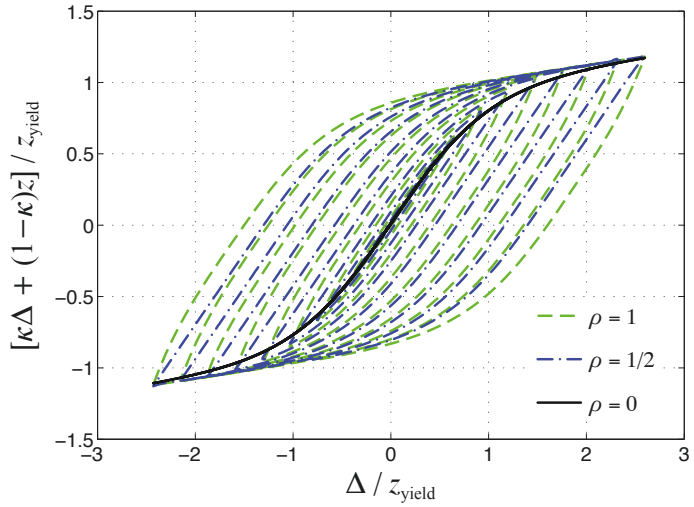

Figure 5.1: Representative hysteresis loops for $\kappa = 0.1$ and $\eta = 2$.

where $\tilde{\boldsymbol{\kappa}} = \mathbf{L}^{-\mathrm{T}}\boldsymbol{\kappa}\mathbf{L}^{\mathrm{T}}$; note that these are the inelastic equations of motion for the lateral displacements relative to the ground.

The mass, damping, and (elastic) stiffness properties of the condensed model are fully specified by the full model, the list of condensed coordinates, and the specified values for modal damping ratios. The inelastic aspects of the condensed model are parameterized by inter-story yield ratios, post-yield stiffness ratios, yielding knee sharpness, and the shape of the hysteretic loops. The inelastic condensed model must be fit to inelastic responses computed from the NFEM by adjusting the inelastic parameters only, to match the dynamic simulations of the NFEM.

5.3 Models for the Structural System Considered

Figure 5.2 shows one of the 2D structural system (frame) considered in this chapter, which is designed as a benchmark for the SAC project for the Los Angeles, California region (Ohtori et al., 2004).

The 9-story (9 above and one below the ground) steel perimeter moment resisting frame has a total height of 134 ft and is expanded in 5 bays of width 30 ft each. The typical story height is 13 ft except for the basement and the first floor, which are 12

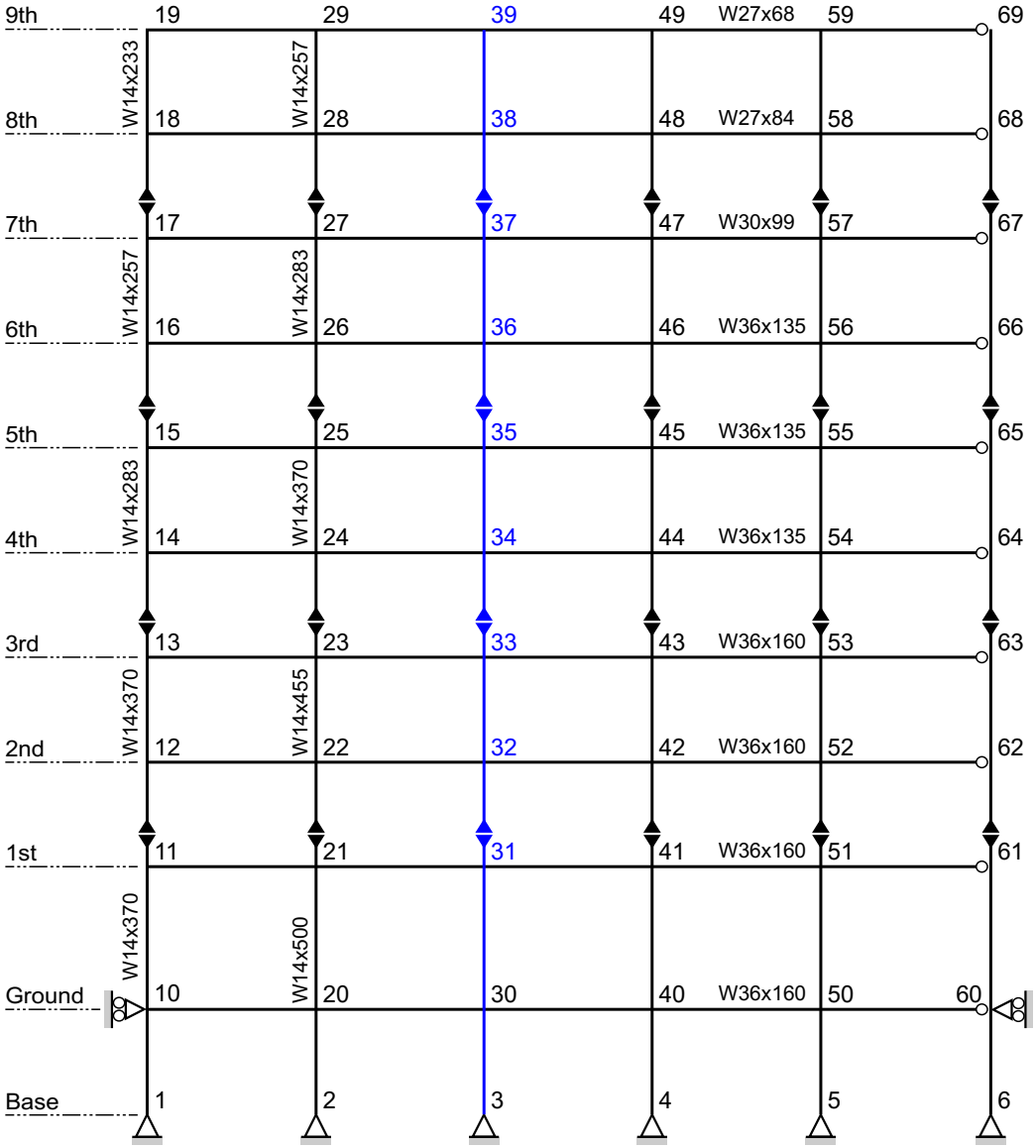

Figure 5.2: Nine-story steel frame (adapted from Ohtori et al. (2004)).

and 18 ft, respectively. The steel member (beam/column) sections and the nodes are labeled in Figure 5.2. The columns are pinned to the based and the structure is laterally restrained at the ground floor elevation. Beam to column connections are moment resisting except for the connections of the beams to the rightest column, which the rotations are released. Column splices located at 6 ft above the centerline of the beams at the first, third, fifth and seventh levels.

The third column from the left, highlighted in blue, is retained in the condensed model. The horizontal responses of nodes 31, 32, 33, 34, 35, 36, 37, 38 and 39 (see Figure 5.2) were selected as the basis of comparison of the models investigated herein. Note that nodes 3 and 30 have zero displacements relative to the ground and are not considered in the condensed model.

5.3.1 Nonlinear Finite Element Model (NFEM)

The NFEM of the 9-story building described here was developed in OpenSees (Mazzoni et al., 2009). The material properties assigned to each element were Young's modulus $E = 29000$ ksi, yield stress $\sigma_{y,c} = 50$ ksi for columns, yield stress $\sigma_{y,b} = 36$ ksi for beams, and 0.002 strain-hardening ratio. Isotropic and kinematic hardening were not included (i.e., $H_{iso} = 0$ and $H_{kin} = 0$).

The beam-column elements that were chosen for this model have a flexibility-based formulation in which the distribution of internal forces satisfy equilibrium exactly, strains and curvatures are computed from the internal forces through the fiber-element discretization of the cross section, and these strains and curvatures are integrated to the nodal displacements of the element using numerical integration. The integration points are based upon the Gauss–Lobatto quadrature rule which states that two integration points are present at the element ends (Mazzoni et al., 2009). Beam-column elements were discretized into fiber elements, which discretize the cross section into sub regions of simpler, regular shapes (e.g., quadrilateral, circular and triangular regions) called "patches". A patch object was constructed with "quad patches" — four vertices define the geometry of the patch. The fiber elements are associated with models for uniaxial material behavior. Deformations of the fibers enforce the Bernoulli beam assumptions (Mazzoni et al., 2009). For stresses that exceed σ_y, the previously-defined strain hardening material was used.

Pushover responses were compared to models with varying numbers of fiber ele-

ments and integration points used for each element. The computed nodal displacements were found to be insensitive to the number of fiber elements used. The displacements were observed to be sensitive to the number of integration points per element when 2 to 6 integration points per element were used, but not for elements with 7 to 10 integration points per element; therefore, 10 integration points per element were selected in order to maintain high accuracy throughout the procedure.

Total floor masses, including the structural elements, are 66.0 kips-s^2/ft for the ground floor, 69.0 kips-s^2/ft for the first floor, 67.7 kips-s^2/ft for second through eighth floors, and for the roof (ninth floor) is 73.2 kips-s^2/ft. The total mass of each floor is lumped at the nodes of that floor. Before performing any transient analyses, the gravity loads are applied first. Damping is added to the NFEM using Rayleigh damping, assuming 2% damping for the first and third modes.

5.3.2 Linear Condensed Frame Model

A linear-elastic frame model given by Eq. (5.1) was constructed by extracting the structural mass (**M**) and stiffness (**K**) matrices from the NFEM in OpenSees. The Rayleigh damping matrix (**C**) was constructed, using the extracted **M** and **K** matrices, assuming 2% damping for the first and third modes to be consistent with the OpenSees model.

The full model was then condensed using the procedure outlined in Section 5.2.2. The retained coordinates were taken to be the horizontal displacements at nodes 31, 32, 33, 34, 35, 36, 37, 38 and 39; i.e.,

$$\mathbf{u} = \mathbf{S}\mathbf{q} = [u_{31}, u_{32}, u_{33}, u_{34}, u_{35}, u_{36}, u_{37}, u_{38}, u_{39}]^{\mathrm{T}} \tag{5.10}$$

The full model has 266 DOFs (82 unconstrained nodes $\times$ 3 DOFs per node, 2 one-constrained nodes $\times$ 2 DOFs per node, 6 two-constrained nodes $\times$ 1 DOFs per node, and 10 additional DOFs) which is reduced to 9 DOFs in the condensed model, corresponding to a 97% reduction in DOFs.

Table 5.1 gives the natural frequencies ($f_i = \omega_i/2\pi$) for the OpenSees, full, and condensed models, which shows excellent agreement. At this stage of the modeling, the condensed model does not incorporate any hysteresis. The selection of the hysteresis parameters is discussed in the next section.

5.4 Fitting of Inelastic Parameters

In order to estimate the hysteretic parameters for the condensed model, the response of the condensed model with variable hysteretic parameters was fit to the response data predicted with the OpenSees NFEM — which is treated as "measured" data. The sum-of-squares error between the OpenSees inter-story drift ratio time-histories in all stories and the condensed model's predictions is minimized over the hysteretic parameters $\boldsymbol{p} = [\kappa, \eta, z_{1,\text{yield}}, z_{2,\text{yield}}, \ldots, z_{9,\text{yield}}]^{\text{T}}$; ρ was fixed at 0.5, and κ and η were kept constant for the entire model.

The OpenSees model "measures" the inter-story drift ratio $\Delta_i(t_j) \div h_i$ $(i = 1, \ldots, 9)$ at times t_j $(j = 1, 2, \ldots, m)$; the corresponding predictions by the condensed model, for a given set of parameters $\boldsymbol{p}$, are denoted $\hat{\Delta}_i(t_j; \boldsymbol{p}) \div h_i$ $\forall i, j$. The minimization problem is posed as follows:

$$\min_{\boldsymbol{p}} \chi^2(\boldsymbol{p}) = \sum_{i=1}^{r} \sum_{j=1}^{m} \left(\frac{1}{w_{ij}} \frac{\Delta_i(t_j) - \hat{\Delta}_i(t_j; \boldsymbol{p})}{h_i} \right)^2 \equiv \sum_{i=1}^{r} (\boldsymbol{\Delta}_i - \hat{\boldsymbol{\Delta}}_i(\boldsymbol{p}))^{\text{T}} \boldsymbol{W}_i (\boldsymbol{\Delta}_i - \hat{\boldsymbol{\Delta}}_i(\boldsymbol{p})) \quad (5.11)$$

where weighting matrices $\boldsymbol{W}_i = \mathbf{diag}(h_i^{-2} w_{ij}^{-2})$. The weights w_{ij} were taken to be:

Table 5.1: Natural frequencies f_i [Hz] for the NFEM in OpenSees, full, and condensed models of the 9-story structure.

	OpenSees	full	condensed
f_1	0.444	0.444	0.444
f_2	1.179	1.179	1.179
f_3	2.049	2.050	2.050
f_4	3.103	3.103	3.103

$$w_{ij} = \sqrt{\frac{m - n_{\mathrm{p}} + 1}{\sum_{i=1}^{r} \boldsymbol{\Delta}_i^{\mathrm{T}} \boldsymbol{\Delta}_i}}$$

where n_{p} is the number of fit parameters.

Any optimization algorithms can be used for this minimization problem. In engineering applications, mathematical or metaheuristic procedures are frequently used (Alberdi and Khandelwal, 2015; Medina and Taflanidis, 2015). In this chapter, the Levenberg–Marquardt algorithm was used to minimize the errors and fit the parameters; the algorithm is briefly described here.

The Levenberg–Marquardt Algorithm (LMA) (Levenberg, 1944; Marquardt, 1963) seeks to minimize χ^2 (Eq. (5.11)) with respect to the parameters $\boldsymbol{p}$, which is carried out iteratively. The goal of each iteration is to find a perturbation $\delta\boldsymbol{p}$ to the parameters $\boldsymbol{p}$ that reduces χ^2. LMA involves a combination of the Gradient Descent Method (GDM) and the Gauss-Newton Algorithm (GNA) (Gavin, 2017). GDM updates the parameter values in the direction opposite to the gradient of the objective function. GNA assumes that the objective function is approximately quadratic in the parameters near the solution and, in general, converges faster than GDM in the vicinity of a minimum. LMA uses a mixture of these methods depending upon the difference between the parameters from their optimal value. If the difference between the parameters and the optimal value is large then the GDM is used; as the difference between the parameters and the optimal value reduces, GNA is used. This algorithm was used in finding the values of the hysteretic parameters used in the model reduction technique for nonlinear inelastic analysis.

5.4.1 Loading Regimes Used to Fit Hysteretic Parameters

To be certain of which type of analysis would be appropriate for identifying the hysteretic parameters, a trial and error method was utilized. Model calibration data sets can

be generated under a variety of *simple* loading regimes. Three loading regimes were considered: (A) quasi-static pushover, (B) push and release, and (C) high amplitude pulse response. While simple loading regimes are the focus of this work, more complex loading, such as modulated sinusoidal loading (Gidaris and Taflanidis, 2013) or white noise (Lin et al., 2001), may produce a better fit than the simple regimes considered, in general.

Regime (A) — Quasi-Static Pushover The curve fitting was initially done using a calibration data set generated from a quasi-static pushover analysis of the OpenSees NFEM with the inelastic condensed model. This involved a slowly increasing ground-motion acceleration given by:

$$\ddot{u}_{\mathrm{g}}(t) = \ddot{u}_{\mathrm{g}o}\frac{t}{t_{\mathrm{f}}} \tag{5.12}$$

where the amplitude of the ground motion, $\ddot{u}_{\mathrm{g}o}$, at the final time $t_{\mathrm{f}} = 60$ sec was taken to be 0.275 g. Table 5.2 gives the fitted values for the hysteretic parameters. Figure 5.3 shows the inter-story drift ratio time-histories of the 1st, 5th,

Table 5.2: Fitted hysteretic parameters of the 9-story structure for loading regimes (A) quasi-static pushover, (B) push and release, (C) high amplitude pulse response, and 1.5×El Centro.

Hysteretic parameter	Loading Regime			
	(A)	(B)	(C)	1.5× El Centro
κ	0.0470	0.0326	0.2424	0.2166
η	2.5152	2.0904	3.5139	3.3978
$z_{1,\mathrm{yield}}$ [in.]	3.0808	3.2251	3.3671	2.8728
$z_{2,\mathrm{yield}}$ [in.]	1.8864	2.0070	1.4200	1.4196
$z_{3,\mathrm{yield}}$ [in.]	1.7757	1.8685	1.5093	1.4664
$z_{4,\mathrm{yield}}$ [in.]	1.7341	1.7887	1.5450	1.4664
$z_{5,\mathrm{yield}}$ [in.]	1.6173	1.6415	1.6450	1.8096
$z_{6,\mathrm{yield}}$ [in.]	1.5207	1.5039	1.7395	1.9968
$z_{7,\mathrm{yield}}$ [in.]	1.9488	1.6213	1.9708	1.7316
$z_{8,\mathrm{yield}}$ [in.]	2.5015	1.7479	2.0207	1.9812
$z_{9,\mathrm{yield}}$ [in.]	2.9632	1.7250	1.7253	1.7160

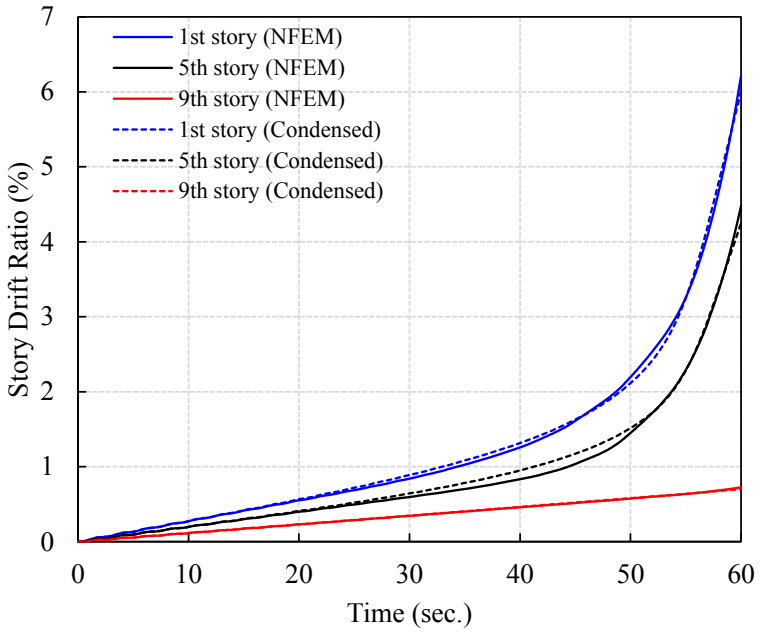

Figure 5.3: Quasi-static pushover analysis — inter-story drift ratio time-histories of the 1st, 5th, and 9th stories of the 9-story structure as calculated by the OpenSees NFEM and by the fitted inelastic condensed model (condensed).

and 9th stories as determined by the OpenSees NFEM and by the fitted inelastic condensed model.

Regime (B) — Push and Release The next regime that used for the curve fitting was a push and release analyses of both the OpenSees NFEM and the inelastic condensed model. This calibration data set is generated by monotonically increasing the ground acceleration from zero to 0.275 g over 60 sec, in accordance with Eq. (5.12), and abruptly dropping the ground acceleration to zero at 60 sec. The push time and the release time are selected to be equal (60 sec) in order to have the same weighting in the fitting process. Unlike the quasi-static pushover analysis (A), this calibration data set captures oscillator behavior of the hysteretic model, as well as its residual displacements. The inter-story drift ratio time-histories of the 1st, 5th, and 9th stories as determined by the OpenSees NFEM and by the fitted inelastic condensed model is depicted in Figure 5.4. The fitted values for

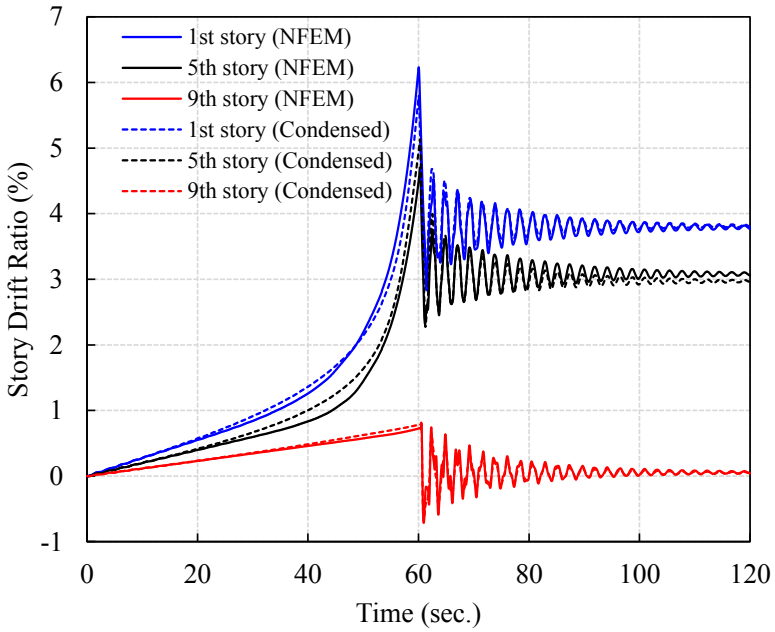

Figure 5.4: Push and release analysis — inter-story drift ratio time-histories of the 1st, 5th, and 9th stories of the 9-story structure as calculated by the OpenSees NFEM and by the fitted inelastic condensed model (condensed).

the hysteretic parameters are given in Table 5.2.

Regime (C) — High Amplitude Pulse Response Finally, the NFEM and the condensed model were subjected to a high amplitude pulse. This high amplitude pulse is a half-cycle sinusoidal pulse with period equal to half of the natural fundamental period of the structure given by:

$$\ddot{u}_{\rm g}(t) = \begin{cases} \ddot{u}_{go} \sin(4\pi f_{\rm n1} t), & 0 \leqslant t \leqslant 1/(2f_{\rm n1}) \\ 0, & 1/(2f_{\rm n1}) < t \leqslant t_{\rm f} \end{cases} \tag{5.13}$$

where amplitude of the pulse $\ddot{u}_{go} = 0.275\ g$ and the final time $t_{\rm f} = 60$ sec. The inter-story drift plots for the OpenSees NFEM and the inelastic condensed model were computed and shown in Figure 5.5 and the corresponding hysteretic parameters are tabulated in Table 5.2.

More refined condensed models may be fit to the NFEM responses by allowing

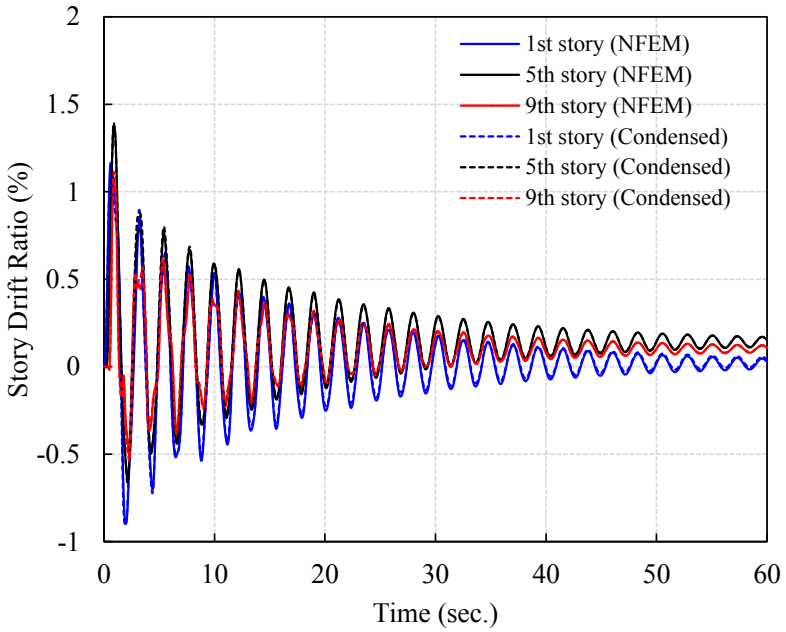

Figure 5.5: Pulse analysis — inter-story drift ratio time-histories of the 1st, 5th, and 9th stories of the 9-story structure as calculated by the OpenSees NFEM and by the fitted inelastic condensed model (condensed).

the fit to find different values of η, κ, and ρ for each story level. Doing so results in a condensed model that has the slightly better predictive capability in terms of inter-story drift ratios, but at the expense of slightly worse predictive capabilities in terms of floor displacements (Mirza, 2014). Mirza (2014) also suggested that the list of $r + 2$ fit parameters (r = number of stories) provides a good trade-off between the complexity of the model and the overall predictive capability.

The fitted hysteretic parameters for the three simple loading regimes are given in Table 5.2. In addition, the parameters were fit directly for the ground motion to be used for evaluation (1.5×El Centro) as the best possible fit. Table 5.2 shows that the parameters fit to each of the loading regimes are generally within ±20 percent of each other. The asymptotic standard errors of the fit parameters are around 0.29% for the $z_{i,\text{yield}}$ parameters, less than 0.04% for κ, and 1.05% for η. The fitting process can be carried out in a few minutes on a standard office computer.

5.5 Comparative Evaluation of Analysis Procedures

5.5.1 Evaluation of IMC for the 9-story Structure

In this section, in order to identify the most robust loading regime for estimating the peak responses of structures, a comparative analysis between the responses of the condensed models — obtained by those loading regimes — and the *exact* response of the NLRHA of the NFEM is performed under a real earthquake scenario. Before performing any analyses, three sets of the parameter values are obtained by the three regimes described earlier (see Table 5.2).

The histories of the displacements to structure height ratios (displacement ratios) as well as the story drift ratios of the 9-story NFEM and the three different condensed models — each obtained by fitting to one loading regime — under 1.5 × El Centro ground motion excitation are plotted for the first story in Figure 5.6 and for the roof in Figure 5.7. As depicted in Figure 5.6 for the first story, the peak responses of each model are highlighted in the time histories; the peak displacement ratio and the peak inter-story drift ratio for NLRHA are 0.234 and 1.587, respectively. The best estimates of these two responses are 0.239 and 1.621 (2.1% errors), respectively, by the condensed model fit to quasi-static pushover data (A). At the roof level, as shown in Figure 5.7, the peak displacement ratio and the peak inter-story drift ratio for NLRHA are 1.181 and 1.467, respectively. The best estimate for the displacement ratio is 1.184 (0.25% error) by the condensed model fit to pulse response data (C), and the best estimate of the drift ratio is 1.457 (0.7% error) by the condensed model fit to push and release data (B), in case of the peak values. However, the condensed model fit to the pulse response data (C) is the only one that has captured the correct peak in time.

The peak responses — displacement to structure height ratios and story drift ratios — for all stories under 1.5 × El Centro are presented in Fi. 5.8 for each of the assessed models. Included in this figure is the condensed model fit to the El Centro time-history

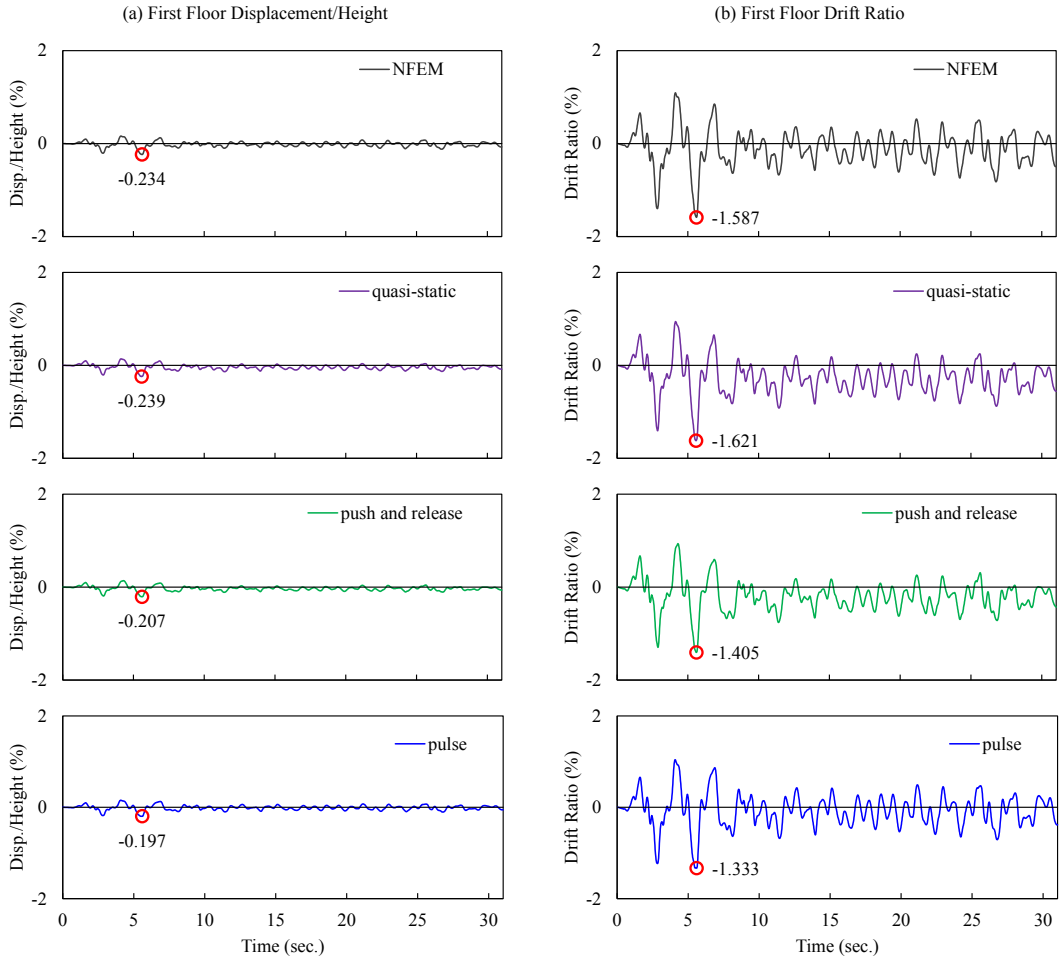

Figure 5.6: Time histories of the first floor of the 9-story structure under 1.5 × El Centro — NLRHA and the condensed models each obtained by different loading regimes: (a) displacement to structure height ratios; and (b) inter-story drift ratios.

data, which may be considered as the best fit in case of minimizing the sum-of-squares error of drift ratios. The errors of these estimations are presented in Figure 5.9, which makes the comparison easier. As shown in these two figures, the condensed model using the pulse regime (C) consistently provides the best estimates of these two responses, except in the first story.

In order to assess the distribution of plasticity in the structure, the procedure — based on the maximum drifts — that is described in Reyes and Chopra (2011) and Tehrani and Khoshnoudian (2014) is used. They have shown that the distribution of

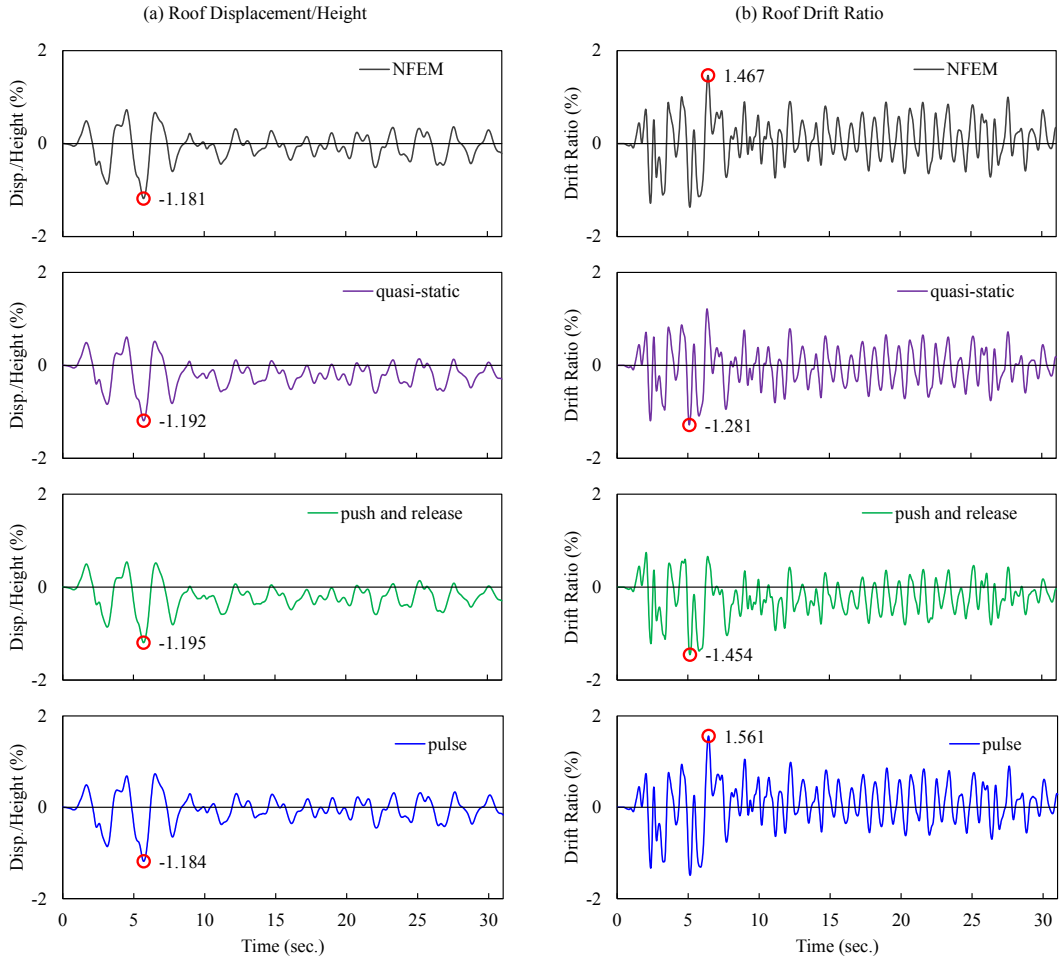

Figure 5.7: Time histories of the roof of the 9-story structure under 1.5 × El Centro — NLRHA and the condensed models each obtained by different loading regimes: (a) displacement to structure height ratios; and (b) inter-story drift ratios.

plasticity is highly correlated with maximum drifts. In this procedure, the maximum drifts obtained from the analysis are converted to a set of cumulative displacements (i.e. converted inter-story drifts to floor displacements and cumulatively added floor displacements as going from the base level to roof) and are imposed to the lateral DOFs in the NFEM as a displacement control pushover analysis. The status of the structure at the end of the pushover analysis would be an estimation of the maximum plasticity distribution.

The maximum drifts obtained from the condensed model fit to the high amplitude

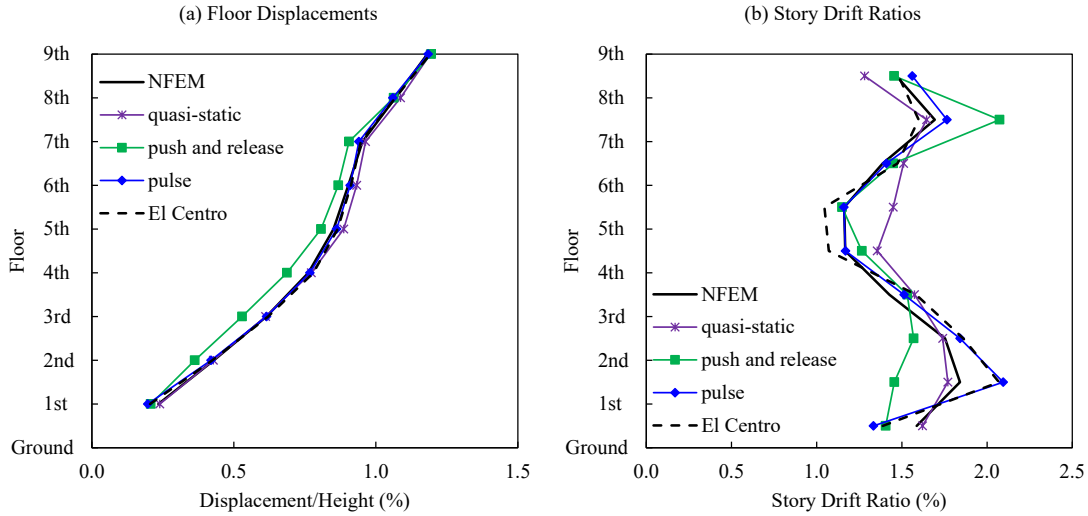

Figure 5.8: Height-wise distribution of peak responses of the 9-story structure under 1.5 × El Centro for the inelastic ty model and different condensed models: (a) displacement to structure height ratios; and (b) inter-story drift ratios.

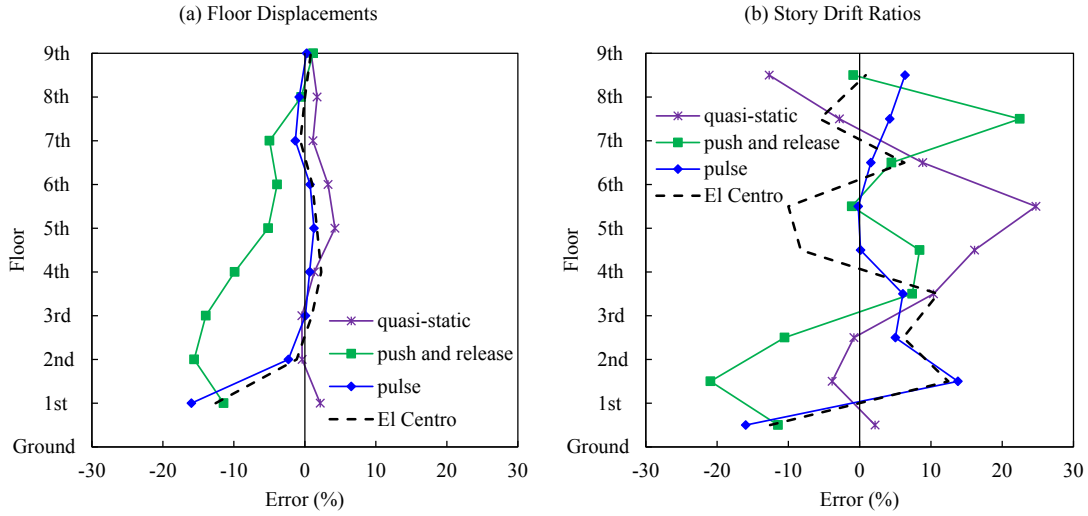

Figure 5.9: Height-wise distribution of peak responses' errors of the 9-story structure under 1.5 × El Centro for different condensed models: (a) displacement to structure height ratios; and (b) inter-story drift ratios.

pulse data (C) are used to estimate plasticity distribution. The simulation can output curvatures at any location along the members. For example, the beams' peak curvatures on the right hand side of the 3rd column from the left are shown in Figure 5.10 and then they are converted to the peak plasticity ratios — ratio of peak curvature to the yield-

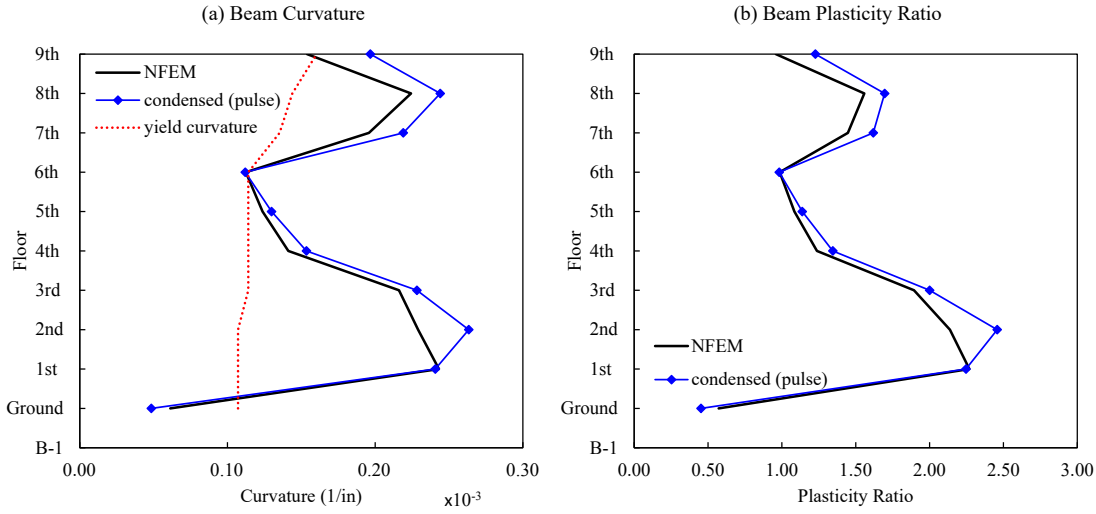

Figure 5.10: The height-wise plasticity distribution of the beams on the right hand side of the 3rd column (highlighted in blue in Figure 5.2) of the 9-story structure under 1.5 × El Centro; (a) Curvatures obtained from the NFEM and the condensed model fit to pulse data and the value of the yielding curvatures; (b) The corresponding plasticity ratios (ratio smaller than 1 is in elastic range and the ratio over 1 is in plastic range).

ing curvature — to better represent if they are in elastic or plastic range. A plasticity ratio smaller than one means the section is in elastic range while a ratio greater than one means the section is in plastic range. This judgment is done using the red dotted line in Figure 5.10(a). Each point on this line represents the yielding curvature for the corresponding section. As shown in Figure 5.11, the moment-curvature of each section is obtained and then the curvature value corresponding to the 5% deviation of the idealized bilinear post-yield curve and the moment-curvature data is used as the yielding curvature to judge if the curvature is in elastic or plastic range. The selection of the yielding curvature value requires engineering judgment and is chosen to best represent the plasticity distribution of the 9-story model presented in Chopra and Goel (2002). However, the comparison with the NFEM is of importance.

Applying the same procedure for all the beams for the 9-story structure reveals the overall beams' plasticity distribution obtained from the condensed model fit to pulse data (C) that is shown in Figure 5.12 and is compared with the beams' plasticity ratios

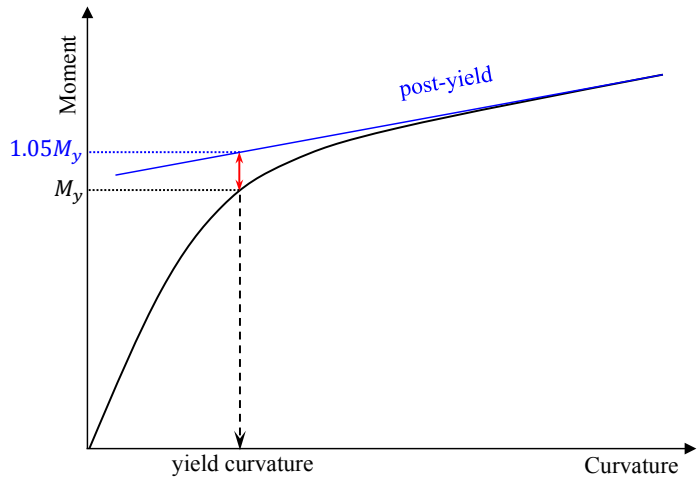

Figure 5.11: The considered value of the yielding curvature from the moment-curvature data provided by the OpenSees NFEM.

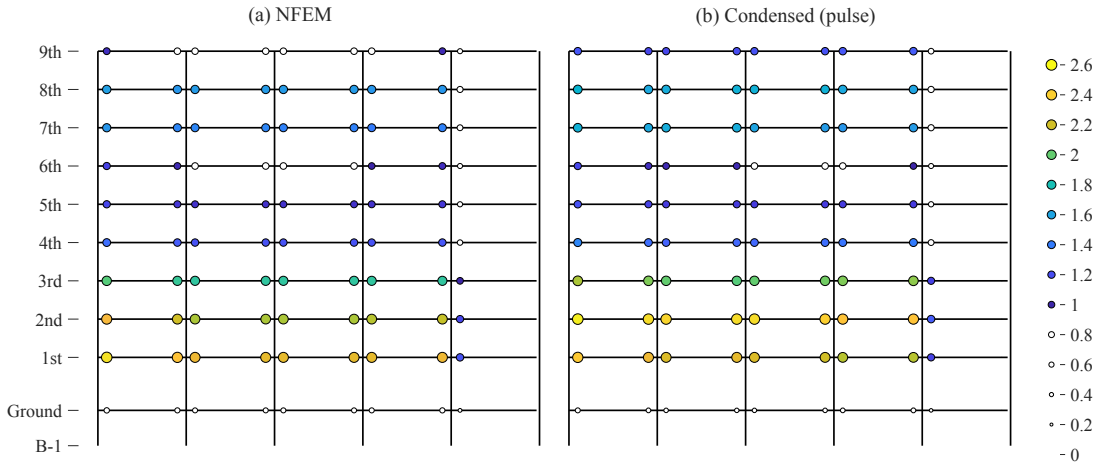

Figure 5.12: Beams' plasticity distribution of the 9-story structure under 1.5 × El Centro: (a) OpenSees NFEM; and (b) Condensed model fit to pulse data (white circles represent rotations in elastic range and colorful circles represent rotations in plastic range).

obtained from the NLRHA of the NFEM.

The distribution of plasticity ratio in each column can be obtained by the same procedure considering the axial loads when calculating the yielding curvatures. For instance, Figure 5.13 shows the height-wise distribution of the curvatures, obtained from the condensed model fit to pulse data (C), of the 3rd column (highlighted in blue in Figure 5.2) under 1.5 × El Centro, which are compared with the curvatures obtained

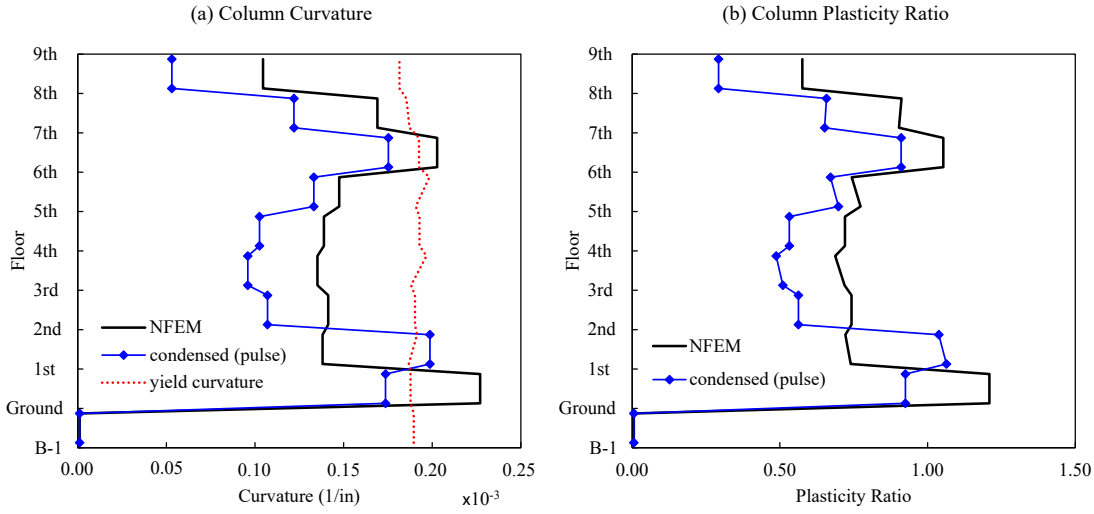

Figure 5.13: The height-wise plasticity distribution of the 3rd column (highlighted in blue in Figure 5.2) of the 9-story structure under 1.5 × El Centro; (a) Curvatures obtained from the NFEM and the condensed model fit to pulse data and the value of the yielding curvature; and (b) The corresponding plasticity ratios (ratio smaller than 1 is in elastic range and the ratio over 1 is in plastic range).

from the NLRHA of the NFEM, and the value of the yielding curvatures at each point in height. The corresponding plasticity ratios are plotted on the same figure.

Excellent agreement in both the distribution and the magnitude of plasticity is observed in Figures 5.10, 5.12, and 5.13, which indicates that responses from the IMC method can be used to accurately predict the distribution of peak plasticity ratios as long as the estimation of maximum drifts are accurate.

Next, the IMC is evaluated for the 9-story structure under 3 × El Centro as a representation of an intense ground motion excitation. The height-wise distribution of the peak responses — displacement to structure height ratios and story drift ratios — under this excitation for each of the assessed models, including the condensed model fit to El Centro time history data, are presented in Figure 5.14 and their corresponding errors are shown in Figure 5.15. As in the other cases analyzed, the inelastic condensed model fit to the high amplitude pulse data (C) consistently provides the best estimates of these two responses. As previously established, having accurate estimates of maximum drifts will result in a good estimates of plasticity distribution (Reyes and Chopra, 2011;

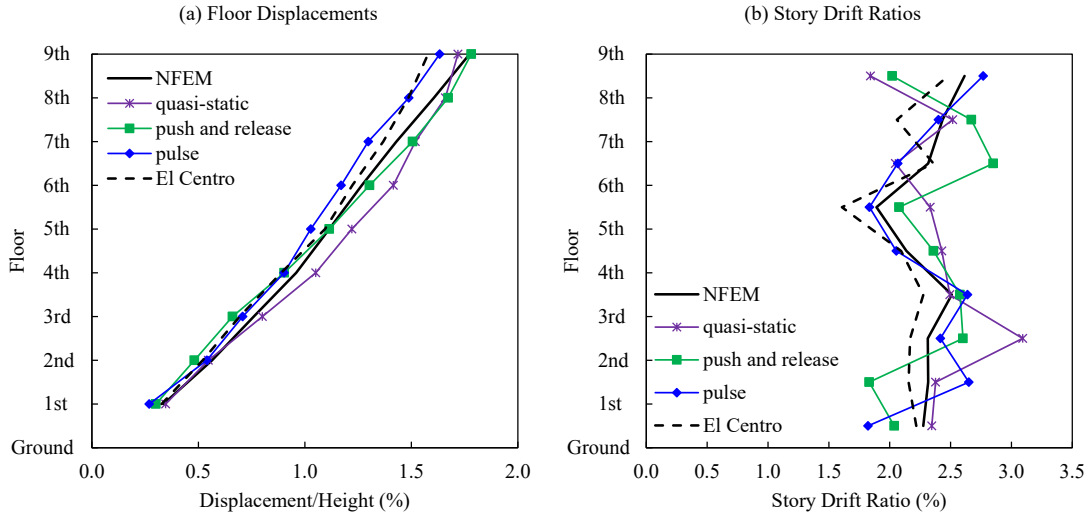

Figure 5.14: Height-wise distribution of peak responses of the 9-story structure under 3 × El Centro for the inelastic NFEM and different condensed models: (a) displacement to structure height ratios; and (b) inter-story drift ratios.

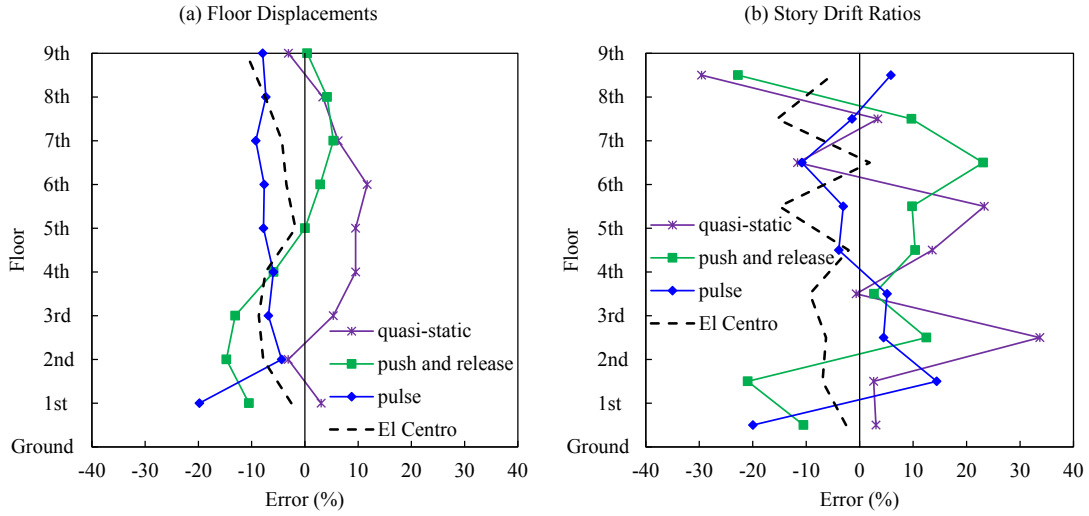

Figure 5.15: Height-wise distribution of peak responses' errors of the 9-story structure under 3 × El Centro for different condensed models: (a) displacement to structure height ratios; and (b) inter-story drift ratios.

Tehrani and Khoshnoudian, 2014).

In order to identify which regime provides the best estimate of hysteretic parameters in a wide range of ground motion intensity, the responses of the NFEM in OpenSees are compared with the responses of the equivalent inelastic condensed models under El

Centro ground motion excitation with different scaling factors: 0.25, 0.5, 0.75, 0.85, 1, 1.5, 2, and 3. The selection of the structure and the scaling factors make this evaluation possible to be compared with the estimates of the Uncoupled Modal Response History Analysis (UMRHA) and the Modal Pushover Analysis (MPA) (Chopra and Goel, 2002).

The NFEM and the inelastic condensed model were subject to the El Centro ground motion with various scaling factors. Maximum errors in estimating the peak displacement to structure height ratios and the peak inter-story drift ratios at all stories are used as a metric to compare different parameter fitting. Also, the linear condensed model (without any hysteretic parameters) is assessed to present the accuracy of the linear condensation method proposed in this chapter for linear elastic structures.

Figure 5.16 summarizes the errors for the linear condensed model (Eq. (5.1)) and the inelastic condensed models fit to calibration data from the three described loading regimes and the El Centro data (for each ground motion multiplier) as well as UMRHA and MPA errors from Chopra and Goel (2002). The linear condensed model estimates the displacement ratios with about 1% error and the drift ratios with about 4% error in the linear range (scale factors 0.25 and 0.5) since the full and the condensed model have the same modal properties (in the selected $r = 9$ modes). The estimation errors increase dramatically as the structure moves to the inelastic range (scale factors 0.75 and higher). Among the three regimes considered in this chapter, inelastic condensed models fit to quasi-static pushover data (A) provide better estimates of displacement ratios and inelastic condensed models fit to high amplitude pulse data (C) provide better estimates of drift ratios. Among these three assessed regimes, inelastic condensed models fit to high amplitude pulse data (C) provide the most consistent results for both displacement ratios and drift ratios. The errors in the estimation of responses increase by increasing the ground motion intensities and reach a plateau at around 20% errors. Both UMRHA and MPA estimation errors of displacement ratios fluctuate with a maximum error of

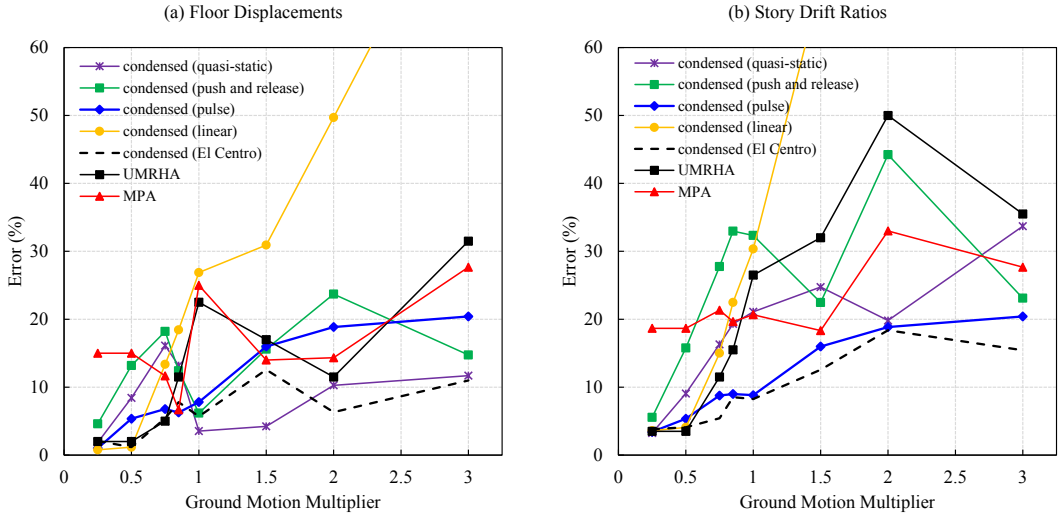

Figure 5.16: Errors in UMRHA, MPA, linear condensed model, and IMC with fitted parameters by quasi-static, push and release, high amplitude pulse regimes, and El Centro as a function of ground motion intensity for the 9-story structure: (a) displacement ratios; and (b) inter-story drift ratios. UMRHA and MPA values are taken from Chopra and Goel (2002).

more than 30%. The UMRHA estimation errors of drift ratios are small in the linear range and increase as the structure moves to the nonlinear range with a maximum error of about 50%. The MPA estimation of drift ratios have around 20% error up to the 1.5 ground motion multiplier and these errors increase to about 33% for larger ground motion multipliers.

A comparison — based on the results presented in this chapter — among MPA, UMRHA, and the condensed model fit to the high amplitude pulse regime (C) reveals the capability of the proposed IMC approach to estimate the structure responses, such as displacements, story drift ratios, and plasticity distribution. This new IMC approach can reduce the errors in estimates of displacements from 30% by MPA and UMRHA to 20% and in estimates of drift ratios from 33% by MPA and 50% by UMRHA to 20%. These errors in the estimation of peak floor displacements and peak inter-story drift are about half of the dispersion in the ground-motion prediction equations used in Performance-Based Earthquake Engineering (PBEE) (Chiou and Youngs, 2008).

5.5.2 Evaluation of IMC for Different Structures

In the previous section, the IMC is evaluated for the 9-story structure in detail. In this section, different structures are evaluated with IMC to cover a wider range of structure heights. The 3-story and the 20-story structure from the SAC project for the Los Angeles, California region are selected (Ohtori et al., 2004). The 3-story structure has the total height of 39 ft and is expanded in 4 bays of width 30 ft each with typical story height of 13 ft. Beam to column connections are moment resisting except the connection of the rightest beams to the surrounding columns. The columns are fixed to the base. The 20-story structure has the total height of 289 ft and is expanded in 5 bays of width 20 ft each with typical story height of 13 ft except the first floor with 18 ft and the two basements with 12 ft each. Beam to column connections are moment resisting except the connection of the beams at the first basement level. The columns are pinned to the base and the structure is laterally restrained at the ground level. More details can be found in Ohtori et al. (2004). In both structures, the third column from the left are retained in the condensed models. In the 3-story structure, the horizontal responses of nodes 8, 13, and 18 (see Fig. 1 in Ohtori et al. (2004)), and in the 20-story structure nodes 21, 27, 33, 39, 45, 51, 57, 63, 69, 75, 81, 87, 93, 99, 105, 111, 117, 123, 129, and 135 (see Fig. 3 in Ohtori et al. (2004)) were selected as the basis of comparison of the models investigated herein.

The NFEM of the 3-story and the 20-story buildings were developed in OpenSees (Mazzoni et al., 2009). The material properties and modeling assumptions are the same as the 9-story building described in Section 5.3.1. The linear condensed model for both structures are developed as described in Section 5.3.2, and the hysteretic parameters are obtained by the fitting procedure as described in Section 5.4 using the three different loading regimes. For the 3-story building, the selected loading amplitudes are 0.475 g for loading regimes (A) and (B), and 0.550 g for loading regime (C). These amplitudes

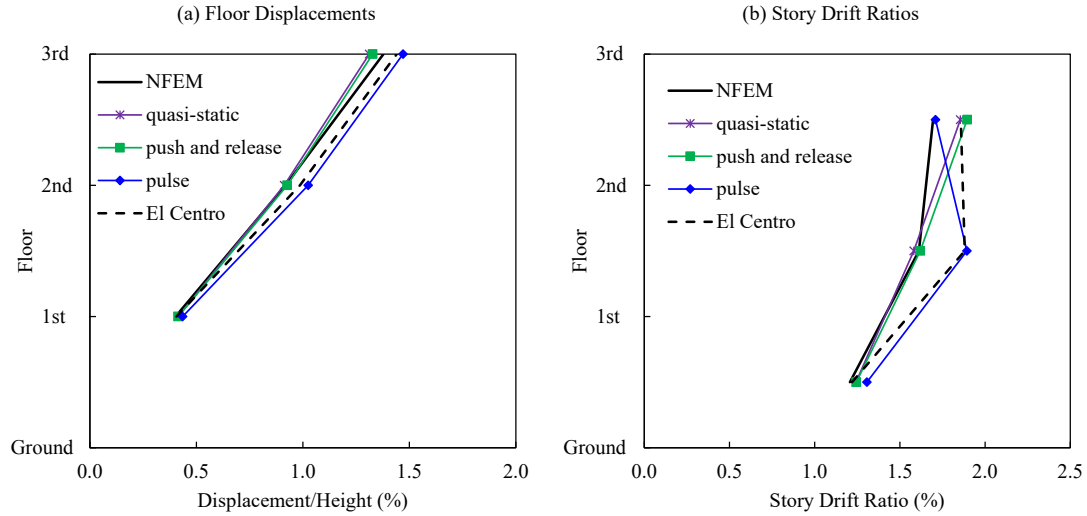

Figure 5.17: Height-wise distribution of peak responses of the 3-story structure under 1.5 × El Centro for the NFEM and different condensed models: (a) displacement to structure height ratios; and (b) inter-story drift ratios.

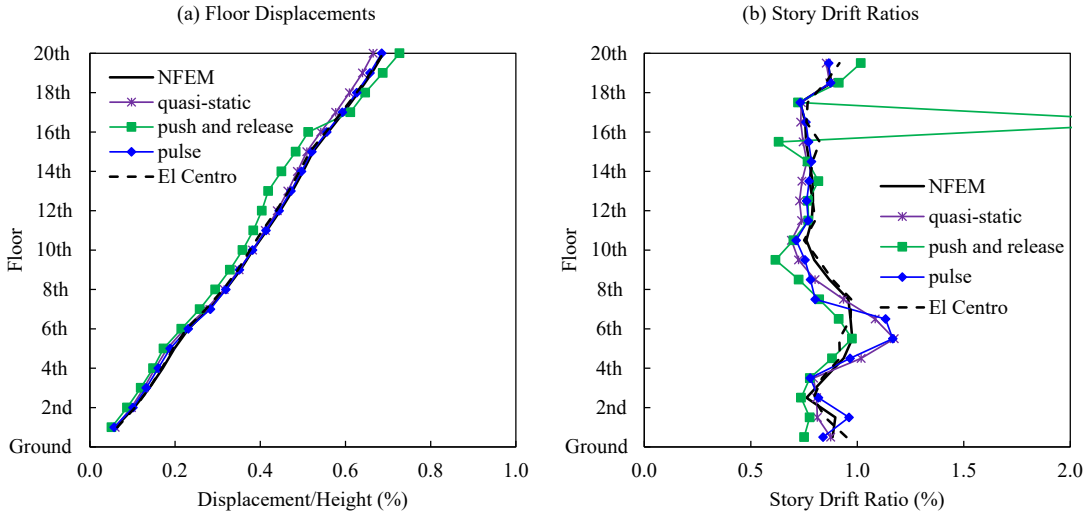

Figure 5.18: Height-wise distribution of peak responses of the 20-story structure under 1.5 × El Centro for the NFEM and different condensed models: (a) displacement to structure height ratios; and (b) inter-story drift ratios.

for the 20-story building are 0.125 g for loading regimes (A) and (B), and 0.175 g for loading regime (C).

The peak responses — displacement to structure height ratios and story drift ratios — for all stories under 1.5 × El Centro are presented in Figure 5.17 for the 3-story

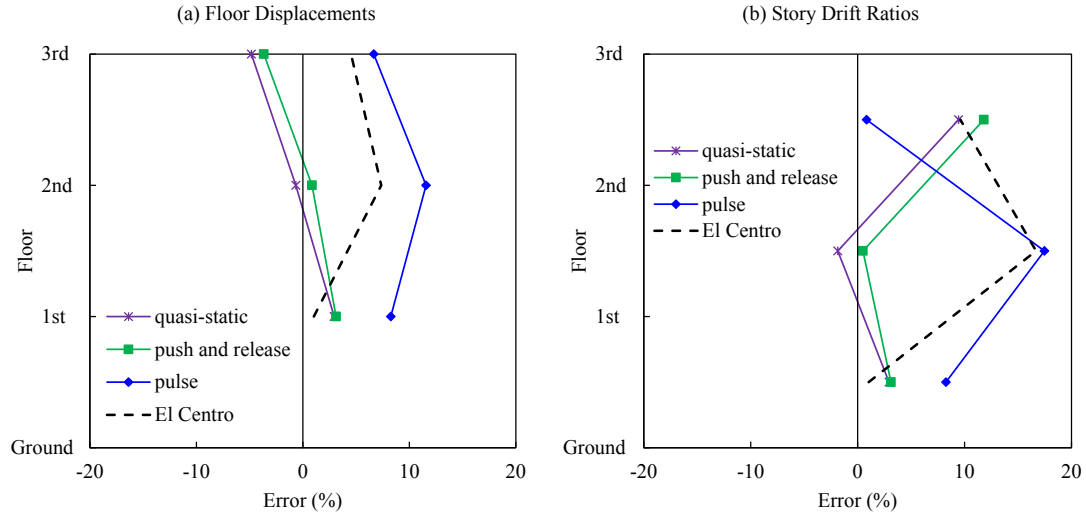

Figure 5.19: Height-wise distribution of peak responses' errors of the 3-story structure under 1.5 × El Centro for different condensed models: (a) displacement to structure height ratios; and (b) inter-story drift ratios.

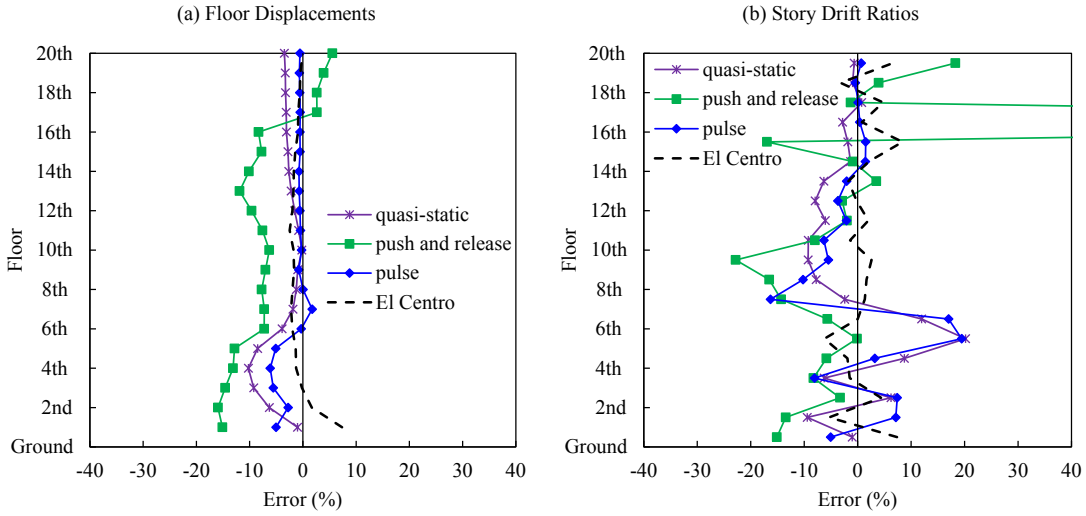

Figure 5.20: Height-wise distribution of peak responses' errors of the 20-story structure under 1.5 × El Centro for different condensed models: (a) displacement to structure height ratios; and (b) inter-story drift ratios.

structure and in Figure 5.18 for the 20-story structure. The errors of these estimations are presented in Figure 5.19 for the 3-story structure and in Figure 5.20 for the 20-story structure. As shown in Figure 5.17, the loading regimes (A) and (B) have better estimation of peak story displacement ratios and story drift ratios than loading regime

(C). The errors of displacement ratios, as shown in Figure 5.19, are less than 10% for loading regimes (A) and (B) and around 12% for loading regime (C). The errors of drift ratios are less than 12% for loading regimes (A) and (B) and less than 20% for loading regime (C). As shown in Figure 5.18, the loading regimes (A) and (C) have better estimations than loading regime (B), which failed to estimate the maximum drift ratio of the 17th story. The errors of displacement ratios, as shown in Figure 5.20, are less than 10% for loading regimes (A) and (C) and less than 20% for loading regime (B). The errors of story drift ratios for loading regimes (A) and (C) are less than 20%, and the loading regime (B) failed to estimate the drift ratio of the 17th floor.

Similar to the 9-story building, the 3-story and 20-story buildings are evaluated for various ground motion excitations' magnitude ranging from 0.25 to 3 $\times$ El Centro. These evaluations are depicted in Figure 5.21 for the 3-story building and in Figure 5.22 for the 20-story building. As shown in Figure 5.21, the IMC fit to quasi-static data (A) or push and release data (B) can estimate the displacement ratios with maximum errors less than 30% and these estimations for the IMC fit to pulse data (C) is less than 20%. The errors in estimation of the story drift ratios of the IMC fit to quasi-static data (A) or push and release data (B) reach to 42% and 35%, respectively. This error for IMC fit to pulse data (C) is less than 20%. As shown in Figure 5.22 for the 20-story building, the IMC fit to pulse data (C) has maximum error around 10% for estimating displacement ratios and around 34% for story drift ratios. These errors for the IMC fit to quasi-static data (A) go to 21% and 43%, respectively. As can be seen, the IMC fit to push and release data (B) is not able to estimate displacement and drift ratios for ground motion multiplier larger than 2 and the errors of story drifts increase dramatically as the structure moves to nonlinear range. The evaluation of IMC on different ground motion multipliers and different structures reveals that IMC fit to pulse data (C) is more robust than other two loading regimes. Moreover, as shown by the IMC fit to El Centro data,

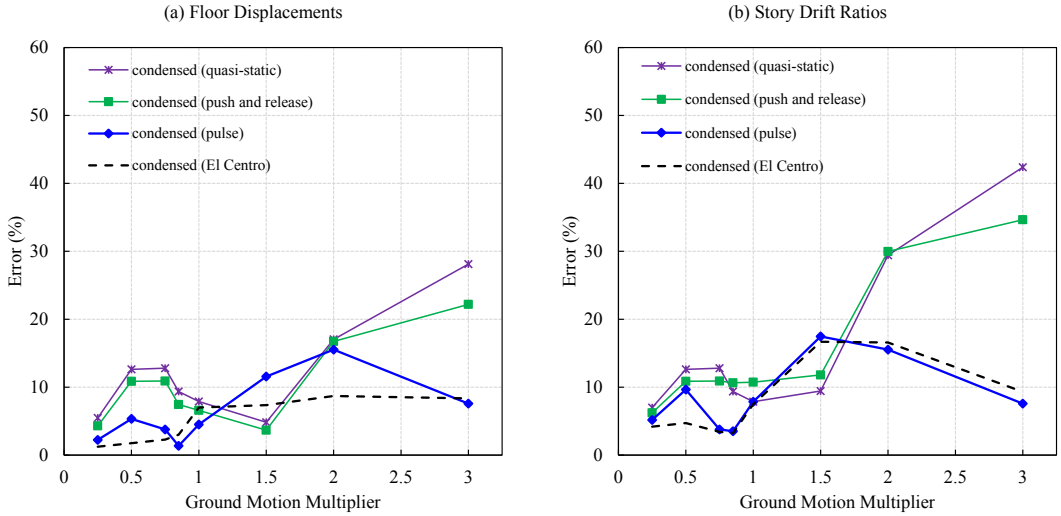

Figure 5.21: Errors of IMC with fitted parameters by quasi-static, push and release, high amplitude pulse regimes, and El Centro as a function of ground motion intensity for the 3-story structure: (a) displacement ratios; and (b) inter-story drift ratios.

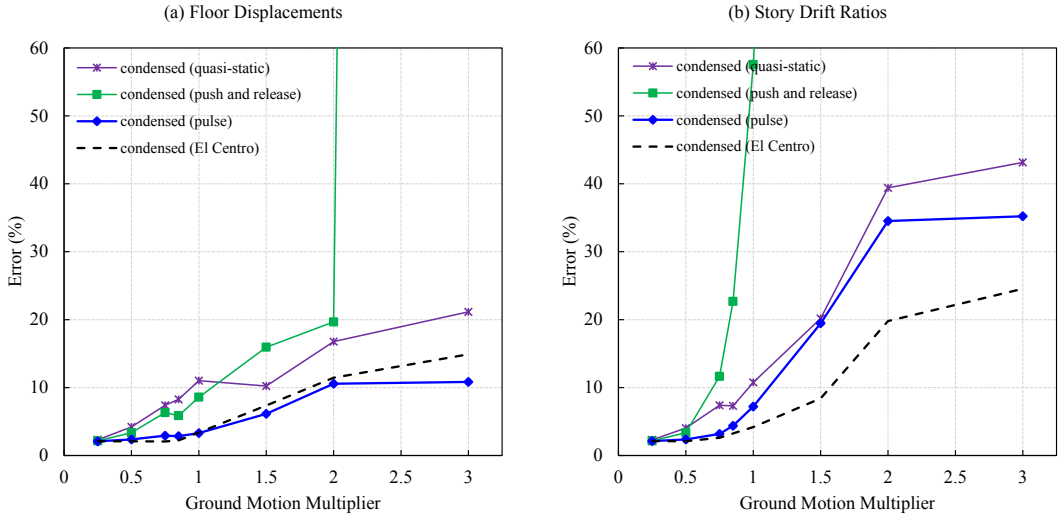

Figure 5.22: Errors of IMC with fitted parameters by quasi-static, push and release, high amplitude pulse regimes, and El Centro as a function of ground motion intensity for the 20-story structure: (a) displacement ratios; and (b) inter-story drift ratios.

there is a room for improving the IMC accuracy, by investigating other loading regimes for creating calibration data.

5.6 Summary and Conclusions

This section presents an inelastic model condensation (IMC) method that retains the accuracy and inelastic behavior of NFEMs. This method involves condensing a linear elastic structural model via its modal properties. The modes of the full model with the highest participation are retained at a set of desired DOFs in the elastic condensed model. Then, these modified mode shapes are used to construct the elastic stiffness, mass, and damping matrices of the condensed model. In this case, the condensed DOFs are one displacement coordinate per story level. Then, the displacement coordinates are transformed to the inter-story drift coordinates and the elastic inter-story forces are replaced with hysteretic forces and finally, the inelastic model is transformed back to the displacement coordinates.

Building this model requires the fitting of a few hysteretic model parameters to a short time history of inelastic responses computed by a NFEM. These responses can be generated from a quasi-static pushover loading, push and release loading, or a high amplitude pulse loading. Inelastic condensed models were fit to each of these three loading scenarios and resulted in a set of inelastic parameters for each calibration loading regime. The condensed model fit with the high amplitude pulse response data predicts earthquake responses better than models fit with quasi-static pushover data or push and release data. Also evaluated is the condensed model fit to the El Centro data for each ground motion multiplier. It can be a representation of the best possible inelastic condensed model. However, in this chapter, the sum-of-squares error of drift ratios is used for finding the hysteretic parameters while the peak maximum responses are used for evaluation.

In the elastic range, predicted responses from such a condensed model are extremely close to responses computed from the NFEM since these two models have almost the same modal properties. The verification study, therefore, focused on high-amplitude

inelastic responses. The condensed model, obtained by the high amplitude pulse loading regime, is recommended in this chapter since it provides the most consistent and accurate estimates especially for inter-story drift ratios. An advantage of the proposed condensed model in estimating accurate drift ratios is that drift ratio is frequently used as a metric to limit the level of damage such as allowable story drifts recommended in ASCE/SEI 7-16 (2017). The decision to demolish a building after an earthquake is informed significantly from the observed residual displacements; the assessment of the IMC method in the context of fidelity in capturing residual inter-story drifts is a topic of continuing work.

Another advantage of the IMC is the significant reduction in computation time. The elapsed time for the 9-story NFEM under 1.5 $\times$ El Centro in OpenSees is around 297 sec, while this time for the equivalent IMC model, including the construction of the condensed model, is around 6 sec in MATLAB, using a variable time step solver (ode45). This shows around 98% reduction in computation time, which can be improved by using low-level programming language codes, such as C.

Fitting different yield displacement parameters at each story, a single post-yield stiffness parameter, and a single hysteretic knee-sharpness parameter resulted in a model that had good predictive capabilities in terms of peak floor displacement ratios and inter-story drift ratios. The relative errors in predicted displacement ratios and inter-story drift ratios were less than 20% even for the high-intensity ground motions. The prediction capability of this inelastic condensed dynamic model compares favorably to the predictions afforded by models developed from existing nonlinear pushover analysis methods. It is worth noting that the inelastic condensed model proposed in this chapter can be easily extended for structures under biaxial excitations by substituting the uniaxial hysteretic model, used in this chapter, with a biaxial hysteretic model (Harvey and Gavin, 2014b). This chapter provided a proof of concept for IMC. In the future,

the IMC should be evaluated under an ensemble of ground motions (with varying frequency characteristics) where the mean responses would be the focus rather than the detail time history responses. In addition, various loading regimes should be assessed to find the most robust loading regimes such as modulated sinusoidal loading (Gidaris and Taflanidis, 2013) or white noise (Lin et al., 2001); in Lin et al. (2001), it is shown that white noise is more efficient than real ground motions for fitting hysteretic parameters. Moreover, IMC should be extended to consider various structural systems with irregularities, which may require to increase the number of hysteretic parameters.

Chapter 6
Summary, Conclusions, and Future Work

6.1 Summary and Conclusions

Loss of operation or harmful damage to buildings and industrial structures, as well as equipment housed in them, have been observed during past extreme seismic events. One of the main reasons for such damages is the performance degradation of both structures and sensitive equipment. Equipment usually suffers from excessive transmitted total acceleration. A common method to reduce equipment acceleration is vibration isolation. Isolation elongates the natural period of the isolated equipment, resulting in a reduction of acceleration at the expense of increasing the displacement demand. Isolation systems have shown acceptable performance under low- to moderate-intensity excitation, while impact is possible under extreme-intensity excitation.

This dissertation was focused on the assessment and design of innovative dual-mode isolation systems—with an emphasis on rolling type isolation systems (RISs)—in order to protect both equipment and the primary structure. First, in Chapter 2, an assessment study was performed on the safety criteria for isolated telecommunication equipment according to the GR-63-CORE guideline (Telcoridia, 2012). In this guideline, only one accelerogram is introduced for the design and testing, which does not agree with the required response spectrum (RRS) prescribed in the same guideline. In order to probabilistically assess the safety of a system designed using the GR-63-CORE guideline, a suite of synthetic accelerograms is needed. To generate such a suite compatible with the

RRS, several filters (i.e., a transfer function in the frequency domain) were developed to convert a nonstationary Gaussian process to a compatible accelerogram. Then, the equation of motion for a RIS with circular profile was developed, and through a numerical study it was shown that the designed isolation system for protecting the telecommunication equipment has a large failure probability under the synthetic accelerograms.

Following this observation, a dual-mode isolation system was proposed for impact mitigation/prevention in Chapter 3. This dual-mode system was designed in a way that not only not mitigates impact under extreme events (i.e., MCE-level), but also does not alter the normal operation of the system under low- to moderate-intensity events (i.e., SLE- or DBE-level). To achieve this, a displacement threshold was defined based on the displacement response under DBE-level. When the displacement demand is below the threshold, the system is allowed to respond without any control action, while when the displacement demand exceeds the threshold, a control mechanism modifies the system's dynamics in order to try to prevent impact. Optimal control was used to find the best control mechanism for the active control region. The objective of this optimal control problem is to effectively utilize the available displacement (beyond the threshold but prior to impact) while seeking to simultaneously reduce the sustained total acceleration. The Euler-Lagrange equations are solved to find the open-loop solutions with a constraint on the control action (to be zero) only when the displacement is smaller than the threshold. The existence of this constraint makes the problem discontinuous and difficult to solve. Besides, solving this open-loop problem requires knowledge of future states (and costates), as well as the external loading history. Therefore, the problem was redefined by solving independent optimal control problems over each excursion into the active control region, in which the final time is not known *a priori*. An iterative procedure was proposed to solve each optimal control problem with unknown fixed final time. Then, based on the new formulation, a numerical exploration was performed,

resulting in several design curves that can be used to obtain the appropriate weights in the optimal control problem. For the purpose of illustration, a system equipped with a Kelvin-Voigt device was designed and evaluated, which returned promising results according to the objective of this formulation.

Moving from low to moderate seismic events to extreme seismic events, the design objective moves away from equipment protection toward primary structure protection. Consequently, the feasibility of a dual-mode vibration isolator/absorber was assessed in Chapter 4. The idea is to have an isolation system to protect a single piece of equipment or a group of equipment under low to moderate seismic events and use the isolated mass as a vibration absorber under extreme seismic events. An isolation system with nonlinear (cubic hardening) restoring force is considered. The hardening nonlinearity makes it possible to transition from isolation behavior to the vibration absorber behavior where the energy can be pumped out of the structure. To assess the feasibility of such a system, the coupled equations of motion for a building system with nonlinear attachments is developed. A reduced order modeling technique is introduced for linear elastic structure with nonlinear attachments to decrease the computational cost of solving the full coupled nonlinear equations of motion. Then, the accuracy of the nonlinear reduced order models (NLROMs) is evaluated by comparing response predictions under a ground motion acceleration with varying amplitude to those of the full coupled model. Then, the steady-state responses of the NLROMs are obtained using the harmonic balanced method. These solutions are obtained in the form of transmissibilities (roof displacement and isolated equipment total acceleration) by varying the frequency and mass ratios (secondary to primary system), the excitation intensity, and the nonlinearity of the attached isolation system.

The reduced order modeling method in Chapter 4 is limited to the linear elastic structure with nonlinear elastic attachment. Therefore, in order to make the assessment

of nonlinear inelastic structures practically possible, a new inelastic model condensation (IMC) method for building structure is proposed in Chapter 5. In this approach, one horizontal degree of freedom per story is kept in the condensed model. The condensation is performed using the selected modal properties obtained from the equivalent full linear elastic structure, matching the modal properties of the full model at the selected frequencies. After linear condensation, the inter-story restoring forces are replaced with nonlinear hysteretic restoring forces. In this study, the Bouc-Wen model is used to simulate the hysteretic behavior; however, other hysteretic models can be used. The hysteresis model has several parameters that needed to be tuned. Optimization is used to fit the responses of the inelastic condensed model with the response of the full high-fidelity inelastic model under several loading regimes by varying hysteresis model parameters. Then, the performance of inelastic condensation models obtained with different loading regimes are validated using 3, 9, and 20 story structures under El Centro ground motion acceleration with varying amplitude. This IMC method has shown acceptable performance.

6.2 Future Work

This research is the first step toward assessing and designing innovative dual-mode isolation systems. As a continuation of this research, the following are several areas that have the potential for further investigation:

- The fragility curves developed in Chapter 2 should be extended to consider different RIS configurations, such as rolling isolation bearings with other rolling profiles (e.g., spherical (Calhoun and Harvey, 2018)), double RISs (Calhoun et al., 2019; Harvey and Gavin, 2014a), or a dual-mode RIS based on Chapter 3.

- The dual-mode system assessed in Chapter 3 is limited to the unforced system. Forced systems with various forcing characteristics (e.g., harmonic loading, sine

sweep, white noise, and real ground/floor motion) need to be considered. Moreover, the dual-mode system described in Chapter 3 is limited to a linear elastic SDOF system. The concept of dual-mode systems needs to be extended for nonlinear elastic/inelastic single or multi-degree-of-freedom systems where the reduced order modeling approaches described in Chapters 4 and 5 can be utilized.

- The reduced order modeling method described in Chapter 4 was evaluated under only one earthquake record (i.e., El Centro). Therefore, the method should be evaluated under an ensemble of real or synthesized ground motion accelerations, in order to capture ground motion variability (e.g., see Chapter 2).

- In Chapter 4, the dual-mode vibration isolator/absorber system was assessed under only one earthquake record (i.e., El Centro) for only one type of nonlinearity (i.e., cubic hardening). In the future, assessment should be done using an ensemble of recorded ground motions, which includes the dominant frequency content existing in the real ground motions. Also, other forms of nonlinearity such as hysteretic, higher-order, or piecewise (i.e., discrete transitioning between two modes of operation) should be assessed.

- The inelastic model condensation method proposed in Chapter 5 should be extended to structures under biaxial excitation. This can be done by substituting the uniaxial hysteretic model, used in Chapter 5, with a biaxial hysteretic model (Harvey and Gavin, 2014b). Furthermore, the method should be extended to consider various structural systems with irregularities, which may require to increase the number of hysteretic parameters.

- The inelastic model condensation method proposed in Chapter 5 should be evaluated under an ensemble of ground motions (with varying frequency characteristics) where the mean responses would be the focus rather than the detail time

history responses. Also, various loading regimes should be assessed to find the most robust loading regimes such as modulated sinusoidal loading (Gidaris and Taflanidis, 2013) or white noise (Lin et al., 2001).

Bibliography

M. M. Abdullah, J. H. Hanif, A. Richardson, J. Sobanjo, Use of a shared tuned mass damper (STMD) to reduce vibration and pounding in adjacent structures, Earthquake Engineering & Structural Dynamics 30 (8) (2001) 1185–1201, doi:10.1002/eqe.58.

R. Alberdi, K. Khandelwal, Comparison of robustness of metaheuristic algorithms for steel frame optimization, Engineering Structures 102 (2015) 40–60, doi:https://doi.org/10.1016/j.engstruct.2015.08.012.

N. A. Alexander, F. Schilder, Exploring the performance of a nonlinear tuned mass damper, Journal of Sound and Vibration 319 (1-2) (2009) 445–462, doi:10.1016/j.jsv.2008.05.018.

C. Alhan, H. P. Gavin, Reliability of base isolation for the protection of critical equipment from earthquake hazards, Engineering Structures 27 (2005) 1435–1449, doi:10.1016/j.engstruct.2005.04.007.

C. Alhan, F. Şahin, Protecting vibration-sensitive contents: an investigation of floor accelerations in seismically isolated buildings, Bulletin of Earthquake Engineering 9 (4) (2011) 1203–1226, doi:10.1007/s10518-010-9236-0.

F. S. Alıcı, H. Sucuoğlu, Practical Implementation of Generalized Force Vectors for the Multimodal Pushover Analysis of Building Structures, Earthquake Spectra 31 (2) (2015) 1043–1067, doi:10.1193/102412EQS316M.

G. Alotta, M. Di Paola, A. Pirrotta, Fractional Tajimi–Kanai model for simulating earthquake ground motion, Bulletin of Earthquake Engineering 12 (6) (2014) 2495–2506, doi:10.1007/s10518-014-9615-z.

H. Anajafi, R. A. Medina, Comparison of the seismic performance of a partial mass isolation technique with conventional TMD and base-isolation systems under broadband and narrow-band excitations, Engineering Structures 158 (2018a) 110–123, doi:10.1016/j.engstruct.2017.12.018.

H. Anajafi, R. A. Medina, Partial mass isolation system for seismic vibration control of buildings, Structural Control and Health Monitoring 25 (2) (2018b) e2088, doi:10.1002/stc.2088.

ASCE/SEI 41-13, Seismic Evaluation and Retrofit of Existing Buildings, American Society of Civil Engineers, doi:10.1061/9780784412855, 2014.

ASCE/SEI 7-16, Minimum Design Loads and Associated Criteria for Buildings and Other Structures, American Society of Civil Engineers, doi:10.1061/9780784414248, 2017.

M. Astroza, S. Ruiz, R. Astroza, Damage assessment and seismic intensity analysis of the 2010 (Mw 8.8) Maule earthquake, Earthquake Spectra 28 (S1) (2012) S145–S164, doi:10.1193/1.4000027.

M. Azimi, A. Rasoulnia, Z. Lin, H. Pan, Improved semi-active control algorithm for hydraulic damper-based braced buildings, Structural Control and Health Monitoring 24 (11) (2017) e1991, doi:10.1002/stc.1991.

S. Baggio, L. Berto, T. Favaretto, A. Saetta, R. Vitaliani, Seismic isolation technique of marble sculptures at the Accademia Gallery in Florence: numerical calibration and simulation modelling, Bulletin of Earthquake Engineering 13 (9) (2015) 2719–2744, doi:10.1007/s10518-015-9741-2.

F. Bamer, C. Bucher, Application of the proper orthogonal decomposition for linear and nonlinear structures under transient excitations, Acta Mechanica 223 (2012) 2549–2563, doi:10.1007/s00707-012-0726-9.

A. Batou, C. Soize, Generation of accelerograms compatible with design specifications using information theory, Bulletin of Earthquake Engineering 12 (2) (2014) 769–794, doi:10.1007/s10518-013-9547-z.

G. Biondi, M. R. Massimino, M. Maugeri, Experimental study in the shaking table of the input motion characteristics in the dynamic SSI of a SDOF model, Bulletin of Earthquake Engineering 13 (6) (2015) 1835–1869, doi:10.1007/s10518-014-9696-8.

S.-H. Boo, P.-S. Lee, An iterative algebraic dynamic condensation method and its performance, Computers and Structures 182 (2017) 419–429, doi:10.1016/j.compstruc.2016.12.011.

D. M. Boore, C. A. Goulet, The effect of sampling rate and anti-aliasing filters on high-frequency response spectra, Bulletin of Earthquake Engineering 12 (1) (2014) 203–216, doi:10.1007/s10518-013-9574-9.

R. Bouc, Forced vibration of mechanical systems with hysteresis, in: Proceedings of the Fourth Conference on Nonlinear Oscillation, Prague, Czechoslovakia, 1967.

Y. Bozorgnia, V. V. Bertero, Earthquake Engineering: From Engineering Seismology to Performance-Based Engineering, CRC Press, Boca Raton, FL, 2004.

S. J. Calhoun, P. S. Harvey, Jr., Enhancing the teaching of seismic isolation using additive manufacturing, Engineering Structures 167 (2018) 494–503, doi:10.1016/j.engstruct.2018.03.084.

S. J. Calhoun, M. H. Tehrani, P. S. Harvey, Jr., On the performance of double rolling isolation systems, Journal of Sound and Vibration 449 (2019) 330–348, doi:10.1016/j.jsv.2019.02.030.

C. Chadwell, K. Brennan, M. Porter, Seismic hazard mitigation of wine barrel stacks, Structures 2009: Don't mess with structural engineers (2009) 1011–1019.

E. Chapin, A. Daniels, R. Elias, D. Aspilcueta, S. Doocy, Impact of the 2007 Ica earthquake on health facilities and health service provision in southern Peru, Prehospital and Disaster Medicine 24 (4) (2009) 326–332, doi:10.1017/S1049023X00007056.

D. C. Charmpis, M. C. Phocas, P. Komodromos, Optimized retrofit of multi-storey buildings using seismic isolation at various elevations: assessment for several earthquake excitations, Bulletin of Earthquake Engineering 13 (9) (2015) 2745–2768, doi:10.1007/s10518-015-9737-y.

Y. Chen, T. T. Soong, Seismic response of secondary systems, Engineering Structures 10 (4) (1988) 218–228, doi:10.1016/0141-0296(88)90043-0.

B. S.-J. Chiou, R. R. Youngs, An NGA Model for the Average Horizontal Component of Peak Ground Motion and Response Spectra, Earthquake Spectra 24 (1) (2008) 173–215, doi:10.1193/1.2894832.

A. K. Chopra, Dynamics of structures: theory and applications to earthquake engineering, Prentice-Hall, 4th edn., 2012.

A. K. Chopra, R. K. Goel, A modal pushover analysis procedure for estimating seismic demands for buildings, Earthquake Engineering & Structural Dynamics 31 (2002) 561–582, doi:10.1002/eqe.144.

G. P. Cimellaro, O. Lavan, A. M. Reinhorn, Design of passive systems for control of inelastic structures, Earthquake Engineering & Structural Dynamics 38 (6) (2009) 783–804, doi:10.1002/eqe.867.

G. P. Cimellaro, D. Lopez-Garcia, Algorithm for design of controlled motion of adjacent structures, Structural Control and Health Monitoring 18 (2) (2011) 140–148, doi:10.1002/stc.357.

R. W. Clough, J. Penzien, Dynamics of Structures, Computers and Structures, Inc., 3rd edn., 2003.

G. L. Cole, R. P. Dhakal, F. M. Turner, Building pounding damage observed in the 2011 Christchurch earthquake, Earthquake Engineering & Structural Dynamics 41 (5) (2012) 893–913, doi:10.1002/eqe.1164.

S. Cui, Integrated design methodology for isolated floor systems in single-degree-of-freedom structural fuse systems, Ph.D. thesis, State University of New York, Buffalo, 2012.

K. Dai, B. Li, J. Wang, A. Li, H. Li, J. Li, S. Tesfamariam, Optimal probability-based partial mass isolation of elevated coal scuttle in thermal power plant building, The Structural Design of Tall and Special Buildings 27 (11) (2018) e1477, doi:10.1002/tal.1477.

M. D'Amico, R. Puglia, E. Russo, C. Maini, F. Pacor, L. Luzi, SYNTHESIS: a web repository of synthetic waveforms, Bulletin of Earthquake Engineering 15 (6) (2017) 2483–2496, doi:10.1007/s10518-016-9982-8.

M. De Angelis, S. Perno, A. Reggio, Dynamic response and optimal design of structures with large mass ratio TMD, Earthquake Engineering & Structural Dynamics 41 (1) (2012) 41–60, doi:10.1002/eqe.1117.

D. De Domenico, G. Ricciardi, An enhanced base isolation system equipped with optimal tuned mass damper inerter (TMDI), Earthquake Engineering & Structural Dynamics 47 (5) (2018a) 1169–1192, doi:10.1002/eqe.3011.

D. De Domenico, G. Ricciardi, Optimal design and seismic performance of tuned mass damper inerter (TMDI) for structures with nonlinear base isolation systems, Earthquake Engineering & Structural Dynamics 47 (12) (2018b) 2539–2560, doi:10.1002/eqe.3098.

D. Demetriou, N. Nikitas, K. D. Tsavdaridis, Performance of fixed-parameter control algorithms on high-rise structures equipped with semi-active tuned mass dampers, The Structural Design of Tall and Special Buildings 25 (7) (2016) 340–354, doi:10.1002/tal.1261.

R. Ding, M. Tao, M. Zhou, J. Nie, Seismic behavior of RC structures with absence of floor slab constraints and large mass turbine as a non-conventional TMD: a case study, Bulletin of Earthquake Engineering 13 (11) (2015) 3401–3422, doi:10.1007/s10518-015-9777-3.

M. Dolce, D. Cardone, G. Palermo, Seismic isolation of bridges using isolation systems based on flat sliding bearings, Bulletin of Earthquake Engineering 5 (4) (2007) 491–509, doi:10.1007/s10518-007-9044-3.

L. Dueñas-Osorio, A. Kwasinski, Quantification of lifeline system interdependencies after the 27 February 2010 Mw 8.8 offshore Maule, Chile, earthquake, Earthquake Spectra 28 (S1) (2012) S581–S603, doi:10.1193/1.4000054.

M. O. Eberhard, S. Baldridge, J. Marshall, W. Mooney, G. J. Rix, The Mw 7.0 Haiti earthquake of January 12, 2010: USGS/EERI advance reconnaissance team report, US Geological Survey Open-File Report 1048 (58) (2010) 2010.

S. Elias, V. Matsagar, T. Datta, Distributed multiple tuned mass dampers for wind response control of chimney with flexible foundation, Procedia Engineering 199 (2017) 1641–1646, doi:10.1016/j.proeng.2017.09.087.

D. M. Fenz, M. C. Constantinou, Modeling triple friction pendulum bearings for response-history analysis, Earthquake Spectra 24 (4) (2008a) 1011–1028, doi:10.1193/1.2982531.

D. M. Fenz, M. C. Constantinou, Spherical sliding isolation bearings with adaptive behavior: Experimental verification, Earthquake Engineering & Structural Dynamics 37 (2) (2008b) 185–205, doi:10.1002/eqe.750.

D. M. Fenz, M. C. Constantinou, Spherical sliding isolation bearings with adaptive behavior: Theory, Earthquake Engineering & Structural Dynamics 37 (2) (2008c) 163–183, doi:10.1002/eqe.751.

O. Flodén, G. Sandberg, K. Persson, Reduced order modelling of elastomeric vibration isolators in dynamic substructuring, Engineering Structures 155 (2018) 102–114, doi:10.1016/j.engstruct.2017.11.001.

M. Fröling, K. Persson, P.-E. Austrell, A reduced model for the design of glass structures subjected to dynamic impulse load, Engineering Structures 80 (2014) 53–60, doi:10.1016/j.engstruct.2014.08.043.

L. Gallanti, D. Forcellini, Numeric Validation of 3D Printer Technology Applied to Story Isolation on Tall Buildings, Journal of Statistical Science and Application 4 (05-06) (2016) 132–143, doi:10.17265/2328-224X/2016.0506.002.

H. P. Gavin, The Levenberg-Marquardt method for nonlinear least squares curve-fitting problems, online, URL http://people.duke.edu/~hpgavin/lm.pdf, 2017.

H. P. Gavin, A. Zaicenco, Performance and reliability of semi-active equipment isolation, Journal of Sound and Vibration 306 (2007) 74–90, doi:10.1016/j.jsv.2007.05.039.

O. Gendelman, Targeted energy transfer in systems with external and self-excitation, Proceedings of the Institution of Mechanical Engineers, Part C: Journal of Mechanical Engineering Science 225 (9) (2011) 2007–2043, doi:10.1177/0954406211413976.

O. Gendelman, L. I. Manevitch, A. F. Vakakis, R. M'Closkey, Energy pumping in nonlinear mechanical oscillator: Part I—Dynamics of the underlying Hamiltonian systems, Journal of Applied Mechanics 68 (2001) 34–41, doi:10.1115/1.1345524.

O. V. Gendelman, Transition of energy to a nonlinear localized mode in a highly asymmetric system of two oscillators, Nonlinear Dynamics 25 (1-3) (2001) 237–253, doi:10.1007/978-94-017-2452-4_13.

L. F. Geschwindner, Non-linear dynamic analysis of modal superposition, Journal of Structural Division-ASCE 107 (1981) 2325–2336.

S. Gholizadeh, O. A. Samavati, Structural optimization by wavelet transforms and neural networks, Applied Mathematical Modelling 35 (2) (2011) 915–929, doi:10.1016/j.apm.2010.07.046.

I. Gidaris, A. A. Taflanidis, Parsimonious modeling of hysteretic structural response in earthquake engineering: Calibration/validation and implementation in probabilistic risk assessment, Engineering Structures 49 (2013) 1017–1033, doi:10.1016/j.engstruct.2012.12.030.

I. Gidaris, A. A. Taflanidis, D. Lopez-Garcia, G. P. Mavroeidis, Multi-objective risk-informed design of floor isolation systems, Earthquake Engineering & Structural Dynamics 45 (8) (2016) 1293–1313, doi:10.1002/eqe.2708.

I. Gidaris, A. A. Taflanidis, G. P. Mavroeidis, Kriging metamodeling in seismic risk assessment based on stochastic ground motion models, Earthquake Engineering & Structural Dynamics 44 (14) (2015) 2377–2399, doi:10.1002/eqe.2586.

R. K. Goel, A. K. Chopra, Evaluation of modal and FEMA pushover analyses: SAC buildings, Earthquake Spectra 20 (1) (2004) 225–254, doi:10.1193/1.1646390.

E. Gourdon, N. A. Alexander, C. A. Taylor, C.-H. Lamarque, S. Pernot, Nonlinear energy pumping under transient forcing with strongly nonlinear coupling: Theoretical and experimental results, Journal of Sound and Vibration 300 (3-5) (2007) 522–551, doi:10.1016/j.jsv.2006.06.074.

E. Gourdon, C.-H. Lamarque, Energy pumping with various nonlinear structures: numerical evidences, Nonlinear Dynamics 40 (3) (2005) 281–307, doi:10.1007/s11071-005-6610-6.

L. Guerreiro, J. Azevedo, A. H. Muhr, Seismic tests and numerical modeling of a rolling-ball isolation system, Journal of Earthquake Engineering 11(1) (2007) 49–66, doi:10.1080/13632460601123172.

R. J. Guyan, Reduction of stiffness and mass matrices, AIAA Journal 3 (1965) 380, doi:10.2514/3.2874.

M. Hamidi, M. H. El Naggar, On the performance of SCF in seismic isolation of the interior equipment of buildings, Earthquake Engineering & Structural Dynamics 36 (2007) 1581–1604, doi:10.1002/eqe.708.

P. S. Harvey, Jr., G. Elisha, C. D. Casey, Experimental investigation of an impact-based, dual-mode vibration isolator/absorber system, International Journal of Non-Linear Mechanics 104 (2018) 59–66, doi:10.1016/j.ijnonlinmec.2018.02.013.

P. S. Harvey, Jr., H. P. Gavin, The nonholonomic and chaotic nature of a rolling isolation system, Journal of Sound and Vibration 332 (14) (2013) 3535–3551, doi:10.1016/j.jsv.2013.01.036.

P. S. Harvey, Jr., H. P. Gavin, Double rolling isolation systems: A mathematical model and experimental validation, International Journal of Non-Linear Mechanics 61 (2014a) 80–92, doi:10.1016/j.ijnonlinmec.2014.01.011.

P. S. Harvey, Jr., H. P. Gavin, Truly isotropic biaxial hysteresis with arbitrary knee sharpness, Earthquake Engineering & Structural Dynamics 43 (2014b) 2051–2057, doi:10.1002/eqe.2436.

P. S. Harvey, Jr., H. P. Gavin, Assessment of a rolling isolation system using reduced order structural models, Engineering Structures 99 (2015) 708–725, doi:10.1016/j.engstruct.2015.05.022.

P. S. Harvey, Jr., H. P. Gavin, J. T. Scruggs, J. M. Rinker, Determining the physical limits on semi-active control performance: A tutorial, Structural Control and Health Monitoring 21 (2014a) 803–816, doi:10.1002/stc.1602.

P. S. Harvey, Jr., K. C. Kelly, A review of rolling-type seismic isolation: Historical development and future directions, Engineering Structures 125 (2016) 521–531, doi:10.1016/j.engstruct.2016.07.031.

P. S. Harvey, Jr., G.-P. Zéhil, H. P. Gavin, Experimental validation of simplified models for rolling isolation systems, Earthquake Engineering & Structural Dynamics 43 (2014b) 1067–1088, doi:10.1002/eqe.2387.

F. Herrada, J. García-Martínez, A. Fraile, L. Hermanns, F. Montáns, A method for performing efficient parametric dynamic analyses in large finite element models undergoing structural modifications, Engineering Structures 131 (2017) 625–638, doi:10.1016/j.engstruct.2016.10.026.

N. Hoang, Y. Fujino, P. Warnitchai, Optimal tuned mass damper for seismic applications and practical design formulas, Engineering Structures 30 (3) (2008) 707–715, doi:10.1016/j.engstruct.2007.05.007.

G. W. Housner, L. A. Bergman, T. K. Caughey, A. G. Chassiakos, R. O. Claus, S. F. Masri, R. E. Skelton, T. T. Soong, B. F. Spencer, J. T. P. Yao, Structural control: Past, present, and future, Journal of Engineering Mechanics 123 (1997) 897–971, doi:10.1061/(ASCE)0733-9399(1997)123:9(897).

G. W. Housner, T. T. Soong, S. F. Masri, Second Generation of Active Structural Control in Civil Engineering, Computer-Aided Civil and Infrastructure Engineering 11 (5) (1996) 289–296, doi:10.1111/j.1467-8667.1996.tb00443.x.

J. B. Hunt, J.-C. Niessen, The broadband dynamic vibration absorber, Journal of Sound and Vibration 83 (1982) 573–578, doi:10.1016/S0022-460X(82)80108-9.

IBM, POWER7 Information: Vibration & Shock. Systems Hardware Information, URL http://pic.dhe.ibm.com/infocenter/poersys/v3r1m5/index.jsp?topic=/p7ebe/p7ebevibrtionandshock.htm, 2010.

H. Iemura, T. Taghikhany, S. K. Jain, Optimum design of resilient sliding isolation system for seismic protection of equipments, Bulletin of Earthquake Engineering 5 (1) (2007) 85–103, doi:10.1007/s10518-006-9010-5.

T. Igusa, A. Der Kiureghian, Dynamic characterization of two-degree-of-freedom equipment-structure systems, Journal of Engineering Mechanics 111 (1) (1985) 1–19, doi:10.1061/(ASCE)0733-9399(1985)111:1(1).

M. Ismail, Elimination of torsion and pounding of isolated asymmetric structures under near-fault ground motions, Structural Control and Health Monitoring 22 (11) (2015b) 1295–1324, doi:10.1002/stc.1746.

M. Ismail, Inner pounding control of the RNC isolator and its impact on seismic isolation efficiency under near-fault earthquakes, Engineering Structures 86 (Supplement C) (2015c) 99–121, doi:10.1016/j.engstruct.2014.12.041.

M. Ismail, An isolation system for limited seismic gaps in near-fault zones, Earthquake Engineering & Structural Dynamics 44 (7) (2015a) 1115–1137, doi:10.1002/eqe.2504.

M. Ismail, J. Rodellar, F. Ikhouane, An innovative isolation bearing for motion-sensitive equipment, Journal of Sound and Vibration 326 (2009) 503–521, doi:10.1016/j.jsv.2009.06.022.

T. Iwatsubo, Damage to industrial equipment in the 1995 Hyogoken–Nanbu Earthquake, Nuclear Engineering and Design 181 (1-3) (1998) 41–53, doi:10.1016/S0029-5493(97)00333-6.

R. S. Jangid, Stochastic seismic response of structures isolated by rolling rods, Engineering Structures 22(8) (2000) 937–946, doi:10.1016/S0141-0296(99)00041-3.

R. S. Jangid, J. M. Kelly, Base isolation for near-fault motions, Earthquake Engineering & Structural Dynamics 30 (5) (2001) 691–707, ISSN 1096-9845, doi:10.1002/eqe.31.

R. Jankowski, S. Mahmoud, Linking of adjacent three-storey buildings for mitigation of structural pounding during earthquakes, Bulletin of Earthquake Engineering 14 (11) (2016) 3075–3097, doi:10.1007/s10518-016-9946-z.

R. Jankowski, K. Wilde, Y. Fujino, Reduction of pounding effects in elevated bridges during earthquakes, Earthquake Engineering & Structural Dynamics 29 (2) (2000) 195–212, doi:10.1002/(SICI)1096-9845(200002)29:2⟨195::AID-EQE897⟩3.0.CO;2-3.

M. Javanbakht, S. Cheng, F. Ghrib, Refined damper design formula for a cable equipped with a positive or negative stiffness damper, Structural Control and Health Monitoring 25 (10) (2018) e2236, doi:10.1002/stc.2236.

P. C. Jennings, G. W. Housner, N. C. Tsai, Simulated earthquake motions, California Institute of Technology, 1968.

B.-G. Jeon, S.-J. Chang, S.-W. Kim, N.-S. Kim, Base isolation performance of a cone-type friction pendulum bearing system, Structural Engineering and Mechanics 53 (2015) 227–248, doi:10.12989/sem.2015.53.2.227.

G. Jia, I. Gidaris, A. A. Taflanidis, G. P. Mavroeidis, Reliability-based assessment/design of floor isolation systems, Engineering Structures 78 (2014) 41–56, doi:10.1016/j.engstruct.2014.07.031.

K. Kanai, Semi-Empirical Formula for the Seismic Characteristics of the Ground, Bulletin of the Earthquake Research Institute 35, University of Tokyo, Tokyo, Japan.

R. Kappagantu, B. F. Feeny, An "optimal" modal reduction of a system with frictional excitation, Journal of Sound and Vibration 224 (1999) 863–877, doi:10.1006/jsvi.1999.2165.

J. M. Kelly, Aseismic base isolation: review and bibliography, Soil Dynamics and Earthquake Engineering 5 (4) (1986) 202–216, doi:10.1016/0267-7261(86)90006-0.

J. M. Kelly, Base Isolation: Linear Theory and Design, Earthquake Spectra 6 (2) (1990) 223–244, doi:10.1193/1.1585566.

J. M. Kelly, The role of damping in seismic isolation, Earthquake Engineering & Structural Dynamics 28 (1999) 3–20, doi:10.1002/(SICI)1096-9845(199901)28:1⟨3::AID-EQE801⟩3.0.CO;2-D.

Z. A. Kemeny, Ball-in-cone rolling isolation systems U.S. Patent 5599106.

H. Khechfe, M. Noori, Z. Hou, J. M. Kelly, G. Ahmadi, An experimental study on the seismic response of base-isolated secondary systems, Journal of Pressure Vessel Technology 124 (1) (2002) 81–88, doi:10.1115/1.1445795.

F. Khoshnoudian, E. Ahmadi, M. Kiani, M. H. Tehrani, Collapse capacity of soil-structure systems under pulse-like earthquakes, Earthquake Engineering & Structural Dynamics 44 (3) (2015b) 481–490, doi:10.1002/eqe.2501.

F. Khoshnoudian, E. Ahmadi, M. Kiani, M. H. Tehrani, Dynamic instability of soil-SDOF structure systems under far-fault earthquakes, Earthquake Spectra 31 (4) (2015a) 2419–2441, doi:10.1193/062613EQS170M.

P. Komodromos, P. C. Polycarpou, L. Papaloizou, M. C. Phocas, Response of seismically isolated buildings considering poundings, Earthquake Engineering & Structural Dynamics 36 (12) (2007) 1605–1622, doi:10.1002/eqe.692.

D. Konstantinidis, N. Makris, Experimental and analytical studies on the response of freestanding laboratory equipment to earthquake shaking, Earthquake Engineering and Structural Dynamics 38 (2009) 827–848, doi:10.1002/eqe.871.

D. Konstantinidis, N. Makris, Experimental and analytical studies on the response of 1/4-scale models of freestanding laboratory equipment subjected to strong earthquake shaking, Bulletin of Earthquake Engineering 8 (6) (2010) 1457–1477, doi:10.1007/s10518-010-9192-8.

R. J. Kuether, B. J. Deaner, J. J. Hollkamp, M. S. Allen, Evaluation of geometrically nonlinear reduced-order models with nonlinear normal modes, AIAA Journal 53 (11) (2015) 3273–3285, doi:10.2514/1.J053838.

N. D. Lagaros, M. Fragiadakis, Evaluation of ASCE-41, ATC-40 and N2 static pushover methods based on optimally designed buildings, Soil Dynamics and Earthquake Engineering 31 (1) (2011) 77–90, doi:10.1016/j.soildyn.2010.08.007.

V. Lambrou, M. C. Constantinou, Study of seismic isolation systems for computer floors, Tech. Rep. NCEER-94-0020, National Center for Earthquake Engineering Research, 1994.

I. F. Lazar, S. A. Neild, D. J. Wagg, Using an inerter-based device for structural vibration suppression, Earthquake Engineering & Structural Dynamics 43 (8) (2014) 1129–1147, doi:10.1002/eqe.2390.

D. Lee, M. C. Constantinou, Combined horizontal–vertical seismic isolation system for high-voltage–power transformers: development, testing and validation, Bulletin of Earthquake Engineering 16 (9) (2018) 4273–4296, doi:10.1007/s10518-018-0311-2.

K. A. Levenberg, A method for the solution of certain non-linear problems in least squares, Quarterly of Applied Mathematics 2 (1944) 164–168.

J.-W. Lin, R. Betti, A. W. Smyth, R. W. Longman, On-line identification of non-linear hysteretic structural systems using a variable trace approach, Earthquake Engineering & Structural Dynamics 30 (9) (2001) 1279–1303, doi:https://doi.org/10.1002/eqe.63.

M.-Y. Liu, W.-L. Chiang, J.-H. Hwang, C.-R. Chu, Wind-induced vibration of high-rise building with tuned mass damper including soil–structure interaction, Journal of Wind Engineering and Industrial Aerodynamics 96 (6-7) (2008) 1092–1102, doi:10.1016/j.jweia.2007.06.034.

Y. Liu, J. Wu, M. Donà, Effectiveness of fluid-viscous dampers for improved seismic performance of inter-storey isolated buildings, Engineering Structures 169 (2018) 276–292, doi:10.1016/j.engstruct.2018.05.031.

D. Lopez Garcia, T. T. Soong, Sliding fragility of block-type non-structural components. Part 1: Unrestrained components, Earthquake Engineering & Structural Dynamics 32 (2003a) 111–129, doi:10.1002/eqe.217.

D. Lopez Garcia, T. T. Soong, Sliding fragility of block-type non-structural components. Part 2: Restrained components, Earthquake Engineering & Structural Dynamics 32 (2003b) 131–149, doi:10.1002/eqe.218.

L.-Y. Lu, T.-Y. Lee, S.-Y. Juang, S.-W. Yeh, Polynomial friction pendulum isolators (PFPIs) for building floor isolation: An experimental and theoretical study, Engineering Structures 56 (2013) 970–982, doi:10.1016/j.engstruct.2013.06.016.

L.-Y. Lu, T.-Y. Lee, S.-W. Yeh, Theory and experimental study for sliding isolators with variable curvature, Earthquake Engineering & Structural Dynamics 40 (2011) 1609–1627, doi:10.1002/eqe.1106.

Z. Lu, X. Chen, D. Zhang, K. Dai, Experimental and analytical study on the performance of particle tuned mass dampers under seismic excitation, Earthquake Engineering & Structural Dynamics 46 (5) (2017) 697–714, doi:10.1002/eqe.2826.

J. Luo, N. E. Wierschem, L. A. Fahnestock, B. F. Spencer Jr, D. D. Quinn, D. M. McFarland, A. F. Vakakis, L. A. Bergman, Design, simulation, and large-scale testing of an innovative vibration mitigation device employing essentially nonlinear elastomeric springs, Earthquake Engineering & Structural Dynamics 43 (12) (2014a) 1829–1851, doi:10.1002/eqe.2424.

J. Luo, N. E. Wierschem, S. A. Hubbard, L. A. Fahnestock, D. D. Quinn, D. M. McFarland, B. F. Spencer Jr, A. F. Vakakis, L. A. Bergman, Large-scale experimental evaluation and numerical simulation of a system of nonlinear energy sinks for seismic mitigation, Engineering Structures 77 (2014b) 34–48, doi:10.1016/j.engstruct.2014.07.020.

N. Makris, S.-P. Chang, Effect of viscous, viscoplastic and friction damping on the response of seismic isolated structures, Earthquake Engineering & Structural Dynamics 29 (1) (2000) 85–107, doi:10.1002/(SICI)1096-9845(200001)29:1⟨85::AID-EQE902⟩3.0.CO;2-N.

G. Manoukas, A. Athanatopoulou, I. Avramidis, Static pushover analysis based on an energy-equivalent SDOF system, Earthquake Spectra 27 (1) (2011) 89–105, doi:10.1193/1.3535597.

C. Marin-Artieda, X. Han, Experimental developments in isolation/energy dissipation platforms for the seismic protection of equipment in multistory facilities, in: Second ATC & SEI conference on improving the seismic performance of existing buildings and other structures, ASCE, San Francisco, CA, USA, 509–523, doi:10.1061/9780784479728.042, 2015.

D. Marquardt, An algorithm for least-squares estimation of nonlinear parameters, SIAM Journal on Applied Mathematics 11(2) (1963) 431–441, doi:10.1137/0111030.

J. D. Marshall, F. A. Charney, A hybrid passive control device for steel structures, I: Development and analysis, Journal of Constructional Steel Research 66 (10) (2010) 1278–1286, doi:10.1016/j.jcsr.2010.04.005.

H. Masaeli, F. Khoshnoudian, M. H. Tehrani, Rocking isolation of nonductile moderately tall buildings subjected to bidirectional near-fault ground motions, Engineering Structures 80 (2014) 298–315, doi:10.1016/j.engstruct.2014.08.053.

E. Matta, Lifecycle cost optimization of tuned mass dampers for the seismic improvement of inelastic structures, Earthquake Engineering & Structural Dynamics 47 (3) (2018) 714–737, doi:10.1002/eqe.2987.

S. Mazzoni, F. McKenna, M. H. Scott, G. L. Fenves, et al., *OpenSees* Command Language Manual, online, URL http://opensees.berkeley.edu/OpenSees/manuals/usermanual/, 2009.

J. C. Medina, A. Taflanidis, Probabilistic measures for assessing appropriateness of robust design optimization solutions, Structural and Multidisciplinary Optimization 51 (4) (2015) 813–834, doi:10.1007/s00158-014-1160-5.

E. Miranda, G. Mosqueda, R. Retamales, G. Pekcan, Performance of nonstructural components during the 27 February 2010 Chile earthquake, Earthquake Spectra 28 (S1) (2012) S453–S471, doi:10.1193/1.4000032.

A. M. Mirza, Verification of model reduction for hysteretic structural response, M.S. Thesis, Duke University, Department of Civil and Environmental Engineering, 2014.

M. Mousavi, A. H. Gandomi, A hybrid damage detection method using dynamic-reduction transformation matrix and modal force error, Engineering Structures 111 (2016) 425–434, doi:10.1016/j.engstruct.2015.12.033.

A. H. Muhr, G. Bergamo, Shaking table tests on rolling-ball rubber-layer isolation system, in: 14th European Conference on Earthquake Engineering, 2010.

F. Naeim, J. M. Kelly, Design of seismic isolated structures: from theory to practice, John Wiley & Sons, New York, NY, 1999.

S. Nagarajaiah, X. Sun, Base-isolated FCC building: impact response in Northridge earthquake, Journal of Structural Engineering 127 (9) (2001) 1063–1075, doi:10.1061/(ASCE)0733-9445(2001)127:9(1063).

B. D. Notohardjono, J. Wilcoski, J. B. Gambill, Design of earthquake resistant server computer structures, Journal of Pressure Vessel Technology 126 (1) (2004) 66–74, doi:10.1115/1.1638389.

Y. Ohtori, R. E. Christenson, B. F. Spencer, Jr., S. J. Dyke, Benchmark Control Problems for Seismically Excited Nonlinear Buildings, Journal of Engineering Mechanics 130 (2004) 366–385, doi:10.1061/(ASCE)0733-9399(2004)130:4(366).

M. J. Olsen, K. F. Cheung, Y. Yamazaki, S. Butcher, M. Garlock, S. Yim, S. McGarity, I. Robertson, L. Burgos, Y. L. Young, Damage assessment of the 2010 Chile earthquake and tsunami using terrestrial laser scanning, Earthquake Spectra 28 (S1) (2012) S179–S197, doi:10.1193/1.4000021.

Y. Pan, C. E. Ventura, W. Liam Finn, Effects of Ground Motion Duration on the Seismic Performance and Collapse Rate of Light-Frame Wood Houses, Journal of Structural Engineering 144 (8) (2018) 04018112, doi:10.1061/(ASCE)ST.1943-541X.0002104.

V. Panchal, R. Jangid, Variable friction pendulum system for near-fault ground motions, Structural Control and Health Monitoring 15 (4) (2008) 568–584, doi:10.1002/stc.216.

J. Parajuli, K. E. Haynes, The earthquake impact on telecommunications infrastructure in Nepal: a preliminary spatial assessment, Regional Science Policy & Practice 8 (3) (2016) 95–109, doi:10.1111/rsp3.12075.

Y. J. Park, Y. K. Wen, A. H.-S. Ang, Random vibration of hysteretic systems under bi-directional ground motion, Earthquake Engineering & Structural Dynamics 14 (1986) 543–557, doi:10.1002/eqe.4290140405.

D. T. R. Pasala, A. A. Sarlis, S. Nagarajaiah, A. M. Reinhorn, M. C. Constantinou, D. Taylor, Adaptive Negative Stiffness: New Structural Modification Approach for Seismic Protection, Journal of Structural Engineering 139 (7) (2012) 1112–1123, doi:10.1061/(ASCE)ST.1943-541X.0000615.

M. Paz, Dynamic condensation, AIAA Journal 22 (1985) 724–727, doi:10.2514/3.48498.

C. Petrone, G. Magliulo, G. Manfredi, Floor response spectra in RC frame structures designed according to Eurocode 8, Bulletin of Earthquake Engineering 14 (3) (2016) 747–767, doi:10.1007/s10518-015-9846-7.

D. Pietrosanti, M. De Angelis, M. Basili, Optimal design and performance evaluation of systems with Tuned Mass Damper Inerter (TMDI), Earthquake Engineering & Structural Dynamics 46 (8) (2017) 1367–1388, doi:10.1002/eqe.2861.

P. C. Polycarpou, P. Komodromos, Earthquake-induced poundings of a seismically isolated building with adjacent structures, Engineering Structures 32 (7) (2010) 1937–1951, doi:10.1016/j.engstruct.2010.03.011.

F. Pratesi, S. Sorace, G. Terenzi, Analysis and mitigation of seismic pounding of a slender R/C bell tower, Engineering Structures 71 (2014) 23–34, doi:10.1016/j.engstruct.2014.04.006.

M. Raghunandan, A. B. Liel, Effect of ground motion duration on earthquake-induced structural collapse, Structural Safety 41 (2013) 119–133, doi:10.1016/j.strusafe.2012.12.002.

S. E. A. Raheem, Mitigation measures for earthquake induced pounding effects on seismic performance of adjacent buildings, Bulletin of Earthquake Engineering 12 (4) (2014) 1705–1724, doi:10.1007/s10518-014-9592-2.

J. C. Ramallo, E. A. Johnson, B. F. Spencer, "Smart" Base Isolation Systems, Journal of Engineering Mechanics 128 (10) (2002) 1088–1099, doi:10.1061/(ASCE)0733-9399(2002)128:10(1088).

M. Ramezani, A. Bathaei, A. K. Ghorbani-Tanha, Application of artificial neural networks in optimal tuning of tuned mass dampers implemented in high-rise buildings subjected to wind load, Earthquake Engineering and Engineering Vibration 17 (4) (2018) 903–915, doi:10.1007/s11803-018-0483-4.

A. Reggio, M. D. Angelis, Optimal energy-based seismic design of non-conventional Tuned Mass Damper (TMD) implemented via inter-story isolation, Earthquake Engineering & Structural Dynamics 44 (10) (2015) 1623–1642.

A. Reggio, M. De Angelis, Optimal design of an equipment isolation system with nonlinear hysteretic behaviour, Earthquake Engineering & Structural Dynamics 42 (13) (2013) 1907–1930, doi:10.1002/eqe.2304.

A. Reggio, M. De Angelis, Combined primary–secondary system approach to the design of an equipment isolation system with High-Damping Rubber Bearings, Journal of Sound and Vibration 333 (9) (2014) 2386–2403, doi:10.1016/j.jsv.2013.12.006.

J. C. Reyes, A. K. Chopra, Evaluation of three-dimensional modal pushover analysis for unsymmetric-plan buildings subjected to two components of ground motion, Earthquake Engineering & Structural Dynamics 40 (13) (2011) 1475–1494, doi:10.1002/eqe.1100.

H. Rice, J. McCraith, Practical non-linear vibration absorber design, Journal of Sound Vibration 116 (1987) 545–559, doi:10.1016/S0022-460X(87)81383-4.

K. L. Ryan, N. D. Dao, Influence of Vertical Ground Shaking on Horizontal Response of Seismically Isolated Buildings with Friction Bearings, Journal of Structural Engineering 142 (1) (2016) 04015089, doi:10.1061/(ASCE)ST.1943-541X.0001352.

K. L. Ryan, C. L. Earl, Analysis and design of inter-story isolation systems with nonlinear devices, Journal of Earthquake Engineering 14 (7) (2010) 1044–1062, doi:10.1080/13632461003668020.

S. K. Saha, V. A. Matsagar, A. K. Jain, Seismic fragility of base-isolated water storage tanks under non-stationary earthquakes, Bulletin of Earthquake Engineering 14 (4) (2016) 1153–1175, doi:10.1007/s10518-016-9874-y.

A. Sahraei, F. Behnamfar, A drift pushover analysis procedure for estimating the seismic demands of buildings, Earthquake Spectra 30 (4) (2014) 1601–1618, doi:10.1193/030811EQS038M.

E. Sato, S. Furukawa, A. Kakehi, M. Nakashima, Full-scale shaking table test for examination of safety and functionality of base-isolated medical facilities, Earthquake Engineering & Structural Dynamics 40 (13) (2011) 1435–1453, doi:10.1002/eqe.1097.

A. H. Schellenberg, T. C. Becker, S. A. Mahin, Hybrid shake table testing method: Theory, implementation and application to midlevel isolation, Structural Control and Health Monitoring 24 (5) (2017) e1915, doi:10.1002/stc.1915.

P. Shahbazi, T. Taghikhany, Sensitivity analysis of variable curvature friction pendulum isolator under near-fault ground motions, SMART STRUCTURES AND SYSTEMS 20 (1) (2017) 23–33, doi:10.12989/sss.2017.20.1.023.

Y. Shi, K. Saburi, M. Nakashima, Second-mode tuned mass dampers in base-isolated structures for reduction of floor acceleration, Earthquake Engineering & Structural Dynamics 47 (12) (2018) 2519–2538, doi:10.1002/eqe.3097.

G. Simoneschi, A. Geniola, A. M. De Leo, A. Di Egidio, On the seismic performances of rigid block-like structures coupled with an oscillating mass working as a TMD, Earthquake Engineering & Structural Dynamics 46 (9) (2017) 1453–1469, doi:10.1002/eqe.2864.

R. Soheilifard, A hierarchical non-iterative extension of the Guyan condensation method for damped structures, Journal of Sound and Vibration 344 (2015) 434–446, doi:10.1016/j.jsv.2015.01.050.

A. Soom, M.-s. Lee, Optimal design of linear and nonlinear vibration absorbers for damped systems, Journal of Vibration, Acoustics, Stress, and Reliability in Design 105 (1) (1983) 112–119, doi:10.1115/1.3269054.

T. T. Soong, G. F. Dargush, Passive energy dissipation systems in structural engineering, Wiley, New York, 1997.

B. F. Spencer, Jr, M. K. Sain, Controlling buildings: a new frontier in feedback, IEEE Control Systems 17 (1997) 19–35, doi:10.1109/37.642972.

R. Stone, Damaged University Mourns Its Dead–and Plans Fast Recovery, doi:10.1126/science.320.5880.1145a, 2008.

H. Sucuoğlu, M. S. Gïay, Generalized force vectors for multi-mode pushover analysis, Earthquake Engineering & Structural Dynamics 40 (1) (2011) 55–74, doi:10.1002/eqe.1020.

T. Sun, Z. Lai, S. Nagarajaiah, H.-N. Li, Negative stiffness device for seismic protection of smart base isolated benchmark building, Structural Control and Health Monitoring 24 (11) (2017) e1968, doi:10.1002/stc.1968.

M. D. Symans, S. W. Kelly, Fuzzy logic control of bridge structures using intelligent semi-active seismic isolation systems, Earthquake Engineering & Structural Dynamics 28 (1) (1999) 37–60, doi:10.1002/(SICI)1096-9845(199901)28:1⟨37::AID-EQE803⟩3.0.CO;2-Z.

H. Tajimi, A statistical method of determining the maximum response of a building structure during an earthquake, in: Proc. 2nd World Conference on Earthquake Engineering, vol. II, 781–798, 1960.

H. Takabatake, M. Yasui, Y. Nakagawa, A. Kishida, Relaxation method for pounding action between adjacent buildings at expansion joint, Earthquake Engineering & Structural Dynamics 43 (9) (2014) 1381–1400, doi:10.1002/eqe.2402.

M. H. Tehrani, P. S. Harvey, Jr., Enhanced passive control of dual-mode systems under extreme seismic loading: An optimal control approach, Structural Control and Health Monitoring 26 (7) (2019b) e2367, doi:10.1002/stc.2367.

M. H. Tehrani, P. S. Harvey, Jr., Generation of synthetic accelerograms for telecommunications equipment: fragility assessment of a rolling isolation system, Bulletin of Earthquake Engineering 17 (3) (2019a) 1715–1737, doi:10.1007/s10518-018-0505-7.

M. H. Tehrani, P. S. Harvey, Jr., H. P. Gavin, A. M. Mirza, Inelastic condensed dynamic models for estimating seismic demands for buildings, Engineering Structures 177 (2018) 616–629, doi:10.1016/j.engstruct.2018.07.083.

M. H. Tehrani, F. Khoshnoudian, Extended consecutive modal pushover procedure for estimating seismic responses of one-way asymmetric plan tall buildings considering soil-structure interaction, Earthquake Engineering and Engineering Vibration 13 (3) (2014) 487–507, doi:10.1007/s11803-014-0257-6.

M. H. Tehrani, A. Mellati, M. Fallahian, F. Khoshnoudian, Evaluation of Different Lateral Load Patterns in Estimating Seismic Demands of 3D Mass Eccentric Mid-rise Building, in: Proc. of the Int. Con. On Advances In Structural, Civil And Environmental Eng. (SCEE), IRED, Kuala Lumpur, Malaysia, 90–94, 2013b.

M. H. Tehrani, A. Mellati, F. Khoshnoudian, New lateral load pattern for estimating seismic demands of elevated water tanks supported on concrete shaft, in: Proc. of the Int. Con. On Advances In Structural, Civil And Environmental Eng. (SCEE), IRED, Kuala Lumpur, Malaysia, 104–108, 2013a.

Telcordia, NEBS Requirements: Physical Protection, GR-63-CORE, Telcordia Technologies, Inc., Piscataway, NJ, 2012.

Telcoridia, NEBS Requirements: Physical Protection, GR-63-CORE, Telcordia Technologies, Inc., Piscataway, NJ, 2012.

S. Tesfamariam, K. Goda, Impact of Earthquake Types and Aftershocks on Loss Assessment of Non-Code-Conforming Buildings: Case Study with Victoria, British Columbia, Earthquake Spectra 33 (2) (2017) 551–579, doi:10.1193/011416EQS013M.

S. Tesfamariam, K. Goda, G. Mondal, Seismic vulnerability of reinforced concrete frame with unreinforced masonry infill due to main shock–aftershock earthquake sequences, Earthquake Spectra 31 (3) (2015) 1427–1449, doi:10.1193/042313EQS111M.

C. Tsai, Y.-C. Lin, W.-S. Chen, H. Su, Tri-directional shaking table tests of vibration sensitive equipment with static dynamics interchangeable-ball pendulum system, Earthquake Engineering and Engineering Vibration 9 (1) (2010) 103–112, doi:10.1007/s11803-010-9009-4.

C. Tsai, C.-P. Tsou, Y.-C. Lin, M.-J. Chen, W.-S. Chen, The material behavior and isolation benefits of ball pendulum system, in: ASME 2006 Pressure Vessels and Piping/ICPVT-11 Conference, American Society of Mechanical Engineers, 19–25, doi:10.1115/PVP2006-ICPVT-11-93252, 2006.

C. S. Tsai, T.-C. Chiang, B.-J. Chen, Experimental evaluation of piecewise exact solution for predicting seismic responses of spherical sliding type isolated structures, Earthquake Engineering & Structural Dynamics 34 (2005) 1027–1046, doi:10.1002/eqe.430.

A. F. Vakakis, Inducing passive nonlinear energy sinks in vibrating systems, Journal of Vibration and Acoustics 123 (3) (2001) 324–332, doi:10.1115/1.1368883.

A. F. Vakakis, O. Gendelman, Energy pumping in nonlinear mechanical oscillators: part IIresonance capture, Journal of Applied Mechanics 68 (1) (2001) 42–48, doi:10.1115/1.1345525.

R. Vargas, M. Bruneau, Experimental response of buildings designed with metallic structural fuses. II, Journal of Structural Engineering 135 (4) (2009) 394–403, doi:10.1061/(ASCE)0733-9445(2009)135:4(394).

R. Villaverde, Roof isolation system to reduce the seismic response of buildings: A preliminary assessment, Earthquake Spectra 14 (3) (1998) 521–532, doi:10.1193/1.1586013.

R. Villaverde, M. M. Hanna, Efficient mode superposition algorithm for seismic analysis of nonlinear structures, Earthquake Engineering & Structural Dynamics 21 (1992) 849–858, doi:10.1002/eqe.4290211002.

D. Wang, T. K. Tse, Y. Zhou, Q. Li, Structural performance and cost analysis of wind-induced vibration control schemes for a real super-tall building, Structure and Infrastructure Engineering 11 (8) (2015a) 990–1011, doi:10.1080/15732479.2014.925941.

J. Wang, N. Wierschem, B. F. Spencer, X. Lu, Experimental study of track nonlinear energy sinks for dynamic response reduction, Engineering Structures 94 (2015b) 9–15, doi:10.1016/j.engstruct.2015.03.007.

J. Wang, N. Wierschem, B. F. Spencer Jr, X. Lu, Numerical and experimental study of the performance of a single-sided vibro-impact track nonlinear energy sink, Earthquake Engineering & Structural Dynamics 45 (4) (2016) 635–652, doi:10.1002/eqe.2677.

S.-J. Wang, B.-H. Lee, W.-C. Chuang, K.-C. Chang, Optimum dynamic characteristic control approach for building mass damper design, Earthquake Engineering & Structural Dynamics 47 (4) (2018) 872–888.

G. P. Warn, K. L. Ryan, A review of seismic isolation for buildings: historical development and research needs, Buildings 2 (3) (2012) 300–325, doi:10.3390/buildings2030300.

Y.-K. Wen, Method for random vibration of hysteretic systems, Journal of Engineering Mechanics 102 (1976) 249–263.

S. Weng, W. Tian, H. Zhu, Y. Xia, F. Gao, Y. Zhang, J. Li, Dynamic condensation approach to calculation of structural responses and response sensitivities, Mechanical Systems and Signal Processing 88 (2017) 302–317, doi:10.1016/j.ymssp.2016.11.025.

N. E. Wierschem, S. A. Hubbard, J. Luo, L. A. Fahnestock, B. F. Spencer, D. M. McFarland, D. D. Quinn, A. F. Vakakis, L. A. Bergman, Response attenuation in a large-scale structure subjected to blast excitation utilizing a system of essentially nonlinear vibration absorbers, Journal of Sound and Vibration 389 (2017) 52–72, doi:10.1016/j.jsv.2016.11.003.

C. W. Wong, Y. Q. Ni, J. M. Ko, Stead-state oscillation of hysteretic differential model II: Performance analysis, Journal of Engineering Mechanics 120 (11) (1994) 2299–2325, doi:10.1061/(ASCE)0733-9399(1994)120:11(2271).

J. Yaghoubian, Isolating building contents from earthquake induced floor motions, Earthquake Spectra 7 (1) (1991) 127–143, doi:10.1193/1.1585617.

J. N. Yang, A. K. Agrawal, Semi-active hybrid control systems for nonlinear buildings against near-field earthquakes, Engineering Structures 24 (3) (2002) 271–280, doi:10.1016/S0141-0296(01)00094-3.

T. Yin, Q.-H. Jiang, K.-V. Yuen, Vibration-based damage detection for structural connections using incomplete modal data by Bayesian approach and model reduction technique, Engineering Structures 132 (2017) 260–277, doi:10.1016/j.engstruct.2016.11.035.

H. Yoshioka, J. C. Ramallo, B. F. Spencer, "Smart" Base Isolation Strategies Employing Magnetorheological Dampers, Journal of Engineering Mechanics 128 (5) (2002) 540–551, doi:10.1061/(ASCE)0733-9399(2002)128:5(540).

H. Zargar, K. L. Ryan, J. D. Marshall, Feasibility study of a gap damper to control seismic isolator displacements in extreme earthquakes, Structural Control and Health Monitoring 20 (8) (2013) 1159–1175, doi:10.1002/stc.1525.

H. Zargar, K. L. Ryan, T. A. Rawlinson, J. D. Marshall, Evaluation of a passive gap damper to control displacements in a shaking test of a seismically isolated three-story frame, Earthquake Engineering & Structural Dynamics 46 (1) (2017) 51–71, doi:10.1002/eqe.2771.

V. A. Zayas, S. S. Low, S. A. Mahin, A simple pendulum technique for achieving seismic isolation, Earthquake Spectra 6 (2) (1990) 317–333, doi:10.1193/1.1585573.

K. Zeynali, H. S. Monir, N. M. Mirzai, J. W. Hu, Experimental and numerical investigation of lead-rubber dampers in chevron concentrically braced frames, Archives of Civil and Mechanical Engineering 18 (1) (2018) 162–178, doi:10.1016/j.acme.2017.06.004.

J. Zhang, N. Makris, Rocking response of free-standing blocks under cycloidal pulses, Journal of Engineering Mechanics 127 (2001) 473–483, doi:10.1061/(ASCE)0733-9399(2001)127:5(473).

Q. Zhou, X. Lu, Q. Wang, D. Feng, Q. Yao, Dynamic analysis on structures base-isolated by a ball system with restoring properties, Earthquake Engineering & Structural Dynamics 27 (1998) 773–791, doi:10.1002/(SICI)1096-9845(199808)27:8⟨773::AID-EQE749⟩3.0.CO;2-A.

M. Ziyaeifar, H. Noguchi, Partial mass isolation in tall buildings, Earthquake Engineering & Structural Dynamics 27 (1) (1998) 49–65, doi:10.1002/(SICI)1096-9845(199801)27:1⟨49::AID-EQE718⟩3.0.CO;2-J.

Appendix A
Tabulated Summary of Optimal and Clipped-LQR Results

A.1 Tabulated Summary of Optimal Results

The following tables summarize the piecewise optimal results for the system with an initial condition of $\boldsymbol{X}(0) = [1, 1]^T$ (Table A.1), $[1, 2]^T$ (Table A.2), $[1, 3]^T$ (Table A.3), $[1, 4]^T$ (Table A.4), $[1, 5]^T$ (Table A.5), $[1, 6]^T$ (Table A.6), $[1, 7]^T$ (Table A.7), $[1, 8]^T$ (Table A.8), $[1, 9]^T$ (Table A.9), and $[1, 10]^T$ (Table A.10).

Table A.1: Summary of piecewise optimal results for the system with an initial condition of $\boldsymbol{X}(0) = [1, 1]^T$.

Q_d/Q_a	Peak X	RMS X	Peak $\ddot{X}$	RMS $\ddot{X}$	τ_f^*	J	K^*	C^*
1×10^{-2} (†)	2.201	1.797	0.529	0.227	7.967	0.335	−1.878	0.418
2×10^{-2} (†)	1.981	1.648	0.648	0.280	6.466	0.429	−2.020	0.511
5×10^{-2} (†)	1.747	1.490	0.849	0.369	4.887	0.605	−2.218	0.669
1×10^{-1} (†)	1.606	1.396	1.046	0.457	3.947	0.796	−2.355	0.824
2×10^{-1}	1.490	1.319	1.292	0.566	3.180	1.063	−2.447	1.017
5×10^{-1}	1.369	1.239	1.715	0.755	2.381	1.592	−2.402	1.347
1×10^{0}	1.296	1.191	2.134	0.945	1.899	2.195	−2.085	1.666
2×10^{0}	1.238	1.153	2.654	1.173	1.530	3.088	−1.383	2.078
5×10^{0}	1.177	1.114	3.565	1.590	1.126	4.914	0.922	2.768
1×10^{1}	1.141	1.091	4.461	1.995	0.896	7.115	4.357	3.451
2×10^{1}	1.113	1.072	5.583	2.497	0.716	10.467	10.237	4.316
5×10^{1}	1.083	1.053	7.595	3.472	0.512	17.266	27.061	5.707
1×10^{2}	1.066	1.042	9.548	4.383	0.405	25.871	48.858	7.150
2×10^{2}	1.053	1.034	11.892	5.358	0.333	40.376	78.588	9.072
5×10^{2}	1.038	1.024	16.507	7.860	0.224	65.604	186.904	11.664
1×10^{3}	1.031	1.020	20.323	9.259	0.192	108.151	266.818	15.092
2×10^{3}	1.024	1.015	25.885	12.112	0.146	161.148	473.053	18.211
5×10^{3}	1.017	1.011	36.176	17.953	0.097	264.537	1069.890	22.893

Note: † = Require an active device.

Table A.2: Summary of piecewise optimal results for the system with an initial condition of $\boldsymbol{X}(0) = [1, 2]^T$.

Q_d/Q_a	Peak X	RMS X	Peak $\ddot{X}$	RMS $\ddot{X}$	τ_{f}^*	J	K^*	C^*
1×10^{-2} (†)	3.625	2.774	0.973	0.410	8.919	1.091	−1.336	0.389
2×10^{-2} (†)	3.167	2.458	1.177	0.498	7.317	1.350	−1.366	0.471
5×10^{-2} (†)	2.676	2.121	1.520	0.648	5.611	1.809	−1.384	0.607
1×10^{-1} (†)	2.375	1.916	1.851	0.793	4.576	2.278	−1.361	0.737
2×10^{-1}	2.125	1.746	2.259	0.973	3.723	2.896	−1.280	0.898
5×10^{-1}	1.859	1.566	2.955	1.281	2.819	4.043	−1.003	1.170
1×10^{0}	1.698	1.458	3.633	1.584	2.276	5.274	−0.561	1.433
2×10^{0}	1.566	1.370	4.478	1.957	1.841	6.978	0.207	1.764
5×10^{0}	1.426	1.277	5.933	2.609	1.378	10.310	2.159	2.327
1×10^{1}	1.342	1.222	7.374	3.271	1.096	14.046	4.945	2.863
2×10^{1}	1.276	1.178	9.148	4.040	0.889	19.596	9.136	3.577
5×10^{1}	1.205	1.132	12.284	5.492	0.651	30.691	20.031	4.725
1×10^{2}	1.165	1.106	15.320	6.832	0.524	44.262	33.429	5.921
2×10^{2}	1.130	1.084	19.284	8.744	0.407	63.406	58.210	7.276
5×10^{2}	1.096	1.062	26.029	11.869	0.300	105.564	112.793	9.771
1×10^{3}	1.077	1.049	32.533	14.722	0.242	159.593	178.012	12.207
2×10^{3}	1.061	1.039	41.188	19.009	0.187	235.042	303.197	14.915
5×10^{3}	1.043	1.028	57.103	27.736	0.126	382.616	656.548	18.783

Note: † = Require an active device.

Table A.3: Summary of piecewise optimal results for the system with an initial condition of $\boldsymbol{X}(0) = [1, 3]^T$.

Q_d/Q_a	Peak X	RMS X	Peak $\ddot{X}$	RMS $\ddot{X}$	τ_f^*	J	K^*	C^*
1×10^{-2} (†)	5.074	3.775	1.413	0.589	9.352	2.287	−1.175	0.380
2×10^{-2} (†)	4.381	3.296	1.702	0.712	7.718	2.794	−1.175	0.458
5×10^{-2} (†)	3.634	2.780	2.182	0.919	5.965	3.669	−1.147	0.586
1×10^{-1} (†)	3.175	2.464	2.640	1.117	4.896	4.540	−1.087	0.708
2×10^{-1}	2.791	2.200	3.201	1.361	4.009	5.656	−0.969	0.857
5×10^{-1}	2.380	1.919	4.150	1.778	3.060	7.656	−0.655	1.105
1×10^{0}	2.129	1.749	5.065	2.180	2.493	9.733	−0.222	1.346
2×10^{0}	1.921	1.608	6.201	2.682	2.022	12.502	0.505	1.642
5×10^{0}	1.701	1.460	8.140	3.541	1.528	17.727	2.219	2.147
1×10^{1}	1.568	1.371	10.037	4.388	1.231	23.428	4.491	2.634
2×10^{1}	1.459	1.298	12.415	5.457	0.989	31.382	8.181	3.244
5×10^{1}	1.344	1.223	16.510	7.300	0.737	47.233	16.702	4.284
1×10^{2}	1.275	1.178	20.611	9.239	0.580	65.008	28.620	5.244
2×10^{2}	1.220	1.142	25.705	11.568	0.463	91.347	46.899	6.524
5×10^{2}	1.165	1.106	34.356	15.349	0.350	148.143	85.847	8.812
1×10^{3}	1.130	1.084	43.302	19.733	0.270	211.449	145.236	10.677
2×10^{3}	1.101	1.066	55.132	26.078	0.203	299.013	257.722	12.933
5×10^{3}	1.075	1.048	74.488	35.353	0.149	504.024	479.869	17.436

Note: † = Require an active device.

Table A.4: Summary of piecewise optimal results for the system with an initial condition of $\boldsymbol{X}(0) = [1, 4]^T$.

Q_d/Q_a	Peak X	RMS X	Peak $\ddot{X}$	RMS $\ddot{X}$	τ_f^*	J	K^*	C^*
1×10^{-2} (†)	6.530	4.785	1.853	0.767	9.604	3.921	−1.099	0.376
2×10^{-2} (†)	5.603	4.142	2.225	0.924	7.953	4.760	−1.085	0.451
5×10^{-2} (†)	4.602	3.449	2.841	1.186	6.179	6.185	−1.037	0.576
1×10^{-1}	3.985	3.022	3.424	1.437	5.090	7.581	−0.962	0.693
2×10^{-1}	3.468	2.666	4.137	1.745	4.183	9.343	−0.830	0.835
5×10^{-1}	2.913	2.284	5.330	2.263	3.217	12.435	−0.510	1.073
1×10^{0}	2.573	2.051	6.477	2.767	2.625	15.570	−0.082	1.298
2×10^{0}	2.290	1.858	7.891	3.385	2.143	19.669	0.600	1.577
5×10^{0}	1.988	1.653	10.290	4.443	1.629	27.195	2.169	2.048
1×10^{1}	1.803	1.529	12.636	5.502	1.311	35.160	4.253	2.492
2×10^{1}	1.652	1.427	15.548	6.799	1.060	46.069	7.489	3.060
5×10^{1}	1.492	1.321	20.556	9.053	0.794	67.158	14.927	4.015
1×10^{2}	1.398	1.258	25.422	11.181	0.643	91.123	24.050	4.973
2×10^{2}	1.319	1.206	31.669	14.107	0.508	124.393	39.936	6.094
5×10^{2}	1.236	1.153	42.547	19.304	0.369	191.289	77.616	8.009
1×10^{3}	1.190	1.123	52.891	23.799	0.300	274.021	120.082	9.941
2×10^{3}	1.150	1.097	66.849	30.955	0.229	384.757	206.008	12.190
5×10^{3}	1.111	1.072	90.006	41.757	0.170	634.661	379.346	16.349

Note: † = Require an active device.

Table A.5: Summary of piecewise optimal results for the system with an initial condition of $\boldsymbol{X}(0) = [1, 5]^T$.

Q_d/Q_a	Peak X	RMS X	Peak $\ddot{X}$	RMS $\ddot{X}$	τ_{f}^*	J	K^*	C^*
1×10^{-2} (†)	7.990	5.799	2.293	0.944	9.769	5.995	−1.055	0.373
2×10^{-2} (†)	6.829	4.992	2.748	1.135	8.109	7.248	−1.033	0.448
5×10^{-2} (†)	5.574	4.122	3.499	1.453	6.320	9.359	−0.975	0.570
1×10^{-1}	4.800	3.586	4.208	1.755	5.224	11.404	−0.891	0.685
2×10^{-1}	4.151	3.137	5.069	2.125	4.307	13.958	−0.753	0.823
5×10^{-1}	3.452	2.655	6.506	2.745	3.324	18.380	−0.431	1.053
1×10^{0}	3.023	2.359	7.879	3.341	2.725	22.798	−0.017	1.271
2×10^{0}	2.664	2.113	9.567	4.081	2.226	28.481	0.642	1.536
5×10^{0}	2.281	1.852	12.414	5.329	1.701	38.728	2.112	1.984
1×10^{1}	2.047	1.693	15.170	6.541	1.383	49.420	3.972	2.418
2×10^{1}	1.853	1.562	18.603	8.077	1.118	63.714	6.941	2.944
5×10^{1}	1.647	1.424	24.471	10.706	0.841	90.822	13.608	3.838
1×10^{2}	1.524	1.342	30.205	13.272	0.677	120.638	22.037	4.721
2×10^{2}	1.423	1.275	37.357	16.435	0.547	162.764	35.055	5.825
5×10^{2}	1.314	1.204	50.020	22.502	0.396	244.125	68.056	7.571
1×10^{3}	1.254	1.164	61.990	27.614	0.324	343.342	104.170	9.539
2×10^{3}	1.202	1.131	77.631	35.040	0.254	481.546	169.883	11.740
5×10^{3}	1.147	1.095	106.087	50.030	0.176	748.640	349.637	14.765

Note: † = Require an active device.

Table A.6: Summary of piecewise optimal results for the system with an initial condition of $\boldsymbol{X}(0) = [1, 6]^T$.

Q_d/Q_a	Peak X	RMS X	Peak $\ddot{X}$	RMS $\ddot{X}$	τ_{f}^*	J	K^*	C^*
1×10^{-2} (†)	9.451	6.814	2.732	1.121	9.885	8.509	−1.025	0.372
2×10^{-2} (†)	8.056	5.845	3.271	1.347	8.219	10.259	−1.000	0.446
5×10^{-2} (†)	6.548	4.798	4.156	1.719	6.424	13.189	−0.934	0.566
1×10^{-1}	5.618	4.153	4.990	2.073	5.319	16.008	−0.846	0.679
2×10^{-1}	4.837	3.612	6.001	2.503	4.396	19.502	−0.704	0.816
5×10^{-1}	3.995	3.029	7.679	3.223	3.404	25.493	−0.383	1.040
1×10^{0}	3.477	2.672	9.277	3.914	2.797	31.411	0.023	1.252
2×10^{0}	3.043	2.373	11.233	4.764	2.294	38.947	0.655	1.511
5×10^{0}	2.578	2.055	14.524	6.208	1.755	52.330	2.063	1.943
1×10^{1}	2.294	1.861	17.690	7.587	1.434	66.104	3.798	2.361
2×10^{1}	2.057	1.700	21.627	9.347	1.161	84.250	6.571	2.860
5×10^{1}	1.807	1.531	28.311	12.301	0.880	118.182	12.621	3.724
1×10^{2}	1.655	1.429	34.834	15.202	0.711	154.829	20.267	4.564
2×10^{2}	1.528	1.345	43.100	19.060	0.565	204.734	33.048	5.580
5×10^{2}	1.397	1.258	57.218	25.496	0.421	303.594	61.005	7.295
1×10^{3}	1.318	1.207	71.232	32.064	0.334	414.631	98.050	9.003
2×10^{3}	1.255	1.165	88.679	40.032	0.267	576.995	154.603	11.090
5×10^{3}	1.188	1.122	119.822	55.418	0.192	897.627	299.100	14.370

Note: † = Require an active device.

Table A.7: Summary of piecewise optimal results for the system with an initial condition of $\boldsymbol{X}(0) = [1, 7]^T$.

Q_d/Q_a	Peak X	RMS X	Peak $\ddot{X}$	RMS $\ddot{X}$	τ_f^*	J	K^*	C^*
1×10^{-2} (†)	10.914	7.830	3.172	1.298	9.973	11.461	−1.005	0.371
2×10^{-2} (†)	9.285	6.698	3.794	1.557	8.303	13.792	−0.976	0.444
5×10^{-2} (†)	7.524	5.475	4.814	1.985	6.502	17.676	−0.906	0.564
1×10^{-1}	6.438	4.721	5.772	2.388	5.393	21.393	−0.814	0.676
2×10^{-1}	5.525	4.088	6.931	2.880	4.464	25.975	−0.671	0.810
5×10^{-1}	4.540	3.406	8.850	3.698	3.468	33.773	−0.352	1.032
1×10^{0}	3.933	2.986	10.671	4.481	2.856	41.414	0.047	1.240
2×10^{0}	3.425	2.636	12.894	5.441	2.348	51.064	0.658	1.494
5×10^{0}	2.878	2.260	16.622	7.070	1.801	68.016	2.010	1.912
1×10^{1}	2.543	2.031	20.204	8.644	1.470	85.225	3.689	2.315
2×10^{1}	2.265	1.841	24.622	10.585	1.198	107.739	6.262	2.808
5×10^{1}	1.968	1.640	32.123	13.898	0.910	149.142	11.939	3.636
1×10^{2}	1.789	1.519	39.406	17.104	0.739	193.324	18.979	4.459
2×10^{2}	1.639	1.419	48.562	21.272	0.592	253.202	30.392	5.428
5×10^{2}	1.483	1.315	64.151	28.184	0.447	370.439	54.973	7.133
1×10^{3}	1.386	1.252	79.889	35.792	0.349	497.494	90.075	8.710
2×10^{3}	1.314	1.203	98.708	43.662	0.288	690.620	135.526	10.871
5×10^{3}	1.229	1.149	133.818	61.724	0.201	1045.879	273.194	13.761

Note: † = Require an active device.

Table A.8: Summary of piecewise optimal results for the system with an initial condition of $\boldsymbol{X}(0) = [1, 8]^T$.

Q_d/Q_a	Peak X	RMS X	Peak $\ddot{X}$	RMS $\ddot{X}$	τ_{f}^*	J	K^*	C^*
1×10^{-2} (†)	12.377	8.847	3.611	1.475	10.040	14.853	−0.990	0.370
2×10^{-2} (†)	10.515	7.553	4.316	1.768	8.368	17.847	−0.958	0.443
5×10^{-2} (†)	8.501	6.154	5.471	2.250	6.563	22.820	−0.885	0.562
1×10^{-1}	7.258	5.290	6.554	2.704	5.450	27.558	−0.791	0.673
2×10^{-1}	6.214	4.566	7.861	3.256	4.518	33.376	−0.646	0.806
5×10^{-1}	5.086	3.784	10.021	4.173	3.518	43.221	−0.329	1.025
1×10^{0}	4.391	3.303	12.064	5.047	2.903	52.805	0.063	1.231
2×10^{0}	3.808	2.900	14.554	6.121	2.388	64.827	0.663	1.479
5×10^{0}	3.181	2.468	18.712	7.921	1.841	85.778	1.961	1.891
1×10^{1}	2.797	2.204	22.695	9.655	1.507	106.856	3.559	2.285
2×10^{1}	2.475	1.984	27.604	11.820	1.228	134.143	6.031	2.764
5×10^{1}	2.133	1.751	35.905	15.470	0.936	183.788	11.400	3.571
1×10^{2}	1.923	1.610	43.989	19.104	0.756	235.848	18.240	4.335
2×10^{2}	1.750	1.493	54.051	23.632	0.610	306.174	28.848	5.308
5×10^{2}	1.570	1.372	71.146	31.129	0.463	442.088	51.511	6.964
1×10^{3}	1.460	1.299	88.041	38.790	0.371	591.540	81.203	8.498
2×10^{3}	1.366	1.239	109.934	49.676	0.287	794.277	134.572	10.281
5×10^{3}	1.277	1.179	145.658	64.830	0.221	1233.017	231.501	13.782

Note: † = Require an active device.

Table A.9: Summary of piecewise optimal results for the system with an initial condition of $\boldsymbol{X}(0) = [1, 9]^T$.

Q_d/Q_a	Peak X	RMS X	Peak $\ddot{X}$	RMS $\ddot{X}$	τ_{f}^*	J	K^*	C^*
1×10^{-2} (†)	13.840	9.865	4.051	1.652	10.094	18.684	−0.978	0.369
2×10^{-2} (†)	11.745	8.408	4.839	1.978	8.419	22.425	−0.945	0.442
5×10^{-2} (†)	9.479	6.833	6.128	2.515	6.612	28.620	−0.869	0.561
1×10^{-1}	8.079	5.861	7.336	3.020	5.498	34.506	−0.774	0.671
2×10^{-1}	6.904	5.044	8.791	3.631	4.564	41.707	−0.628	0.803
5×10^{-1}	5.633	4.163	11.191	4.647	3.559	53.837	−0.312	1.020
1×10^{0}	4.850	3.620	13.457	5.613	2.940	65.584	0.075	1.224
2×10^{0}	4.193	3.166	16.212	6.795	2.424	80.244	0.662	1.469
5×10^{0}	3.485	2.678	20.801	8.772	1.873	105.614	1.923	1.876
1×10^{1}	3.050	2.378	25.188	10.685	1.534	130.928	3.477	2.261
2×10^{1}	2.687	2.129	30.576	13.042	1.254	163.484	5.840	2.732
5×10^{1}	2.299	1.864	39.659	17.005	0.960	222.158	10.934	3.531
1×10^{2}	2.060	1.702	48.510	21.016	0.774	282.943	17.514	4.269
2×10^{2}	1.864	1.570	59.429	25.826	0.629	364.769	27.303	5.216
5×10^{2}	1.656	1.430	78.166	34.248	0.473	519.225	49.405	6.786
1×10^{3}	1.528	1.346	96.791	43.081	0.374	685.611	79.320	8.254
2×10^{3}	1.430	1.279	119.175	52.348	0.309	930.032	118.332	10.327
5×10^{3}	1.318	1.207	159.962	72.420	0.221	1386.714	228.389	13.164

Note: † = Require an active device.

Table A.10: Summary of piecewise optimal results for the system with an initial condition of $\boldsymbol{X}(0) = [1, 10]^T$.

Q_d/Q_a	Peak X	RMS X	Peak $\ddot{X}$	RMS $\ddot{X}$	τ_{f}^*	J	K^*	C^*
1×10^{-2} (†)	15.304	10.883	4.490	1.829	10.138	22.955	−0.969	0.369
2×10^{-2} (†)	12.975	9.263	5.361	2.188	8.462	27.526	−0.934	0.441
5×10^{-2} (†)	10.457	7.513	6.786	2.779	6.652	35.078	−0.856	0.560
1×10^{-1}	8.901	6.431	8.117	3.335	5.536	42.234	−0.760	0.669
2×10^{-1}	7.594	5.524	9.721	4.007	4.600	50.967	−0.613	0.801
5×10^{-1}	6.181	4.543	12.360	5.120	3.592	65.621	−0.298	1.016
1×10^{0}	5.310	3.939	14.848	6.176	2.973	79.753	0.083	1.218
2×10^{0}	4.578	3.433	17.868	7.468	2.453	97.313	0.661	1.461
5×10^{0}	3.790	2.888	22.889	9.632	1.897	127.517	1.898	1.861
1×10^{1}	3.305	2.554	27.675	11.707	1.557	157.473	3.404	2.240
2×10^{1}	2.900	2.275	33.537	14.247	1.277	195.771	5.672	2.705
5×10^{1}	2.466	1.978	43.417	18.578	0.977	264.120	10.616	3.478
1×10^{2}	2.199	1.797	52.977	22.836	0.793	334.586	16.798	4.213
2×10^{2}	1.979	1.647	64.820	28.105	0.643	428.218	26.262	5.122
5×10^{2}	1.747	1.490	84.933	36.930	0.489	604.624	46.617	6.700
1×10^{3}	1.601	1.394	105.038	46.544	0.385	791.641	75.116	8.037
2×10^{3}	1.488	1.318	129.487	57.151	0.314	1059.205	114.398	10.033
5×10^{3}	1.366	1.238	172.176	76.654	0.234	1581.606	207.634	13.148

Note: † = Require an active device.

A.2 Tabulated Summary of Clipped-LQR Results

The following tables summarize the clipped-LQR results for the system with an initial condition of $\boldsymbol{X}(0) = [1, 1]^T$ (Table A.11), $[1, 2]^T$ (Table A.12), $[1, 3]^T$ (Table A.13), $[1, 4]^T$ (Table A.14), $[1, 5]^T$ (Table A.15), $[1, 6]^T$ (Table A.16), $[1, 7]^T$ (Table A.17), $[1, 8]^T$ (Table A.18), $[1, 9]^T$ (Table A.19), and $[1, 10]^T$ (Table A.20).

Table A.11: Summary of clipped-LQR results for the system with an initial condition of $\boldsymbol{X}(0) = [1, 1]^T$.

Q_d/Q_a	Peak X	RMS X	Peak $\ddot{X}$	RMS $\ddot{X}$	τ_f^*	J	K^*	C^*
1×10^{-2} (†)	2.149	1.758	0.547	0.241	7.489	0.334	−1.903	0.436
2×10^{-2} (†)	1.929	1.614	0.673	0.305	5.873	0.425	−2.038	0.521
5×10^{-2} (†)	1.695	1.461	0.892	0.419	4.218	0.595	−2.196	0.658
1×10^{-1} (†)	1.554	1.368	1.111	0.538	3.258	0.777	−2.247	0.784
2×10^{-1} (†)	1.439	1.291	1.393	0.698	2.498	1.025	−2.146	0.934
5×10^{-1}	1.319	1.212	1.896	0.998	1.740	1.505	−1.453	1.178
1×10^{0}	1.248	1.165	2.414	1.321	1.313	2.037	0.000	1.404
2×10^{0}	1.191	1.127	3.096	1.768	0.983	2.785	3.140	1.674
5×10^{0}	1.134	1.089	4.351	2.631	0.664	4.268	12.829	2.115
1×10^{1}	1.101	1.068	5.677	3.588	0.490	5.948	28.922	2.527
2×10^{1}	1.076	1.051	7.463	4.931	0.359	8.330	60.610	3.038
5×10^{1}	1.052	1.035	10.832	7.576	0.236	13.088	153.300	3.911
1×10^{2}	1.038	1.026	14.472	10.540	0.171	18.493	303.905	4.759
2×10^{2}	1.028	1.019	19.460	14.733	0.123	26.122	598.360	5.959
5×10^{2}	1.019	1.013	29.048	22.981	0.080	41.628	1460.550	7.561
1×10^{3}	1.013	1.009	39.575	32.325	0.057	58.806	2866.694	9.933
2×10^{3}	1.010	1.007	54.179	45.630	0.040	82.185	5622.740	14.873
5×10^{3}	1.006	1.004	82.603	71.993	0.025	127.847	13709.998	25.529

Note: † = Require an active device.

Table A.12: Summary of clipped-LQR results for the system with an initial condition of $\boldsymbol{X}(0) = [1, 2]^T$.

Q_d/Q_a	Peak X	RMS X	Peak $\ddot{X}$	RMS $\ddot{X}$	τ_f^*	J	K^*	C^*
1×10^{-2} (†)	3.562	2.673	0.994	0.404	9.362	1.100	−1.356	0.437
2×10^{-2} (†)	3.109	2.381	1.205	0.499	7.502	1.358	−1.385	0.522
5×10^{-2} (†)	2.621	2.066	1.561	0.663	5.556	1.814	−1.393	0.658
1×10^{-1} (†)	2.323	1.871	1.907	0.828	4.400	2.278	−1.347	0.785
2×10^{-1}	2.074	1.709	2.339	1.040	3.464	2.884	−1.211	0.935
5×10^{-1}	1.808	1.535	3.086	1.421	2.502	3.998	−0.755	1.179
1×10^{0}	1.647	1.429	3.828	1.815	1.941	5.180	0.000	1.404
2×10^{0}	1.515	1.342	4.778	2.339	1.496	6.785	1.434	1.673
5×10^{0}	1.376	1.250	6.466	3.317	1.048	9.860	5.387	2.108
1×10^{1}	1.294	1.196	8.192	4.367	0.794	13.249	11.433	2.514
2×10^{1}	1.228	1.152	10.454	5.802	0.598	17.999	22.637	2.994
5×10^{1}	1.161	1.107	14.592	8.572	0.406	27.365	53.466	3.788
1×10^{2}	1.122	1.082	18.944	11.625	0.301	37.953	101.209	4.520
2×10^{2}	1.092	1.062	24.779	15.911	0.221	52.902	191.255	5.465
5×10^{2}	1.063	1.042	35.735	24.313	0.146	82.817	445.282	7.026
1×10^{3}	1.047	1.032	47.528	33.730	0.106	116.704	848.178	8.589
2×10^{3}	1.035	1.024	63.636	47.110	0.076	163.962	1623.046	11.095
5×10^{3}	1.023	1.016	94.495	73.469	0.049	258.638	3859.015	15.397

Note: † = Require an active device.

Table A.13: Summary of clipped-LQR results for the system with an initial condition of $\boldsymbol{X}(0) = [1, 3]^T$.

Q_d/Q_a	Peak X	RMS X	Peak $\ddot{X}$	RMS $\ddot{X}$	τ_{f}^*	J	K^*	C^*
1×10^{-2} (†)	4.993	3.590	1.442	0.565	10.309	2.312	−1.195	0.437
2×10^{-2} (†)	4.309	3.153	1.737	0.691	8.341	2.821	−1.197	0.522
5×10^{-2} (†)	3.571	2.679	2.230	0.906	6.266	3.698	−1.168	0.659
1×10^{-1}	3.116	2.386	2.702	1.118	5.021	4.567	−1.102	0.785
2×10^{-1}	2.736	2.140	3.284	1.386	4.004	5.677	−0.963	0.935
5×10^{-1}	2.327	1.874	4.275	1.855	2.945	7.655	−0.576	1.179
1×10^{0}	2.078	1.711	5.243	2.330	2.319	9.692	0.000	1.404
2×10^{0}	1.870	1.575	6.460	2.947	1.815	12.386	1.021	1.672
5×10^{0}	1.650	1.431	8.580	4.066	1.300	17.400	3.653	2.106
1×10^{1}	1.517	1.343	10.707	5.241	1.001	22.781	7.463	2.510
2×10^{1}	1.408	1.272	13.444	6.814	0.766	30.166	14.224	2.990
5×10^{1}	1.295	1.197	18.353	9.777	0.532	44.476	31.986	3.769
1×10^{2}	1.229	1.153	23.416	12.997	0.400	60.369	58.447	4.503
2×10^{2}	1.176	1.118	30.097	17.429	0.299	82.768	106.859	5.375
5×10^{2}	1.123	1.083	42.423	26.055	0.201	127.108	239.119	6.853
1×10^{3}	1.093	1.062	55.481	35.613	0.148	177.377	443.540	8.231
2×10^{3}	1.070	1.047	73.094	49.070	0.108	248.413	829.356	10.059
5×10^{3}	1.047	1.032	106.387	75.472	0.071	391.187	1920.871	12.983

Note: † = Require an active device.

Table A.14: Summary of clipped-LQR results for the system with an initial condition of $\boldsymbol{X}(0) = [1, 4]^T$.

Q_d/Q_a	Peak X	RMS X	Peak $\ddot{X}$	RMS $\ddot{X}$	τ_{f}^*	J	K^*	C^*
1×10^{-2} (†)	6.429	4.503	1.889	0.725	10.903	3.970	−1.118	0.437
2×10^{-2} (†)	5.515	3.922	2.269	0.882	8.873	4.815	−1.108	0.522
5×10^{-2} (†)	4.527	3.292	2.899	1.148	6.723	6.249	−1.064	0.659
1×10^{-1}	3.918	2.903	3.497	1.406	5.425	7.649	−0.988	0.785
2×10^{-1}	3.407	2.574	4.230	1.730	4.360	9.411	−0.850	0.936
5×10^{-1}	2.857	2.219	5.464	2.290	3.243	12.493	−0.496	1.179
1×10^{0}	2.519	1.999	6.657	2.847	2.578	15.603	0.000	1.404
2×10^{0}	2.237	1.816	8.141	3.562	2.037	19.640	0.843	1.672
5×10^{0}	1.936	1.619	10.695	4.835	1.480	26.992	2.922	2.106
1×10^{1}	1.753	1.499	13.222	6.146	1.153	34.722	5.818	2.507
2×10^{1}	1.602	1.399	16.435	7.876	0.892	45.135	10.797	2.987
5×10^{1}	1.442	1.294	22.113	11.077	0.629	64.935	23.427	3.765
1×10^{2}	1.348	1.232	27.889	14.490	0.479	86.616	41.669	4.488
2×10^{2}	1.271	1.181	35.415	19.139	0.362	116.781	74.207	5.356
5×10^{2}	1.193	1.129	49.110	28.063	0.247	175.974	160.690	6.799
1×10^{3}	1.147	1.099	63.434	37.832	0.184	242.746	291.311	8.113
2×10^{3}	1.112	1.076	82.551	51.618	0.135	336.029	533.330	9.958
5×10^{3}	1.077	1.052	118.279	78.274	0.090	524.645	1205.449	12.651

Note: † = Require an active device.

Table A.15: Summary of clipped-LQR results for the system with an initial condition of $X(0) = [1, 5]^T$.

Q_d/Q_a	Peak X	RMS X	Peak $\ddot{X}$	RMS $\ddot{X}$	τ_f^*	J	K^*	C^*
1×10^{-2} (†)	7.868	5.412	2.336	0.883	11.319	6.074	−1.073	0.437
2×10^{-2} (†)	6.723	4.689	2.801	1.071	9.249	7.339	−1.056	0.522
5×10^{-2} (†)	5.486	3.904	3.567	1.387	7.048	9.466	−1.003	0.659
1×10^{-1}	4.723	3.418	4.293	1.692	5.716	11.524	−0.924	0.785
2×10^{-1}	4.082	3.008	5.176	2.072	4.618	14.088	−0.786	0.936
5×10^{-1}	3.391	2.564	6.653	2.722	3.462	18.514	−0.452	1.179
1×10^{0}	2.966	2.289	8.071	3.364	2.769	22.919	0.000	1.404
2×10^{0}	2.610	2.059	9.823	4.177	2.204	28.564	0.745	1.672
5×10^{0}	2.229	1.810	12.810	5.610	1.616	38.668	2.525	2.106
1×10^{1}	1.995	1.658	15.737	7.062	1.270	49.123	4.937	2.507
2×10^{1}	1.802	1.531	19.426	8.959	0.991	63.002	8.987	2.985
5×10^{1}	1.597	1.396	25.874	12.416	0.707	88.959	18.978	3.762
1×10^{2}	1.474	1.315	32.361	16.056	0.543	116.952	33.055	4.484
2×10^{2}	1.373	1.248	40.734	20.931	0.415	155.565	57.642	5.335
5×10^{2}	1.269	1.180	55.798	30.236	0.286	230.262	121.466	6.776
1×10^{3}	1.208	1.139	71.386	40.286	0.215	313.936	215.923	8.074
2×10^{3}	1.159	1.107	92.008	54.246	0.160	431.462	388.162	9.701
5×10^{3}	1.111	1.075	130.171	81.479	0.107	664.185	857.899	12.511

Note: † = Require an active device.

Table A.16: Summary of clipped-LQR results for the system with an initial condition of $X(0) = [1, 6]^T$.

Q_d/Q_a	Peak X	RMS X	Peak $\ddot{X}$	RMS $\ddot{X}$	τ_f^*	J	K^*	C^*
1×10^{-2} (†)	9.307	6.319	2.783	1.041	11.629	8.624	−1.043	0.437
2×10^{-2} (†)	7.933	5.454	3.332	1.259	9.531	10.393	−1.022	0.522
5×10^{-2} (†)	6.447	4.514	4.236	1.625	7.295	13.351	−0.964	0.659
1×10^{-1}	5.530	3.932	5.088	1.977	5.937	16.193	−0.882	0.785
2×10^{-1}	4.760	3.441	6.122	2.412	4.816	19.709	−0.745	0.936
5×10^{-1}	3.928	2.909	7.842	3.152	3.631	25.721	−0.423	1.179
1×10^{0}	3.416	2.579	9.485	3.877	2.918	31.644	0.000	1.404
2×10^{0}	2.986	2.303	11.505	4.791	2.334	39.158	0.684	1.672
5×10^{0}	2.525	2.003	14.925	6.383	1.725	52.444	2.279	2.105
1×10^{1}	2.242	1.819	18.251	7.982	1.364	66.009	4.394	2.506
2×10^{1}	2.006	1.665	22.416	10.046	1.072	83.814	7.880	2.983
5×10^{1}	1.756	1.501	29.635	13.769	0.772	116.644	16.295	3.757
1×10^{2}	1.604	1.401	36.833	17.649	0.597	151.580	27.911	4.477
2×10^{2}	1.479	1.319	46.052	22.804	0.459	199.192	47.845	5.334
5×10^{2}	1.349	1.233	62.485	32.489	0.320	290.560	98.558	6.750
1×10^{3}	1.272	1.182	79.339	42.893	0.242	391.698	172.270	8.057
2×10^{3}	1.211	1.142	101.466	57.269	0.181	532.681	304.696	9.707
5×10^{3}	1.148	1.099	142.063	84.762	0.123	813.564	660.259	12.253

Note: † = Require an active device.

Table A.17: Summary of clipped-LQR results for the system with an initial condition of $\boldsymbol{X}(0) = [1, 7]^T$.

Q_d/Q_a	Peak X	RMS X	Peak $\ddot{X}$	RMS $\ddot{X}$	τ_f^*	J	K^*	C^*
1×10^{-2} (†)	10.747	7.223	3.230	1.198	11.872	11.621	−1.022	0.437
2×10^{-2} (†)	9.144	6.216	3.864	1.447	9.752	13.979	−0.998	0.522
5×10^{-2} (†)	7.409	5.123	4.905	1.863	7.489	17.904	−0.936	0.659
1×10^{-1}	6.338	4.445	5.883	2.260	6.113	21.655	−0.852	0.785
2×10^{-1}	5.438	3.874	7.067	2.750	4.973	26.272	−0.716	0.936
5×10^{-1}	4.466	3.254	9.032	3.581	3.766	34.114	−0.403	1.179
1×10^{0}	3.867	2.870	10.899	4.389	3.038	41.779	0.000	1.404
2×10^{0}	3.364	2.546	13.187	5.401	2.441	51.431	0.641	1.672
5×10^{0}	2.823	2.197	17.039	7.155	1.814	68.321	2.111	2.105
1×10^{1}	2.491	1.981	20.766	8.903	1.441	85.386	4.027	2.506
2×10^{1}	2.214	1.801	25.407	11.143	1.138	107.564	7.138	2.983
5×10^{1}	1.917	1.607	33.395	15.140	0.826	147.992	14.514	3.756
1×10^{2}	1.737	1.489	41.305	19.261	0.643	190.543	24.526	4.473
2×10^{2}	1.589	1.391	51.370	24.707	0.497	247.914	41.452	5.331
5×10^{2}	1.433	1.288	69.173	34.793	0.350	357.095	83.768	6.726
1×10^{3}	1.340	1.227	87.292	45.582	0.266	476.598	144.304	8.038
2×10^{3}	1.265	1.177	110.923	60.241	0.201	643.233	251.649	9.598
5×10^{3}	1.188	1.126	153.955	88.435	0.137	970.161	535.569	12.216

Note: † = Require an active device.

Table A.18: Summary of clipped-LQR results for the system with an initial condition of $\boldsymbol{X}(0) = [1, 8]^T$.

Q_d/Q_a	Peak X	RMS X	Peak $\ddot{X}$	RMS $\ddot{X}$	τ_f^*	J	K^*	C^*
1×10^{-2} (†)	12.188	8.126	3.678	1.355	12.067	15.065	−1.007	0.437
2×10^{-2} (†)	10.355	6.977	4.396	1.634	9.932	18.095	−0.980	0.522
5×10^{-2} (†)	8.371	5.730	5.574	2.099	7.648	23.124	−0.915	0.659
1×10^{-1}	7.147	4.957	6.678	2.543	6.256	27.910	−0.830	0.785
2×10^{-1}	6.117	4.305	8.013	3.087	5.103	33.780	−0.695	0.936
5×10^{-1}	5.005	3.598	10.221	4.008	3.878	43.694	−0.389	1.179
1×10^{0}	4.319	3.160	12.314	4.899	3.138	53.324	0.000	1.404
2×10^{0}	3.744	2.791	14.869	6.010	2.529	65.377	0.610	1.672
5×10^{0}	3.123	2.391	19.154	7.924	1.889	86.306	1.989	2.105
1×10^{1}	2.742	2.144	23.281	9.822	1.506	107.264	3.763	2.506
2×10^{1}	2.423	1.937	28.398	12.236	1.195	134.292	6.607	2.983
5×10^{1}	2.081	1.714	37.156	16.518	0.872	183.041	13.253	3.756
1×10^{2}	1.873	1.578	45.777	20.895	0.682	233.844	22.144	4.473
2×10^{2}	1.701	1.465	56.689	26.608	0.531	301.877	36.985	5.322
5×10^{2}	1.519	1.345	75.860	37.165	0.376	429.816	73.527	6.720
1×10^{3}	1.410	1.273	95.244	48.287	0.288	569.116	125.078	8.003
2×10^{3}	1.321	1.215	120.381	63.472	0.218	760.954	215.388	9.599
5×10^{3}	1.230	1.154	165.847	92.199	0.150	1137.096	451.092	12.151

Note: † = Require an active device.

Table A.19: Summary of clipped-LQR results for the system with an initial condition of $\boldsymbol{X}(0) = [1, 9]^T$.

Q_d/Q_a	Peak X	RMS X	Peak $\ddot{X}$	RMS $\ddot{X}$	τ_f^*	J	K^*	C^*
1×10^{-2} (†)	13.629	9.027	4.125	1.512	12.229	18.954	−0.995	0.437
2×10^{-2} (†)	11.566	7.737	4.928	1.821	10.080	22.742	−0.966	0.522
5×10^{-2} (†)	9.334	6.336	6.242	2.335	7.780	29.011	−0.900	0.659
1×10^{-1}	7.956	5.468	7.474	2.824	6.376	34.959	−0.813	0.785
2×10^{-1}	6.797	4.736	8.959	3.424	5.211	42.231	−0.678	0.936
5×10^{-1}	5.545	3.942	11.410	4.433	3.972	54.459	−0.377	1.179
1×10^{0}	4.772	3.450	13.728	5.408	3.222	66.280	0.000	1.404
2×10^{0}	4.124	3.035	16.550	6.618	2.604	81.002	0.587	1.672
5×10^{0}	3.424	2.586	21.269	8.694	1.952	106.393	1.897	2.105
1×10^{1}	2.993	2.307	25.796	10.739	1.562	131.646	3.564	2.506
2×10^{1}	2.633	2.074	31.388	13.328	1.244	163.989	6.209	2.982
5×10^{1}	2.247	1.823	40.916	17.897	0.912	221.813	12.314	3.756
1×10^{2}	2.010	1.668	50.249	22.522	0.717	281.597	20.382	4.470
2×10^{2}	1.814	1.540	62.007	28.548	0.560	360.928	33.701	5.322
5×10^{2}	1.606	1.403	82.547	39.523	0.400	509.172	66.064	6.703
1×10^{3}	1.481	1.321	103.197	51.109	0.307	668.692	111.149	8.002
2×10^{3}	1.379	1.253	129.838	66.687	0.234	887.959	189.287	9.563
5×10^{3}	1.274	1.183	177.739	96.066	0.162	1314.403	390.711	12.095

Note: † = Require an active device.

Table A.20: Summary of clipped-LQR results for the system with an initial condition of $\boldsymbol{X}(0) = [1, 10]^T$.

Q_d/Q_a	Peak X	RMS X	Peak $\ddot{X}$	RMS $\ddot{X}$	τ_f^*	J	K^*	C^*
1×10^{-2} (†)	15.070	9.928	4.572	1.668	12.364	23.290	−0.985	0.437
2×10^{-2} (†)	12.777	8.495	5.460	2.007	10.205	27.920	−0.955	0.522
5×10^{-2} (†)	10.297	6.941	6.911	2.570	7.892	35.565	−0.887	0.659
1×10^{-1}	8.765	5.978	8.269	3.105	6.479	42.803	−0.800	0.785
2×10^{-1}	7.477	5.166	9.905	3.759	5.304	51.626	−0.665	0.936
5×10^{-1}	6.085	4.285	12.599	4.857	4.053	66.412	−0.368	1.179
1×10^{0}	5.226	3.739	15.142	5.914	3.295	80.647	0.000	1.404
2×10^{0}	4.504	3.278	18.232	7.223	2.669	98.304	0.568	1.672
5×10^{0}	3.726	2.779	23.383	9.458	2.008	128.595	1.825	2.105
1×10^{1}	3.246	2.471	28.311	11.653	1.611	158.536	3.409	2.506
2×10^{1}	2.844	2.211	34.379	14.424	1.286	196.651	5.901	2.982
5×10^{1}	2.413	1.931	44.677	19.268	0.948	264.339	11.590	3.754
1×10^{2}	2.149	1.758	54.721	24.151	0.748	333.771	19.030	4.468
2×10^{2}	1.929	1.615	67.325	30.490	0.586	425.227	31.195	5.321
5×10^{2}	1.695	1.462	89.235	41.982	0.420	594.603	60.406	6.711
1×10^{3}	1.554	1.369	111.150	53.977	0.324	775.779	100.647	8.004
2×10^{3}	1.439	1.293	139.296	70.042	0.248	1023.157	169.709	9.564
5×10^{3}	1.319	1.213	189.631	100.047	0.173	1502.093	345.741	12.060

Note: † = Require an active device.

Appendix B
Nonlinear Transmissibility Curves

The following sections present the nonlinear transmissibility curves for all cases considered, highlighting the effects of frequency ratio Ω (Section B.1), mass ratio μ (Section B.2), nonlinearity parameter κ (Section B.3), and excitation amplitude coefficient a (Section B.4).

B.1 Effect of Varying Frequency Ratio Ω

B.1.1 Roof Displacement

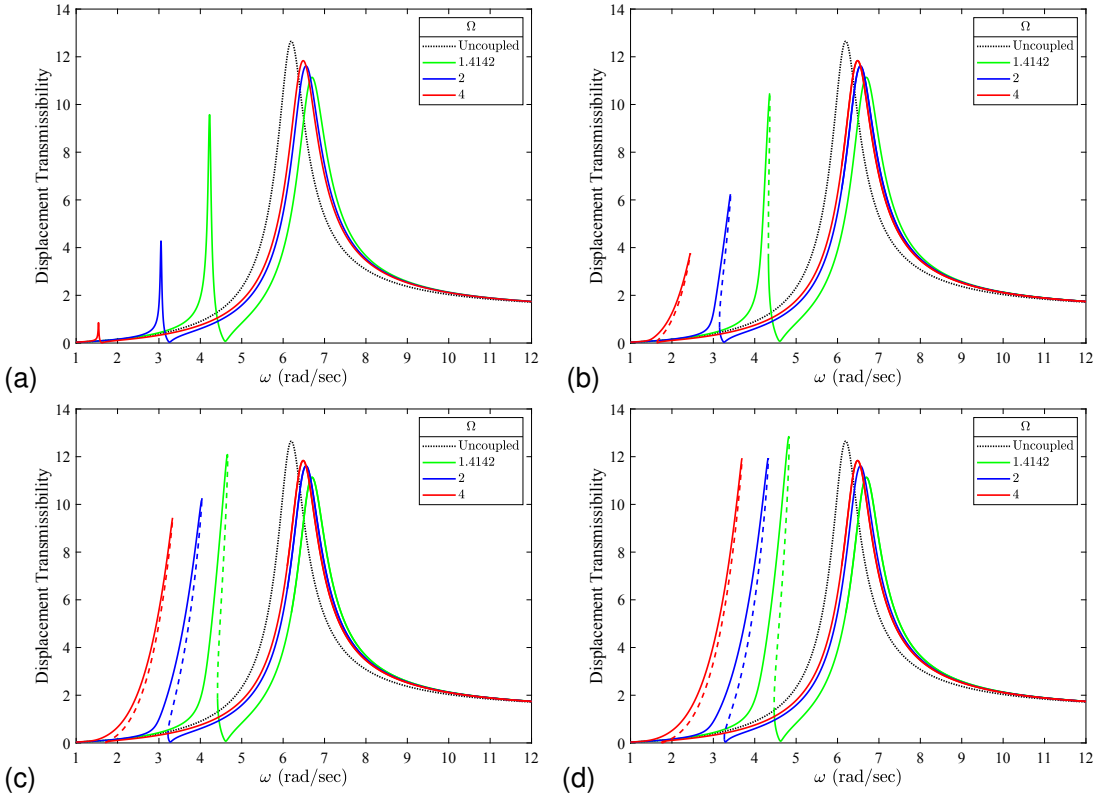

Figure B.1: Effect of frequency ratio Ω on nonlinear transmissibility TR_{Δ_r} of the roof displacement, for $\mu = 0.3$, κ = (a) 0, (b) 0.001, (c) 0.005, and (d) 0.01 in.$^{-2}$, $a = 1.414\ g$.

B.1.2 Isolated Mass Total Acceleration

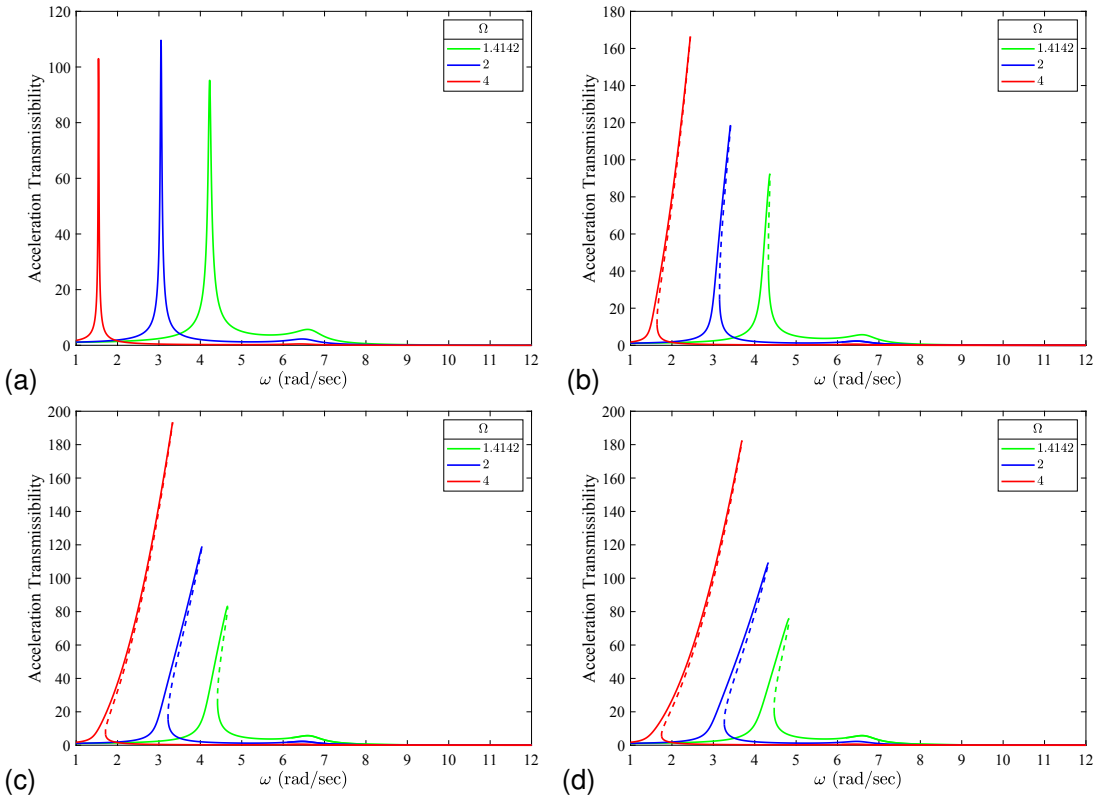

Figure B.2: Effect of frequency ratio Ω on nonlinear transmissibility $\mathrm{TR}_{a_{\mathrm{total}}}$ of the isolated mass total acceleration, for $\mu = 0.3$, κ = (a) 0, (b) 0.001, (c) 0.005, and (d) 0.01 in.$^{-2}$, $a = 1.414\ g$.

B.2 Effect of Varying Mass Ratio μ

B.2.1 Roof Displacement

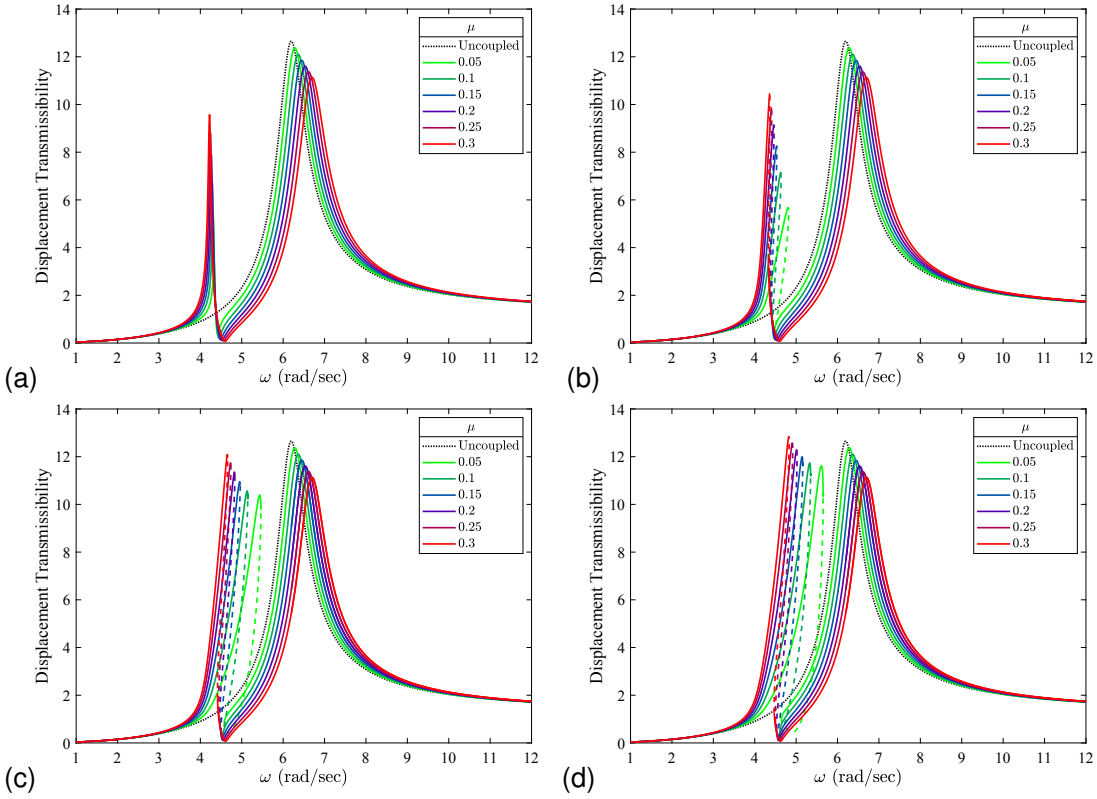

Figure B.3: Effect of mass ratio μ on nonlinear transmissibility TR_{Δ_r} of the roof displacement, for $\Omega = \sqrt{2}$, κ = (a) 0, (b) 0.001, (c) 0.005, and (d) 0.01 in.$^{-2}$, $a = 1.414\ g$.

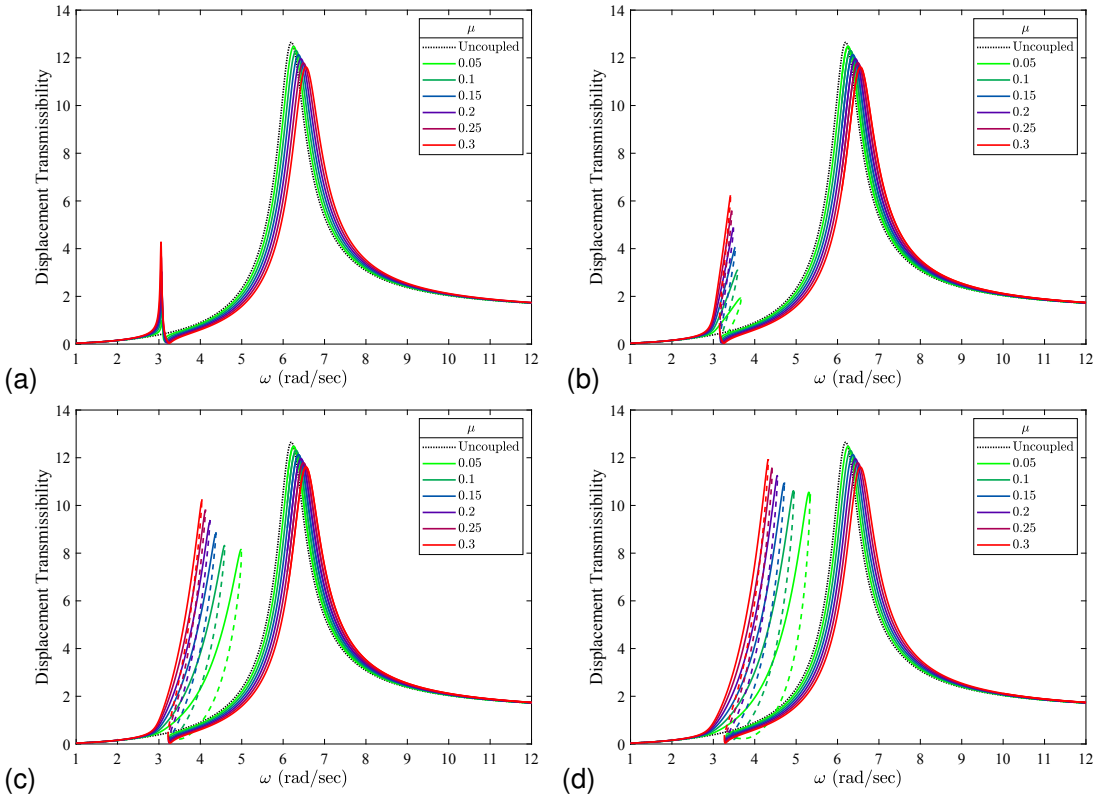

Figure B.4: Effect of mass ratio μ on nonlinear transmissibility TR_{Δ_r} of the roof displacement, for $\Omega = 2$, $\kappa =$ (a) 0, (b) 0.001, (c) 0.005, and (d) 0.01 in.$^{-2}$, $a = 1.414\ g$.

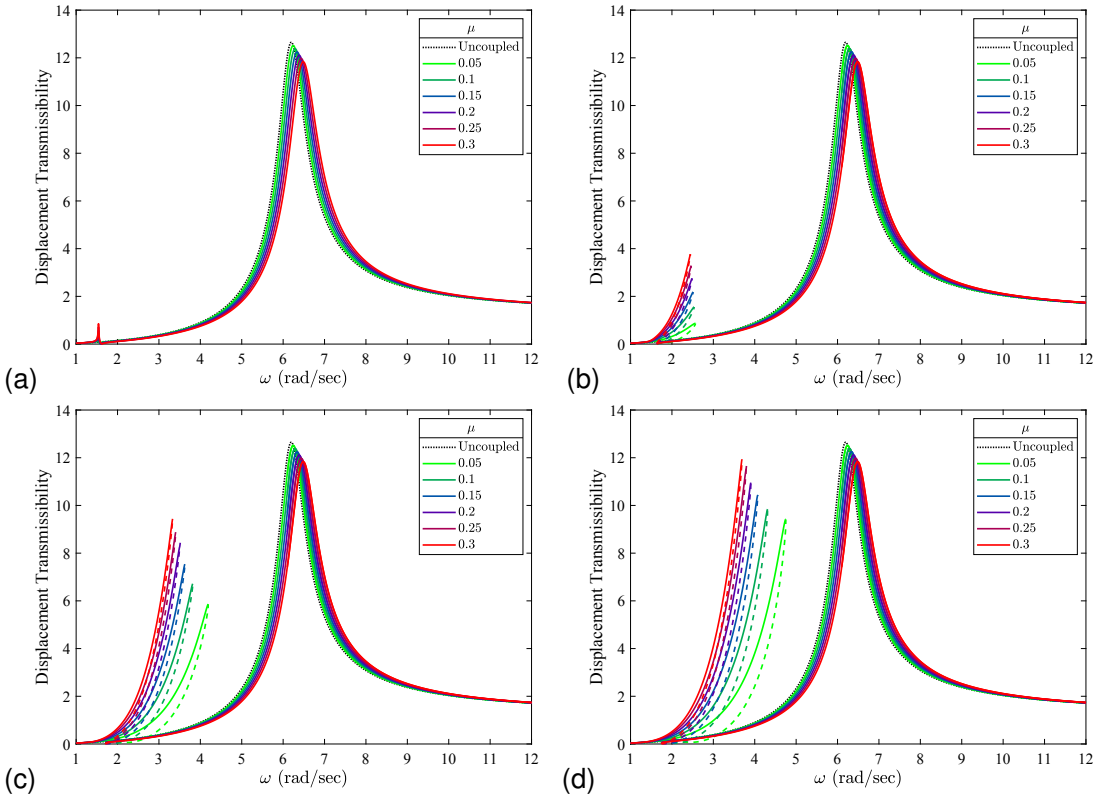

Figure B.5: Effect of mass ratio μ on nonlinear transmissibility TR_{Δ_r} of the roof displacement, for $\Omega = 4$, $\kappa =$ (a) 0, (b) 0.001, (c) 0.005, and (d) 0.01 in.$^{-2}$, $a = 1.414\ g$.

B.2.2 Isolated Mass Total Acceleration

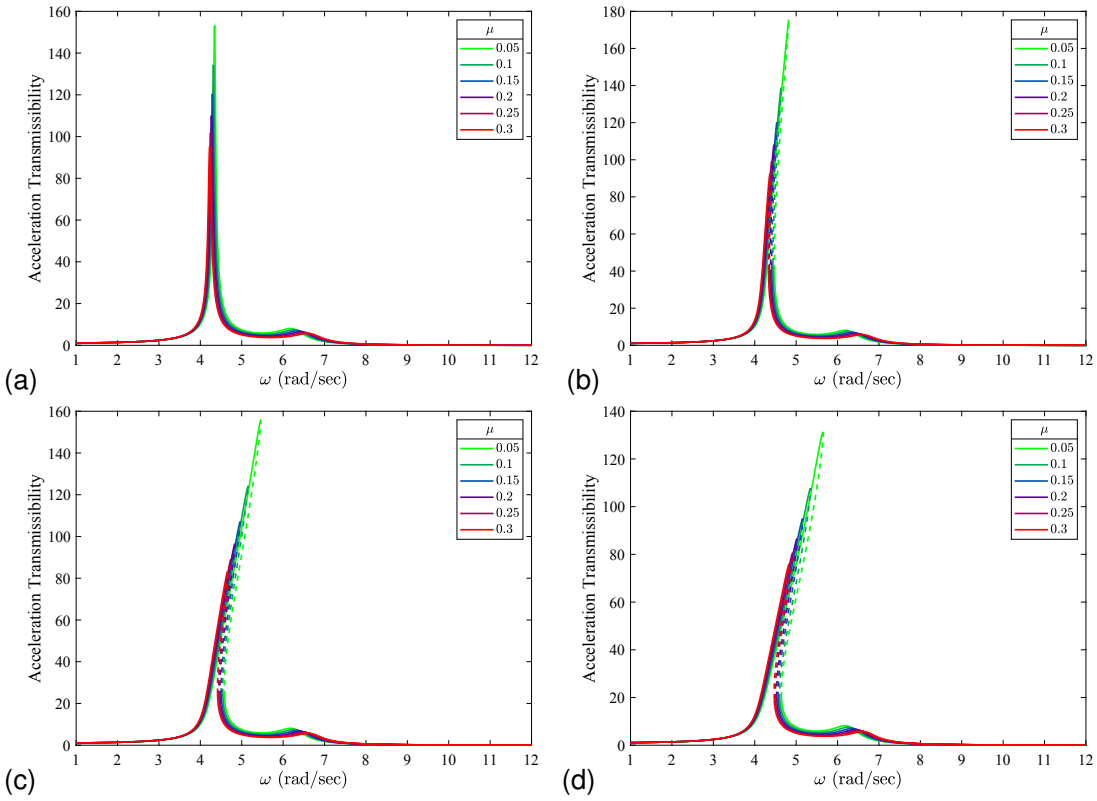

Figure B.6: Effect of mass ratio μ on nonlinear transmissibility $\mathrm{TR}_{a_{\mathrm{total}}}$ of the isolated mass total acceleration, for $\Omega = \sqrt{2}$, κ = (a) 0, (b) 0.001, (c) 0.005, and (d) 0.01 in.$^{-2}$, $a = 1.414\ g$.

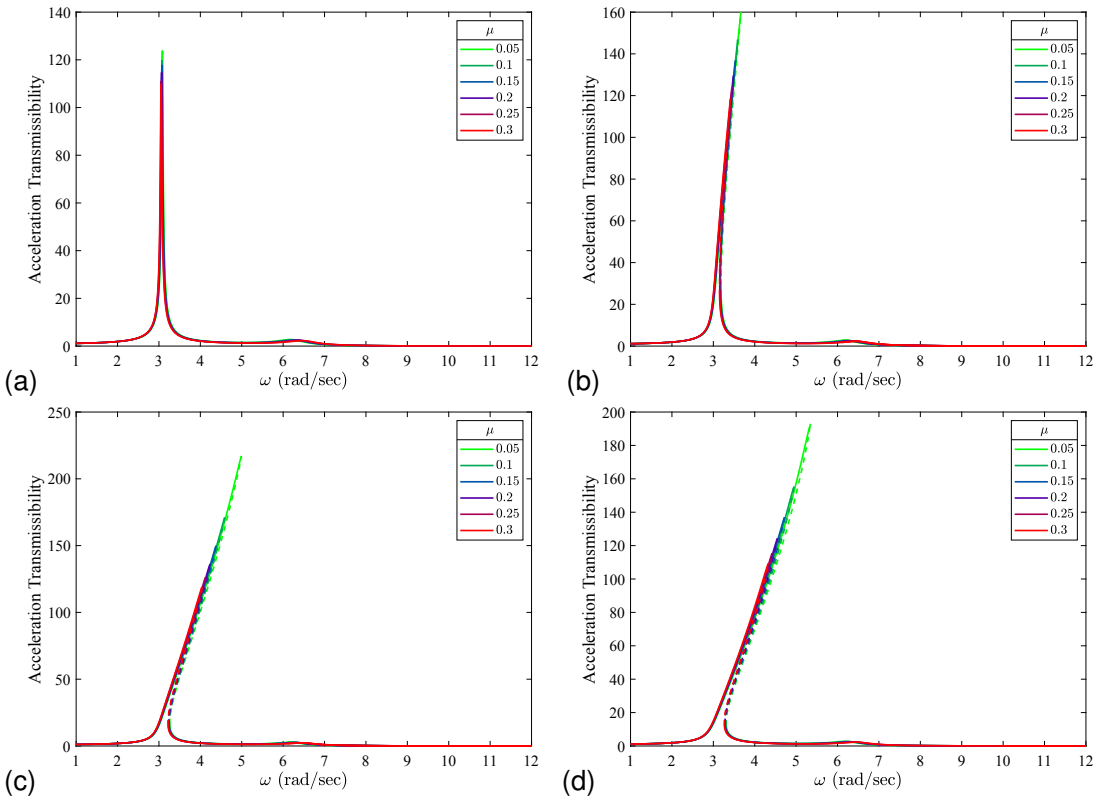

Figure B.7: Effect of mass ratio μ on nonlinear transmissibility $\mathrm{TR}_{a_{\mathrm{total}}}$ of the isolated mass total acceleration, for $\Omega = 2$, κ = (a) 0, (b) 0.001, (c) 0.005, and (d) 0.01 in.$^{-2}$, $a = 1.414\ g$.

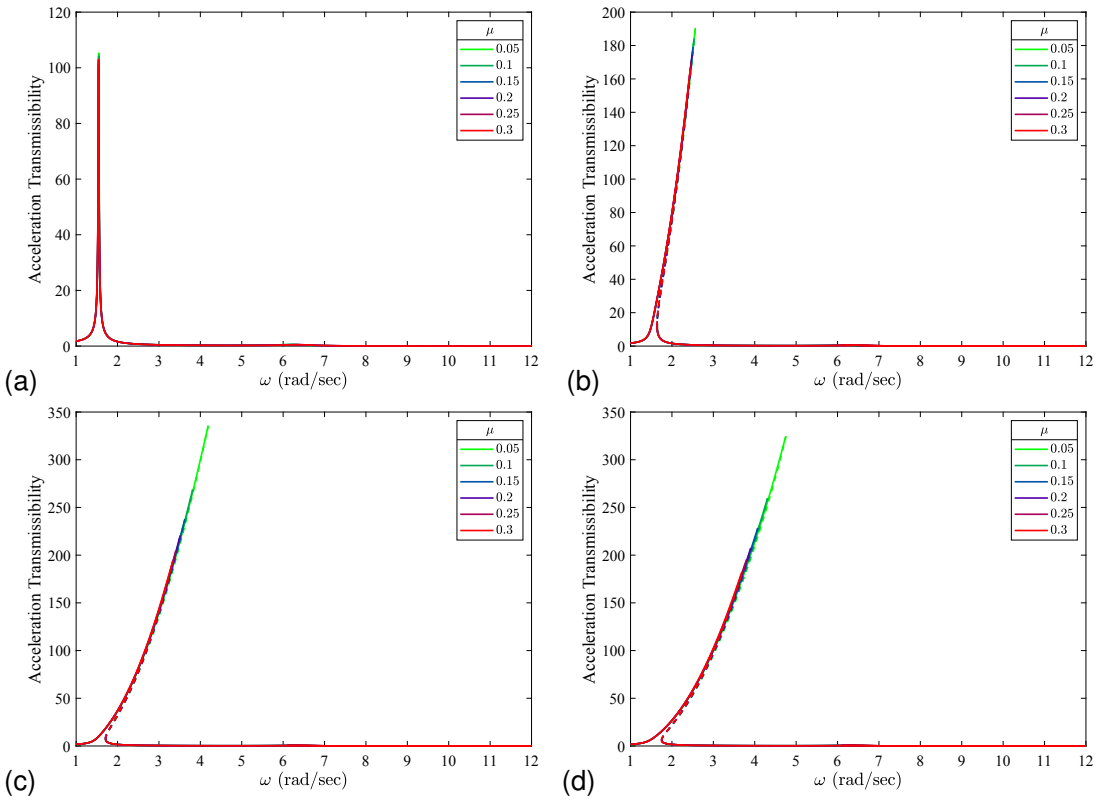

Figure B.8: Effect of mass ratio μ on nonlinear transmissibility $\mathrm{TR}_{a_{\mathrm{total}}}$ of the isolated mass total acceleration, for $\Omega = 4$, κ = (a) 0, (b) 0.001, (c) 0.005, and (d) 0.01 in.$^{-2}$, $a = 1.414\ g$.

B.3 Effect of Varying Nonlinearity Parameter κ

B.3.1 Roof Displacement

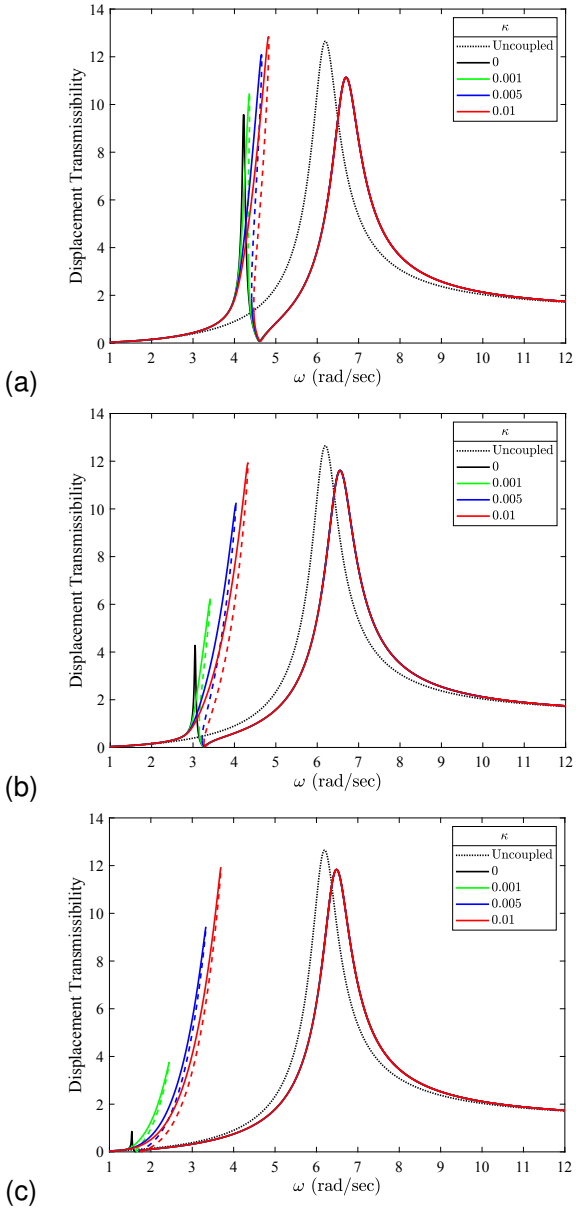

Figure B.9: Effect of nonlinearity parameter κ [in.$^{-2}$] on nonlinear transmissibility TR_{Δ_r} of the roof displacement, for Ω = (a) $\sqrt{2}$, (b) 2, and (c) 4, $\mu = 0.3$, $a = 1.414\ g$.

B.3.2 Isolated Mass Total Acceleration

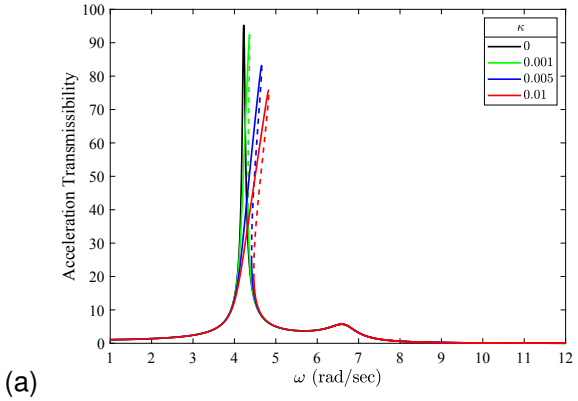

(a)

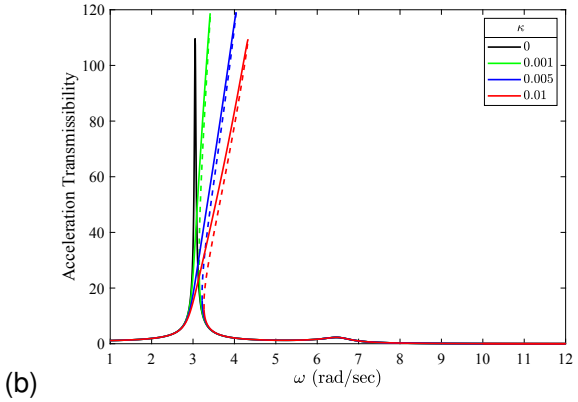

(b)

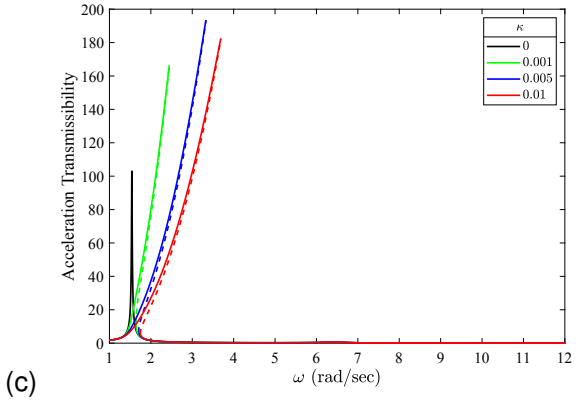

(c)

Figure B.10: Effect of nonlinearity parameter κ [in.$^{-2}$] on nonlinear transmissibility $\mathrm{TR}_{a_{\text{total}}}$ of the isolated mass total acceleration, for Ω = (a) $\sqrt{2}$, (b) 2, and (c) 4, $\mu = 0.3$, $a = 1.414\ g$.

B.4 Effect of Varying Excitation Amplitude Coefficient a

B.4.1 Roof Displacement

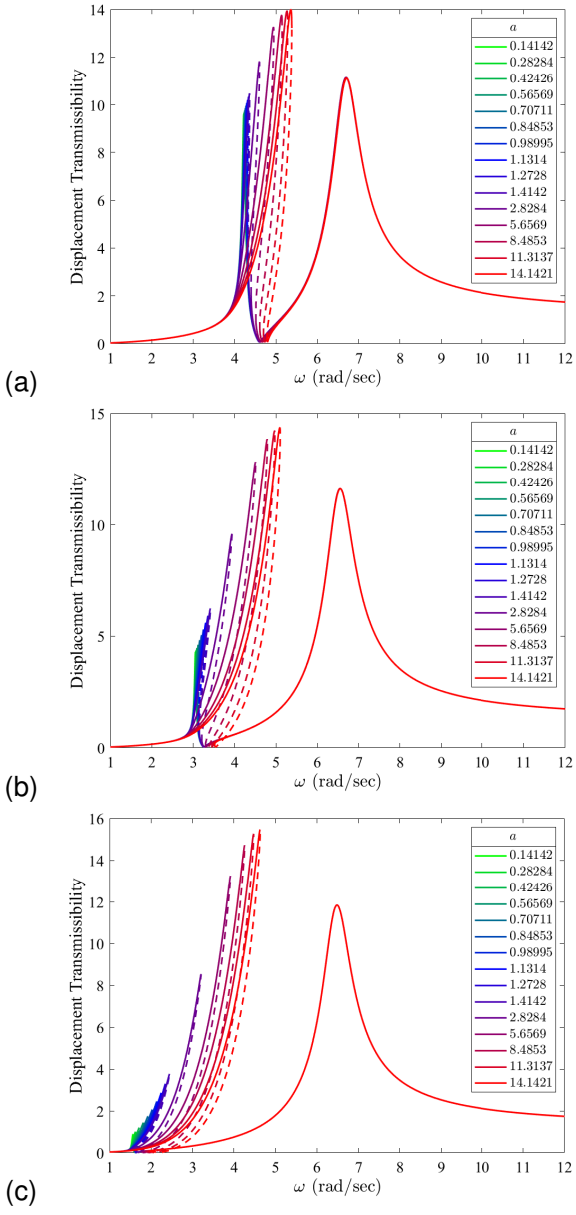

Figure B.11: Effect of excitation amplitude coefficient a [g] on nonlinear transmissibility TR_{Δ_r} of the roof displacement, for Ω = (a) $\sqrt{2}$, (b) 2, and (c) 4, $\mu = 0.3$, $\kappa = 0.001$ in.$^{-2}$.

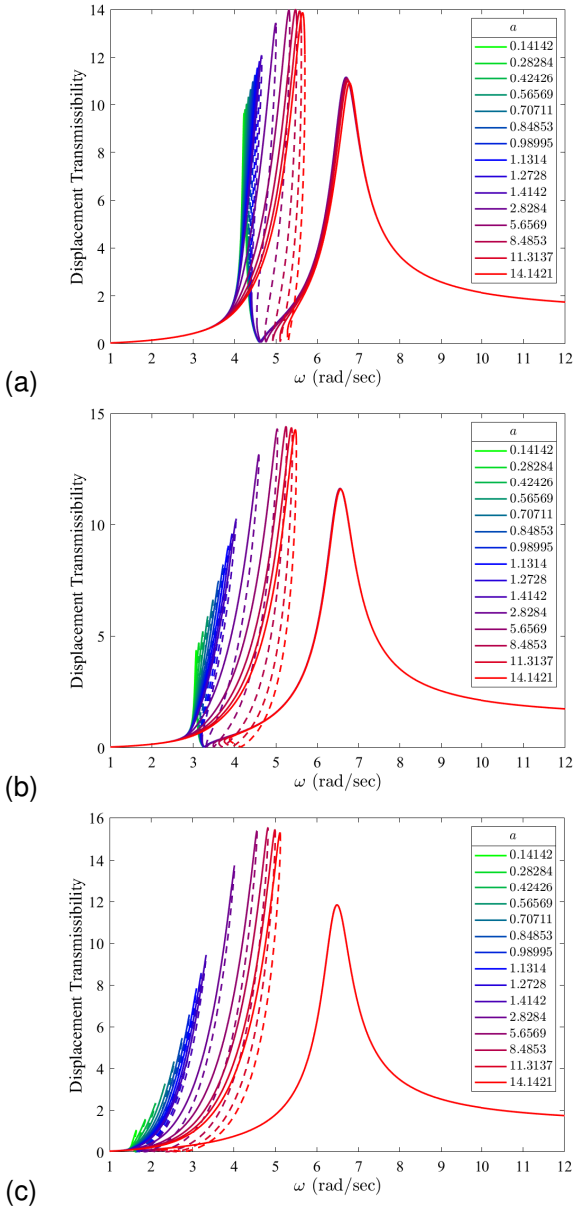

Figure B.12: Effect of excitation amplitude coefficient a [g] on nonlinear transmissibility TR_{Δ_r} of the roof displacement, for Ω = (a) $\sqrt{2}$, (b) 2, and (c) 4, $\mu = 0.3$, $\kappa = 0.005$ in.$^{-2}$.

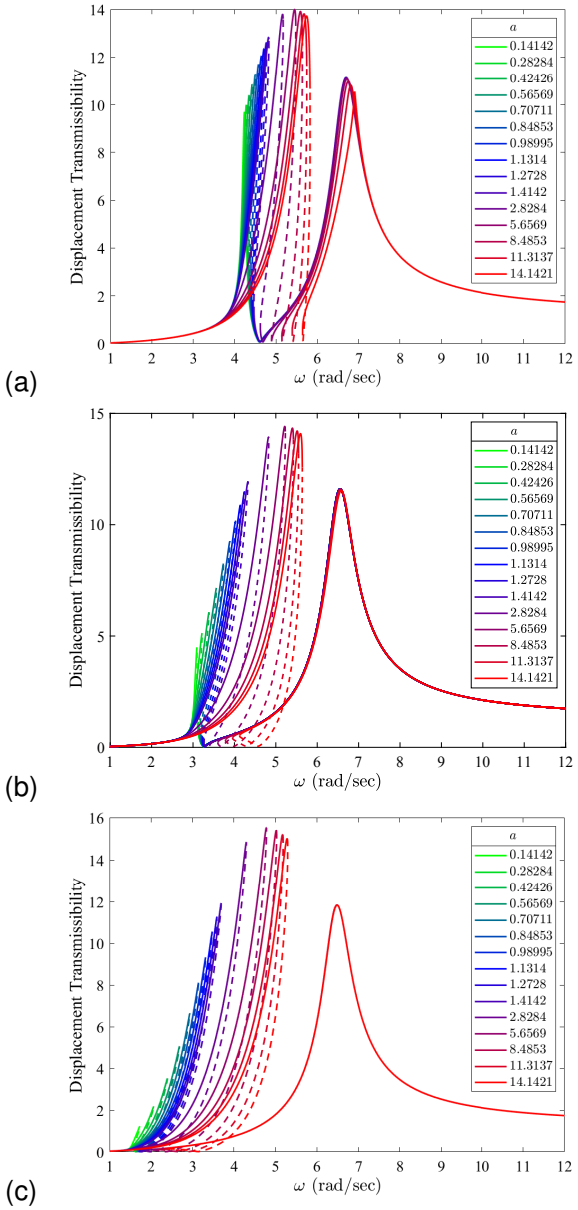

Figure B.13: Effect of excitation amplitude coefficient a [g] on nonlinear transmissibility TR_{Δ_r} of the roof displacement, for Ω = (a) $\sqrt{2}$, (b) 2, and (c) 4, $\mu = 0.3$, $\kappa = 0.01$ in.$^{-2}$.

B.4.2 Isolated Mass Total Acceleration

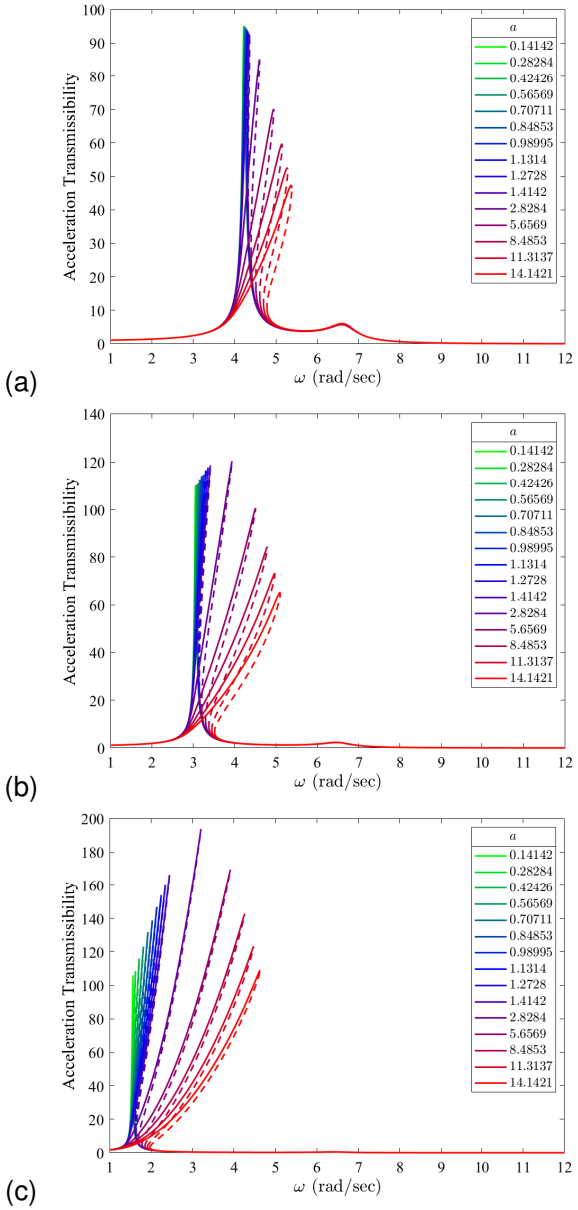

Figure B.14: Effect of excitation amplitude coefficient a [g] on nonlinear transmissibility $\mathrm{TR}_{a_{\text{total}}}$ of the isolated mass total acceleration, for Ω = (a) $\sqrt{2}$, (b) 2, and (c) 4, $\mu = 0.3$, $\kappa = 0.001$ in.$^{-2}$.

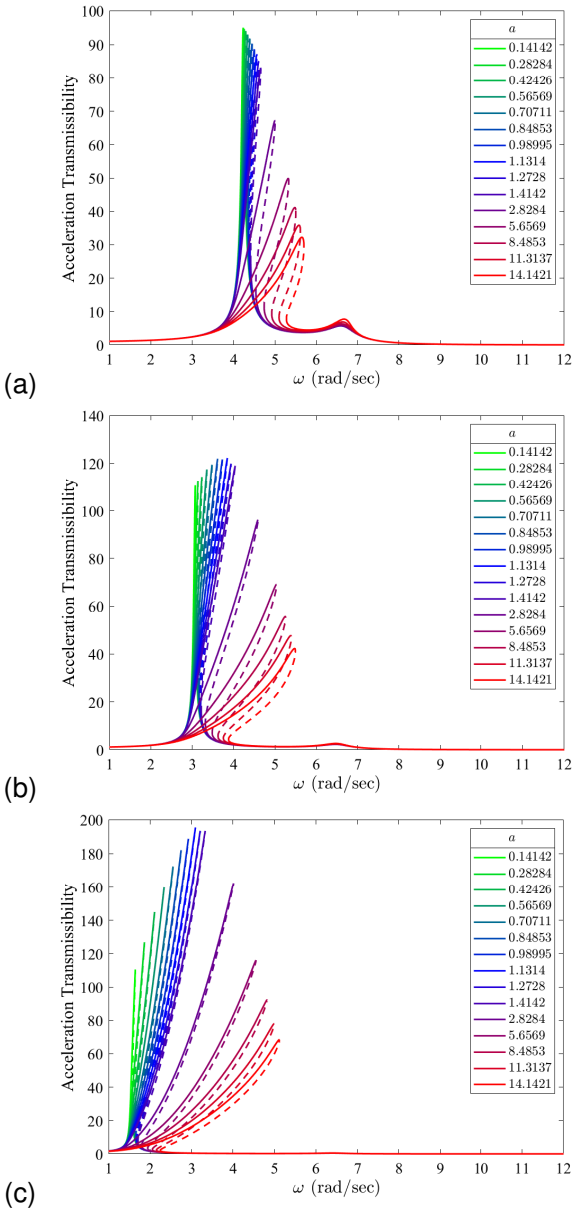

Figure B.15: Effect of excitation amplitude coefficient a [g] on nonlinear transmissibility $\mathrm{TR}_{a_{\text{total}}}$ of the isolated mass total acceleration, for Ω = (a) $\sqrt{2}$, (b) 2, and (c) 4, $\mu = 0.3$, $\kappa = 0.005$ in.$^{-2}$.

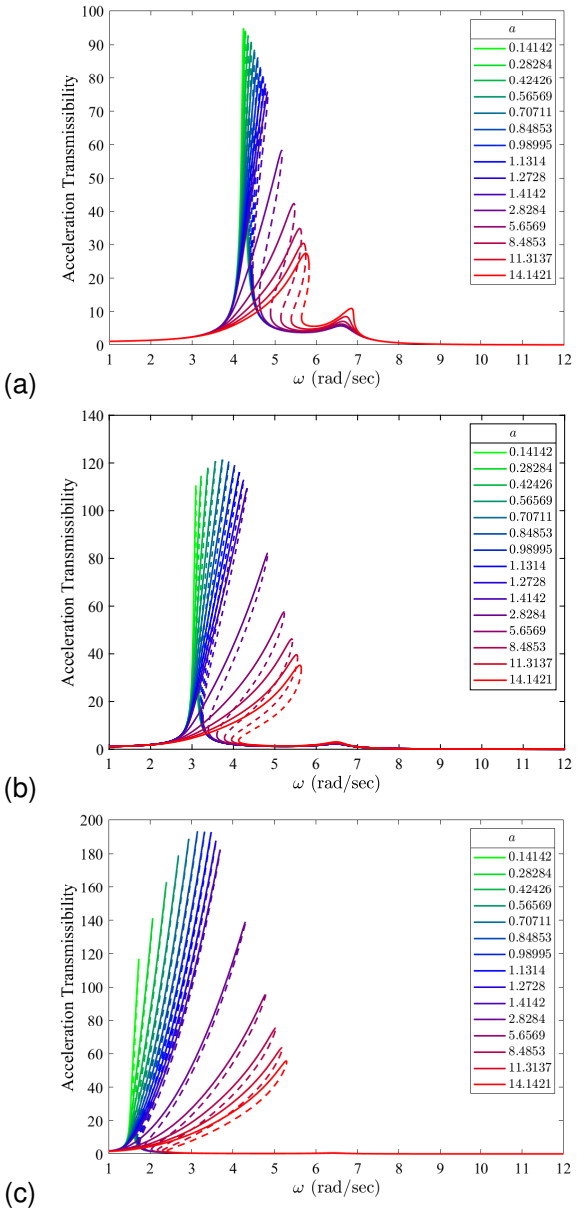

Figure B.16: Effect of excitation amplitude coefficient a [g] on nonlinear transmissibility $\mathrm{TR}_{a_{\text{total}}}$ of the isolated mass total acceleration, for Ω = (a) $\sqrt{2}$, (b) 2, and (c) 4, $\mu = 0.3$, $\kappa = 0.01$ in.$^{-2}$.